PhD Thesis

Finite Element Method with Embedded Strong Discontinuities for Coupled Hydro-Mechanical Problems

Danilo Borges Cavalcanti

Advisor: Dr. Deane Roehl Gattass
Advisor: Dr. Luiz Fernando Campos Ramos Martha
Advisor: Dr. Ignasi de Pouplana Sardà

This thesis was developed under a cotutelle agreement between Pontifícia Universidade Católica do Rio de Janeiro (PUC-Rio) and the Universitat Politècnica de Catalunya (UPC-BarcelonaTech).

Thesis presented to the Programa de Pós-Graduação em Engenharia Civil, Department of Civil and Environmental Engineering of PUC-Rio, and to the Doctoral Programme in Structural Analysis, Department of Civil and Environmental Engineering, Universitat Politècnica de Catalunya (UPC-BarcelonaTech), in partial fulfillment of the requirements for the doctoral degrees of Doutor em Engenharia Civil by PUC-Rio and Doctor by Universitat Politècnica de Catalunya.

Barcelona, April 20, 2026

Finite Element Method with Embedded Strong Discontinuities for Coupled Hydro-Mechanical Problems

Danilo Borges Cavalcanti

Thesis presented to the Programa de Pós-Graduação em Engenharia Civil, Department of Civil and Environmental Engineering of PUC-Rio, and to the Doctoral Programme in Structural Analysis, Department of Civil and Environmental Engineering, Universitat Politècnica de Catalunya (UPC-BarcelonaTech), in partial fulfillment of the requirements for the doctoral degrees of Doutor em Engenharia Civil by PUC-Rio and Doctor by Universitat Politècnica de Catalunya. Approved by the Examination Committee:

Dr. Deane Roehl Gattass
Advisor
Department of Civil and Environmental Engineering
PUC-Rio

Dr. Luiz Fernando Campos Ramos Martha
Advisor
Department of Civil and Environmental Engineering
PUC-Rio

Dr. Ignasi de Pouplana Sardà
Advisor
Universitat Politècnica de Catalunya
UPC-BarcelonaTech

Dr. Víctor Vilarrasa Riaño
CSIC

Dr. Leonardo José do Nascimento Guimarães
UFPE

Dr. Sebastià Olivella Pastellé
UPC-BarcelonaTech

Dr. Heber Agnelo Antonel Fabbri
Department of Civil and Environmental Engineering
PUC-Rio

Barcelona, April 20, 2026

Danilo Borges Cavalcanti

Graduated in Civil Engineering from the Federal University of Goiás (UFG) in 2020 and earned an M.Sc. in Structural Engineering from UFG in 2022 on topology optimization. He enrolled in the Ph.D. in Civil Engineering at PUC-Rio in 2022; in 2023 he joined the Ph.D. in Structural Analysis at the Universitat Politècnica de Catalunya (UPC-BarcelonaTech) under a formal co-tutelle with PUC-Rio.

Bibliographic data

Cavalcanti, Danilo Borges

Finite Element Method with Embedded Strong Discontinuities for Coupled Hydro-Mechanical Problems / Danilo Borges Cavalcanti; advisors: Deane Roehl Gattass, Luiz Fernando Campos Ramos Martha, Ignasi de Pouplana Sardà. – 2026.
164 f.: ill. color. 30 cm

Cotutelle between Pontifical Catholic University of Rio de Janeiro and UPC-BarcelonaTech.
Doctoral thesis – Pontifical Catholic University of Rio de Janeiro, Department of Civil and Environmental Engineering, 2026.
Includes bibliography.

1. Civil and Environmental Engineering – Theses. 2. Finite elements. 3. Embedded strong discontinuities. 4. Coupled hydro-mechanical problems. I. Roehl, Deane. II. Martha, Luiz Fernando Campos Ramos. III. de Pouplana, Ignasi. IV. Pontifical Catholic University of Rio de Janeiro. Department of Civil and Environmental Engineering. V. Universitat Politècnica de Catalunya. VI. Title.

CDD: 004

Acknowledgments

To my advisors, Prof. Deane Roehl, Prof. Luiz Fernando Martha, and Prof. Ignasi de Pouplana, for their guidance, for welcoming me in Rio de Janeiro and Barcelona, and for all the opportunities they have provided over the past years.

To Prof. Eugenio Oñate, for his advice, support, and for welcoming me to CIMNE.

To my colleagues at Tecgraf and CIMNE, in particular Cristian Mejia, Guillermo Casas, Carlos A. Mendes, Carlos Souza, and Rafael Rangel, for their collaboration.

To PUC-Rio, Tecgraf, UPC, and CIMNE for the institutional support, without which this work could not have been accomplished.

To all my professors, especially those at UFG, Sylvia, Renata, Fred, Zenon, and Daniel, for their encouragement, influence, and support in my pursuit of a doctoral degree.

Aos meus pais, Ruy e Luciene, e aos meus avós, Simone, Rael, Ruy e José, por todo o suporte e carinho, e por terem tornado possível que eu concluísse esta etapa.

I l'agraïment més important és per en Francesc: no ho hauria pogut fer sense tu.

I acknowledge the funding from: (i) the R&D project "Risk assessment of geological fault reactivation by CO_2 injection" (PUC-Rio/ ExxonMobil Exploração Brasil Ltda./ ANP) sponsored by ExxonMobil Exploração Brasil Ltda. under the ANP R&D levy regulation and ANP project number 23449-2; (ii) the grant TED2021-130510A-I00 funded by the "European Union NextGenerationEU/PRTR" and by MCIN/AEI/10.13039/501100011033.

This study was financed in part by the Coordenação de Aperfeiçoamento de Pessoal de Nível Superior - Brasil (CAPES) - Finance Code 001.

Abstract

Cavalcanti,Danilo Borges; Roehl, Deane (Advisor); Martha, Luiz Fernando (Co-Advisor); de Pouplana, Ignasi (Co-Advisor). **Finite Element Method with Embedded Strong Discontinuities for Coupled Hydro-Mechanical Problems**. Barcelona, 2026. 164p. Tese de Doutorado – Departamento de Civil and Environmental Engineering, Pontifical Catholic University of Rio de Janeiro.

Coupled hydro–mechanical (HM) processes in fractured porous media govern the performance and safety of several subsurface engineering applications, where pressure-driven changes in stress and permeability can control injectivity, leakage pathways, and fault reactivation potential. This thesis develops a robust and versatile finite element formulation for transient HM problems in the presence of pre-existing strong discontinuities that remains practical for integration into standard finite element workflows. The proposed approach is formulated within the Embedded Finite Element Method (E-FEM) and grounded on the Strong Discontinuity Approach (SDA), enabling an implicit representation of fractures and faults while circumventing mesh conformity constraints. A unified description is introduced to model discontinuities acting either as preferential flow paths or as hydraulic barriers, capturing the longitudinal flow along the discontinuity and the transversal exchange with the porous matrix in steady-state and transient settings. The formulation is systematically verified against discrete fracture models with interface elements and applied to benchmark problems representative of fractured-reservoir conditions, including a coupled fault reactivation scenario. In addition, the thesis investigates the occurrence of spurious oscillations in cohesive traction fields along embedded discontinuities and demonstrates that the choice of an SDA-based embedded formulation can markedly improve traction smoothness. These improvements strengthen the use of E-FEM for HM assessments involving pre-existing fractures and faults.

Keywords

Embedded Finite Element; Strong Discontinuity Approach; Coupled hydromechanical problems.

Resumo

Cavalcanti,Danilo Borges; Roehl, Deane; Martha, Luiz Fernando; de Pouplana, Ignasi. **Finite Element Method with Embedded Strong Discontinuities for Coupled Hydro-Mechanical Problems**. Barcelona, 2026. 164p. Tese de Doutorado – Departamento de Civil and Environmental Engineering, Pontifical Catholic University of Rio de Janeiro.

Processos hidromecânicos (HM) acoplados em meios porosos fraturados governam o desempenho e a segurança de diversas aplicações de engenharia de subsuperfície, nas quais alterações de tensão e permeabilidade induzidas pela pressão podem controlar a injetividade, caminhos de fuga e o potencial de reativação de falhas. Esta tese desenvolve uma formulação de elementos finitos robusta e versátil para problemas HM transientes na presença de descontinuidades fortes pré-existentes, mantendo-se prática para integração em fluxos de trabalho padrão de elementos finitos. A abordagem proposta é formulada no âmbito do Método dos Elementos Finitos Embutidos (E-FEM) e fundamentada na Abordagem de Descontinuidade Forte (SDA), permitindo a representação implícita de fraturas e falhas sem exigir conformidade de malha. Introduz-se uma descrição unificada para modelar descontinuidades que atuam tanto como caminhos preferenciais de escoamento quanto como barreiras hidráulicas, capturando o fluxo longitudinal ao longo da descontinuidade e a troca transversal com a matriz porosa em regimes estacionário e transiente. A formulação é verificada sistematicamente em comparação com modelos de fratura discreta com elementos de interface e aplicada a problemas de referência representativos de condições de reservatórios fraturados, incluindo um cenário acoplado de reativação de falhas. Além disso, a tese investiga a ocorrência de oscilações espúrias em campos de tensão coesiva ao longo de descontinuidades embutidas e demonstra que a escolha de uma formulação embutida baseada em SDA pode melhorar significativamente a suavidade e a confiabilidade das tensões coesivas, reforçando o uso do E-FEM para avaliações HM envolvendo fraturas e falhas pré-existentes.

Palavras-chave

Elementos Finitos; Descontinuidades Fortes Embutidas; Problemas Hidromecânicos Acoplados.

Resumen

Cavalcanti,Danilo Borges; Roehl, Deane; Martha, Luiz Fernando; de Pouplana, Ignasi. **Método de los Elementos Finitos con Discontinuidades Fuertes Embebidas para Problemas Hidromecánicos Acoplados**. Barcelona, 2026. 164p. Tese de Doutorado – Departamento de Civil and Environmental Engineering, Pontifical Catholic University of Rio de Janeiro.

Los procesos hidromecánicos (HM) acoplados en medios porosos fracturados gobiernan el rendimiento y la seguridad de numerosas aplicaciones de ingeniería del subsuelo, donde los cambios de tensiones y permeabilidad inducidos por la presión pueden controlar la inyectividad, las vías de fuga y el potencial de reactivación de fallas. Esta tesis desarrolla una formulación de elementos finitos robusta y versátil para problemas HM transitorios en presencia de discontinuidades fuertes preexistentes, manteniéndose práctica para su integración en flujos de trabajo estándar de elementos finitos. El enfoque propuesto se formula en el marco del Método de Elementos Finitos Embebidos (E-FEM) y se fundamenta en el Enfoque de Discontinuidad Fuerte (SDA), lo que permite una representación implícita de fracturas y fallas sin exigir conformidad de malla. Se introduce una descripción unificada para modelar discontinuidades que actúan tanto como vías preferenciales de flujo como barreras hidráulicas, capturando el flujo longitudinal a lo largo de la discontinuidad y el intercambio transversal con la matriz porosa en regímenes estacionario y transitorio. La formulación se verifica de forma sistemática frente a modelos de fractura discreta con elementos de interfaz y se aplica a problemas de referencia representativos de condiciones de reservorios fracturados, incluido un escenario acoplado de reactivación de fallas. Además, la tesis investiga la aparición de oscilaciones espurias en campos de tracción cohesiva a lo largo de discontinuidades embebidas y demuestra que la elección de una formulación embebida basada en SDA puede mejorar notablemente la suavidad y la fiabilidad de las tracciones, reforzando el uso de E-FEM para evaluaciones HM que involucren fracturas y fallas preexistentes.

Palabras clave

Elementos finitos embebidos; Enfoque de discontinuidad fuerte; Problemas hidromecánicos acoplados.

Resum

Cavalcanti,Danilo Borges; Roehl, Deane; Martha, Luiz Fernando; de Pouplana, Ignasi. **Mètode dels Elements Finits amb Discontinuïtats Fortes Incrustades per a Problemes Hidromecànics Acoblats**. Barcelona, 2026. 164p. Tese de Doutorado – Departamento de Civil and Environmental Engineering, Pontifical Catholic University of Rio de Janeiro.

Els processos hidromecànics (HM) acoblats en medis porosos fracturats governen el rendiment i la seguretat de diverses aplicacions d'enginyeria del subsòl, en què els canvis de tensió i permeabilitat induïts per la pressió poden controlar la injectivitat, les vies de fugida i el potencial de reactivació de falles. Aquesta tesi desenvolupa una formulació d'elements finits robusta i versàtil per a problemes HM transitoris en presència de discontinuïtats fortes preexistents, i que es manté pràctica per a la integració en fluxos de treball estàndard d'elements finits. L'enfocament proposat es formula en el marc del Mètode d'Elements Finits Encabit (E-FEM) i es fonamenta en l'Approach de Discontinuïtat Forta (SDA), cosa que permet una representació implícita de fractures i falles sense requerir conformitat de malla. S'introdueix una descripció unificada per modelar discontinuïtats que actuen tant com a camins preferents de flux com com a barreres hidràuliques, capturant el flux longitudinal al llarg de la discontinuïtat i l'intercanvi transversal amb la matriu porosa en règims estacionari i transitori. La formulació es verifica sistemàticament en comparació amb models de fractura discreta amb elements d'interfície i s'aplica a problemes de referència representatius de condicions de reservoris fracturats, incloent-hi un escenari acoblat de reactivació de falles. A més, la tesi investiga l'aparició d'oscil·lacions espúries en camps de tracció cohesiva al llarg de discontinuïtats encabides i demostra que l'elecció d'una formulació encabida basada en SDA pot millorar de manera notable la suavitat i la fiabilitat de les traccions, reforçant l'ús d'E-FEM per a avaluacions HM que impliquin fractures i falles preexistents.

Paraules clau

Elements finits incrustats; Enfocament de discontinuïtat forta; Problemes hidromecànics acoblats.

Table of contents

List of figures

List of tables

List of Abreviations

CFE	–	Coupling Finite Element
DE-FEM	–	Discontinuity-Enriched Finite Element Method
DFM	–	Discrete Fracture Model
DOF	–	Degree of Freedom
DPDP	–	Dual-porosity/Dual-permeability
EAS	–	Enhanced Assumed Strain
ECM	–	Equivalent Continuum Method
E-FEM	–	Embedded Finite Element Method
EGS	–	Enhanced Geothermal System
FDM	–	Finite Difference Method
FEM	–	Finite Element Method
FVM	–	Finite Volume Method
HAR	–	High-Aspect Ratio
HM	–	Hydro-Mechanical
KOS	–	Kinematically Optimal Symmetric
OOP	–	Object Oriented Programming
PDE	–	Partial Differential Equation
RVE	–	Representative Elementary Volume
SDA	–	Strong Discontinuity Approach
SKON	–	Statically and Kinematically Optimal Nonsymmetric
SOS	–	Statically Optimal Symmetric
THM	–	Thermo-Hydro-Mechanical
UML	–	Unified Modeling Language
XFEM	–	Extended Finite Element Method

1
Introduction

1.1
Motivation

The safe and efficient use of the subsurface increasingly relies on large-scale operations that perturb the in-situ pore-pressure and stress fields of fractured porous media. Such perturbations are inherent to geological storage of carbon dioxide (CO_2) [11, 12], underground storage of hydrogen (H_2) [13, 14], enhanced geothermal systems (EGS) [15, 16, 17, 18], and deep geological repositories for nuclear waste [19, 20, 21, 22]. Across these application domains, pre-existing fractures and faults frequently dominate system response, because they concentrate deformation, control permeability anisotropy, and provide preferential pathways or barriers for fluid migration. Besides, these operations lead to coupled processes: pore-pressure diffusion alters effective stresses and may promote slip and aperture changes, while the evolving fracture state feeds back into permeability and pressure propagation [1, 23, 24]. This coupled hydro-mechanical (HM) setting is summarized schematically in Fig. 1.1, which highlights near-well interactions between matrix deformation, matrix–fracture transfer, and stress- and slip-dependent transmissivity.

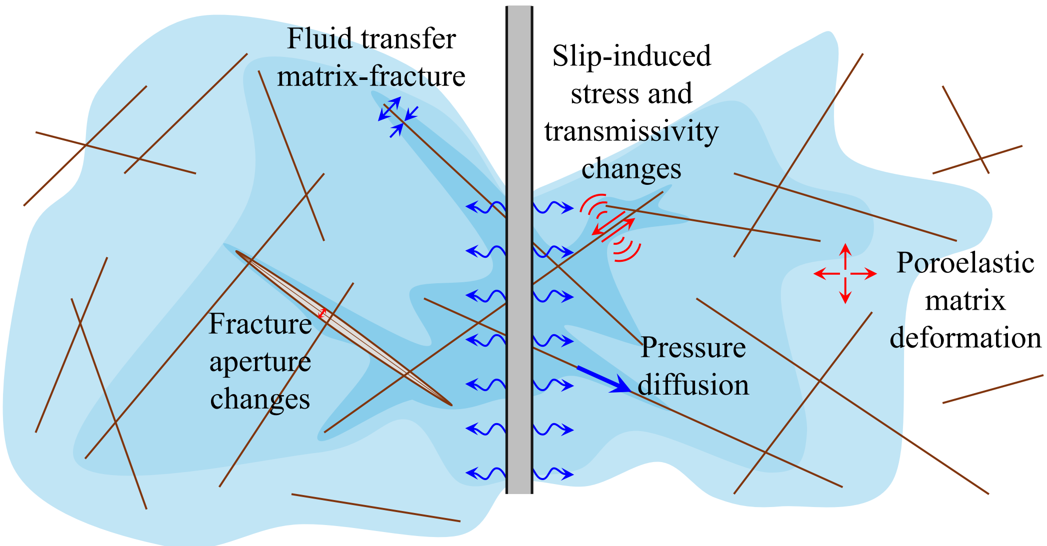

Figure 1.1: Representation of coupled HM processes in a fractured porous medium in the vicinity of an injection well (adapted from Vaezi et al. [1])

These issues are central to geological CO_2 storage, where injection-induced pressurization is used to place CO_2 into deep formations while maintaining containment over long timescales [25]. Field and numerical studies have shown that relatively modest changes in pressure and temperature can activate critically stressed faults, alter permeability, and trigger felt seismicity, with consequences that range from loss of injectivity to leakage risk or induced earthquakes [11, 12, 26, 27, 28]. In this context, fault reactivation is a primary integrity concern because slip and transmissivity changes can connect pressurized reservoirs to overlying formations, and seismic events may undermine public acceptance and regulatory feasibility. Figure 1.2 shows the potential impacts of fault reactivation during CO_2 injection.

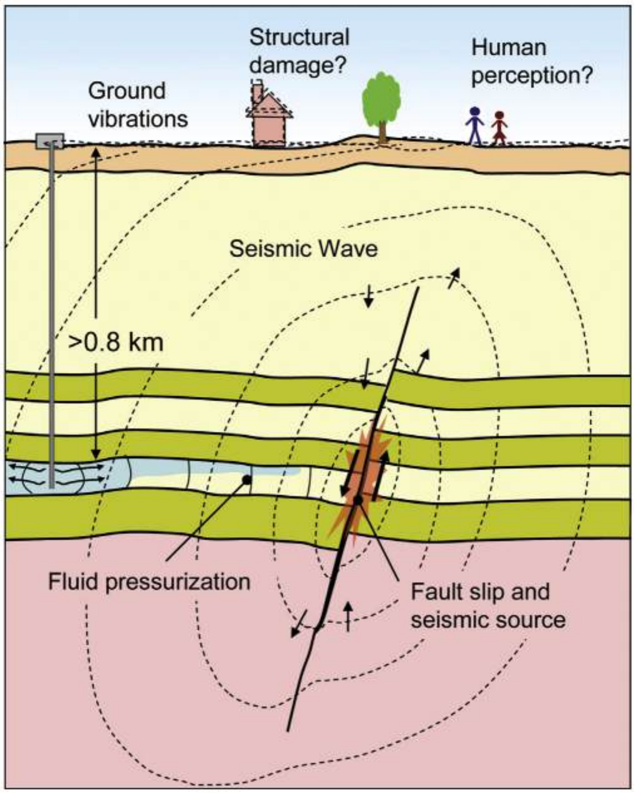

Figure 1.2: Fault reactivation induced due to CO_2 injection and its potential impacts [2]

Across CO_2 storage, H_2 storage, EGS, and nuclear waste disposal, the most critical operational risks and performance limits are tied to the HM response of fractures and faults-reactivation of critically stressed discontinuities, stress-dependent changes in transmissivity and connectivity, and interactions between stimulated and pre-existing fracture sets [1, 24]. Besides, the available field data, while essential, is typically insufficient to fully characterize these coupled mechanisms or to extrapolate behavior to future operational scenarios. For these reasons, numerical simulations based on coupled HM formulations play a central role in subsurface engineering practice and research. They are used to [29]:

- Site characterization and operational planning: help determine the injection capacity [30], and specify operating conditions, such as injection pressure and volume, avoiding fault reactivation and fracture initiation [31];
- Risk assessment: assess fault stability, induced-seismicity, and leakage potential [32, 33, 34];
- Interpret monitoring data: verify that the project is operating as predicted by verifying the monitoring result with the simulation ones, as surface deformation, microseismicity, and pressure records in terms of subsurface stress and permeability evolution [35, 36].

This motivates the development of robust coupled HM numerical tools that can represent pre-existing strong discontinuities, while remaining practical for large-scale applications.

1.2 Objectives

The primary objective of this thesis is to develop a robust and versatile numerical formulation for transient hydro-mechanical processes in fractured porous media that:

- provides a simple and practical workflow for model set-up and analysis;
- accommodates a wide range of scenarios relevant to subsurface engineering applications;
- can be integrated into standard finite element (FE) frameworks with minimal modifications.

To achieve the primary objective, the following specific objectives are pursued:

- to adopt an embedded representation in which discontinuities are introduced implicitly, simplifying model and mesh generation;
- to formulate a fully coupled hydro–mechanical approach in which discontinuities may act either as barriers or as preferential flow paths, while remaining applicable to transient problems;
- to enable an element-level treatment of discontinuity-related degrees of freedom through static condensation, facilitating incorporation into existing FE codes;
- to conduct a systematic numerical assessment of the behavior of embedded formulations, with emphasis on their influence on spurious oscillations of cohesive tractions.

1.3 Thesis outline

This thesis is presented as a compendium of articles. The purpose of this document is to provide a unified presentation of the formulations and the supporting literature review underlying the included publications.

Chapter 1 introduces the motivation and objectives, and summarizes the scientific context and research outputs. Chapter 2 reviews the state of the art on the finite element modeling of strong discontinuities in porous media. Chapter 3 presents the strong form of the governing equations for coupled hydro–mechanical processes in deformable porous media with strong discontinuities. Chapter 4 develops the embedded finite element formulation based on the Strong Discontinuity Approach. Chapter 5 summarizes the main contributions and outlines perspectives for future work.

The articles forming the compendium are included in Appendix A. Appendix B details the elastoplastic cohesive law adopted in the mechanical formulation. Appendix C presents the derivation of the enhanced deformation modes. Appendix D collects the derivations and definitions of the discretized system matrices and vectors.

1.4 Research dissemination

Articles in peer-reviewed journals

This thesis is presented as a compendium of the following articles:

1. Cavalcanti, D., Mejia, C., Roehl, D., de-Pouplana, I., Casas, G., and Martha, L. F. (2024). Embedded Finite Element formulation for fluid flow in fractured porous medium. *Computers and Geotechnics*, 171, 106384.

2. Cavalcanti, D., Mejia, C., Roehl, D., de-Pouplana, I., and Oñate, E. (2024). Hydromechanical embedded finite element for conductive and impermeable strong discontinuities in porous media. *Computers and Geotechnics*, 172, 106427.

3. Cavalcanti, D., Mejia, C., Souza, C., Mendes, C. A., de-Pouplana, I., Casas, G., Roehl, D. (2025). Behavior of Cohesive Stresses in Embedded Finite Elements Based on the Strong Discontinuity Approach. *Finite Elements in Analysis and Design*, 253, 104485.

Presentations at international conferences

During the PhD, the partial advances and results were presented in the following international conferences:

1. XLIII Ibero-Latin-American Congress on Computational Methods in Engineering (CILAMCE 2022), Foz do Iguaçu/PR, Brazil, November 21–25, 2022.

2. XVII International Conference on Computational Plasticity (COMPLAS 2023), Barcelona, Spain, September 5–7, 2023.

3. XLIV Ibero-Latin-American Congress on Computational Methods in Engineering (CILAMCE 2023), Porto, Portugal, November 13–16, 2023.

4. 9$^{\text{th}}$ European Congress on Computational Methods in Applied Sciences and Engineering (ECCOMAS 2024), Lisbon, Portugal, June 3–7, 2024.

5. XVIII International Conference on Computational Plasticity (COMPLAS), Barcelona, Spain, September 2–5, 2025.

Numerical implementations

The computational implementations were performed in the multiphysics framework GeMA (Geo Modeling Analysis), a C++ framework for multiphysics and multiscale simulations that offers plugin-based extensibility, Lua-scripted orchestration, and coupling of multiple physics on distinct meshes.[1] [37, 38].

For prototyping the numerical formulations, a MATLAB framework named `PorousLab`[2] was developed by the author. It is an open-source, object-oriented finite element (FEM) framework designed to facilitate rapid prototyping and teaching of coupled porous-media formulations.

[1] https://web.tecgraf.puc-rio.br/gema/
[2] https://github.com/dbcavalcanti/porousLab

2
Finite element modeling of strong discontinuities

A variety of numerical methods are available for the numerical simulation of deformation and flow in geomaterials, including finite difference methods (FDM), finite volume methods (FVM), the finite element method (FEM), boundary element methods (BEM), discrete or distinct element methods (DEM), and hybrid finite–discrete approaches [39, 40, 41]. For solid mechanics and for many coupled thermo–hydro–mechanical (THM) applications in geomaterials, finite elements are the reference method. FEM emerges naturally from a variational weak form of the balance equations, handles unstructured meshes and arbitrary element shapes with high-order interpolation, and is particularly well suited to complex constitutive models, mixed formulations, and multi-field couplings [42]. Consequently, many widely used multiphysics simulators adopt FEM such as GeMA [37, 38], CODE_BRIGHT [43], OpenGeoSys [44], and MOOSE [45].

In this chapter, a review of commonly used approaches for strong discontinuities modelling based on the FEM for hydromechanical problems is presented, with emphasis on discrete fracture models (DFM), equivalent continuum models (ECM), the extended finite element method (XFEM), the Discontinuity-Enriched Finite Element Method (DE-FEM), and embedded finite element methods (E-FEM). Beyond these formulations, several other FEM-based strategies have been proposed for the numerical treatment of fractures in geomaterials. Examples include coupling finite elements (CFE) [46, 47], Lagrange multipliers [48, 49], phase-field approaches to fracture [50, 51, 52, 53], and discontinuous Galerkin formulations [54, 55]. Comprehensive reviews are available on general numerical methods in rock mechanics [39], computational methods for fracture in brittle and quasi-brittle solids [40], finite-element-based models for quasi-brittle cracking [56], flow in fractured porous media [23], and THM modeling of coupled processes in fractured rock [1].

2.1
Discrete fracture models

In a discrete fracture model, fractures are represented explicitly as lower-dimensional entities in the continuum domain. In the finite element context, this is typically achieved either by inserting zero-thickness interface elements along element boundaries [57, 58, 59, 60, 61, 62, 63], or by using high-aspect-ratio (HAR) elements [64, 65, 66, 67], as illustrated in Fig 2.1. Their main difference lies in the fact that the interface elements require a traction-separation law or a fracture-specific transmissivity and storage model [58, 59, 61, 68]. In contrast, HAR elements use continuum constitutive laws, since they are formulated based on the Continuum Strong Discontinuity Approach [69, 70].

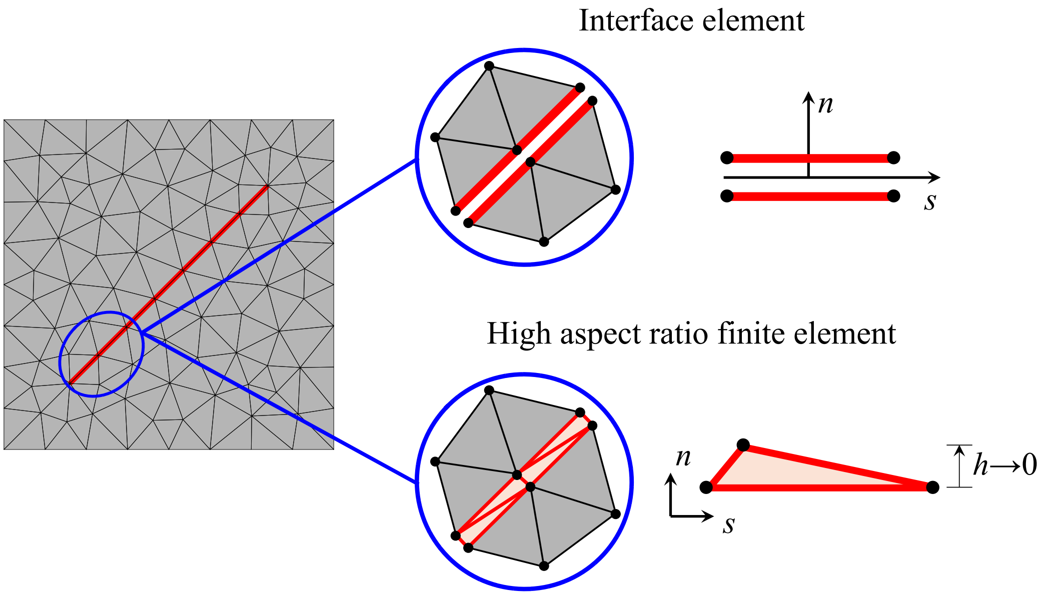

Figure 2.1: Discrete fracture model with interface elements

The main advantage of DFM formulations is their physical transparency. Since fractures are explicitly represented, it is straightforward to prescribe different mechanical or hydraulic properties to the fractures and the surrounding matrix, track opening, sliding, or aperture evolution, and post-process quantities along the discontinuity [58, 59, 60]. This explicit representation also facilitates the incorporation of complex interface laws, for example nonlinear cohesive behavior, contact, or aperture-dependent flow, and makes it possible to combine different fracture types within the same model, from highly conductive to nearly sealing fractures [61, 62, 68].

The main drawback is the strong constraint imposed on mesh generation: the grid must conform to each fracture and to all their intersections, which becomes particularly demanding in three dimensions and for dense or stochastic networks [60, 23, 71]. Constructing high-quality conforming meshes can require algorithms that balance geometric fidelity and element quality, since the resulting mesh may contain very small or highly stretched elements that degrade conditioning and restrict the time step in transient analyses [57, 72]. Recent work on fracture-conforming mesh generation for DFM has addressed many of these issues but still highlights the trade-off between geometric fidelity and mesh quality in complex fracture networks [72, 73, 74, 75, 71].

DFM approaches have been widely used in different multiphysics settings. For flow problems, DFM formulations have been used for single-phase Darcy flow and multiphase flow in fractured reservoirs [76, 77], as documented in benchmark studies and reviews of conceptual and numerical models for fractured porous media [57, 23]. For practical coupled hydromechanical problems, it has been successfully used in applications such as assessing fault reactivation [78, 79, 80, 81, 82] and hydraulic fracturing [68, 83, 84].

2.2 Continuum approaches

Equivalent continuum models treat the fractured rock mass as an effective porous medium in which the detailed fracture geometry is not resolved explicitly. Instead, the combined effect of fractures and matrix is represented through upscaled properties such as permeability, porosity, storage capacity, thermal and mechanical parameters [85]. Within this family, single-continuum, and multi-continuum formulations can be distinguished, together with more recent variants such as the equivalent fracture layer concept [86]. These approaches are well established in hydrogeology and reservoir engineering and are increasingly used for coupled thermo–hydro–mechanical simulations in fractured rock [87, 88, 1].

In single-continuum or equivalent porous medium (EPM) models, the fractured formation is described by a single Darcy continuum with an effective permeability tensor and porosity that account for both matrix and fractures. Upscaling procedures include analytical effective-medium approaches based on fracture orientation, aperture, and density [89, 90] and numerical upscaling, in which fine-scale flow problems are solved to obtain grid-block permeabilities and, when needed, anisotropic tensors [91, 87, 88]. These models are computationally efficient and straightforward to implement in standard finite element formulations for flow and coupled hydro–mechanical problems, as the only change is in the determination of the constitutive parameters based on homogenized coefficients/tensors.

The applicability of single-continuum models is conditioned by the existence of a representative elementary volume (REV) and a sufficient scale separation between fractures and the numerical grid [23, 92]. When fracture spacing is small compared to the element size and fracture connectivity is high, an equivalent permeability tensor can be defined that reproduces the large-scale flow response of the discrete system [89, 87]. In contrast, when the fracture network is sparse, strongly channelized, or dominated by a few major features, equivalent continuum properties become highly scale-dependent and may fail to capture preferential pathways or strong heterogeneities.

Multi-continuum models extend the EPM concept by representing fractures and matrix as overlapping continua coupled by transfer terms, as sketched in Fig. 2.2. In classical double-porosity and dual-permeability (DPDP) formulations, the fractured rock is decomposed into a high-permeability, low-storage fracture continuum and a low-permeability, high-storage matrix continuum, with mass exchange governed by transfer functions or shape factors derived from idealized block geometries such as the sugar-cube model [93, 94, 95, 96]. In this view, the DPDP system superposes a fracture continuum onto the rock-matrix continuum, and the fracture network enters the model mainly through the structure and parameters of the transfer function, Fig. 2.2. The multiple interacting continua (MINC) method and subsequent multiple-continuum generalizations refine this idea by introducing nested continua to resolve gradients inside the matrix blocks or additional pore domains [97, 98]. These formulations have been extended to coupled THM settings through double-porosity poromechanical models, in which separate pressures and, in some cases, temperatures are assigned to fractures and matrix, and the effective stress law is generalized accordingly [99, 100].

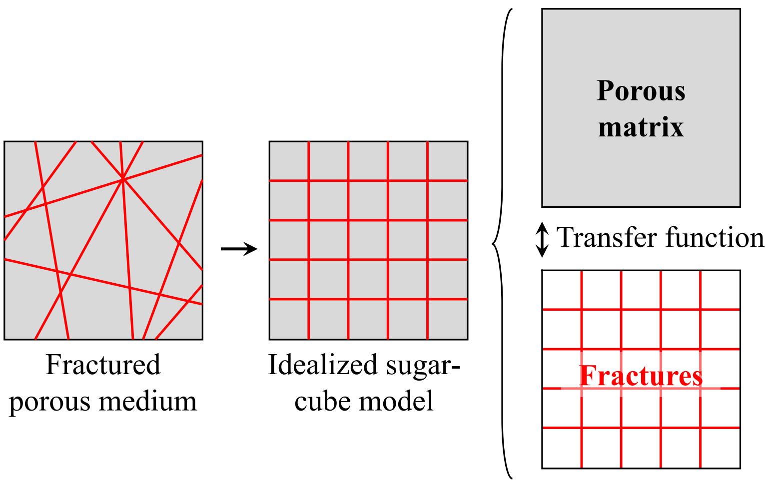

Figure 2.2: Schematic DPDP representation of a fractured porous medium: overlapping fracture and matrix continua coupled through a transfer function, typically derived from an idealized sugar-cube conceptualization of the fracture network

In practice, standard DPDP formulations rely on transfer functions calibrated for relatively regular and homogeneous fracture configurations, and are therefore unsuitable for complex or highly heterogeneous fracture networks [95, 96]. Recent work has begun to relax this limitation by using machine-learning techniques to infer effective transfer functions from detailed discrete-fracture simulations, thus extending the DPDP concept to more irregular fracture systems [101].

The main advantage of multi-continuum models is their ability to capture fracture–matrix interaction without resolving individual fractures in the numerical mesh. This makes them particularly attractive for large-scale simulations and for problems with strong contrasts between fracture and matrix hydraulic or mechanical properties. Their limitations stem from the underlying conceptual assumptions (idealized block geometry, parameterization of shape factors, choice and structure of the continua) and from the difficulty of calibrating exchange terms from field data. Moreover, because fractures are not explicitly represented, it is challenging to resolve localized mechanical responses such as fracture opening/closure, shear slip, or strongly anisotropic stress redistributions. To alleviate some of these drawbacks, Vaezi et al. [86] proposed an enhanced equivalent-continuum formulation, termed Equivalent Fracture Layer, for linear-elastic porous media, which preserves fracture transmissivity, storage, and stiffness so as to recover the dominant features of flow, stress, and deformation. A similar concept is used by Constitutive Law with Embedded Discontinuity (CLED) [102, 103], which defines equivalent constitutive tensors, considering the presence of a strong discontinuity, in hydro-mechanical problems.

2.3 Extended/Generalized Finite Element Method

The Extended finite element method (XFEM) allows discontinuities to be represented without having the finite element mesh conform to their geometry, as shown in Fig. 2.3. This is achieved through an enrichment of the primary fields following a Partition of Unity to discretize them [104, 105, 106, 107, 108, 109].

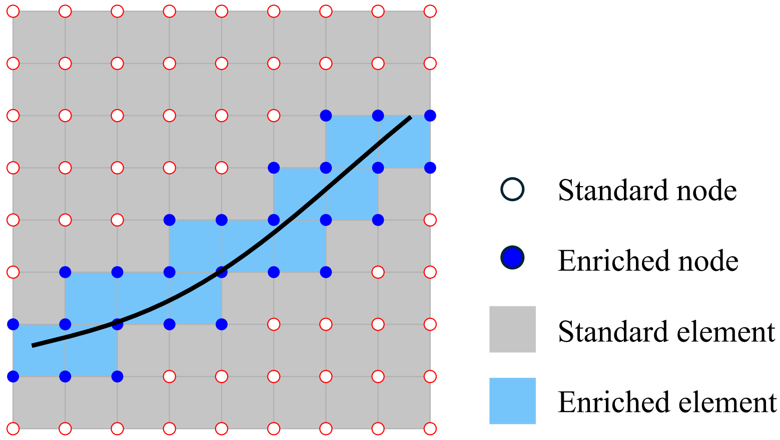

Figure 2.3: XFEM mesh for a domain with a strong discontinuity (Adapted from Khoei [3])

The main advantages of XFEM for fracture modeling stem from the mesh-independence of the discontinuity representation. Since the discontinuity geometry does not need to conform to element boundaries, it is possible to introduce complex fracture networks (non-planar, branched, intersecting) and to let them propagate according to local fracture criteria without remeshing. This approach is particularly attractive in three dimensions and when fracture paths are not known a priori [107, 110, 3]. XFEM maintains the continuum finite element framework in the bulk, so that it can be coupled with advanced constitutive models, poromechanical formulations, and multi-field couplings in a relatively natural way [3]. Cohesive and frictional laws along the discontinuity can be implemented directly in the enriched formulation, which allows one to describe, within a single framework, crack initiation and propagation, opening/closure, shear slip, and possible reactivation of pre-existing fractures in response to changes in stress and pore pressure [110, 111]. Several works have also shown that, when appropriate enrichments and integration strategies are used, XFEM formulations can be made equivalent to zero-thickness interface elements, providing a useful bridge between interface-based DFMs and enriched formulations [112].

These advantages come at the price of several numerical and implementation difficulties. Accurate integration over cut elements is nontrivial, especially in three dimensions and in the presence of multiple or intersecting discontinuities. In this case, numerical integration may require elaborate subcell constructions or high-order quadrature rules [113], as illustrated in Figure 2.4. Overall, XFEM formulations are considerably more complex to implement than classical interface-element DFMs or equivalent continuum approaches [114, 3].

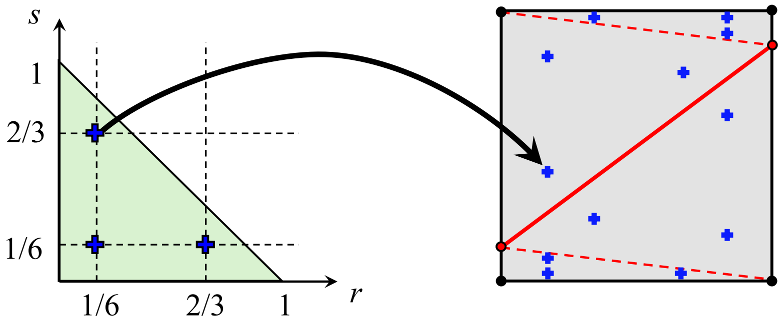

Figure 2.4: Example of numerical integration in a quadrilateral element cut by a discontinuity using subcell quadrature.

Despite these challenges, XFEM has been extensively used to model geological media, particularly in problems that couple deformation and fluid flow in fractured rocks. In this context, discontinuities can be represented either as highly conductive features or as barriers to flow, allowing XFEM to capture a wide range of hydraulic behaviors in fractured systems [115, 116, 117]. In coupled hydro–mechanical settings, XFEM has been adopted to model fracture initiation and propagation in saturated and multiphase porous media, including two-phase fluid flow in deformable fractured rock and THM fracture processes [111, 118, 119]. More specialized developments employ XFEM to simulate hydraulic fracturing in porous formations with proppant transport and tip screen-out [118, 120].

2.4 Discontinuity-Enriched Finite Element Method

The Discontinuity-Enriched Finite Element Method (DE-FEM) was proposed by Aragón and Simone [4] as an enriched finite element formulation for problems with weak and strong discontinuities, while keeping the finite element mesh independent of the discontinuity geometry. In DE-FEM, the background mesh is left unchanged and elements intersected by interfaces or cracks are subdivided into an internal integration mesh. On this submesh, enrichment functions are built as linear combinations of the Lagrange shape functions of the integration elements so that they reproduce jumps in the primary field and/or in its gradient along the discontinuity, as illustrated in Fig. 2.5. Additional enriched degrees of freedom are attached to the nodes created at the intersections between the discontinuity and the finite element mesh, are shared by all neighbouring cut elements, and are treated as global variables. The enrichment functions are constructed to vanish at all original mesh nodes, which preserves the Kronecker-delta property of the standard finite element basis and allows essential boundary conditions to be prescribed exactly at physical nodes, as in classical FEM.

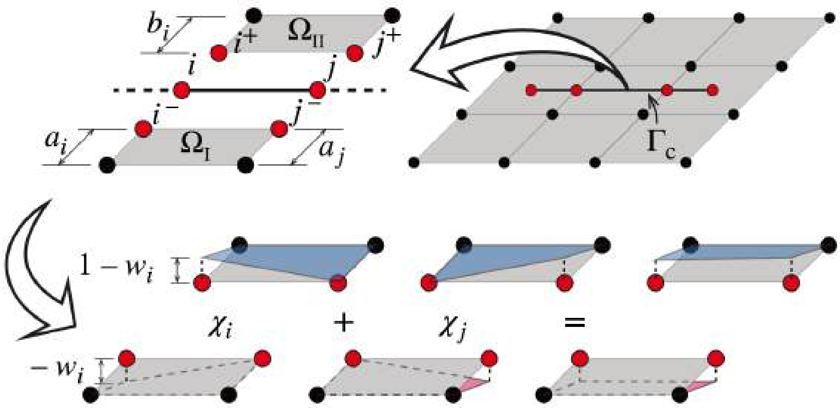

Figure 2.5: Example of construction of the discontinuous enrichment function in a quadrilateral element cut by a crack [4].

For problems with strong discontinuities, DE-FEM introduces both weak and strong enrichment functions associated with the same enriched nodes [4, 5]. In both two and three-dimensional settings, geometric processing is required to generate a conforming integration mesh inside cut elements and to manage the hierarchical subdivision induced by multiple weak and strong discontinuities within a single element [5], as shown in Fig. 2.6. This hierarchical construction has been further exploited to treat complex configurations such as intersecting cracks, multi-material junctions, and polycrystalline microstructures within a unified formulation [121, 122].

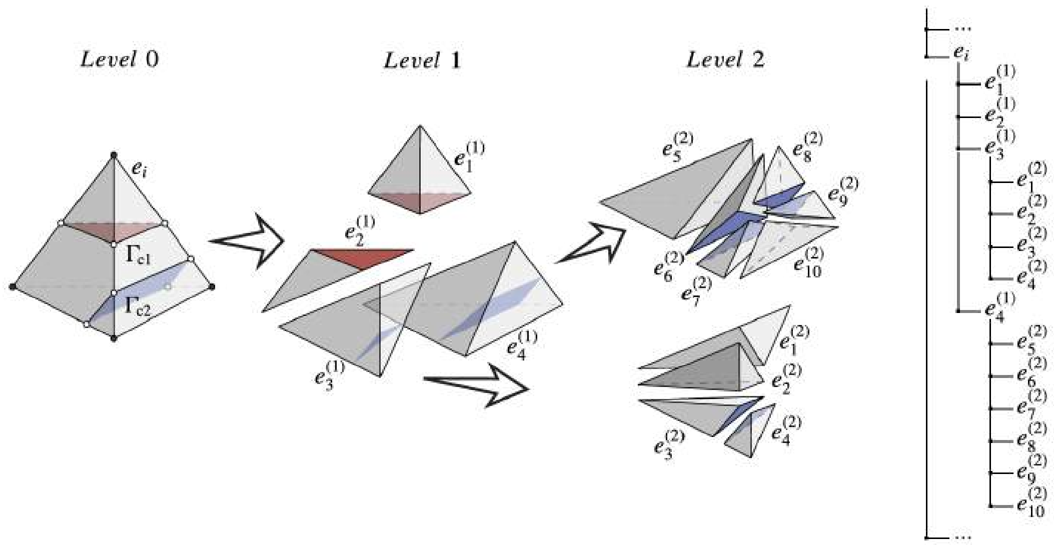

Figure 2.6: Hierarchical subdivision of a tetrahedral element cut by two discontinuities in the DE-FEM [5].

Compared with XFEM, DE-FEM preserves the mesh-independent representation of discontinuities but with a more compact and standard finite element structure. Enriched degrees of freedom are associated only with nodes lying on the discontinuity, rather than with all nodes of intersected elements, Fig. 2.3, so the increase in global unknowns is moderate and scales primarily with the extension of the discontinuity [4, 5]. The original nodal unknowns and connectivity remain unchanged, which simplifies implementation and facilitates the strong imposition of Dirichlet boundary conditions, including in immersed-boundary applications [123]. Numerical studies show that DE-FEM achieves convergence rates comparable to fitted-mesh FEM for problems without singular fields and that the conditioning of the global stiffness matrix scales with mesh size in essentially the same way as for standard FEM, indicating good stability under mesh refinement [5, 123].

To date, DE-FEM developments have focused almost exclusively on solid and fracture mechanics applications. Extensions of the method to model flow in porous media or fully coupled hydro–mechanical and THM processes in fractured rock have not yet been reported. The DE-FEM is reviewed here because it shares several key features with XFEM and with the E-FEM formulations.

2.5 Embedded Finite Element Method

The Embedded Finite Element Method (E-FEM) shares with XFEM and DE-FEM the goal of representing discontinuities without forcing the mesh conformity to discontinuity geometry, and both rely on enrichment functions to capture their presence. The key difference lies in the localization of the enrichment [7, 124, 125]. In classical XFEM, based on the partition-of-unity concept, enriched degrees of freedom (DOFs) are attached to the nodes of the background mesh and are shared by neighbouring elements, Fig. 2.3, which leads to a global increase in the system size. In the original SDA-based embedded formulations, the discontinuity is introduced at the element level through internal enhanced modes. These additional DOFs are local to the element and are typically eliminated by static condensation, so that they do not appear as global unknowns. The cost of this local treatment for the discontinuity inside the element is that the enriched field is generally non-conforming: neighbouring elements may represent slightly different discontinuity kinematics along a common embedded surface, producing the kind of non-matching behaviour illustrated in Fig. 2.7 [6, 56].

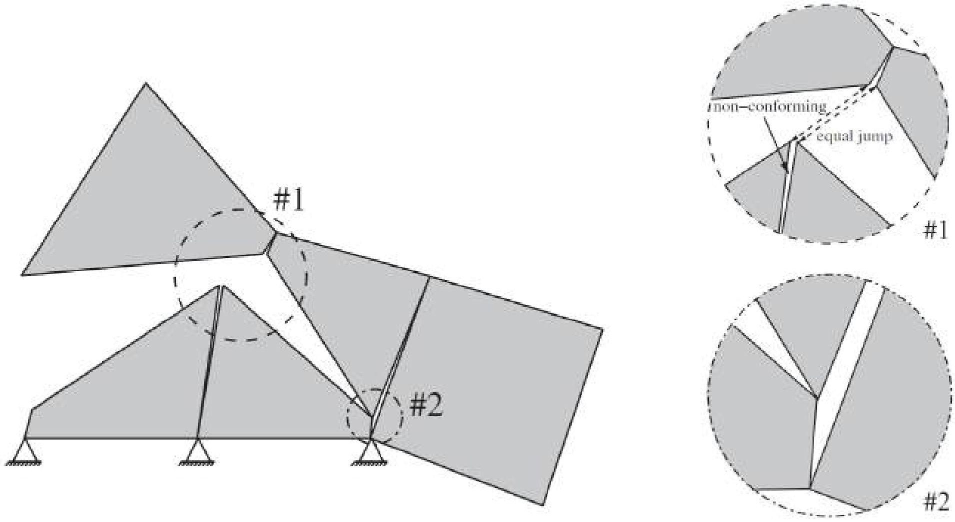

(a) Deformed mesh (b) Details

Figure 2.7: Non-conformity in E-FEM [6].

2.5.1 Classes of E-FEM formulations

There are different classes of embedded strong-discontinuity formulations. They differ not only in where the enriched DOFs are placed, but also in whether these DOFs are eliminated by element-level static condensation, in the need for subcell numerical integration inside the cut elements (Fig. 2.4), and in the type of continuity enforced along the discontinuity. Table 2.1 summarizes three representative families: the classical SDA-based E-FEM [126, 127], the Discrete Strong Discontinuity Approach (DSDA) [128], and the Elemental Enriched Space formulation proposed by Idelsohn et al. [129]. For each family, the table indicates whether the enriched DOFs can be statically condensed at element level, whether subcell quadrature is required, and whether the discrete fields remain continuous along the embedded discontinuity.

Table 2.1: Qualitative comparison of embedded strong-discontinuity formulations.

Family	Location of enrichment DOFs	Element-level condensation of enrichment DOFs	Subcells required	Continuity of discrete fields along the discontinuity
Classical SDA-based	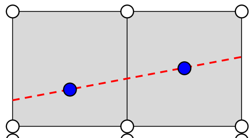	Yes	No	No
DSDA	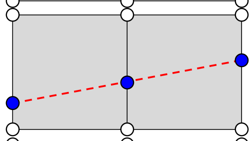	No	No	Yes
Elemental Enriched Space	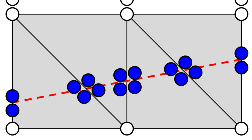	Yes	Yes	No

2.5.1.1 Classical SDA-based formulations

Classical SDA-based embedded formulations build on the seminal works of Dvorkin et al. [130, 131], Simo and Rifai [132] and Simo et al. [126]. In these models, the enrichment DOFs are associated with incompatible deformation modes. The enriched strain field is split into a compatible part and an enhanced part, the latter representing the strong discontinuity through element internal modes, usually condensed at the element-level.

Over the years, this basic idea has been extended in several directions, including three-dimensional formulations with constant jumps in constant-strain elements [133], two-dimensional and three-dimensional formulations with linear jumps and general element types [134, 135], and finite-strain extensions [136, 137]. Jirásek [138] provides a comprehensive review of these classical SDA-based formulations for constant-strain elements with embedded discontinuities and constant displacement jumps. The same family of models has been systematically compared with smeared crack formulations [139] and with XFEM approaches [7, 125, 124], highlighting the formulation ability to capture localized failure.

The formulation has also been extended to multiphysics applications, including hydro-mechanical [140, 141, 142, 143, 144, 145, 146, 147] and electromechanical [148, 149] problems.

2.5.1.2
Discrete Strong Discontinuity Approach

The Discrete Strong Discontinuity Approach (DSDA) is a variant of the classical SDA-based E-FEM proposed by Dias-da-Costa et al. [128]. The main difference with respect to the original SDA-based formulation is that the enrichment DOFs are taken as the jumps of the primary field at the nodes where the discontinuity intersects the background mesh. These enriched DOFs are shared by all elements cut by the discontinuity and are treated as global unknowns, resembling the DE-FEM presented in sec. 2.4. As a result, the jump of the primary field is continuous from one element to the next along the embedded interface. However, the enriched approximation inside each element remains defined locally and the overall embedded formulation is still non-conforming in the conventional finite element sense.

In the initial DSDA formulation [128], the element was enriched with rigid-body modes only. An extension, termed Generalized Strong Discontinuity Approach (GSDA), introduced an additional tangential stretching mode to better capture sliding along the discontinuity [150]. To resolve non-conformity effects, Dias-da-Costa et al. [6] also proposed non-local definitions of the enrichment deformation modes, which average contributions from neighbouring elements and reduce sensitivity to the relative position of the discontinuity within the mesh.

DSDA-type enrichments have been extended beyond purely mechanical problems to model fluid flow in fractured porous media and coupled hydromechanical processes, for instance in the works of Damirchi et al. [151, 152] and in the formulations developed in this thesis [153, 154].

2.5.1.3
Elemental Enriched Space

In the elemental enriched space formulation proposed by Idelsohn et al. [129], each triangular or tetrahedral element cut by an internal interface is subdivided into a small mesh of standard linear sub-elements. When the interface carries a strong discontinuity, the nodes lying on the intersection between the interface and the element edges are duplicated, so that the approximation can represent independent fields on each side of the interface. The sub-elements are assembled into a single "super-element" with additional internal degrees of freedom, and these enriched DOFs are statically condensed at the element level. After condensation, the global system retains the same nodal unknowns and connectivity as the underlying unfitted mesh, while the element still captures kinks, jumps, or combined kink–jump discontinuities with a linear variation of the jump along the interface.

To mitigate the non-conformity of the enriched space, Idelsohn et al. [129] modify the weak form by adding, for every enriched element, a contour integral of the normal traction along its boundary, evaluated with the stresses computed inside that element. These additional contributions, referred to as inter-element forces, can be interpreted as a "do-nothing" boundary condition between adjacent enriched elements. In the numerical examples, these inter-element forces substantially reduce or even eliminate spurious inter-element jumps while preserving the efficiency advantages of elemental enrichment.

In the first paper [129], the methodology was only applied to thermal problems (scalar fields). Later, the formulation was generalized to a vectorial field and applied to the solution of incompressible Navier-Stokes equations for multifluid flows and moving interfaces [155].

2.5.2 Challenges involving hydromechanical problems

To achieve the objectives outlined in Sec. 1.2, the existing E-FEM formulations have limitations. The ones addressed in this thesis are summarized in the following subsections.

2.5.2.1 Generic fluid-flow description

Most embedded formulations for fractured porous media idealize fractures as highly conductive features that act as preferential flow paths [140, 141, 142, 152, 156]. This assumption is reflected in the preservation of pressure continuity and may represent only gradient jumps across the discontinuity. While appropriate for open and highly permeable fractures, this description is not suitable for low-permeability faults or cemented fractures that act as hydraulic barriers.

A few works instead allow for a discontinuous pore-pressure field and, therefore, can represent a discontinuity as a barrier to flow [143, 144, 145, 146]. These studies, however, focus on poro-plastic strain localization (shear bands) and aim at capturing pore-pressure excess generated within the localization zone. As a result, they do not describe fluid flow along the localized path as an internal conduit, since the discontinuity is not treated as a fracture.

A formulation that accounts for both longitudinal and transversal flow effects was proposed by Damirchi et al. [151]. This approach belongs to the DSDA E-FEM family, but it is limited to steady-state conditions and relies on coupling finite elements to exchange flow between the discontinuity and the porous matrix. Another approach was presented by Beserra et al. [157, 158], who derived an effective permeability tensor for the limiting case of a fully sealed discontinuity fault, assuming that no fluid is stored within the discontinuity, and applied it to steady-state problems.

The first article of this thesis [154] addresses this gap by developing an embedded finite element formulation for transient single-phase flow in fractured porous media. The formulation captures the influence of the discontinuity on both longitudinal flow along the discontinuity and transversal exchange with the porous matrix by enriching the pore-pressure field within the SDA framework. The coupling between discontinuity flow and matrix flow follows directly from the governing equations and constitutive relations, without introducing additional coupling parameters. In Chapters 3 and 4, this formulation is further generalized to three-dimensional problems following the classical SDA E-FEM setting.

2.5.2.2 Generic fluid-flow description coupled with mechanical deformations

Existing E-FEM formulations for coupled hydro-mechanical problems exhibit limitations similar to those of the purely hydraulic setting. They are typically restricted either to conductive discontinuities [140, 141, 142, 159, 152, 160, 147] or to strain-localization settings in poro-plasticity [143, 144, 145, 146].

The second article of this thesis extends the previous contribution to a fully coupled hydro-mechanical formulation. The approach is fully based on the Strong Discontinuity Approach, enriching both displacement and pore-pressure fields. An additional outcome is the identification of spurious oscillations in cohesive tractions along the embedded discontinuity. These oscillations can bias fault-reactivation assessments when elastoplastic cohesive laws are used, potentially indicating premature failure. While mesh refinement alleviates this effect, the observation raises a broader methodological question regarding how the choice of an SDA-based embedded formulation affects the smoothness of cohesive traction fields in E-FEM.

2.5.2.3 Cohesive stresses and formulation choice in SDA-based E-FEM

Within classical SDA-based E-FEM for mechanical problems, the literature contains a limited discussion of spurious oscillations in cohesive tractions [161, 162, 163], whereas stress-locking mechanisms have been extensively studied. In particular, several works compare SDA-based variants and quantify their impact on global load–displacement responses [138, 164, 136, 165, 7, 166, 167]. However, a systematic understanding of the influence of these variants on the local cohesive traction field along the discontinuity remains lacking.

The third article of this thesis addresses this gap by systematically analyzing cohesive traction behavior in SDA-based E-FEM formulations. A set of two- and three-dimensional examples is used to investigate stick and slip conditions, different element types, and structured and unstructured meshes. The results show that enforcing local equilibrium along the discontinuity yields markedly smoother cohesive traction profiles. Overall, the study demonstrates that an appropriate choice of SDA-based embedded formulation can substantially improve the reliability of cohesive traction fields, thereby resolving the methodological limitation identified in the coupled hydro-mechanical work and strengthening the use of embedded strong-discontinuity formulations in fault-reactivation and related hydro-mechanical applications.

3
Governing equations

Consider the boundary-value problem depicted in Figure 3.1, defined on a domain $\Omega \in \mathbb{R}^n$ ($n = 2, 3$) with external boundary $\partial\Omega$. For the displacement field, the boundary is decomposed as $\partial\Omega = \Gamma_\mathrm{D}^u \cup \Gamma_\mathrm{N}^u$, with $\Gamma_\mathrm{D}^u \cap \Gamma_\mathrm{N}^u = \emptyset$, where Γ_D^u and Γ_N^u denote the Dirichlet and Neumann parts, respectively. Similarly, for the pore-pressure field, $\partial\Omega = \Gamma_\mathrm{D}^p \cup \Gamma_\mathrm{N}^p$, with $\Gamma_\mathrm{D}^p \cap \Gamma_\mathrm{N}^p = \emptyset$, where Γ_D^p and Γ_N^p correspond to Dirichlet and Neumann boundary conditions, respectively. The domain is intersected by a discontinuity Γ_d, which divides it into two subdomains, Ω^+ and Ω^-, defined with respect to the unit normal vector to the discontinuity $\mathbf{n}_\mathrm{d}$, such that Ω^+ denotes the subdomain towards which $\mathbf{n}_\mathrm{d}$ points and Ω^- the opposite one. The problem is governed by three primary fields: the displacement, $\mathbf{u}$, the pore-pressure in the porous medium, p, and the pore-pressure inside the discontinuity, p_d.

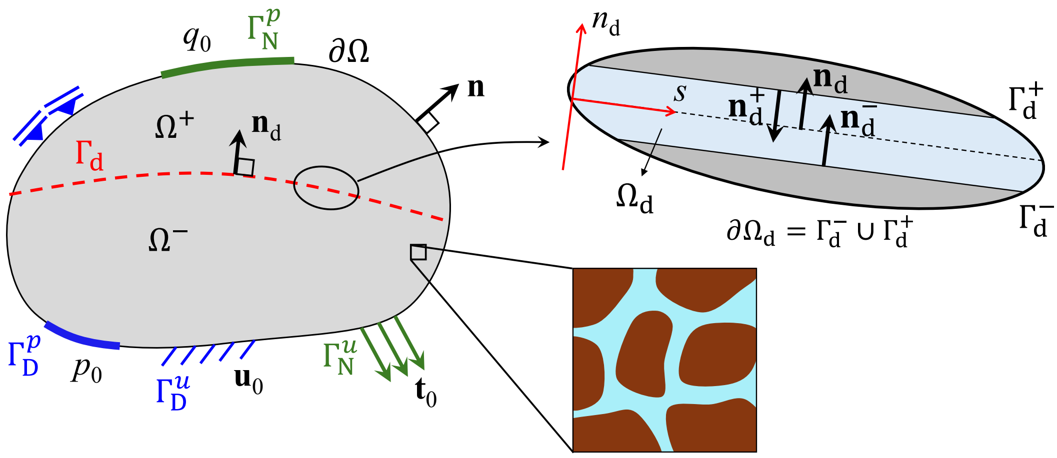

Figure 3.1: Schematic representation of the hydromechanical boundary-value problem

A smooth discontinuity surface is considered, and opposite unit normals on each side is adopted, as indicated in Fig. 3.1, so that

$$\mathbf{n}_\mathrm{d}^- = -\mathbf{n}_\mathrm{d}^+ =: \mathbf{n}_\mathrm{d}. \tag{3-1}$$

The boundary conditions are defined as follows. On the Dirichlet boundary, Γ_D^u, the displacement field is prescribed as

$$\mathbf{u} = \mathbf{u}_0, \qquad \mathbf{x} \in \Gamma_\mathrm{D}^u, \tag{3-2}$$

while on the Neumann boundary, Γ_N^u, the traction vector, $\mathbf{t}$, is imposed as

$$\mathbf{t} = \mathbf{t}_0, \qquad \mathbf{x} \in \Gamma^u_{\mathrm{N}}, \tag{3-3}$$

with $\mathbf{t} = \boldsymbol{\sigma} \cdot \mathbf{n}$, where $\mathbf{n}$ is the outward unit normal vector to the boundary of the domain $\partial\Omega$.

On the Dirichlet boundary, Γ^p_{D}, the pore pressure is prescribed as

$$p = p_0 \quad \text{on } \Gamma^p_{\mathrm{D}}, \tag{3-4}$$

where p_0 denotes the imposed fluid pressure. On the Neumann boundary, Γ^p_{N}, the volumetric flux is imposed as

$$\mathbf{q} \cdot \mathbf{n} = q_0 \quad \text{on } \Gamma^p_{\mathrm{N}}, \tag{3-5}$$

where q_0 is the prescribed volumetric flux (positive for outflow with outward normal $\mathbf{n}$).

3.1 Mechanical equilibrium in deformable porous media

By neglecting inertial forces, the linear momentum balance is given by

$$\nabla \cdot \boldsymbol{\sigma} + \mathbf{b} = \mathbf{0}, \qquad \mathbf{x} \in \Omega \backslash \Omega_{\mathrm{d}}, \tag{3-6}$$

where $\boldsymbol{\sigma}$ is the Cauchy stress tensor, $\mathbf{b}$ is the body force vector, and ∇ denotes the nabla operator.

The stress–strain relationship is described in terms of the effective stress tensor, $\boldsymbol{\sigma}'$, which, adopting a Solid Mechanics convention (negative compression), is expressed as

$$\boldsymbol{\sigma}' = \boldsymbol{\sigma} + \alpha\, p\, \mathbf{I}, \tag{3-7}$$

where $\mathbf{I}$ denotes the identity tensor, α is the Biot coefficient. The effective stress evolves according to the mechanical constitutive law, expressed in the general form

$$\boldsymbol{\sigma}'(\mathbf{x}) = \boldsymbol{\Sigma}\Big(\boldsymbol{\varepsilon}(\mathbf{x})\Big), \qquad \mathbf{x} \in \Omega \backslash \Omega_{\mathrm{d}}, \tag{3-8}$$

where the operator $\boldsymbol{\Sigma}(\cdot)$ denotes the constitutive relation, and $\boldsymbol{\varepsilon}$ is the small strain tensor, which is given by

$$\boldsymbol{\varepsilon}(\mathbf{x}) = \nabla^{\mathrm{s}}\mathbf{u}(\mathbf{x}) := \tfrac{1}{2}\Big(\nabla\mathbf{u}(\mathbf{x}) + \nabla\mathbf{u}(\mathbf{x})^{\mathsf{T}}\Big), \qquad \mathbf{x} \in \Omega \backslash \Omega_{\mathrm{d}}, \tag{3-9}$$

where the superscript $()^{\mathrm{s}}$ in the nabla operator indicates the symmetric part of a second-order tensor.

Finally, along the discontinuity, the cohesive stresses, $\mathbf{t}_{\mathrm{d}}$, must be in equilibrium with the tractions on each side of the discontinuity:

$$\boldsymbol{\sigma}^{+} \cdot \mathbf{n}_{\mathrm{d}}^{+} = -\boldsymbol{\sigma}^{-} \cdot \mathbf{n}_{\mathrm{d}}^{-} = -\mathbf{t}_{\mathrm{d}}, \qquad \mathbf{x} \in \Gamma_{\mathrm{d}}, \tag{3-10}$$

where superscripts $(\cdot)^{\pm}$ denote quantities evaluated on the two faces of Γ_{d}.

The cohesive stresses are determined by a cohesive law $\mathbf{t}_{\mathrm{d}} = \mathbf{t}_{\mathrm{d}}\left(\llbracket \mathbf{u} \rrbracket\right)$, with $\llbracket \mathbf{u} \rrbracket$ being the displacement jump at the discontinuity surface, defined on Γ_{d} as

$$\llbracket \mathbf{u} \rrbracket = \mathbf{u}^{+} - \mathbf{u}^{-}. \tag{3-11}$$

Appendix B presents in detail the cohesive laws used in this work.

3.2 Mass conservation in a deformable saturated porous medium

The local conservation law for a generic extensive quantity ψ is derived as follows. In the context of porous media, ψ may represent, for example, the mass of a given phase. Take $\rho^{\psi}(\mathbf{x}, t)$ as the bulk density of ψ, $\mathbf{j}^{\psi}$ as its flux vector, and $f^{\psi}(\mathbf{x}, t)$ as a volumetric source term (positive when ψ is produced inside the control volume). The flux $\mathbf{j}^{\psi}$ is taken positive in the outward normal direction on the boundary.

For a control volume $V \subset \Omega$ with boundary ∂V and unit outward normal $\mathbf{n}$, the integral balance reads

$$\frac{d}{dt} \int_{V} \rho^{\psi} \, dV + \int_{\partial V} \mathbf{j}^{\psi} \cdot \mathbf{n} \, d\Gamma = \int_{V} f^{\psi} \, dV. \tag{3-12}$$

This relation states that the rate of change of ψ stored in V plus the net flux of ψ leaving V through its boundary equals the amount of ψ created inside V by sources. Then, applying the Divergence theorem leads to the local conservation law

$$\frac{\partial \rho^{\psi}}{\partial t} + \nabla \cdot \mathbf{j}^{\psi} = f^{\psi}. \tag{3-13}$$

Since the flux vector can be written as the product of a density and a velocity,

$$\mathbf{j}^{\psi} = \rho^{\psi} \, \mathbf{v}^{\psi},$$

with $\mathbf{v}^{\psi}$ being the absolute velocity associated with ψ, the local balance can be expressed as

$$\frac{\partial \rho^{\psi}}{\partial t} + \nabla \cdot \left(\rho^{\psi} \, \mathbf{v}^{\psi}\right) = f^{\psi}, \tag{3-14}$$

which serves as the starting point for the derivation of the mass balance equations of each phase in the porous medium.

3.2.1 Solid mass balance equation

In a porous medium, the solid occupies a volume fraction $1-\phi$, where ϕ is the porosity. Then, applying eq. (3-14) to the solid phase, with $\rho^\psi = \rho_\mathrm{s}(1-\phi)$, $\mathbf{v}^\psi = \dot{\mathbf{u}}$ and no sources, we obtain

$$\frac{\partial\left(\rho_\mathrm{s}\left(1-\phi\right)\right)}{\partial t} + \nabla\cdot\left(\rho_\mathrm{s}\left(1-\phi\right)\dot{\mathbf{u}}\right) = 0, \tag{3-15}$$

where ρ_s is the solid density.

To describe how porosity changes with deformation and pressure, it is convenient to introduce the material derivative following the solid motion. For any scalar field $\chi(\mathbf{x},t)$, the material derivative with respect to the solid phase is defined as

$$\frac{D_\mathrm{s}\chi}{Dt} = \frac{\partial\chi}{\partial t} + \nabla\chi\cdot\dot{\mathbf{u}}, \tag{3-16}$$

Using this notation, equation (3-15) can be manipulated to express the porosity rate as

$$\frac{D_\mathrm{s}\,\phi}{Dt} = \left(1-\phi\right)\left(\dot{\varepsilon}_\mathrm{v} + \frac{1}{\rho_\mathrm{s}}\frac{D_\mathrm{s}\,\rho_\mathrm{s}}{Dt}\right), \tag{3-17}$$

which relates the change of porosity to the volumetric deformation rate, $\dot{\varepsilon}_\mathrm{v} = \nabla\cdot\dot{\mathbf{u}}$, and to changes in the solid density, which can be expressed as [168]

$$\frac{1}{\rho_\mathrm{s}}\frac{D_\mathrm{s}\,\rho_\mathrm{s}}{Dt} = \frac{1}{1-\phi}\left(\frac{\alpha-\phi}{K_\mathrm{s}}\frac{D_\mathrm{s}\,p}{Dt} - \left(1-\alpha\right)\dot{\varepsilon}_\mathrm{v}\right), \tag{3-18}$$

where K_s is the bulk modulus of the solid matrix.

3.2.2 Fluid mass balance in the porous matrix

Considering a saturated porous medium, the fluid phase occupies the porous space, determined by the porosity, ϕ. Then applying eq. (3-14) with $\rho^\psi = \rho_\mathrm{l}\,\phi$, and $\mathbf{v}^\psi = \mathbf{v}_\mathrm{l}$, gives

$$\frac{\partial\left(\rho_\mathrm{l}\,\phi\right)}{\partial t} + \nabla\cdot\left(\rho_\mathrm{l}\,\phi\,\mathbf{v}_\mathrm{l}\right) = 0, \tag{3-19}$$

where ρ_l is the fluid density and $\mathbf{v}_\mathrm{l}$ is the absolute fluid velocity. The latter is decomposed into a relative velocity with respect to the solid matrix, $\mathbf{v}_\mathrm{ls}$, and the solid motion,

$$\mathbf{v}_\mathrm{l} = \mathbf{v}_\mathrm{ls} + \dot{\mathbf{u}}, \tag{3-20}$$

Defining the volumetric advective flux as

$$\mathbf{q} = \phi\, \mathbf{v}_{\mathrm{ls}}, \tag{3-21}$$

using the material derivative (3-16) together with the decomposition (3-20), the fluid mass balance (3-19) can be rewritten as

$$\frac{D_{\mathrm{s}}\left(\phi\, \rho_{\mathrm{l}}\right)}{Dt} + \nabla \cdot \left(\rho_{\mathrm{l}}\, \mathbf{q}\right) + \left(\rho_{\mathrm{l}}\, \phi\right) \dot{\varepsilon}_{\mathrm{v}} = 0. \tag{3-22}$$

By expanding eq. (3-22) and incorporating eqs. (3-17)–(3-18), we obtain

$$\phi\, \frac{D_{\mathrm{s}}\, \rho_{\mathrm{l}}}{Dt} + \rho_{\mathrm{l}} \left(\frac{\alpha - \phi}{K_{\mathrm{s}}} \frac{D_{\mathrm{s}}\, p}{Dt}\right) + \nabla \cdot \left(\rho_{\mathrm{l}}\, \mathbf{q}\right) + \alpha\, \rho_{\mathrm{l}}\, \dot{\varepsilon}_{\mathrm{v}} = 0. \tag{3-23}$$

Equations (3-6), (3-15) and (3-23) provide the macroscopic governing equations of the coupled hydromechanical problem once constitutive relations are specified.

3.2.3 Constitutive laws

The advective volumetric flux in the porous matrix is governed by Darcy's law,

$$\mathbf{q} = \frac{\mathbf{k}}{\mu_{\mathrm{l}}} \left(-\nabla p + \rho_{\mathrm{l}}\, \mathbf{g}\right), \tag{3-24}$$

where $\mathbf{k}$ is the intrinsic permeability tensor, μ_{l} is the dynamic viscosity of the fluid, and $\mathbf{g}$ is the gravitational acceleration vector.

For a compressible fluid, under isothermal conditions, the fluid density is given by [169, 170]

$$\rho_{\mathrm{l}} = \rho_{\mathrm{l0}} \exp\left(\frac{1}{K_{\mathrm{l}}} \left(p - p_{\mathrm{l0}}\right)\right), \tag{3-25}$$

where K_{l} is the fluid bulk modulus, p_{l0} is a reference pore pressure, and ρ_{l0} is the corresponding reference density. The derivative of the fluid density with respect to the pore pressure is then

$$\frac{\partial\, \rho_{\mathrm{l}}}{\partial\, p} = \frac{1}{K_{\mathrm{l}}} \rho_{\mathrm{l0}} \exp\left(\frac{1}{K_{\mathrm{l}}} \left(p - p_{\mathrm{l0}}\right)\right) = \frac{\rho_{\mathrm{l}}}{K_{\mathrm{l}}}. \tag{3-26}$$

3.2.4 Fluid flow in the discontinuity

Considering the discontinuity as a fully saturated layer with unit porosity, the mass conservation of the fluid inside the discontinuity is obtained by applying eq. (3-14) with $\rho^{\psi} = \rho_{\mathrm{l}}$ and $\mathbf{v}^{\psi} = \mathbf{v}_{\mathrm{l}}$, which gives

$$\frac{\partial\, \rho_{\mathrm{l}}}{\partial t} + \nabla_{\mathrm{d}} \cdot \left(\rho_{\mathrm{l}}\, \mathbf{v}_{\mathrm{dl}}\right) = 0, \tag{3-27}$$

where $\nabla_{\mathrm{d}}(\cdot)$ denotes the gradient operator in the local coordinate system of the discontinuity, and $\mathbf{v}_{\mathrm{dl}}$ is the absolute fluid velocity also in the system. The same compressibility law (3-25) is adopted for the fluid inside the discontinuity.

The absolute velocity is decomposed into the relative velocity with respect to the solid matrix, $\mathbf{v}_{\mathrm{dls}}$, and the solid motion in the discontinuity local system:

$$\mathbf{v}_{\mathrm{dl}} = \mathbf{v}_{\mathrm{dls}} + \dot{\mathbf{u}}_{\mathrm{d}}, \tag{3-28}$$

where $\dot{\mathbf{u}}_{\mathrm{d}}$ is the displacement rate of the discontinuity in local coordinates. The volumetric advective flux inside the discontinuity is defined as

$$\mathbf{q}_{\mathrm{dl}} := \mathbf{v}_{\mathrm{dls}}. \tag{3-29}$$

Substituting eq. (3-28) into eq. (3-27) and using the material derivative (3-16) leads to

$$\frac{D_{\mathrm{s}}\,\rho_{\mathrm{l}}}{Dt} + \nabla_{\mathrm{d}} \cdot (\rho_{\mathrm{l}}\,\mathbf{q}_{\mathrm{d}}) + \rho_{\mathrm{l}}\,\nabla_{\mathrm{d}} \cdot \dot{\mathbf{u}}_{\mathrm{d}} = 0 \quad \text{in } \Omega_{\mathrm{d}}, \tag{3-30}$$

where Ω_{d} denotes the discontinuity domain, see Fig. 3.1.

The advective volumetric flux inside the discontinuity is also governed by Darcy's law, expressed in the local coordinate system as

$$\mathbf{q}_{\mathrm{d}} = -\frac{\mathbf{k}_{\mathrm{d}}}{\mu_{\mathrm{l}}} \left(\nabla_{\mathrm{d}}\, p_{\mathrm{d}} - \rho_{\mathrm{l}} \begin{bmatrix} \mathbf{m}_1{}^{\top} \\ \mathbf{m}_2{}^{\top} \\ \mathbf{n}_{\mathrm{d}}{}^{\top} \end{bmatrix} \mathbf{g} \right), \tag{3-31}$$

where $\mathbf{k}_{\mathrm{d}} = \mathrm{diag}(k_{\mathrm{d}}^{\mathrm{L}}, k_{\mathrm{d}}^{\mathrm{L}}, k_{\mathrm{d}}^{\mathrm{N}})$ is the intrinsic permeability tensor of the discontinuity, and $\mathbf{m}_1$ and $\mathbf{m}_2$ are unit tangent vectors at the discontinuity plane. This diagonal permeability tensor, combined with the assumption that the pressure field is uniform across the aperture, implies that only the tangential entries $k_{\mathrm{d}}^{\mathrm{L}}$ will contribute to the weak form derived in Section 4.4. The longitudinal permeability, $k_{\mathrm{d}}^{\mathrm{L}}$, is defined by the cubic law [171]

$$k_{\mathrm{d}}^{\mathrm{L}} = \frac{w^2}{12}, \tag{3-32}$$

where w is the discontinuity aperture.

3.2.5
Matrix–discontinuity flux compatibility

Flux exchange between the porous matrix and the discontinuity is described in terms of the normal components of the Darcy fluxes on the two sides of the interface, as schematically illustrated in Figure 3.2. Let $\mathbf{q}^{+}$ and $\mathbf{q}^{-}$ denote the Darcy fluxes in the porous matrix evaluated on the two faces

Γ_d^+ and Γ_d^-, with outward unit normals $\mathbf{n}_d^+$ and $\mathbf{n}_d^-$, respectively. Likewise, let $\mathbf{q}_d^+$ and $\mathbf{q}_d^-$ denote the Darcy fluxes in the discontinuity evaluated on the two faces Γ_d^+ and Γ_d^-, with outward unit normals $\hat{\mathbf{n}}_d^+$ and $\hat{\mathbf{n}}_d^-$, respectively, where $\hat{\mathbf{n}}_d$ is the outward unit normal to Ω_d, defined in the discontinuity local system. The outward normals on the two sides satisfy

$$\mathbf{n}_d^- = -\mathbf{n}_d^+ =: \mathbf{n}_d, \qquad \hat{\mathbf{n}}_d^- = -\hat{\mathbf{n}}_d^+ =: \hat{\mathbf{n}}_d. \tag{3-33}$$

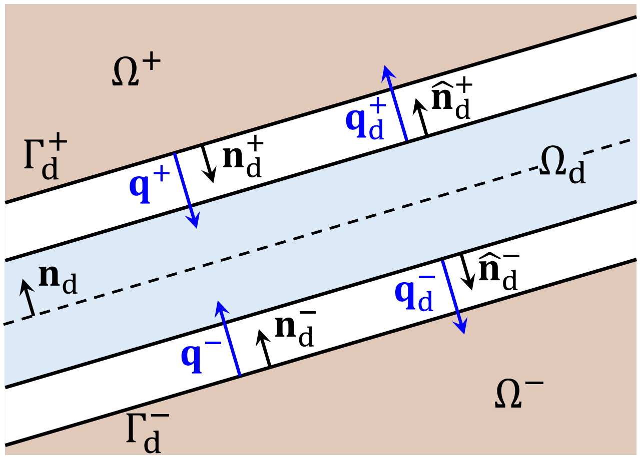

Figure 3.2: Discontinuity boundaries and normal vectors for the matrix ($\mathbf{n}_d^\pm$) and the discontinuity domain ($\hat{\mathbf{n}}_d^\pm$).

Local mass balance at each matrix–discontinuity interface enforces continuity of the normal flux:

$$\mathbf{q}^+ \cdot \mathbf{n}_d^+ + \mathbf{q}_d^+ \cdot \hat{\mathbf{n}}_d^+ = 0 \quad \text{on } \Gamma_d^+, \tag{3-34}$$

$$\mathbf{q}^- \cdot \mathbf{n}_d^- + \mathbf{q}_d^- \cdot \hat{\mathbf{n}}_d^- = 0 \quad \text{on } \Gamma_d^-. \tag{3-35}$$

The matrix–discontinuity coupling is enforced by a balance of normal fluxes across the discontinuity surface Γ_d. The scalar quantity q_d^t denotes the normal transfer flux from the discontinuity to the porous matrix and is taken as positive when fluid leaves the discontinuity and enters the matrix. Using the above relations and the normal orientations, local mass balance across Γ_d can be written as

$$\left(\mathbf{q}^+ - \mathbf{q}^-\right) \cdot \mathbf{n}_d = -\left(\mathbf{q}_d^+ - \mathbf{q}_d^-\right) \cdot \hat{\mathbf{n}}_d = q_d^t \quad \text{on } \Gamma_d, \tag{3-36}$$

so that, with this sign convention, the net normal flux exiting the discontinuity equals q_d^t, whereas the net normal flux exiting the porous matrix equals $-q_d^t$.

3.2.6 Transfer law

The exchange flux q_d^t is specified by a linear transfer law that relates it to the pore pressure fields in the porous matrix and in the discontinuity as

$$q_\mathrm{d}^\mathrm{t} = k_\mathrm{d}^{\mathrm{t}+} \left(p_\mathrm{d} - p^+\right) + k_\mathrm{d}^{\mathrm{t}-} \left(p_\mathrm{d} - p^-\right), \tag{3-37}$$

where p^+ and p^- denote the pore pressures in the matrix on the two sides of the discontinuity, and $k_\mathrm{d}^{\mathrm{t}+}$ and $k_\mathrm{d}^{\mathrm{t}-}$ are non-negative transfer coefficients. For $k_\mathrm{d}^{\mathrm{t}\pm} > 0$, a higher pressure inside the discontinuity ($p_\mathrm{d} > p^\pm$) produces a positive contribution to q_d^t, meaning a leakage of fluid from the discontinuity into the porous matrix.

3.3 Summary

This section summarises the governing equations of the coupled hydromechanical problem and their associated primary fields. Table 3.1 collects, for each primary variable, the corresponding strong-form governing equation and its reference.

Table 3.1: Governing equations of the coupled hydromechanical problem and the associated primary fields.

Primary field	Governing equation	
$\mathbf{u}$	$\nabla \cdot (\boldsymbol{\sigma}' - \alpha\, p\, \mathbf{I}) + \mathbf{b} = \mathbf{0}$	(3-6)
p	$\frac{\rho_\mathrm{l}}{M} \frac{\partial p}{\partial t} + \nabla \cdot (\rho_\mathrm{l}\, \mathbf{q}) + \alpha\, \rho_\mathrm{l}\, \dot{\varepsilon}_\mathrm{v} = 0$	(3-23)
p_d	$\frac{\partial \rho_\mathrm{l}}{\partial t} + \nabla_\mathrm{d} \cdot (\rho_\mathrm{l}\, \mathbf{q}_\mathrm{d}) + \rho_\mathrm{l}\, \nabla_\mathrm{d} \cdot \dot{\mathbf{u}}_\mathrm{d} = 0$	(3-30)

In Table 3.1, the mass balance equation for the fluid in the porous medium, Eq. (3-23), is written in terms of the Biot modulus M,

$$M = \left(\frac{\phi}{K_\mathrm{l}} + \frac{\alpha - \phi}{K_\mathrm{s}} \right)^{-1}, \tag{3-38}$$

which is obtained by substituting the fluid compressibility relation (3-25) and its derivative (3-26) into the fluid mass balance, Eq. (3-23). The table also includes the simplification that, under small strains, the material derivative with respect to the solid is approximated by its Eulerian form [43]:

$$\frac{D_\mathrm{s}\,(\cdot)}{Dt} \approx \frac{\partial\,(\cdot)}{\partial t}. \tag{3-39}$$

4
Finite elements with embedded strong discontinuities

4.1
Strong Discontinuity Approach

To understand how a discontinuity can be implicitly represented in the domain, consider a one-dimensional problem for a generic field $g(x)$, defined on a domain $\Omega \subset \mathbb{R}$ containing a strong discontinuity at $x = x_{\Gamma_\mathrm{d}}$, as illustrated in Fig. 4.1.

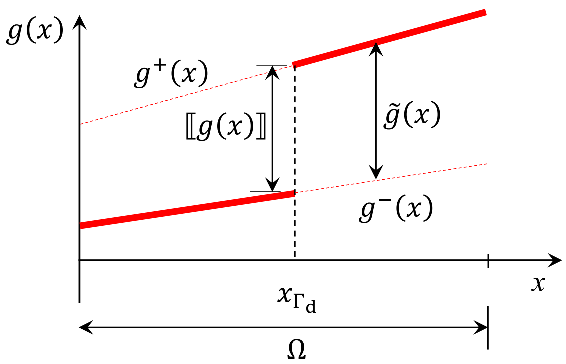

Figure 4.1: One-dimensional problem with an embedded strong discontinuity (adapted from Wu [7]).

The domain is decomposed as $\Omega = \Omega^- \cup \{x_{\Gamma_\mathrm{d}}\} \cup \Omega^+$, where Ω^- and Ω^+ are the subdomains on the negative and positive side of the discontinuity, respectively. In Fig. 4.1, $g^-(x)$ and $g^+(x)$ denote continuous fields that coincide with the total field $g(x)$ in their respective subdomains,

$$g(x) = \begin{cases} g^-(x), & x \in \Omega^-, \\ g^+(x), & x \in \Omega^+. \end{cases}$$

The relative field is defined as

$$\tilde{g}(x) = g^+(x) - g^-(x)\,, \tag{4-1}$$

and the actual jump of the field at the discontinuity is given by

$$[\![g\,(x)]\!] = \lim_{x \to x_{\Gamma_\mathrm{d}}^+} g(x) - \lim_{x \to x_{\Gamma_\mathrm{d}}^-} g(x) = g^+(x_{\Gamma_\mathrm{d}}) - g^-(x_{\Gamma_\mathrm{d}}) = \tilde{g}(x_{\Gamma_\mathrm{d}})\,. \tag{4-2}$$

Using the Heaviside function associated with the discontinuity,

$$\mathcal{H}_{\Gamma_\mathrm{d}}(x) = \begin{cases} 1, & x \in \Omega^+, \\ 0, & x \in \Omega^-, \end{cases} \tag{4-3}$$

the total field can be written compactly as

$$g(x) = g^-(x) + \mathcal{H}_{\Gamma_\mathrm{d}}(x)\,\tilde{g}(x). \tag{4-4}$$

For $x \in \Omega^-$, $\mathcal{H}_{\Gamma_\mathrm{d}}(x) = 0$ and $g(x) = g^-(x)$, whereas for $x \in \Omega^+$, $\mathcal{H}_{\Gamma_\mathrm{d}}(x) = 1$ and $g(x) = g^+(x)$.

In eq. (4-4), the fields $g^-(x)$ and $\tilde{g}(x)$ are, in principle, independent. Therefore, prescribing an essential boundary condition at a point would require a constraint involving both $g^-(x)$ and $\tilde{g}(x)$. To avoid this complication, and following the strategy proposed in [134, 7], a local decomposition of the total field is introduced. Consider a subdomain $\Omega_h \subset \Omega$ that surrounds the discontinuity, as shown in Fig. 4.2. The total field is decomposed as

$$g(x) = \hat{g}(x) + \bar{g}(x), \tag{4-5}$$

where $\hat{g}(x)$ is a continuous regular field defined over Ω, and $\bar{g}(x)$ is an enhanced field with support restricted to Ω_h. The enhanced contribution is required to vanish on the boundary of this subdomain,

$$\bar{g}(x) = 0 \quad \text{for } x \in \partial\Omega_h, \tag{4-6}$$

so that $g(x) = \hat{g}(x)$ on $\partial\Omega_h$ and essential boundary conditions can be imposed directly on the regular field.

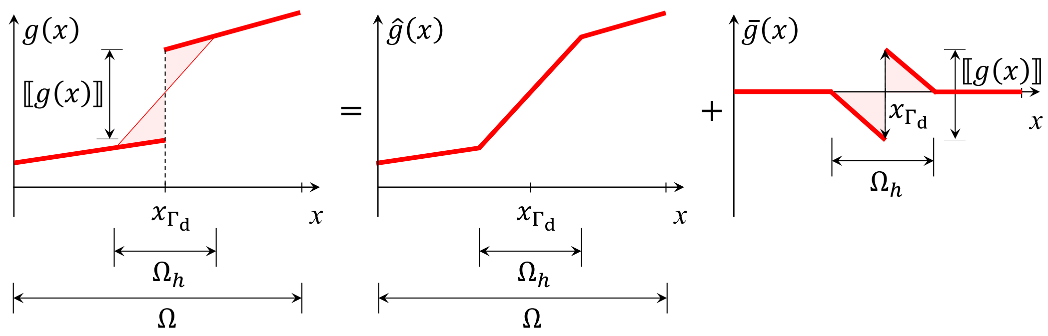

Figure 4.2: Composition of regular and enhanced contributions in the neighborhood of the discontinuity (adapted from Oliver [8]).

The enhanced field can be expressed in terms of the relative field $\tilde{g}(x)$ and a regular correction field $g'(x)$ as [7]

$$\bar{g}(x) = \mathcal{H}_{\Gamma_\mathrm{d}}(x)\,\tilde{g}(x) - g'(x), \qquad x \in \Omega_h, \tag{4-7}$$

where $g'(x)$ is continuous in Ω_h. The term $\mathcal{H}_{\Gamma_\mathrm{d}}(x)\,\tilde{g}(x)$ carries the jump across the discontinuity, while $g'(x)$ corrects this contribution so that $\bar{g}(x)$ remains localized inside Ω_h, as shown in Fig. 4.3.

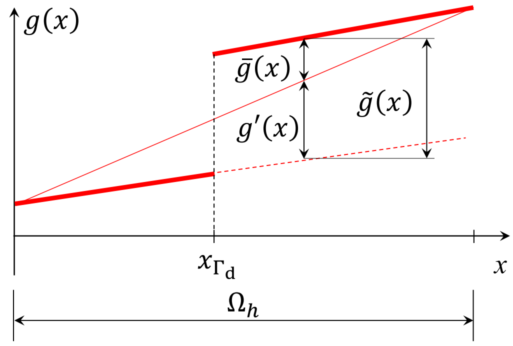

Figure 4.3: Composition of the enhanced contribution inside the enriched region (adapted from Wu [7]).

To define the regular correction field $g'(x)$, two conditions must be satisfied. First, imposing the localization condition (4-6) together with (4-7) leads to

$$g'(x) = \mathcal{H}_{\Gamma_\mathrm{d}}(x)\,\tilde{g}(x) \quad \text{for } x \in \partial\Omega_h, \tag{4-8}$$

so that $\bar{g}(x)$ is strictly zero on $\partial\Omega_h$ and different from zero only inside Ω_h.

A second requirement is that the kinematics must be able to reproduce a state in which the field exhibits a pure jump across the discontinuity, with the negative side undeformed and the positive side given by the relative field,

$$g^-(x) = 0, \qquad g^+(x) = \tilde{g}(x) \quad \Rightarrow \quad g(x) = \mathcal{H}_{\Gamma_\mathrm{d}}(x)\,\tilde{g}(x). \tag{4-9}$$

In this situation, the decomposition $g(x) = \widehat{g}(x) + \bar{g}(x)$ together with (4-7) gives

$$\mathcal{H}_{\Gamma_\mathrm{d}}(x)\,\tilde{g}(x) = \widehat{g}(x) + \mathcal{H}_{\Gamma_\mathrm{d}}(x)\,\tilde{g}(x) - g'(x), \tag{4-10}$$

which implies

$$g'(x) = \widehat{g}(x) \qquad \text{in } \Omega_h, \tag{4-11}$$

as illustrated in Fig. 4.4.

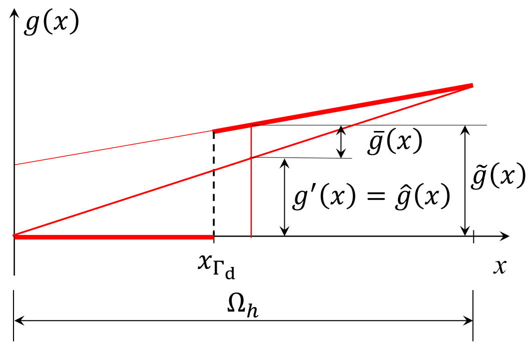

Figure 4.4: Enhanced contribution inside the enriched region for the pure jump state, corresponding to $g'(x) = \widehat{g}(x)$ (adapted from Wu [7]).

To connect this construction with the finite element interpolation, let the regular field be approximated in the standard way as

$$\widehat{g}(x) = \mathbf{N}(x)\,\widehat{\mathbf{g}}, \tag{4-12}$$

where $\mathbf{N}(x)$ collects the shape functions of the underlying finite element space and $\widehat{\mathbf{g}}$ groups the nodal values of $\widehat{g}$. Combining (4-8) and (4-11) at the boundary of the enriched region yields

$$\widehat{g}(x) = g'(x) = \mathcal{H}_{\Gamma_\mathrm{d}}(x)\,\widetilde{g}(x) \quad \text{for } x \in \partial\Omega_h. \tag{4-13}$$

For simplicity, consider the case where the enriched region Ω_h coincides with the element domain and the element has no interior nodes, so that all n_n nodes lie on $\partial\Omega_h$. In this case,

$$\widehat{g}(x_i) = \mathcal{H}_{\Gamma_\mathrm{d}}(x_i)\,\widetilde{g}(x_i), \qquad x_i \in \partial\Omega_h, \tag{4-14}$$

and using (4-11) and (4-12) leads to

$$g'(x) = \mathbf{N}(x)\begin{bmatrix} \mathcal{H}_{\Gamma_\mathrm{d}}(x_1)\,\widetilde{g}(x_1) \\ \vdots \\ \mathcal{H}_{\Gamma_\mathrm{d}}(x_{n_\mathrm{n}})\,\widetilde{g}(x_{n_\mathrm{n}}) \end{bmatrix} = \sum_{i=1}^{n_\mathrm{n}} N_i(x)\,\mathcal{H}_{\Gamma_\mathrm{d}}(x_i)\,\widetilde{g}(x_i),\; x \in \Omega_h, \tag{4-15}$$

where the column vector collects the nodal values $\mathcal{H}_{\Gamma_\mathrm{d}}(x_i)\,\widetilde{g}(x_i)$. Substitution of (4-15) into (4-7) finally provides an explicit expression for the localized enhanced contribution $\bar{g}(x)$ in terms of the relative field and the finite element interpolation. In this way, the essential boundary conditions are imposed solely on the regular field $\widehat{g}(x)$, whereas the discontinuity is represented by the localized contribution $\bar{g}(x)$ inside Ω_h, as illustrated in Figs. 4.2 and 4.3.

Substitution of Eq. (4-15) into Eq. (4-7) gives, for $x \in \Omega_h$,

$$\bar{g}(x) = \mathcal{H}_{\Gamma_\mathrm{d}}(x)\,\widetilde{g}(x) - \sum_{i=1}^{n_\mathrm{n}} N_i(x)\,\mathcal{H}_{\Gamma_\mathrm{d}}(x_i)\,\widetilde{g}(x_i), \tag{4-16}$$

and the total field can be written as

$$g(x) = \widehat{g}(x) + \mathcal{H}_{\Gamma_\mathrm{d}}(x)\,\widetilde{g}(x) - \sum_{i=1}^{n_\mathrm{n}} N_i(x)\,\mathcal{H}_{\Gamma_\mathrm{d}}(x_i)\,\widetilde{g}(x_i), \qquad x \in \Omega_h. \tag{4-17}$$

Although the above derivation was presented in one dimension, the final expression extends directly to a scalar field $g(\mathbf{x}) : \Omega \to \mathbb{R}$ in a multidimensional domain $\Omega \subset \mathbb{R}^n$ by replacing x with $\mathbf{x}$:

$$g(\mathbf{x}) = \widehat{g}(\mathbf{x}) + \mathcal{H}_{\Gamma_\mathrm{d}}(\mathbf{x})\,\widetilde{g}(\mathbf{x}) - \sum_{i=1}^{n_\mathrm{n}} N_i(\mathbf{x})\,\mathcal{H}_{\Gamma_\mathrm{d}}(\mathbf{x}_i)\,\widetilde{g}(\mathbf{x}_i), \qquad \mathbf{x} \in \Omega_h. \tag{4-18}$$

The gradient of $g(\mathbf{x})$ is

$$\begin{aligned}\nabla g\,(\mathbf{x}) = {} & \nabla \widehat{g}\,(\mathbf{x}) + \mathcal{H}_{\Gamma_\mathrm{d}}(\mathbf{x})\,\nabla\widetilde{g}(\mathbf{x}) - \sum_{i=1}^{n_\mathrm{n}} \nabla N_i(\mathbf{x})\,\mathcal{H}_{\Gamma_\mathrm{d}}(\mathbf{x}_i)\,\widetilde{g}(\mathbf{x}_i) \\ & + \delta_{\Gamma_\mathrm{d}}(\mathbf{x})\,[\![g(\mathbf{x})]\!]\,\mathbf{n}_\mathrm{d}(\mathbf{x}),\end{aligned} \tag{4-19}$$

where $\delta_{\Gamma_\mathrm{d}}$ is the Dirac delta distribution supported on Γ_d.

Based on the total field $g(\mathbf{x})$, Eq. (4-18), the admissible affine set is defined as

$$\mathcal{G} = \left\{ g \;\middle|\; g = \widehat{g} + \bar{g},\ \widehat{g} \in \widehat{\mathcal{G}},\ \bar{g} \in \bar{\mathcal{G}} \right\}, \tag{4-20}$$

with

$$\widehat{\mathcal{G}} = \left\{ \widehat{g} \;\middle|\; \widehat{g} \in H^1(\Omega),\ \widehat{g}\Big|_{\Gamma_\mathrm{D}} = g_0 \right\}, \tag{4-21}$$

$$\bar{\mathcal{G}} = \left\{ \bar{g} \;\middle|\; \bar{g} \in L^2(\Omega),\ \mathrm{supp}(\bar{g}) \subset \Omega_h,\ \bar{g}\Big|_{\partial\Omega_h} = 0 \right\}. \tag{4-22}$$

where $L^2(\Omega)$ denotes the space of square–integrable real functions on Ω,

$$L^2(\Omega) = \left\{ f \;\middle|\; \int_\Omega f^2\, d\Omega < \infty \right\}, \tag{4-23}$$

and $H^1(\Omega)$ is the Sobolev space

$$H^1(\Omega) = \left\{ f \;\middle|\; f \in L^2(\Omega),\ \nabla f \in [L^2(\Omega)]^d \right\}, \qquad d = \dim \Omega. \tag{4-24}$$

The relative field $\widetilde{g}$, which acts as an amplitude of the enrichment, is only required to be square–integrable in the enriched region, $\widetilde{g} \in L^2(\Omega_h)$.

4.2 Weak form of the linear momentum balance

To incorporate the kinematics of a strong discontinuity, the displacement field is defined following the Strong Discontinuity Approach [126, 127, 8], eq. (4-18), as

$$\mathbf{u}(\mathbf{x}) = \hat{\mathbf{u}}(\mathbf{x}) + \mathcal{H}_{\Gamma_\mathrm{d}}(\mathbf{x})\,\tilde{\mathbf{u}}(\mathbf{x}) - \sum_{i=1}^{n_\mathrm{n}} N_i(\mathbf{x})\,\mathcal{H}_{\Gamma_\mathrm{d}}(\mathbf{x}_i)\,\tilde{\mathbf{u}}(\mathbf{x}_i), \tag{4-25}$$

where $\hat{\mathbf{u}}$ is the regular part of the displacement field and $\tilde{\mathbf{u}}$ is the enhanced part of the displacement field.

Substituting the displacement field, eq. (4-25), into the compatibility equation, eq. (3-9), leads to

$$\boldsymbol{\varepsilon}(\mathbf{x}) = \nabla^\mathrm{s}\hat{\mathbf{u}}(\mathbf{x}) + \tilde{\boldsymbol{\varepsilon}}(\mathbf{x}), \tag{4-26}$$

where

$$\tilde{\boldsymbol{\varepsilon}}(\mathbf{x}) = \tilde{\boldsymbol{\varepsilon}}_\mathrm{b}(\mathbf{x}) + \delta_{\Gamma_\mathrm{d}}(\mathbf{x})\left(\llbracket\mathbf{u}\rrbracket(\mathbf{x}) \otimes \mathbf{n}_\mathrm{d}(\mathbf{x})\right)^\mathrm{s}, \tag{4-27}$$

where $\tilde{\boldsymbol{\varepsilon}}_\mathrm{b}$ the bounded part of the enhanced strain field, given by

$$\tilde{\boldsymbol{\varepsilon}}_\mathrm{b}(\mathbf{x}) = \mathcal{H}_{\Gamma_\mathrm{d}}(\mathbf{x})\,\nabla^\mathrm{s}\tilde{\mathbf{u}}(\mathbf{x}) - \sum_{i=1}^{n_\mathrm{n}} \mathbf{B}_u^i(\mathbf{x})\,\mathcal{H}_{\Gamma_\mathrm{d}}(\mathbf{x}_i)\,\tilde{\mathbf{u}}(\mathbf{x}_i). \tag{4-28}$$

with $\mathbf{B}_u^i$ being the usual displacement-strain matrix associated with the shape functions of node i:

$$\mathbf{B}_u^i(\mathbf{x}) = \begin{bmatrix} \dfrac{\partial N_i(\mathbf{x})}{\partial x} & 0 & 0 & \dfrac{\partial N_i(\mathbf{x})}{\partial y} & 0 & \dfrac{\partial N_i(\mathbf{x})}{\partial z} \\ 0 & \dfrac{\partial N_i(\mathbf{x})}{\partial y} & 0 & \dfrac{\partial N_i(\mathbf{x})}{\partial x} & \dfrac{\partial N_i(\mathbf{x})}{\partial z} & 0 \\ 0 & 0 & \dfrac{\partial N_i(\mathbf{x})}{\partial z} & 0 & \dfrac{\partial N_i(\mathbf{x})}{\partial y} & \dfrac{\partial N_i(\mathbf{x})}{\partial x} \end{bmatrix}^\top \tag{4-29}$$

The strain tensor, including the kinematics of a strong discontinuity, eq. (4-26), has the same algebraic structure as the strain field used in Enhanced Assumed Strain (EAS) formulations [132, 126]. This analogy allows the strong discontinuity to be incorporated directly into the strain field as an incompatible strain mode. In EAS formulations, the weak form is derived from the Hu–Washizu functional, in which displacements, strains, and stresses are treated as independent fields. The corresponding stationarity conditions provide, respectively, the weak form of the linear momentum balance, eq. (3-6), the weak enforcement of compatibility, eq. (3-9), and the weak form of the constitutive equations, eq. (3-8), namely

$$\begin{cases} \displaystyle\int_\Omega \nabla^\mathrm{s}\delta\mathbf{u} : \boldsymbol{\sigma}\,d\Omega - \int_{\Gamma_\mathrm{N}^u} \delta\mathbf{u}\cdot\mathbf{t}\,d\Gamma - \int_\Omega \delta\mathbf{u}\cdot\mathbf{b}\,d\Omega = 0, \\ \displaystyle\int_\Omega \boldsymbol{\gamma} : \left(\boldsymbol{\Sigma}\left(\boldsymbol{\varepsilon}\right) - \boldsymbol{\sigma}'\right)\,d\Omega = 0, \\ \displaystyle\int_\Omega \boldsymbol{\tau} : \left(\boldsymbol{\varepsilon} - \nabla^\mathrm{s}\mathbf{u}\right)d\Omega = 0, \end{cases} \tag{4-30}$$

where $\delta\mathbf{u} \in \mathcal{V}$, $\boldsymbol{\gamma} \in \mathcal{E}$ and $\boldsymbol{\tau} \in \mathcal{S}$ are, respectively, the admissible variations of the displacement, strains, and stress fields, where $\mathcal{S} = \mathcal{E} = \left[L^2(\Omega)\right]^{n\times n}$ and $\mathcal{V} = \left\{\delta\mathbf{u} \mid \delta\mathbf{u} \in \left[H^1(\Omega)\right]^n, \delta\mathbf{u}\big|_{\Gamma_{\mathrm{D}}^u} = \mathbf{0}\right\}$.

By decomposing the admissible variation of the strain field into a compatible, $\nabla^{\mathrm{s}}\delta\mathbf{u}$, and an incompatible part, $\widetilde{\boldsymbol{\gamma}} \in \widetilde{\mathcal{E}} \in \left[L^2(\Omega)\right]^{n\times n}$, and subtituting Biot's stress decomposition, eq. (3-7), the system (4-30) can be rewritten as

$$\begin{cases} \displaystyle\int_\Omega \nabla^{\mathrm{s}}\delta\mathbf{u} : \left(\boldsymbol{\Sigma}(\boldsymbol{\varepsilon}) - \alpha\, p\,\mathbf{I}\right) d\Omega - \int_{\Gamma_{\mathrm{N}}^u} \delta\mathbf{u}\cdot\mathbf{t}_0\, d\Gamma - \int_\Omega \delta\mathbf{u}\cdot\mathbf{b}\, d\Omega = 0, \\ \displaystyle\int_\Omega \widetilde{\boldsymbol{\gamma}} : \left(\boldsymbol{\Sigma}(\boldsymbol{\varepsilon}) - \boldsymbol{\sigma} - \alpha\, p\,\mathbf{I}\right) d\Omega = 0, \\ \displaystyle\int_\Omega \boldsymbol{\tau} : \widetilde{\boldsymbol{\varepsilon}}\, d\Omega = 0, \end{cases} \tag{4-31}$$

By choosing the space $\mathcal{S}$ as L^2-orthogonal to $\widetilde{\mathcal{E}}$, the problem is reduced to [132]:

$$\begin{cases} \displaystyle\int_\Omega \nabla^{\mathrm{s}}\delta\mathbf{u} : \left(\boldsymbol{\Sigma}(\boldsymbol{\varepsilon}) - \alpha\, p\,\mathbf{I}\right) d\Omega - \int_{\Gamma_{\mathrm{N}}^u} \delta\mathbf{u}\cdot\mathbf{t}_0\, d\Gamma - \int_\Omega \delta\mathbf{u}\cdot\mathbf{b}\, d\Omega = 0, \\ \displaystyle\int_\Omega \widetilde{\boldsymbol{\gamma}} : \left(\boldsymbol{\Sigma}(\boldsymbol{\varepsilon}) - \alpha\, p\,\mathbf{I}\right) d\Omega = 0, \end{cases} \tag{4-32}$$

The last equation in the system (4-31) is not present in (4-32) since it becomes trivial with the orthogonality assumption.

Following the definition of the enhanced strains in eq. (4-27), its admissible variation is also decomposed into a bounded and a discontinuous part as [172]

$$\widetilde{\boldsymbol{\gamma}}(\mathbf{x}) = \widetilde{\boldsymbol{\gamma}}_{\mathrm{b}}(\mathbf{x}) + \delta_{\Gamma_{\mathrm{d}}}(\mathbf{x}) \left([\![\delta\mathbf{u}]\!](\mathbf{x}) \otimes \mathbf{n}_{\mathrm{d}}(\mathbf{x})\right)^{\mathrm{s}}, \tag{4-33}$$

Then, substituting eq.(4-33) into (4-32), using Dirac's delta property, considering the traction continuity condition in eq. (3-10), and rewriting the tensor double-contraction, leads to

$$\begin{cases} \displaystyle\int_\Omega \nabla^{\mathrm{s}}\delta\mathbf{u} : \left(\boldsymbol{\Sigma}(\boldsymbol{\varepsilon}) - \alpha\, p\,\mathbf{I}\right) d\Omega - \int_{\Gamma_{\mathrm{N}}^u} \delta\mathbf{u}\cdot\mathbf{t}_0\, d\Gamma - \int_\Omega \delta\mathbf{u}\cdot\mathbf{b}\, d\Omega = 0, \\ \displaystyle\int_\Omega \widetilde{\boldsymbol{\gamma}}_{\mathrm{b}} : \left(\boldsymbol{\Sigma}(\boldsymbol{\varepsilon}) - \alpha\, p\,\mathbf{I}\right) d\Omega + \int_{\Gamma_{\mathrm{d}}} \delta\mathbf{u}_{\mathrm{d}} \cdot \left(\mathbf{t}'_{\mathrm{d}}(\mathbf{u}_{\mathrm{d}}) - p_{\mathrm{d}}\,\mathbf{n}_{\mathrm{d}}\right) d\Gamma = 0. \end{cases} \tag{4-34}$$

4.3 Weak form of the fluid mass balance in the porous medium

The weak form of eq. (3-23) is obtained by the Galerkin method, followed by the application of the Divergence theorem,

$$\begin{aligned} \int_\Omega \delta p\, \frac{\rho_{\mathrm{l}}}{M}\frac{\partial p}{\partial t}\, d\Omega - \int_\Omega \nabla\delta p \cdot \left(\rho_{\mathrm{l}}\,\mathbf{q}\right) d\Omega + \int_{\partial\Omega} \delta p\, \rho_{\mathrm{l}} \left(\mathbf{q}\cdot\mathbf{n}\right) d\Gamma \\ + \int_\Omega \delta p\, \alpha\, \rho_{\mathrm{l}}\, \dot{\varepsilon}_{\mathrm{v}}\, d\Omega = 0, \end{aligned} \tag{4-35}$$

where $\delta p \in \mathcal{W}$ is the admissible variation of the pore-pressure field in the porous matrix, with $\mathcal{W} = \left\{ \delta p \mid \delta p \in H^1(\Omega), \delta p\big|_{\Gamma^p_{\mathrm{D}}} = 0 \right\}$.

Decomposing the integral over the boundary of the domain,

$$\begin{aligned}&\int_\Omega \delta p \, \frac{\rho_\mathrm{l}}{M} \frac{\partial p}{\partial t} \, d\Omega - \int_\Omega \nabla \delta p \cdot (\rho_\mathrm{l} \, \mathbf{q}) \, d\Omega + \int_{\Gamma^p_\mathrm{N}} \delta p \, \rho_\mathrm{l} \, q_0 \, d\Gamma \\ &+ \int_{\Gamma^+_\mathrm{d}} \delta p \, \rho_\mathrm{l} \left(\mathbf{q} \cdot \mathbf{n}^+_\mathrm{d} \right) d\Gamma + \int_{\Gamma^-_\mathrm{d}} \delta p \, \rho_\mathrm{l} \left(\mathbf{q} \cdot \mathbf{n}^-_\mathrm{d} \right) d\Gamma \\ &+ \int_\Omega \delta p \, \alpha \, \rho_\mathrm{l} \, \dot{\varepsilon}_\mathrm{v} \, d\Omega = 0.\end{aligned} \tag{4-36}$$

Since $\Gamma^-_\mathrm{d} = \Gamma^+_\mathrm{d} = \Gamma_\mathrm{d}$ and $\mathbf{n}^-_\mathrm{d} = -\mathbf{n}^+_\mathrm{d} = \mathbf{n}_\mathrm{d}$, and dividing by the fluid density,

$$\begin{aligned}&\int_\Omega \delta p \, \frac{1}{M} \frac{\partial p}{\partial t} \, d\Omega - \int_\Omega \nabla \delta p \cdot \mathbf{q} \, d\Omega + \int_{\Gamma^p_\mathrm{N}} \delta p \, q_0 \, d\Gamma \\ &- \int_{\Gamma_\mathrm{d}} \delta p \left(\mathbf{q}^+ - \mathbf{q}^- \right) \cdot \mathbf{n}_\mathrm{d} \, d\Gamma + \int_\Omega \delta p \, \alpha \, \dot{\varepsilon}_\mathrm{v} \, d\Omega = 0,\end{aligned} \tag{4-37}$$

where $\mathbf{q}^+$ and $\mathbf{q}^-$ are the flux vectors at boundaries Γ^+_d and Γ^-_d, respectively. Then, substituting eq. (3-36) leads to

$$\begin{aligned}\int_\Omega \delta p \, \frac{1}{M} \frac{\partial p}{\partial t} \, d\Omega - \int_\Omega \nabla \delta p \cdot \mathbf{q} \, d\Omega + \int_{\Gamma^p_\mathrm{N}} \delta p \, q_0 \, d\Gamma - \int_{\Gamma_\mathrm{d}} \delta p \, q^\mathrm{t}_\mathrm{d} \, d\Gamma \\ + \int_\Omega \delta p \, \alpha \, \dot{\varepsilon}_\mathrm{v} \, d\Omega = 0.\end{aligned} \tag{4-38}$$

4.4
Weak form of the fluid mass balance in the discontinuity

The weak form of Eq. (3-30) is obtained by the Galerkin method, followed by the application of the Divergence theorem, which gives

$$\begin{aligned}&\int_{\Omega_\mathrm{d}} \delta p_\mathrm{d} \, \frac{\rho_\mathrm{l}}{K_\mathrm{l}} \frac{\partial p_\mathrm{d}}{\partial t} \, d\Omega - \int_{\Omega_\mathrm{d}} \nabla_\mathrm{d} \delta p_\mathrm{d} \cdot (\rho_\mathrm{l} \, \mathbf{q}_\mathrm{d}) \, d\Omega \\ &+ \int_{\partial\Omega_\mathrm{d}} \delta p_\mathrm{d} \, \rho_\mathrm{l} \, (\mathbf{q}_\mathrm{d} \cdot \hat{\mathbf{n}}_\mathrm{d}) \, d\Gamma + \int_{\Omega_\mathrm{d}} \delta p_\mathrm{d} \, \rho_\mathrm{l} \, \nabla_\mathrm{d} \cdot \dot{\mathbf{u}}_\mathrm{d} \, d\Omega = 0,\end{aligned} \tag{4-39}$$

where δp_d is the admissible variation of the pore-pressure field in the discontinuity.

Decomposing the integral over the boundary of the domain,

$$\begin{aligned}&\int_{\Omega_\mathrm{d}} \delta p_\mathrm{d} \, \frac{\rho_\mathrm{l}}{K_\mathrm{l}} \frac{\partial p_\mathrm{d}}{\partial t} \, d\Omega - \int_{\Omega_\mathrm{d}} \nabla_\mathrm{d} \delta p_\mathrm{d} \cdot (\rho_\mathrm{l} \, \mathbf{q}_\mathrm{d}) \, d\Omega \\ &+ \int_{\Gamma^+_d} \delta p_\mathrm{d} \, \rho_\mathrm{l} \left(\mathbf{q}_\mathrm{d} \cdot \hat{\mathbf{n}}^+_\mathrm{d} \right) d\Gamma + \int_{\Gamma^-_d} \delta p_\mathrm{d} \, \rho_\mathrm{l} \left(\mathbf{q}_\mathrm{d} \cdot \hat{\mathbf{n}}^-_\mathrm{d} \right) d\Gamma \\ &+ \int_{\Omega_\mathrm{d}} \delta p_\mathrm{d} \, \rho_\mathrm{l} \, \nabla_\mathrm{d} \cdot \dot{\mathbf{u}}_\mathrm{d} \, d\Omega = 0.\end{aligned} \tag{4-40}$$

Using $\hat{\mathbf{n}}^-_\mathrm{d} = -\hat{\mathbf{n}}^+_\mathrm{d} = \hat{\mathbf{n}}_\mathrm{d}$ and the flux-compatibility relation (3-36), and dividing by the fluid density,

$$\int_{\Omega_\mathrm{d}} \delta p_\mathrm{d} \frac{1}{K_\mathrm{l}} \frac{\partial p_\mathrm{d}}{\partial t} \, d\Omega - \int_{\Omega_\mathrm{d}} \nabla_\mathrm{d} \delta p_\mathrm{d} \cdot \mathbf{q}_\mathrm{d} \, d\Omega + \int_{\Gamma_d} \delta p_\mathrm{d} \, q_\mathrm{d}^\mathrm{t} \, d\Gamma + \int_{\Omega_\mathrm{d}} \delta p_\mathrm{d} \, \nabla_\mathrm{d} \cdot \dot{\mathbf{u}}_\mathrm{d} \, d\Omega = 0. \tag{4-41}$$

The formulation is now reduced from the discontinuity domain Ω_d to its mid-surface Γ_d by integrating across the local aperture. Assuming that the discontinuity pressure and its admissible variation do not vary in the thickness direction, the storage term becomes

$$\begin{aligned}\int_{\Omega_\mathrm{d}} \delta p_\mathrm{d} \frac{1}{K_\mathrm{l}} \frac{\partial p_\mathrm{d}}{\partial t} \, d\Omega &= \int_{\Gamma_\mathrm{d}} \int_{-\frac{w}{2}}^{\frac{w}{2}} \delta p_\mathrm{d} \frac{1}{K_\mathrm{l}} \frac{\partial p_\mathrm{d}}{\partial t} \, dn \, d\Gamma \\ &= \int_{\Gamma_\mathrm{d}} \delta p_\mathrm{d} \frac{w}{K_\mathrm{l}} \frac{\partial p_\mathrm{d}}{\partial t} \, d\Gamma\end{aligned}$$

Introducing a local orthonormal basis $\mathbf{m}_1, \mathbf{m}_2, \mathbf{n}_\mathrm{d}$ aligned with the discontinuity, with coordinates (s_1, s_2, n), and considering only the tangential components of $\mathbf{q}_\mathrm{d}$ in the in-plane divergence, the flux term can be written as

$$\begin{aligned}\int_{\Omega_\mathrm{d}} \nabla_\mathrm{d} \delta p_\mathrm{d} \cdot \mathbf{q}_\mathrm{d} \, d\Omega &= \int_{\Omega_\mathrm{d}} \begin{bmatrix} \frac{\partial \delta p_\mathrm{d}}{\partial s_1} \\ \frac{\partial \delta p_\mathrm{d}}{\partial s_2} \\ 0 \end{bmatrix}^\top \left(-\frac{\mathbf{k}_\mathrm{d}}{\mu_\mathrm{l}} \left(\begin{bmatrix} \frac{\partial p_\mathrm{d}}{\partial s_1} \\ \frac{\partial p_\mathrm{d}}{\partial s_2} \\ 0 \end{bmatrix} - \rho_\mathrm{l} \begin{bmatrix} \mathbf{m}_1{}^\top \\ \mathbf{m}_2{}^\top \\ \mathbf{n}_\mathrm{d}{}^\top \end{bmatrix} \mathbf{g} \right) \right) d\Omega \\ &= \int_{\Gamma_\mathrm{d}} \int_{-\frac{w}{2}}^{\frac{w}{2}} \begin{bmatrix} \frac{\partial \delta p_\mathrm{d}}{\partial s_1} \\ \frac{\partial \delta p_\mathrm{d}}{\partial s_2} \end{bmatrix}^\top \left(-\frac{k_\mathrm{d}^\mathrm{L}}{\mu_\mathrm{l}} \left(\begin{bmatrix} \frac{\partial p_\mathrm{d}}{\partial s_1} \\ \frac{\partial p_\mathrm{d}}{\partial s_2} \end{bmatrix} - \rho_\mathrm{l} \begin{bmatrix} \mathbf{m}_1{}^\top \\ \mathbf{m}_2{}^\top \end{bmatrix} \mathbf{g} \right) \right) dn \, d\Gamma \\ &= \int_{\Gamma_\mathrm{d}} \begin{bmatrix} \frac{\partial \delta p_\mathrm{d}}{\partial s_1} \\ \frac{\partial \delta p_\mathrm{d}}{\partial s_2} \end{bmatrix}^\top w \left(-\frac{k_\mathrm{d}^\mathrm{L}}{\mu_\mathrm{l}} \left(\begin{bmatrix} \frac{\partial p_\mathrm{d}}{\partial s_1} \\ \frac{\partial p_\mathrm{d}}{\partial s_2} \end{bmatrix} - \rho_\mathrm{l} \begin{bmatrix} \mathbf{m}_1{}^\top \\ \mathbf{m}_2{}^\top \end{bmatrix} \mathbf{g} \right) \right) d\Gamma\end{aligned}$$

The volumetric-deformation contribution is expressed in local coordinates as

$$\begin{aligned}\int_{\Omega_\mathrm{d}} \delta p_\mathrm{d} \, \nabla_\mathrm{d} \cdot \dot{\mathbf{u}}_\mathrm{d} \, d\Omega &= \int_{\Omega_\mathrm{d}} \delta p_\mathrm{d} \left(\frac{\partial \dot{u}_\mathrm{d}^{s_1}}{\partial s_1} + \frac{\partial \dot{u}_\mathrm{d}^{s_2}}{\partial s_2} + \frac{\partial \dot{u}_\mathrm{d}^{n}}{\partial n} \right) d\Omega. \\ &= \int_{\Gamma_\mathrm{d}} \int_{-\frac{w}{2}}^{\frac{w}{2}} \delta p_\mathrm{d} \left(\frac{\partial \dot{u}_\mathrm{d}^{s_1}}{\partial s_1} + \frac{\partial \dot{u}_\mathrm{d}^{s_2}}{\partial s_2} + \frac{\partial \dot{u}_\mathrm{d}^{n}}{\partial n} \right) dn \, d\Gamma. \\ &= \int_{\Gamma_\mathrm{d}} \delta p_\mathrm{d} \left(\frac{\partial \dot{u}_\mathrm{d}^{s_1}}{\partial s_1} n + \frac{\partial \dot{u}_\mathrm{d}^{s_2}}{\partial s_2} n + \dot{u}_\mathrm{d}^{n} \right) \Bigg|_{-\frac{w}{2}}^{\frac{w}{2}} d\Gamma. \\ &= \int_{\Gamma_\mathrm{d}} \delta p_\mathrm{d} \frac{w}{2} \left(\frac{\partial \dot{u}_\mathrm{d}^{s_1}}{\partial s_1} \bigg|_{-\frac{w}{2}} + \frac{\partial \dot{u}_\mathrm{d}^{s_1}}{\partial s_1} \bigg|_{\frac{w}{2}} \right) d\Gamma \\ &+ \int_{\Gamma_\mathrm{d}} \delta p_\mathrm{d} \frac{w}{2} \left(\frac{\partial \dot{u}_\mathrm{d}^{s_2}}{\partial s_2} \bigg|_{-\frac{w}{2}} + \frac{\partial \dot{u}_\mathrm{d}^{s_2}}{\partial s_2} \bigg|_{\frac{w}{2}} \right) d\Gamma \\ &+ \int_{\Gamma_\mathrm{d}} \delta p_\mathrm{d} \, [\![\dot{u}_\mathrm{d}^{n}]\!] \, d\Gamma \\ &= \int_{\Gamma_\mathrm{d}} \delta p_\mathrm{d} \, w \left\langle \nabla_\mathrm{d}^\mathrm{tan} \cdot \dot{\mathbf{u}}_\mathrm{d}^\mathrm{s} \right\rangle d\Gamma + \int_{\Gamma_\mathrm{d}} \delta p_\mathrm{d} \, [\![\dot{u}_\mathrm{d}^{n}]\!] \, d\Gamma.\end{aligned} \tag{4-42}$$

where $\nabla_{\mathrm{d}}^{\tan}$ contains only the tangential components (s_1, s_2) from ∇_{d}, $\dot{\mathbf{u}}_{\mathrm{d}}^{\mathrm{s}} = [\,\dot{u}_{\mathrm{d}}^{s_1},\, \dot{u}_{\mathrm{d}}^{s_2}\,]^{\mathsf{T}}$ collects the tangential components of the discontinuity velocity field, and $\langle\cdot\rangle$ denotes the mean operator across the discontinuity, defined as $\langle a \rangle = \frac{1}{2}(a^+ + a^-)$.

Collecting the previous expressions, the weak form posed on the discontinuity mid-surface Γ_{d} reads

$$\begin{aligned}
&\int_{\Gamma_{\mathrm{d}}} \delta p_{\mathrm{d}} \frac{w}{K_{\mathrm{l}}} \frac{\partial p_{\mathrm{d}}}{\partial t}\, d\Gamma + \int_{\Gamma_d} \delta p_{\mathrm{d}}\, q_{\mathrm{d}}^{\mathrm{t}}\, d\Gamma \\
&- \int_{\Gamma_{\mathrm{d}}} \begin{bmatrix} \frac{\partial \delta p_{\mathrm{d}}}{\partial s_1} \\ \frac{\partial \delta p_{\mathrm{d}}}{\partial s_2} \end{bmatrix}^{\top} w \left(-\frac{k_{\mathrm{d}}^{\mathrm{L}}}{\mu_{\mathrm{l}}} \left(\begin{bmatrix} \frac{\partial p_{\mathrm{d}}}{\partial s_1} \\ \frac{\partial p_{\mathrm{d}}}{\partial s_2} \end{bmatrix} - \rho_{\mathrm{l}} \begin{bmatrix} \mathbf{m}_1{}^{\top} \\ \mathbf{m}_2{}^{\top} \end{bmatrix} \mathbf{g} \right) \right) d\Gamma \\
&+ \int_{\Gamma_{\mathrm{d}}} \delta p_{\mathrm{d}}\, w \left\langle \nabla_{\mathrm{d}}^{\tan} \cdot \dot{\mathbf{u}}_{\mathrm{d}}^{\mathrm{s}} \right\rangle d\Gamma + \int_{\Gamma_{\mathrm{d}}} \delta p_{\mathrm{d}} \, [\![\dot{u}_{\mathrm{d}}^{n}]\!]\, d\Gamma = 0.
\end{aligned} \tag{4-43}$$

4.5
Geometric characterization of the discontinuities

In both two- and three-dimensional problems, the discontinuity within each finite element is assumed to be straight, represented by a line segment in two dimensions and a planar surface in three dimensions. At the element level, the discontinuity geometry is characterized by a reference point, taken here as its centroid, $\mathbf{x}_{\mathrm{ref}}$, together with a set of orientation vectors.

4.5.1
Two-dimensional problems

Figure 4.5 illustrates a linear quadrilateral element crossed by a straight discontinuity segment.

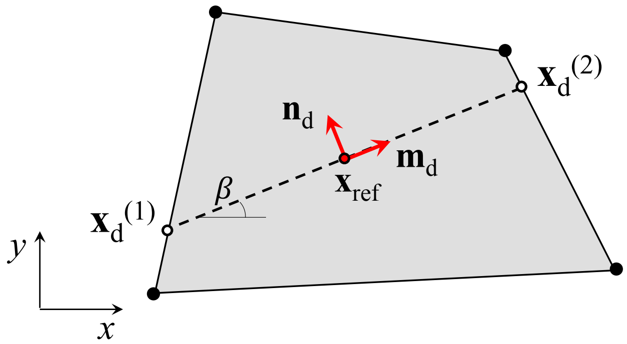

Figure 4.5: Two-dimensional finite element with embedded discontinuity

Let $\mathbf{x}_{\mathrm{d}}^{(1)}$ and $\mathbf{x}_{\mathrm{d}}^{(2)}$ denote the intersection points between the discontinuity and the element edges, expressed in the global Cartesian coordinate system. The tangential unit vector of the discontinuity is obtained as

$$\mathbf{m}_{\mathrm{d}} = \frac{\mathbf{x}_{\mathrm{d}}^{(2)} - \mathbf{x}_{\mathrm{d}}^{(1)}}{\left\|\mathbf{x}_{\mathrm{d}}^{(2)} - \mathbf{x}_{\mathrm{d}}^{(1)}\right\|} = [\cos(\beta) \quad \sin(\beta) \quad 0]^{\top} \tag{4-44}$$

where β is the angle between $\mathbf{m}_{\mathrm{d}}$ and the global x-axis.

The associated unit normal vector is defined by the cross product between the out-of-plane unit vector $\mathbf{e}_z = [0 \quad 0 \quad 1]^{\top}$ as

$$\mathbf{n}_{\mathrm{d}} = \mathbf{e}_z \times \mathbf{m}_{\mathrm{d}} = [-\sin(\beta) \quad \cos(\beta) \quad 0]^{\top} \tag{4-45}$$

4.5.2 Three-dimensional problems

Figure 4.6 illustrates a linear hexahedral element crossed by a planar discontinuity surface.

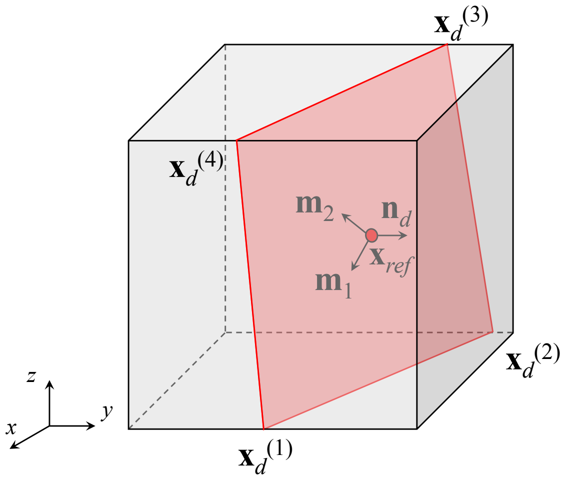

Figure 4.6: Three-dimensional finite element with embedded discontinuity [9]

Let $\mathbf{x}_{\mathrm{d}}^{(1)}$ and $\mathbf{x}_{\mathrm{d}}^{(2)}$ denote two distinct points of this surface. The unit normal vector to the discontinuity is obtained as

$$\mathbf{n}_{\mathrm{d}} = \frac{\left(\mathbf{x}_{\mathrm{d}}^{(1)} - \mathbf{x}_{\mathrm{ref}}\right) \times \left(\mathbf{x}_{\mathrm{d}}^{(2)} - \mathbf{x}_{\mathrm{ref}}\right)}{\left\|\left(\mathbf{x}_{\mathrm{d}}^{(1)} - \mathbf{x}_{\mathrm{ref}}\right) \times \left(\mathbf{x}_{\mathrm{d}}^{(2)} - \mathbf{x}_{\mathrm{ref}}\right)\right\|}, \tag{4-46}$$

A first tangential unit vector lying in the discontinuity plane is defined by

$$\mathbf{m}_1 = \frac{\left(\mathbf{x}_{\mathrm{d}}^{(1)} - \mathbf{x}_{\mathrm{ref}}\right)}{\left\|\left(\mathbf{x}_{\mathrm{d}}^{(1)} - \mathbf{x}_{\mathrm{ref}}\right)\right\|}, \tag{4-47}$$

and the second tangential unit vector is obtained from the cross product

$$\mathbf{m}_2 = \mathbf{n}_{\mathrm{d}} \times \mathbf{m}_1. \tag{4-48}$$

4.6 Finite element discretization

This section presents the spatial discretization of the primary fields and other state variables following the Finite Element Method.

4.6.1 Regular part of the displacement field

The regular part of the displacement field in eq. (4-25) is approximated using the standard finite element shape function matrix, $\mathbf{N}_{\mathrm{u}}(\mathbf{x})$, as

$$\hat{\mathbf{u}}^h(\mathbf{x}, t) = \mathbf{N}_{\mathrm{u}}(\mathbf{x})\,\mathbf{d}(t)\,, \tag{4-49}$$

where $\mathbf{d}$ is the global vector collecting the nodal values of the regular displacement field. The symmetric part of the displacement gradient is discretized as

$$\nabla^{\mathrm{S}}\hat{\mathbf{u}}^h(\mathbf{x}, t) = \mathbf{B}_{\mathrm{u}}(\mathbf{x})\,\mathbf{d}(t)\,, \tag{4-50}$$

where $\mathbf{B}_{\mathrm{u}}(\mathbf{x})$ is the standard finite element strain-displacement matrix.

4.6.2 Admissible variations of the displacement field

The admissible variations of the displacement field, $\delta\mathbf{u}^h$, and its symmetric gradient follow the same interpolation as

$$\delta\mathbf{u}^h(\mathbf{x}, t) = \mathbf{N}_{\mathrm{u}}(\mathbf{x})\,\delta\mathbf{d}(t)\,, \tag{4-51}$$

$$\nabla^{\mathrm{S}}\delta\mathbf{u}^h(\mathbf{x}, t) = \mathbf{B}_{\mathrm{u}}(\mathbf{x})\,\delta\mathbf{d}(t)\,, \tag{4-52}$$

where $\delta\mathbf{d}$ is the vector of nodal variations associated with the displacement field.

4.6.3 Displacement jump

The displacement jump along the discontinuity in the discontinuity local coordinate system, $\mathbf{u}_{\mathrm{d}}^h$, is defined in terms of the enriched DOFs, $\boldsymbol{\alpha}_{\mathrm{u}}$, as

$$\mathbf{u}_{\mathrm{d}}^h(s_1, s_2, t) = \mathbf{N}_{\mathrm{du}}(s_1, s_2)\,\boldsymbol{\alpha}_{\mathrm{u}}(t). \tag{4-53}$$

For a displacement jump with a linear variations along s_1 and s_2,

$$\mathbf{N}_{\mathrm{du}}(s_1, s_2) = \begin{bmatrix} 1 & 0 & 0 & s_1 & 0 & 0 & s_2 & 0 & 0 \\ 0 & 1 & 0 & 0 & s_1 & 0 & 0 & s_2 & 0 \\ 0 & 0 & 1 & 0 & 0 & s_1 & 0 & 0 & s_2 \end{bmatrix}, \tag{4-54}$$

$$\boldsymbol{\alpha}_{\mathrm{u}} = \begin{bmatrix} \alpha_0^{m_1} & \alpha_0^{m_2} & \alpha_0^{n} & \alpha_1^{m_1} & \alpha_1^{m_2} & \alpha_1^{n} & \alpha_2^{m_1} & \alpha_2^{m_2} & \alpha_2^{n} \end{bmatrix}^{\top}. \tag{4-55}$$

The admissible variation of the displacement jump, $\delta\mathbf{u}_{\mathrm{d}}^{h}$, is approximated with the same shape function matrix as

$$\delta\mathbf{u}_{\mathrm{d}}^{h}(s_1, s_2, t) = \mathbf{N}_{\mathrm{du}}(s_1, s_2)\, \delta\boldsymbol{\alpha}_{\mathrm{u}}(t), \tag{4-56}$$

where $\delta\boldsymbol{\alpha}_{\mathrm{u}}$ represents the admissible variation of the enriched dofs.

4.6.4 Enhanced part of the displacement field

The definition of the enhanced part of the displacement field in eq. (4-25) is based on the discontinuity jump field, since each enriched DOF in $\boldsymbol{\alpha}_{\mathrm{u}}$ is associated with an enhanced deformation mode. Armero and Kim [135] presented the deformation modes for a three-dimensional problem with a linear displacement jump along the discontinuity:

$$\begin{aligned}
\tilde{\mathbf{u}}^{h}(\mathbf{x}) = {} & \underbrace{\alpha_0^{m_1}\, \mathbf{m}_1 + \alpha_0^{m_2}\, \mathbf{m}_2 + \alpha_0^{n}\, \mathbf{n}_{\mathrm{d}}}_{\text{Relative translation}} \\
& + \underbrace{\alpha_1^{n} \left(\mathbf{n}_{\mathrm{d}}\, {\mathbf{m}_1}^{\top} - \mathbf{m}_1\, {\mathbf{n}_{\mathrm{d}}}^{\top} \right) \Delta\mathbf{x} + \alpha_2^{n} \left(\mathbf{n}_{\mathrm{d}}\, {\mathbf{m}_2}^{\top} - \mathbf{m}_2\, {\mathbf{n}_{\mathrm{d}}}^{\top} \right) \Delta\mathbf{x}}_{\text{Relative rotation around in-plane vectors}} \\
& + \underbrace{\alpha_1^{m_1} \left(\mathbf{m}_1\, {\mathbf{m}_1}^{\top} \right) \Delta\mathbf{x} + \alpha_2^{m_2} \left(\mathbf{m}_2\, {\mathbf{m}_2}^{\top} \right) \Delta\mathbf{x}}_{\text{Relative stretching}} \\
& + \underbrace{(\alpha_1^{m_2} + \alpha_2^{m_1})\, \frac{1}{2} \left(\mathbf{m}_2\, {\mathbf{m}_1}^{\top} + \mathbf{m}_2\, {\mathbf{m}_1}^{\top} \right) \Delta\mathbf{x}}_{\text{In-plane shear}} \\
& + \underbrace{(\alpha_1^{m_2} - \alpha_2^{m_1})\, \frac{1}{2} \left(\mathbf{m}_2\, {\mathbf{m}_1}^{\top} - \mathbf{m}_2\, {\mathbf{m}_1}^{\top} \right) \Delta\mathbf{x},}_{\text{Relative rotation round normal vector}}
\end{aligned} \tag{4-57}$$

where $\Delta\mathbf{x} = \mathbf{x} - \mathbf{x}_{\mathrm{ref}}$.

The derivation of these modes is presented in Appendix C.

4.6.5 Bounded part of the enhanced strain field

The discretized enhanced part of the strain field, eq. (4-28), can be obtained from

$$\tilde{\boldsymbol{\varepsilon}}_{\mathrm{b}}^{h}(\mathbf{x}) = \mathcal{H}_{\Gamma_{\mathrm{d}}}(\mathbf{x})\, \nabla^{\mathrm{s}} \tilde{\mathbf{u}}^{h}(\mathbf{x}) - \sum_{i=1}^{n_{\mathrm{n}}} \mathbf{B}_{u}^{i}(\mathbf{x})\, \mathcal{H}_{\Gamma_{\mathrm{d}}}(\mathbf{x}_i)\, \tilde{\mathbf{u}}^{h}(\mathbf{x}_i). \tag{4-58}$$

which can be written more compactly as

$$\tilde{\boldsymbol{\varepsilon}}_{\mathrm{b}}^{h}(\mathbf{x}, t) = \widetilde{\mathbf{B}}_{\mathrm{u}}(\mathbf{x})\, \boldsymbol{\alpha}_{\mathrm{u}}(t)\,, \tag{4-59}$$

Then the strain field, (4-26), is discretized as

$$\boldsymbol{\varepsilon}^h(\mathbf{x},t) = \mathbf{B}_\mathrm{u}(\mathbf{x})\,\mathbf{d}(t) + \widetilde{\mathbf{B}}_\mathrm{u}(\mathbf{x})\,\boldsymbol{\alpha}_\mathrm{u}(t)\,,\ \ \mathbf{x} \in \Omega\backslash\Gamma_\mathrm{d}. \tag{4-60}$$

4.6.6 Admissible variation of the bounded part of the enhanced strain field

The discretization of the admissible variation in the bounded part of the enhanced strain field, $\tilde{\boldsymbol{\gamma}}_\mathrm{b}^h$, is

$$\tilde{\boldsymbol{\gamma}}_\mathrm{b}^h(\mathbf{x},t) = \mathbf{G}(\mathbf{x})\,\delta\boldsymbol{\alpha}_\mathrm{u}(t)\,. \tag{4-61}$$

In the Kinematically Optimal Symmetric (KOS) versions of embedded finite element formulation, matrix $\mathbf{G}$ is equal to $\widetilde{\mathbf{B}}_\mathrm{u}$. In the Statically and Kinematically Optimal Nonsymmetric (SKON) versions, $\mathbf{G}$ is defined based on the orthogonality condition between the enhanced strain and the stress fields, which poses that

$$\int_\Omega \widetilde{\boldsymbol{\gamma}}_\mathrm{b} : \boldsymbol{\sigma}\, d\Omega + \int_{\Gamma_\mathrm{d}} \delta\mathbf{u}_\mathrm{d}\cdot(\boldsymbol{\sigma}\cdot\mathbf{n}_\mathrm{d})\ d\Gamma = 0, \tag{4-62}$$

The projection of the stress tensor in a plane given by the normal $\mathbf{n}$ is defined as,

$$\boldsymbol{\sigma}\cdot\mathbf{n} = \mathbf{P}^\top\,\boldsymbol{\sigma}^h, \tag{4-63}$$

where $\boldsymbol{\sigma}^h = \{\sigma_{xx},\sigma_{yy},\sigma_{zz},\sigma_{xy},\sigma_{yz},\sigma_{xz}\}^\top$ is the approximated stress tensor in Voigt notation, and $\mathbf{P}$ is a projection matrix defined as

$$\mathbf{P} = \begin{bmatrix} n_x & 0 & 0 & n_y & 0 & n_z \\ 0 & n_y & 0 & n_x & n_z & 0 \\ 0 & 0 & n_z & 0 & n_y & n_x \end{bmatrix}^\top. \tag{4-64}$$

Then, substituting the discretized fields defined in eqs. (4-61) and (4-56), provides the relation

$$\int_\Omega \mathbf{G}^\top\,\boldsymbol{\sigma}^h\,d\Omega = -\int_{\Gamma_\mathrm{d}} {\mathbf{N}_\mathrm{du}}^\top\,\boldsymbol{\Lambda}^\top\,\mathbf{P}^\top\,\boldsymbol{\sigma}^h\,d\Gamma. \tag{4-65}$$

where $\boldsymbol{\Lambda} = [\mathbf{m}_1\ \mathbf{m}_2\ \mathbf{n}_\mathrm{d}]$ is the discontinuity orientation matrix, which is introduced because the enriched DOFs are defined in the discontinuity local coordinate system, see Eq. (4-56). Therefore, it acts as a rotation matrix of the displacement jumps and the traction vector. Figure 4.7 illustrates that the matrix $\mathbf{G}$ in eq. (4-65) can be interpreted as a matrix that recovers the continuum stresses from the bulk integration point to the integration points at the discontinuity.

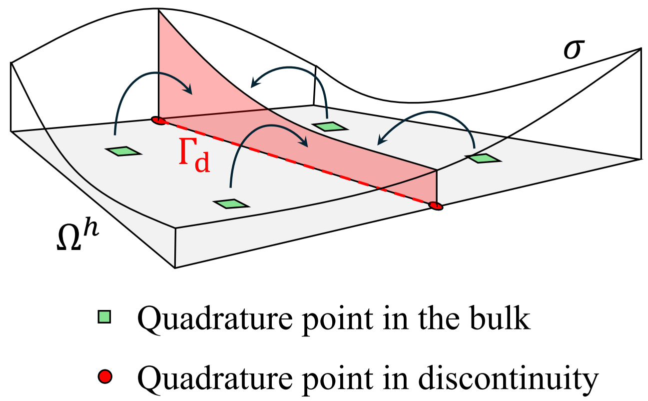

Figure 4.7: Representation of the projection of the stresses from the bulk to the discontinuity in a linear quadrilateral finite element (adapted from Armero and Linder [10])

In equation (4-65), the term on the right-hand side can be rewritten using the displacement jump discretization, eq. (4-54), as

$$\int_{\Omega} \mathbf{G}^{\top} \boldsymbol{\sigma}^h \, d\Omega = -\int_{\Gamma_{\mathrm{d}}} \begin{bmatrix} \mathbf{P}\,\boldsymbol{\Lambda} & s_1\,\mathbf{P}\,\boldsymbol{\Lambda} & s_2\,\mathbf{P}\,\boldsymbol{\Lambda} \end{bmatrix}^{\top} \boldsymbol{\sigma}^h \, d\Gamma \tag{4-66}$$

Then, assuming that the matrices inside the integrals are proportional to each other through a polynomial function $g_k(\mathbf{x})$, $k = 0, 1, 2$, [134, 7, 135, 173]:

$$\mathbf{G}(\mathbf{x}) = -\begin{bmatrix} g_0(\mathbf{x})\;\mathbf{P}\boldsymbol{\Lambda} & g_1(\mathbf{x})\;\mathbf{P}\,\boldsymbol{\Lambda} & g_2(\mathbf{x})\;\mathbf{P}\,\boldsymbol{\Lambda} \end{bmatrix}^{\top}. \tag{4-67}$$

The polynomial $g_k(\mathbf{x})$ is assumed to have an order that matches the polynomial approximation of the discrete stress field $\boldsymbol{\sigma}^h(\mathbf{x})$ [174],

$$g_k(\mathbf{x}) = \mathbf{h}(\mathbf{x})^{\top} \begin{bmatrix} c_0^{(k)} & c_1^{(k)} & c_2^{(k)} & c_3^{(k)} \end{bmatrix}^{\top} = \mathbf{h}(\mathbf{x})^{\top} \mathbf{c}_k, \tag{4-68}$$

$$\boldsymbol{\sigma}^h(\mathbf{x}) = \mathbf{h}(\mathbf{x})^{\top} \begin{bmatrix} \boldsymbol{\sigma}_0{}^{\top} & \boldsymbol{\sigma}_1{}^{\top} & \boldsymbol{\sigma}_2{}^{\top} & \boldsymbol{\sigma}_3{}^{\top} \end{bmatrix}^{\top} = \mathbf{h}(\mathbf{x})^{\top} \mathbf{S}, \tag{4-69}$$

where $\mathbf{h}(\mathbf{x})$ is the polynomial basis. Its definition depends on the finite element used. For example, for linear hexahedral elements, $\mathbf{h}(\mathbf{x}) = \begin{bmatrix} 1 & x & y & z \end{bmatrix}^{\top}$.

Substituting equations (4-67), (4-68) and (4-69) into the left-hand side of eq. (4-66), leads to

$$
\begin{aligned}
\int_\Omega \mathbf{G}^\top \boldsymbol{\sigma}^h \, d\Omega &= -\int_\Omega \begin{bmatrix} \boldsymbol{\Lambda}^\top \mathbf{P}^\top \left(\mathbf{h}(\mathbf{x})^\top \mathbf{c}_0\right) \mathbf{h}(\mathbf{x})^\top \mathbf{S} \\ \boldsymbol{\Lambda}^\top \mathbf{P}^\top \left(\mathbf{h}(\mathbf{x})^\top \mathbf{c}_1\right) \mathbf{h}(\mathbf{x})^\top \mathbf{S} \\ \boldsymbol{\Lambda}^\top \mathbf{P}^\top \left(\mathbf{h}(\mathbf{x})^\top \mathbf{c}_2\right) \mathbf{h}(\mathbf{x})^\top \mathbf{S} \end{bmatrix} d\Omega \\
&= -\boldsymbol{\Lambda}^\top \mathbf{P}^\top \int_\Omega \begin{bmatrix} \mathbf{c}_0{}^\top \mathbf{h}(\mathbf{x}) \, \mathbf{h}(\mathbf{x})^\top \\ \mathbf{c}_1{}^\top \mathbf{h}(\mathbf{x}) \, \mathbf{h}(\mathbf{x})^\top \\ \mathbf{c}_2{}^\top \mathbf{h}(\mathbf{x}) \, \mathbf{h}(\mathbf{x})^\top \end{bmatrix} d\Omega \, \mathbf{S} \\
&= -\boldsymbol{\Lambda}^\top \mathbf{P}^\top \begin{bmatrix} \mathbf{c}_0{}^\top \\ \mathbf{c}_1{}^\top \\ \mathbf{c}_2{}^\top \end{bmatrix} \int_\Omega \mathbf{h}(\mathbf{x}) \, \mathbf{h}(\mathbf{x})^\top \, d\Omega \, \mathbf{S},
\end{aligned} \tag{4-70}
$$

doing the same to the right-hand side,

$$
\begin{aligned}
\int_{\Gamma_\mathrm{d}} \begin{bmatrix} \mathbf{P}\boldsymbol{\Lambda} & s_1 \mathbf{P}\boldsymbol{\Lambda} & s_2 \mathbf{P}\boldsymbol{\Lambda} \end{bmatrix}^\top \boldsymbol{\sigma}^h \, d\Gamma &= \int_{\Gamma_\mathrm{d}} \begin{bmatrix} \boldsymbol{\Lambda}^\top \mathbf{P}^\top \mathbf{h}(\mathbf{x})^\top \mathbf{S} \\ s_1 \boldsymbol{\Lambda}^\top \mathbf{P}^\top \mathbf{h}(\mathbf{x})^\top \mathbf{S} \\ s_2 \boldsymbol{\Lambda}^\top \mathbf{P}^\top \mathbf{h}(\mathbf{x})^\top \mathbf{S} \end{bmatrix} d\Gamma \\
&= \boldsymbol{\Lambda}^\top \mathbf{P}^\top \int_{\Gamma_\mathrm{d}} \begin{bmatrix} \mathbf{h}(\mathbf{x})^\top \\ s_1 \mathbf{h}(\mathbf{x})^\top \\ s_2 \mathbf{h}(\mathbf{x})^\top \end{bmatrix} d\Gamma \, \mathbf{S},
\end{aligned} \tag{4-71}
$$

gives,

$$
\boldsymbol{\Lambda}^\top \mathbf{P}^\top \left(-\begin{bmatrix} \mathbf{c}_0{}^\top \\ \mathbf{c}_1{}^\top \\ \mathbf{c}_2{}^\top \end{bmatrix} \int_\Omega \mathbf{h}(\mathbf{x}) \, \mathbf{h}(\mathbf{x})^\top \, d\Omega + \int_{\Gamma_\mathrm{d}} \begin{bmatrix} \mathbf{h}(\mathbf{x})^\top \\ s_1 \mathbf{h}(\mathbf{x})^\top \\ s_2 \mathbf{h}(\mathbf{x})^\top \end{bmatrix} d\Gamma \right) \mathbf{S} = \mathbf{0}. \tag{4-72}
$$

Therefore, the coefficients of the polynomial approximation can be determined by solving the linear system,

$$
\begin{bmatrix} \mathbf{c}_0 & \mathbf{c}_1 & \mathbf{c}_2 \end{bmatrix} = \left(\int_\Omega \mathbf{h} \, \mathbf{h}^\top \, d\Omega \right)^{-1} \begin{bmatrix} \int_{\Gamma_\mathrm{d}} \mathbf{h} \, d\Gamma & \int_{\Gamma_\mathrm{d}} s_1 \mathbf{h} \, d\Gamma & \int_{\Gamma_\mathrm{d}} s_2 \mathbf{h} \, d\Gamma \end{bmatrix}. \tag{4-73}
$$

4.6.6.1 Average surface divergence of the tangential displacement

In Eq. (4-43), the computation of $\langle \nabla_\mathrm{d}^\mathrm{tan} \cdot \dot{\mathbf{u}}_\mathrm{d}^\mathrm{s} \rangle$ is required. This quantity represents the surface divergence of the tangential component of the displacement rate along the discontinuity, and is expressed as

$$
\nabla_\mathrm{d}^\mathrm{tan} \cdot \dot{\mathbf{u}}_\mathrm{d}^\mathrm{s} = \left(\mathbf{r}_\varepsilon(\mathbf{m}_1) + \mathbf{r}_\varepsilon(\mathbf{m}_2)\right) \dot{\boldsymbol{\varepsilon}}^h, \tag{4-74}
$$

where

$$
\mathbf{r}_\varepsilon(\mathbf{m}) = \begin{bmatrix} m_x{}^2 & m_y{}^2 & m_z{}^2 & m_x m_y & m_y m_z & m_x m_z \end{bmatrix} \tag{4-75}
$$

and $\boldsymbol{\varepsilon}^h$ is obtained from eq. (4-60) and $\boldsymbol{\varepsilon}^h = \{\varepsilon_{xx}, \varepsilon_{yy}, \varepsilon_{zz}, \gamma_{xy}, \gamma_{yz}, \gamma_{xz}\}^\top$.

Finally, the average surface divergence of the tangential displacement rate is computed by averaging the contributions on both faces of the discontinuity,

$$\begin{aligned}\left\langle \nabla_{\mathrm{d}}^{\tan} \cdot \dot{\mathbf{u}}_{\mathrm{d}}^{\mathrm{s}} \right\rangle &= \frac{1}{2} \left(\mathbf{r}_{\varepsilon}(\mathbf{m}_1) + \mathbf{r}_{\varepsilon}(\mathbf{m}_2) \right) \left(\left(\dot{\boldsymbol{\varepsilon}}^h \right)^+ + \left(\dot{\boldsymbol{\varepsilon}}^h \right)^- \right) \\ &= \left(\mathbf{r}_{\varepsilon}(\mathbf{m}_1) + \mathbf{r}_{\varepsilon}(\mathbf{m}_2) \right) \left(\mathbf{B}_{\mathrm{u}} \, \dot{\mathbf{d}} + \left\langle \widetilde{\mathbf{B}}_{\mathrm{u}} \right\rangle \dot{\boldsymbol{\alpha}}_{\mathrm{u}} \right).\end{aligned} \tag{4-76}$$

4.6.7 Pore-pressure field

To allow the discontinuities to act as a barrier for the fluid flow, the pore-pressure field is defined following the Strong Discontinuity Approach, eq. (4-18), as

$$p(\mathbf{x}) = \widehat{p}(\mathbf{x}) + \mathcal{H}_{\Gamma_{\mathrm{d}}}(\mathbf{x}) \, \widetilde{p}(\mathbf{x}) - \sum_{i=1}^{n_{\mathrm{n}}} N_i(\mathbf{x}) \, \mathcal{H}_{\Gamma_{\mathrm{d}}}(\mathbf{x}_i) \, \widetilde{p}(\mathbf{x}_i), \tag{4-77}$$

where $\widehat{p}$ and $\widetilde{p}$ are the regular and the enhanced parts of the pore-pressure field, respectively.

The regular part of the pore-pressure field is approximated using the standard finite element shape function vector $\mathbf{N}_{\mathrm{p}}(\mathbf{x})$ as

$$\widehat{p}^h \left(\mathbf{x}, t \right) = \mathbf{N}_{\mathrm{p}}(\mathbf{x}) \; \mathbf{p}(t) \,, \tag{4-78}$$

where $\mathbf{p}$ collects the nodal values of the regular pressure field.

The enrichment part of the pore-pressure field is approximated by

$$\widetilde{p}^h(\mathbf{x}, t) = \mathbf{N}_{\alpha_{\mathrm{p}}}(\mathbf{x}) \, \boldsymbol{\alpha}_{\mathrm{p}}(t). \tag{4-79}$$

where

$$\boldsymbol{\alpha}_{\mathrm{p}}(t) = \begin{bmatrix} \alpha_{\mathrm{p}}^0(t) & \alpha_{\mathrm{p}}^1(t) & \alpha_{\mathrm{p}}^2(t) \end{bmatrix}^{\top}, \tag{4-80}$$

and,

$$\mathbf{N}_{\alpha_{\mathrm{p}}}(\mathbf{x}) = \begin{bmatrix} 1 & \mathbf{m}_1 \cdot \Delta\mathbf{x} & \mathbf{m}_2 \cdot \Delta\mathbf{x} \end{bmatrix}. \tag{4-81}$$

Substituting eqs. (4-78) and (4-79) into eq. (4-77) leads to

$$p^h(\mathbf{x}, t) = \mathbf{N}_{\mathrm{p}}(\mathbf{x}) \, \mathbf{p}(t) + \widetilde{\mathbf{N}}_{\mathrm{p}}(\mathbf{x}) \, \boldsymbol{\alpha}_{\mathrm{p}}(t), \tag{4-82}$$

where

$$\widetilde{\mathbf{N}}_{\mathrm{p}}(\mathbf{x}) = \mathcal{H}_{\Gamma_{\mathrm{d}}}(\mathbf{x}) \, \mathbf{N}_{\alpha_{\mathrm{p}}}(\mathbf{x}) - \sum_{i=1}^{n_{\mathrm{n}}} N_i(\mathbf{x}) \, \mathcal{H}_{\Gamma_{\mathrm{d}}}(\mathbf{x}_i) \, \mathbf{N}_{\alpha_{\mathrm{p}}}(\mathbf{x}_i). \tag{4-83}$$

The corresponding gradient matrices are

$$\mathbf{B}_{\mathrm{p}}(\mathbf{x}) = \nabla \mathbf{N}_{\mathrm{p}}(\mathbf{x}), \qquad \widetilde{\mathbf{B}}_{\mathrm{p}}(\mathbf{x}) = \nabla \widetilde{\mathbf{N}}_{\mathrm{p}}(\mathbf{x}). \tag{4-84}$$

The transfer law, eq. (3-37), requires the pore pressure at the adjacent matrix faces of the discontinuity, which are discretized as

$$p^{\pm}(\mathbf{x}) = \mathbf{N}_{\mathrm{p}}(\mathbf{x})\ \mathbf{p}(t) + \widetilde{\mathbf{N}}_{\mathrm{p}}^{\pm}(\mathbf{x})\ \boldsymbol{\alpha}_{\mathrm{p}}(t)\,, \tag{4-85}$$

where $\widetilde{\mathbf{N}}_{\mathrm{p}}^{\pm}$ denote the enriched shape functions evaluated on the two sides of the discontinuity:

$$\widetilde{\mathbf{N}}_{\mathrm{p}}^{+}(\mathbf{x}) = \mathbf{N}_{\alpha_{\mathrm{p}}}(\mathbf{x}) - \sum_{i=1}^{n_{\mathrm{n}}} N_i(\mathbf{x})\,\mathcal{H}_{\Gamma_{\mathrm{d}}}(\mathbf{x}_i)\,\mathbf{N}_{\alpha_{\mathrm{p}}}(\mathbf{x}_i). \tag{4-86}$$

$$\widetilde{\mathbf{N}}_{\mathrm{p}}^{-}(\mathbf{x}) = - \sum_{i=1}^{n_{\mathrm{n}}} N_i(\mathbf{x})\,\mathcal{H}_{\Gamma_{\mathrm{d}}}(\mathbf{x}_i)\,\mathbf{N}_{\alpha_{\mathrm{p}}}(\mathbf{x}_i). \tag{4-87}$$

Finally, a standard symmetric Galerkin method is adopted, and then the admissible variations are interpolated with the same shape function vectors.

4.6.8 Pore-pressure inside the discontinuity

Following a standard symmetric Galerkin method, the pore pressure along the discontinuity mid-surface Γ_{d} and its admissible variation are approximated as

$$p_{\mathrm{dl}}^{h}(s_1, s_2, t) = \mathbf{N}_{\mathrm{dp}}(s_1, s_2)\,\mathbf{p}_{\mathrm{d}}(t), \qquad \delta p_{\mathrm{d}}^{h}(s_1, s_2) = \mathbf{N}_{\mathrm{dp}}(s_1, s_2)\,\delta\mathbf{p}_{\mathrm{d}}, \tag{4-88}$$

with $\mathbf{N}_{\mathrm{dp}}(s_1, s_2)$ the vector of one-dimensional shape functions along Γ_{d} and $\mathbf{p}_{\mathrm{d}}(t)$ the corresponding nodal values. The derivatives with respect to the tangential coordinate are expressed as

$$\begin{bmatrix} \frac{\partial\, p_{\mathrm{d}}^{h}}{\partial\, s_1} \\ \frac{\partial\, p_{\mathrm{d}}^{h}}{\partial\, s_2} \end{bmatrix} = \mathbf{B}_{\mathrm{dp}}(s_1, s_2)\,\mathbf{p}_{\mathrm{d}}(t), \qquad \begin{bmatrix} \frac{\partial\, \delta p_{\mathrm{d}}^{h}}{\partial\, s_1} \\ \frac{\partial\, \delta p_{\mathrm{d}}^{h}}{\partial\, s_2} \end{bmatrix} = \mathbf{B}_{\mathrm{dp}}(s_1, s_2)\,\delta\mathbf{p}_{\mathrm{d}}(t). \tag{4-89}$$

4.7 Solution scheme

Substituting the discretized fields into the weak forms of the governing equations (4-34), (4-38), and (4-43), and adopting a fully implicit (backward Euler) time integration scheme

$$\mathbf{x}\,(t_{n+1}) = \mathbf{x}\,(t_n) + \Delta t\,\dot{\mathbf{x}}\,(t_{n+1}) \tag{4-90}$$

leads, at each time step t_{n+1}, to the nonlinear residual system

$$
\begin{bmatrix} \mathbf{r}_{\mathrm{u}}\left(t_{n+1}\right) \\ \mathbf{r}_{\alpha_{\mathrm{u}}}\left(t_{n+1}\right) \\ \mathbf{r}_{\mathrm{p}}\left(t_{n+1}\right) \\ \mathbf{r}_{\alpha_{\mathrm{p}}}\left(t_{n+1}\right) \\ \mathbf{r}_{\mathrm{p_d}}\left(t_{n+1}\right) \end{bmatrix} = \begin{bmatrix} \mathbf{f}^{\mathrm{i}}_{\mathrm{u}}\left(t_{n+1}\right) \\ \mathbf{f}^{\mathrm{i}}_{\alpha_{\mathrm{u}}}\left(t_{n+1}\right) \\ \mathbf{f}^{\mathrm{i}}_{\mathrm{p}}\left(t_{n+1}\right) \\ \mathbf{f}^{\mathrm{i}}_{\alpha_{\mathrm{p}}}\left(t_{n+1}\right) \\ \mathbf{f}^{\mathrm{i}}_{\mathrm{p_d}}\left(t_{n+1}\right) \end{bmatrix} - \begin{bmatrix} \mathbf{f}^{\mathrm{e}}_{\mathrm{u}}\left(t_{n+1}\right) \\ \mathbf{f}^{\mathrm{e}}_{\alpha_{\mathrm{u}}}\left(t_{n+1}\right) \\ \mathbf{f}^{\mathrm{e}}_{\mathrm{p}}\left(t_{n+1}\right) \\ \mathbf{f}^{\mathrm{e}}_{\alpha_{\mathrm{p}}}\left(t_{n+1}\right) \\ \mathbf{f}^{\mathrm{e}}_{\mathrm{p_d}}\left(t_{n+1}\right) \end{bmatrix}
$$

$$
+ \begin{bmatrix} \mathbf{0} & \mathbf{0} & -\mathbf{Q}_{\mathrm{pu}}{}^{\top} & -\mathbf{Q}_{\alpha_{\mathrm{p}}\mathrm{u}}{}^{\top} & \mathbf{0} \\ \mathbf{0} & \mathbf{0} & -\mathbf{Q}_{\alpha_{\mathrm{u}}\mathrm{p}} & -\mathbf{Q}_{\alpha_{\mathrm{u}}\alpha_{\mathrm{p}}} & -\mathbf{Q}_{\alpha_{\mathrm{u}}\mathrm{p_d}} \\ \mathbf{0} & \mathbf{0} & \mathbf{H}_{\mathrm{pp}} + \mathbf{L}_{\mathrm{pp}} & \mathbf{H}_{\mathrm{p}\alpha_{\mathrm{p}}} + \mathbf{L}_{\mathrm{p}\alpha_{\mathrm{p}}} & -\mathbf{L}_{\mathrm{pp_d}} \\ \mathbf{0} & \mathbf{0} & \mathbf{H}_{\alpha_{\mathrm{p}}\mathrm{p}} + \mathbf{L}_{\alpha_{\mathrm{p}}\mathrm{p}} & \mathbf{H}_{\alpha_{\mathrm{p}}\alpha_{\mathrm{p}}} + \mathbf{L}_{\alpha_{\mathrm{p}}\alpha_{\mathrm{p}}} & -\mathbf{L}_{\alpha_{\mathrm{p}}\mathrm{p_d}} \\ \mathbf{0} & \mathbf{0} & -\mathbf{L}_{\mathrm{p_d p}} & -\mathbf{L}_{\mathrm{p_d}\alpha_{\mathrm{p}}} & \mathbf{H}_{\mathrm{p_d p_d}} + \mathbf{L}_{\mathrm{p_d p_d}} \end{bmatrix} \begin{bmatrix} \mathbf{d}\left(t_{n+1}\right) \\ \boldsymbol{\alpha}_{\mathrm{u}}\left(t_{n+1}\right) \\ \mathbf{p}\left(t_{n+1}\right) \\ \boldsymbol{\alpha}_{\mathrm{p}}\left(t_{n+1}\right) \\ \mathbf{p}_{\mathrm{d}}\left(t_{n+1}\right) \end{bmatrix} \quad (4\text{-}91)
$$

$$
+ \frac{1}{\Delta t} \begin{bmatrix} \mathbf{0} & \mathbf{0} & \mathbf{0} & \mathbf{0} & \mathbf{0} \\ \mathbf{0} & \mathbf{0} & \mathbf{0} & \mathbf{0} & \mathbf{0} \\ \mathbf{Q}_{\mathrm{pu}} & \mathbf{Q}_{\mathrm{p}\alpha_{\mathrm{u}}} & \mathbf{S}_{\mathrm{pp}} & \mathbf{S}_{\mathrm{p}\alpha_{\mathrm{p}}} & \mathbf{0} \\ \mathbf{Q}_{\alpha_{\mathrm{p}}\mathrm{u}} & \mathbf{Q}_{\alpha_{\mathrm{p}}\alpha_{\mathrm{u}}} & \mathbf{S}_{\alpha_{\mathrm{p}}\mathrm{p}} & \mathbf{S}_{\alpha_{\mathrm{p}}\alpha_{\mathrm{p}}} & \mathbf{0} \\ \mathbf{Q}_{\mathrm{p_d u}} & \mathbf{Q}_{\mathrm{p_d}\alpha_{\mathrm{u}}} & \mathbf{0} & \mathbf{0} & \mathbf{S}_{\mathrm{p_d p_d}} \end{bmatrix} \begin{bmatrix} \mathbf{d}\left(t_{n+1}\right) - \mathbf{d}\left(t_n\right) \\ \boldsymbol{\alpha}_{\mathrm{u}}\left(t_{n+1}\right) - \boldsymbol{\alpha}_{\mathrm{u}}\left(t_n\right) \\ \mathbf{p}\left(t_{n+1}\right) - \mathbf{p}\left(t_n\right) \\ \boldsymbol{\alpha}_{\mathrm{p}}\left(t_{n+1}\right) - \boldsymbol{\alpha}_{\mathrm{p}}\left(t_n\right) \\ \mathbf{p}_{\mathrm{d}}\left(t_{n+1}\right) - \mathbf{p}_{\mathrm{d}}\left(t_n\right) \end{bmatrix}
$$

where $\mathbf{r}_{\mathrm{u}}$ and $\mathbf{r}_{\mathrm{p}}$ are the residual vectors associated with the momentum balance and the matrix fluid mass balance, respectively, $\mathbf{r}_{\alpha_{\mathrm{u}}}$ and $\mathbf{r}_{\alpha_{\mathrm{p}}}$ are the residuals of the enriched displacement and pressure fields, and $\mathbf{r}_{\mathrm{p_d}}$ is the residual of the discontinuity fluid mass balance. The vectors $\mathbf{f}^{\mathrm{i}}_{\bullet}$ and $\mathbf{f}^{\mathrm{e}}_{\bullet}$ denote the internal and external force/flow vectors. The matrices $\mathbf{Q}_{\bullet\bullet}$ represent hydro–mechanical coupling, $\mathbf{H}_{\bullet\bullet}$ the conductivity operators, $\mathbf{L}_{\bullet\bullet}$ the fluid flow coupling between matrix and discontinuity, and $\mathbf{S}_{\bullet\bullet}$ the storage matrices arising from fluid compressibility and the time discretization. The definition of these sub-matrices is presented in Appendix D, as well as the derivation of the derivatives of these residual vectors with respect to the DOFs.

For the solution of the nonlinear system, a Newton-Raphson scheme is adopted. At iteration k of time step t_{n+1}, the residual is linearized with respect to the increments of the unknowns, leading to

$$
\mathbf{J}\left(t^k_{n+1}\right) \begin{Bmatrix} \Delta\mathbf{u}\left(t^k_{n+1}\right) \\ \Delta\mathbf{p}\left(t^k_{n+1}\right) \\ \hdashline \Delta\boldsymbol{\alpha}_{\mathrm{u}}\left(t^k_{n+1}\right) \\ \Delta\boldsymbol{\alpha}_{\mathrm{p}}\left(t^k_{n+1}\right) \\ \Delta\mathbf{p}_{\mathrm{d}}\left(t^k_{n+1}\right) \end{Bmatrix} = - \begin{Bmatrix} \mathbf{r}_{\mathrm{u}}\left(t^k_{n+1}\right) \\ \mathbf{r}_{\mathrm{p}}\left(t^k_{n+1}\right) \\ \hdashline \mathbf{r}_{\alpha_{\mathrm{u}}}\left(t^k_{n+1}\right) \\ \mathbf{r}_{\alpha_{\mathrm{p}}}\left(t^k_{n+1}\right) \\ \mathbf{r}_{\mathrm{p_d}}\left(t^k_{n+1}\right) \end{Bmatrix}, \quad (4\text{-}92)
$$

where the increment vector groups first the regular degrees of freedom $(\mathbf{u}, \mathbf{p})$ and then the enriched degrees of freedom $(\boldsymbol{\alpha}_{\mathrm{u}}, \boldsymbol{\alpha}_{\mathrm{p}}, \mathbf{p}_{\mathrm{d}})$. After reordering the unknowns and equations in this way, the Jacobian matrix $\mathbf{J}$ takes the block form

$$\mathbf{J}\left(t_{n+1}^{k}\right)=\left[\begin{array}{cc|ccc}\dfrac{\partial \mathbf{r}_u}{\partial \mathbf{d}} & \dfrac{\partial \mathbf{r}_u}{\partial \mathbf{p}} & \dfrac{\partial \mathbf{r}_u}{\partial \boldsymbol{\alpha}_{\mathrm{u}}} & \dfrac{\partial \mathbf{r}_u}{\partial \boldsymbol{\alpha}_{\mathrm{p}}} & \dfrac{\partial \mathbf{r}_u}{\partial \mathbf{p}_{\mathrm{d}}} \\ \dfrac{\partial \mathbf{r}_p}{\partial \mathbf{d}} & \dfrac{\partial \mathbf{r}_p}{\partial \mathbf{p}} & \dfrac{\partial \mathbf{r}_p}{\partial \boldsymbol{\alpha}_{\mathrm{u}}} & \dfrac{\partial \mathbf{r}_p}{\partial \boldsymbol{\alpha}_{\mathrm{p}}} & \dfrac{\partial \mathbf{r}_p}{\partial \mathbf{p}_{\mathrm{d}}} \\ \hline \dfrac{\partial \mathbf{r}_{\alpha_{\mathrm{u}}}}{\partial \mathbf{d}} & \dfrac{\partial \mathbf{r}_{\alpha_{\mathrm{u}}}}{\partial \mathbf{p}} & \dfrac{\partial \mathbf{r}_{\alpha_{\mathrm{u}}}}{\partial \boldsymbol{\alpha}_{\mathrm{u}}} & \dfrac{\partial \mathbf{r}_{\alpha_{\mathrm{u}}}}{\partial \boldsymbol{\alpha}_{\mathrm{p}}} & \dfrac{\partial \mathbf{r}_{\alpha_{\mathrm{u}}}}{\partial \mathbf{p}_{\mathrm{d}}} \\ \dfrac{\partial \mathbf{r}_{\alpha_{\mathrm{p}}}}{\partial \mathbf{d}} & \dfrac{\partial \mathbf{r}_{\alpha_{\mathrm{p}}}}{\partial \mathbf{p}} & \dfrac{\partial \mathbf{r}_{\alpha_{\mathrm{p}}}}{\partial \boldsymbol{\alpha}_{\mathrm{u}}} & \dfrac{\partial \mathbf{r}_{\alpha_{\mathrm{p}}}}{\partial \boldsymbol{\alpha}_{\mathrm{p}}} & \dfrac{\partial \mathbf{r}_{\alpha_{\mathrm{p}}}}{\partial \mathbf{p}_{\mathrm{d}}} \\ \dfrac{\partial \mathbf{r}_{\mathrm{p_d}}}{\partial \mathbf{d}} & \dfrac{\partial \mathbf{r}_{\mathrm{p_d}}}{\partial \mathbf{p}} & \dfrac{\partial \mathbf{r}_{\mathrm{p_d}}}{\partial \boldsymbol{\alpha}_{\mathrm{u}}} & \dfrac{\partial \mathbf{r}_{\mathrm{p_d}}}{\partial \boldsymbol{\alpha}_{\mathrm{p}}} & \dfrac{\partial \mathbf{r}_{\mathrm{p_d}}}{\partial \mathbf{p}_{\mathrm{d}}}\end{array}\right]_{n+1}^{k}=\left[\begin{array}{c|c}\mathbf{J}_{\mathrm{rr}} & \mathbf{J}_{\mathrm{re}} \\ \hline \mathbf{J}_{\mathrm{er}} & \mathbf{J}_{\mathrm{ee}}\end{array}\right]_{n+1}^{k}. \tag{4-93}$$

The linear system is thus organized with two groups of DOFs: the regular group (r), collecting the displacement and matrix-pressure DOFs $(\mathbf{u}, \mathbf{p})$, and the enriched group (e), collecting the discontinuity DOFs $(\boldsymbol{\alpha}_{\mathrm{u}}, \boldsymbol{\alpha}_{\mathrm{p}}, \mathbf{p}_{\mathrm{d}})$.

4.7.1 Static condensation of the enriched DOFs

The DOFs associated with the discontinuity can be statically condensed. This is achieved using a local–global operator split approach [175], in which the equations associated with the discontinuity DOFs ($\boldsymbol{\alpha}_{\mathrm{u}}$, $\boldsymbol{\alpha}_{\mathrm{p}}$, and $\mathbf{p}_{\mathrm{d}}$) are solved locally within each enriched element, while the regular degrees of freedom $\mathbf{u}$ and $\mathbf{p}$ are kept fixed at their current iteration values. In this local problem, the residual equations associated with $\mathbf{r}_{\alpha_{\mathrm{u}}}$, $\mathbf{r}_{\alpha_{\mathrm{p}}}$, and $\mathbf{r}_{\mathrm{p_d}}$ are enforced to vanish. The resulting block system reads

$$\left[\begin{array}{c|c}\mathbf{J}_{\mathrm{rr}} & \mathbf{J}_{\mathrm{re}} \\ \hline \mathbf{J}_{\mathrm{er}} & \mathbf{J}_{\mathrm{ee}}\end{array}\right]_{n+1}^{k}\left\{\begin{array}{c}\Delta\mathbf{u}\left(t_{n+1}^{k}\right) \\ \Delta\mathbf{p}\left(t_{n+1}^{k}\right) \\ \hline \Delta\boldsymbol{\alpha}_{\mathrm{u}}\left(t_{n+1}^{k}\right) \\ \Delta\boldsymbol{\alpha}_{\mathrm{p}}\left(t_{n+1}^{k}\right) \\ \Delta\mathbf{p}_{\mathrm{d}}\left(t_{n+1}^{k}\right)\end{array}\right\}=-\left\{\begin{array}{c}\mathbf{r}_{\mathrm{u}}\left(t_{n+1}^{k}\right) \\ \mathbf{r}_{\mathrm{p}}\left(t_{n+1}^{k}\right) \\ \hline \mathbf{0} \\ \mathbf{0} \\ \mathbf{0}\end{array}\right\}, \tag{4-94}$$

from which the increments of the enriched DOFs are obtained locally as

$$\left\{\begin{array}{c}\Delta\boldsymbol{\alpha}_{\mathrm{u}}\left(t_{n+1}^{k}\right) \\ \Delta\boldsymbol{\alpha}_{\mathrm{p}}\left(t_{n+1}^{k}\right) \\ \Delta\mathbf{p}_{\mathrm{d}}\left(t_{n+1}^{k}\right)\end{array}\right\}=-\mathbf{J}_{\mathrm{ee}}{}^{-1}\mathbf{J}_{\mathrm{er}}\left\{\begin{array}{c}\Delta\mathbf{u}\left(t_{n+1}^{k}\right) \\ \Delta\mathbf{p}\left(t_{n+1}^{k}\right)\end{array}\right\}, \tag{4-95}$$

Substitution into the upper block yields a reduced system in terms of the regular DOFs only,

$$\underbrace{\left(\mathbf{J}_{\mathrm{rr}}-\mathbf{J}_{\mathrm{re}}\mathbf{J}_{\mathrm{ee}}{}^{-1}\mathbf{J}_{\mathrm{er}}\right)}_{\text{Condensed Jacobian}}\left\{\begin{array}{c}\Delta\mathbf{u}\left(t_{n+1}^{k}\right) \\ \Delta\mathbf{p}\left(t_{n+1}^{k}\right)\end{array}\right\}=-\left\{\begin{array}{c}\mathbf{r}_{\mathrm{u}}\left(t_{n+1}^{k}\right) \\ \mathbf{r}_{\mathrm{p}}\left(t_{n+1}^{k}\right)\end{array}\right\}, \tag{4-96}$$

which incorporates the effect of the discontinuity enrichment into the global system while retaining only the regular displacement and pressure DOFs. Once $\Delta\mathbf{u}$ and $\Delta\mathbf{p}$ are computed, the increments of the enriched DOFs are recovered locally from the previous relation.

4.7.2 Global nodal jump DOFs

The enriched DOFs $\boldsymbol{\alpha}_{\mathrm{u}}$ and $\boldsymbol{\alpha}_{\mathrm{p}}$ are defined locally and are directly associated with the jump field of a discontinuity inside an element, as presented in eqs. (4-57) and (4-79). Treating these enriched DOFs as global unknowns in the linear system or statically condensing them at the element level leads to the same discrete solution. However, following the work of Dias-da-Costa et al. [128, 150], the enriched DOFs can be redefined as nodal jumps at the nodes where the discontinuity intersects the element edges. When these nodal jump DOFs are considered as global variables and the augmented linear system is solved, eq. (4-92), the jump field becomes continuous along the discontinuity, since the nodal jumps are shared by adjacent enriched elements. Figure 4.8 compares both choices, and eq. (4-97) presents the relationship between the local enriched DOFs and the nodal jumps.

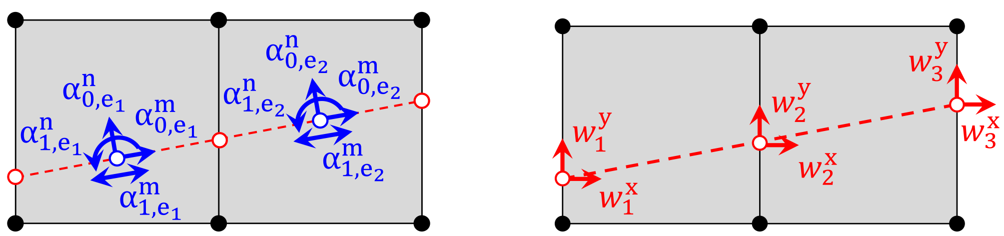

(a) Local element DOFs (b) Global nodal jump DOFs

Figure 4.8: Discretization of the enriched displacement field

For a two-dimensional element cut by a straight discontinuity segment with two intersection nodes, the relation between the local enriched DOFs $\{\alpha^{\mathrm{m}}_0, \alpha^{\mathrm{n}}_0, \alpha^{\mathrm{m}}_1, \alpha^{\mathrm{n}}_1\}$ and the nodal jumps $\{w^{\mathrm{x}}_1, w^{\mathrm{y}}_1, w^{\mathrm{x}}_2, w^{\mathrm{y}}_2\}$ can be written as

$$\begin{Bmatrix} \alpha^{\mathrm{m}}_0 \\ \alpha^{\mathrm{n}}_0 \\ \alpha^{\mathrm{m}}_1 \\ \alpha^{\mathrm{n}}_1 \end{Bmatrix} = \begin{bmatrix} \frac{1}{2} & 0 & \frac{1}{2} & 0 \\ 0 & \frac{1}{2} & 0 & \frac{1}{2} \\ -\frac{1}{l_d} & 0 & \frac{1}{l_d} & 0 \\ 0 & -\frac{1}{l_d} & 0 & \frac{1}{l_d} \end{bmatrix} \begin{bmatrix} \mathbf{m}_{\mathrm{d}}{}^{\top} & \mathbf{0} \\ \mathbf{n}_{\mathrm{d}}{}^{\top} & \mathbf{0} \\ \mathbf{0} & \mathbf{m}_{\mathrm{d}}{}^{\top} \\ \mathbf{0} & \mathbf{n}_{\mathrm{d}}{}^{\top} \end{bmatrix} \begin{Bmatrix} w^{\mathrm{x}}_1 \\ w^{\mathrm{y}}_1 \\ w^{\mathrm{x}}_2 \\ w^{\mathrm{y}}_2 \end{Bmatrix}, \qquad (4\text{-}97)$$

where l_d is the length of the discontinuity segment inside the element.

The explicit transformation in (4-97) was applied only to the two-dimensional case, where a straight discontinuity segment cuts the element and always leads to two intersection nodes. In three-dimensional problems, the intersection between a planar discontinuity and a hexahedral element may generate polygons with a variable number of intersection nodes, so the relation between local enriched DOFs and nodal jumps depends on the specific intersection topology and is no longer given by a unique fixed transformation matrix.

4.8 Numerical integration

The numerical integration over the bulk domain, Ω, depends on the regularity of the fields appearing in the integrands. In Eq. (4-28), when only rigid-body deformation modes are included in the enrichment [128, 175], the bounded enhanced strain field remains continuous in Ω,

$$\nabla^{\mathrm{s}}\tilde{\mathbf{u}}(\mathbf{x}) = \mathbf{0} \rightarrow \tilde{\boldsymbol{\varepsilon}}_{\mathrm{b}}(\mathbf{x}) = -\sum_{i=1}^{n_{\mathrm{n}}} \mathbf{B}_u^i(\mathbf{x})\, \mathcal{H}_{\Gamma_{\mathrm{d}}}(\mathbf{x}_i)\, \tilde{\mathbf{u}}(\mathbf{x}_i). \tag{4-98}$$

and the bulk contributions can be evaluated using standard Gauss quadrature rules, as in classical small-strain elasticity. In contrast, the inclusion of the relative stretching deformation modes or a discontinuous pore-pressure field introduces jumps in the enriched fields, so that the integrands become discontinuous across the embedded surface. In these cases, the element must be partitioned into sub-cells that conform to the discontinuity, and numerical integration is carried out at the sub-cell level. In this thesis, the implementation of this special numerical integration was carried out only in two-dimensional problems.

Table 4.1 summarizes the resulting requirements for bulk integration. The columns indicate whether rigid-body or full kinematic enrichment is used, and whether the discontinuity behaves as a conductive path or as a hydraulic barrier. Depending on this combination, either a regular Gauss rule or a sub-cell quadrature is required for the bulk.

Table 4.1: Required numerical integration rule for the bulk depending on the embedded formulation setting. An “X” marks the options activated in each case.

Kinematic enrichment		**Hydraulic behaviour**		**Numerical integration**
Rigid-body	Full	Conductive	Barrier	
X				Regular
		X		Regular
X		X		Regular
	X			Sub-cell
			X	Sub-cell
X			X	Sub-cell

A first-order Newton–Cotes rule is used to numerically evaluate the integrals over the discontinuity surface Γ_{d} [176, 177, 124]. In three-dimensional problems, the intersection between the discontinuity surface and the background mesh generally yields polygonal regions inside the elements. Each such polygon is triangulated, as illustrated in Fig. 4.9, and the integration points in every triangle are defined according to the same first-order Newton–Cotes rule.

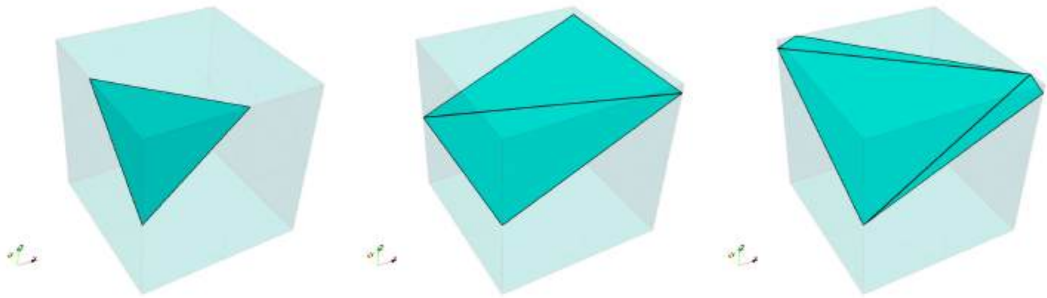

Figure 4.9: Triangulation of the discontinuity surface inside the finite element in different intersection scenarios [9]

5
Conclusions

This thesis has addressed the numerical modelling of strong discontinuities in hydro–mechanical processes in porous media using the Embedded Finite Element Method (E-FEM). The work presented in the published articles, Appendix A, develops, analyzes, and validates an embedded formulation for fractured porous media and investigates its behaviour with respect to cohesive traction oscillations.

5.1
Thesis contributions

The objectives presented in sec. 1.2 have been achieved by the scientific and technical contributions of the thesis, by presenting a finite element formulation with embedded strong discontinuities that:

- models the influence of discontinuities on both longitudinal and transversal flow;
- treats sealing fractures acting as hydraulic barriers and highly conductive fractures within a unified framework;
- handles both steady-state and transient flow problems;
- couples fluid flow between the discontinuity and the porous matrix directly from the governing equations and constitutive modelling, without introducing additional coupling parameters;
- allows the fluid injection inside discontinuities in a straightforward way;
- incorporates an internal fracture pressure that can be statically condensed, thereby emulating, within a single formulation, different interface-element configurations found in discrete fracture models;
- captures the essential hydro–mechanical coupling mechanisms governing fracture opening, slip, and changes in permeability; and
- has been systematically verified against discrete fracture models with interface elements and applied to benchmark problems representative of fractured reservoir conditions.

The formulation was applied to a fault reactivation problem, demonstrating its capability to reproduce the main reactivation mechanisms in a hydro–mechanically coupled setting.

In addition, the thesis addresses the issue of spurious oscillations in the cohesive stresses along the discontinuity, which can compromise the assessment of the reactivation of pre-existing fractures and faults. Different SDA-based embedded formulations were compared to evaluate their influence on the cohesive traction profiles. The study indicates that an SDA-based formulation that enforces local equilibrium along the discontinuity in a stronger sense (the SKON variant) is a viable and effective option, as it substantially reduces spurious oscillations and mesh dependency while retaining the advantages of the embedded approach.

5.2
Perspectives for future research

Building on the developments and findings of this thesis, several directions for future work can be identified:

- **Extension to multiphase and THM processes.** Extend the hydro–mechanical embedded formulation to multiphase flow and fully coupled thermo–hydro–mechanical (THM) processes, to better represent conditions relevant to geological storage and geothermal applications.
- **Fracture initiation and propagation.** Couple the present embedded formulations with fracture propagation models, such as cohesive fracture evolution laws, damage mechanics, or phase-field approaches, in order to simulate the onset and growth of fractures and faults in addition to pre-existing discontinuities.
- **Advanced treatments for traction oscillations.** Investigate additional enrichment modes involving weak discontinuities or discontinuous bulk strains, non-local regularization techniques, and Nitsche-type interface stabilization as means to further reduce or eliminate residual cohesive traction oscillations under slip conditions.
- **Intersecting discontinuities.** Enhance the formulation to deal more accurately with intersecting discontinuities. In the current version, enrichments are simply superposed when multiple discontinuities are present inside an element, without a specific treatment of their intersections, which can lead to severe stress locking and affect the accuracy of the results.

Pursuing these directions would further extend the applicability of embedded finite element methods to complex hydro–mechanical problems in fractured porous media and contribute to more reliable assessments of subsurface operations such as hydrocarbon production, CO_2 sequestration, geothermal energy extraction, and underground storage.

6
Bibliography

1 VAEZI, I.; YOSHIOKA, K.; SIMONE, S. D.; GÓMEZ-CASTRO, B. M.; PALUSZNY, A.; JALALI, M.; BERRE, I.; RUTQVIST, J.; MIN, K.-B.; LEI, Q.; MAKHNENKO, R. Y.; HU, M.; TSANG, C.-F.; VILARRASA, V. A review of thermo–hydro–mechanical modeling of coupled processes in fractured rock: From continuum to discontinuum perspective. **Journal of Rock Mechanics and Geotechnical Engineering**, v. 17, n. 11, p. 7460–7488, 2025. Cited 5 times in pages 11, 15, 16, 20, and 22.

2 RUTQVIST, J.; CAPPA, F.; RINALDI, A. P.; GODANO, M. Modeling of induced seismicity and ground vibrations associated with geologic co2 storage, and assessing their effects on surface structures and human perception. **International Journal of Greenhouse Gas Control**, Elsevier, v. 24, p. 64–77, 2014. Cited 2 times in pages 11 and 16.

3 KHOEI, A. M. **Extended Finite Element Method: theory and applications**. [S.l.]: John Wiley & Sons, 2015. Cited 2 times in pages 11 and 25.

4 ARAGÓN, A. M.; SIMONE, A. The Discontinuity-Enriched Finite Element Method. **International Journal for Numerical Methods in Engineering**, v. 112, n. 11, p. 1589–1613, 2017. ISSN 10970207. Cited 4 times in pages 11, 26, 27, and 28.

5 ZHANG, J.; BOOM, S. J. van den; KEULEN, F. van; ARAGÓN, A. M. A stable discontinuity-enriched finite element method for 3-D problems containing weak and strong discontinuities. **Computer Methods in Applied Mechanics and Engineering**, Elsevier B.V., v. 355, p. 1097–1123, 2019. ISSN 00457825. Cited 3 times in pages 11, 27, and 28.

6 COSTA, D. Dias-da; ALFAIATE, J.; SLUYS, L.; AREIAS, P.; JúLIO, E. An embedded formulation with conforming finite elements to capture strong discontinuities. **International Journal for Numerical Methods in Engineering**, v. 93, n. 2, p. 224–244, 2013. ISSN 1097-0207. Cited 4 times in pages 11, 28, 29, and 31.

7 WU, J.-Y. Unified analysis of enriched finite elements for modeling cohesive cracks. **Computer methods in applied mechanics and engineering**, Elsevier, v. 200, n. 45-46, p. 3031–3050, 2011. Cited 9 times in pages 11, 28, 30, 34, 43, 44, 45, 46, and 57.

8 OLIVER, J. Modelling strong discontinuities in solid mechanics via strain softening constitutive equations. part ii: Numerical simulation. **International Journal for Numerical Methods in Engineering**, v. 39, n. 21, p. 3601–3623, 1996. Cited 3 times in pages 11, 44, and 47.

9 CAVALCANTI, D.; MEJIA, C.; SOUZA, C.; MENDES, C. A.; POUPLANA, I. de; CASAS, G.; ROEHL, D. Behavior of cohesive stresses in

embedded finite elements based on the strong discontinuity approach. **Finite Elements in Analysis and Design**, v. 253, p. 104485, 2025. Cited 4 times in pages 11, 12, 53, and 65.

10 ARMERO, F.; LINDER, C. Numerical simulation of dynamic fracture using finite elements with embedded discontinuities. **International Journal of Fracture**, Springer, v. 160, n. 2, p. 119–141, 2009. Cited 2 times in pages 11 and 57.

11 CASTELLETTO, N.; TEATINI, P.; GAMBOLATI, G. Multiphysics modeling of CO_2 sequestration in a faulted saline formation in italy. **Advances in Water Resources**, v. 62, p. 13–26, 2013. Cited 2 times in pages 15 and 16.

12 WHITE, J. A.; CHIARAMONTE, L.; EZZEDINE, S.; FOXALL, W.; HAO, Y.; MCNAB, W.; RAMIREZ, A. Geomechanical behavior of the reservoir and caprock system at the In Salah CO_2 storage project. **Proceedings of the National Academy of Sciences of the USA**, v. 111, n. 24, p. 8747–8752, 2014. Cited 2 times in pages 15 and 16.

13 ZHAO, X.; POUPLANA, I. de; ROEHL, D. et al. Modelling lined rock caverns subject to hydrogen embrittlement and cyclic pressurisation in fractured rock masses. **International Journal of Hydrogen Energy**, 2025. In press. Cited in page 15.

14 DAMASCENO, L.; POUPLANA, I. de; ROEHL, D.; CAVALCANTI, D. et al. Reliability-based design tool for gas storage in lined rock caverns. **Geomechanics and Geoengineering**, v. 19, n. 1, p. 1–17, 2024. Online first. Cited in page 15.

15 KOHL, T.; MEGEL, T. Predictive modelling of reservoir response to hydraulic stimulations at the European EGS site Soultz-sous-Forêts. **International Journal for Numerical and Analytical Methods in Geomechanics**, v. 31, n. 5, p. 643–659, 2007. Cited in page 15.

16 MAHMOODPOUR, S.; JOODAT, A.; EGLI, D. et al. Numerical simulation of thermo–hydro–mechanical processes at Soultz-sous-Forêts enhanced geothermal system. **Energies**, v. 15, n. 24, p. 9285, 2022. Cited in page 15.

17 BACHMANN, C. E.; WIEMER, S.; GOERTZ-ALLMANN, B.; WOESSNER, J. Influence of pore-pressure on the event-size distribution of induced earthquakes. **Geophysical Journal International**, v. 186, n. 2, p. 793–807, 2011. Cited in page 15.

18 STEFANSSON, I.; BERRE, I.; KEILEGAVLEN, E. A fully coupled numerical model of thermo–hydro–mechanical processes and fracture contact mechanics in porous media. **Computer Methods in Applied Mechanics and Engineering**, v. 386, p. 114122, 2021. Cited in page 15.

19 ALONSO, E. E.; ALCOVERRO, J.; COSTE, F.; MALINSKY, L.; MERRIEN-SOUKATCHOFF, V.; KADIRI, I.; NOWAK, T.; SHAO, H.;

NGUYEN, T. S.; SELVADURAI, A. P. S.; ARMAND, G.; SOBOLIK, S. R.; ITAMURA, M.; STONE, C. M.; WEBB, S. W.; REJEB, A.; TIJANI, M.; MAOUCHE, Z.; KOBAYASHI, A.; KURIKAMI, H.; ITO, A.; SUGITA, Y.; CHIJIMATSU, M.; BÖRGESSON, L.; HERNELIND, J.; RUTQVIST, J.; TSANG, C.-F.; JUSSILA, P. The FEBEX benchmark test: case definition and comparison of modeling approaches. **International Journal of Rock Mechanics and Mining Sciences**, v. 42, n. 5–6, p. 611–638, 2005. Cited in page 15.

20 RUTQVIST, J. Results from an international simulation study on coupled thermal, hydrological, and mechanical processes near geological nuclear waste repositories. **Lawrence Berkeley National Laboratory Report LBNL-125E**, 2008. DECOVALEX project report. Cited in page 15.

21 ZHANG, J.; CHEN, J.; ZHAO, Z.; CHEN, S.; LIU, G.; ZHAO, X.; WANG, J.; LIN, T.; LIU, B. Numerical modeling on nuclide transport around a nuclear waste repository under coupled thermo-hydro-mechanical condition. **Computers and Geotechnics**, Elsevier, v. 164, p. 105776, 2023. Cited in page 15.

22 WANG, Q.; LEI, K.; ZHU, Z.; ZHANG, A. A review of multiphysics coupling numerical modeling techniques for risk assessment in geological disposal of high-level radioactive waste. **Journal of Environmental Radioactivity**, Elsevier, v. 293, p. 107902, 2026. Cited in page 15.

23 BERRE, I.; DOSTER, F.; KEILEGAVLEN, E. Flow in fractured porous media: A review of conceptual models and discretization approaches. **Transport in Porous Media**, v. 130, n. 1, p. 215–236, 2019. Cited 4 times in pages 15, 20, 21, and 22.

24 LEI, Q.; TSANG, C.-F. Coupled processes in fractured media: a key to the energy transition. **GeoEnergy Communications**, Springer, v. 1, n. 1, p. 11, 2025. Cited 2 times in pages 15 and 16.

25 RUTQVIST, J. The geomechanics of co2 storage in deep sedimentary formations. **Geotechnical and Geological Engineering**, Springer, v. 30, n. 3, p. 525–551, 2012. Cited in page 15.

26 VILARRASA, V.; CARRERA, J.; OLIVELLA, S.; RUTQVIST, J.; LALOUI, L. Induced seismicity in geologic carbon storage. **Solid Earth**, Copernicus GmbH, v. 10, n. 3, p. 871–892, 2019. Cited in page 16.

27 VILARRASA, V.; SIMONE, S. D.; CARRERA, J.; VILLASEÑOR, A. Unravelling the causes of the seismicity induced by underground gas storage at Castor, Spain. **Geophysical Research Letters**, v. 48, n. 7, p. e2020GL092038, 2021. Cited in page 16.

28 VILARRASA, V.; SIMONE, S. D.; CARRERA, J.; VILLASEÑOR, A. Multiple induced seismicity mechanisms at Castor underground gas storage illustrate the need for thorough monitoring. **Nature Communications**, v. 13, n. 1, p. 3447, 2022. Cited in page 16.

29 LACKEY, G.; STRAZISAR, B. R.; KOBELSKI, B.; MCEVOY, M.; BACON, D. H.; CIHAN, A.; IYER, J.; LIVERS-DOUGLAS, A.; PAWAR, R. J.; SMINCHAK, J. et al. **Rules and Tools Crosswalk: A Compendium of Computational Tools to Support Geologic Carbon Storage Environmentally Protective UIC Class VI Permitting**. [S.l.], 2022. Cited in page 16.

30 HAN, B.; WANG, S.; ZHANG, Z.; WANG, Y. Numerical simulation of geothermal reservoir thermal recovery of heterogeneous discrete fracture network-rock matrix system. **Energy**, Elsevier, v. 305, p. 132306, 2024. Cited in page 17.

31 GUZMAN, J. de la T.; BABAEI, M.; SHI, J.-Q.; KORRE, A.; DURUCAN, S. Coupled flow-geomechanical performance assessment of co2 storage sites using the ensemble kalman filter. **Energy Procedia**, Elsevier, v. 63, p. 3475–3482, 2014. Cited in page 17.

32 FIGUEIREDO, B.; TSANG, C.-F.; RUTQVIST, J.; BENSABAT, J.; NIEMI, A. Coupled hydro-mechanical processes and fault reactivation induced by co2 injection in a three-layer storage formation. **International Journal of Greenhouse Gas Control**, Elsevier, v. 39, p. 432–448, 2015. Cited in page 17.

33 LELE, S. P.; HSU, S.-Y.; GARZON, J. L.; DEDONTNEY, N.; SEARLES, K. H.; GIST, G. A.; SANZ, P. F.; BIEDIGER, E. A.; DALE, B. A. Geomechanical modeling to evaluate production-induced seismicity at groningen field. In: SPE. **Abu Dhabi International Petroleum Exhibition and Conference**. [S.l.], 2016. p. D021S045R001. Cited in page 17.

34 SANZ, P. F.; LELE, S. P.; SEARLES, K. H.; HSU, S.-Y.; GARZON, J. L.; BURDETTE, J. A.; KLINE, W. E.; DALE, B. A.; HECTOR, P. D. Geomechanical analysis to evaluate production-induced fault reactivation at groningen gas field. In: SPE. **SPE Annual Technical Conference and Exhibition?** [S.l.], 2015. p. D011S002R001. Cited in page 17.

35 MORRIS, J. P.; HAO, Y.; FOXALL, W.; MCNAB, W. A study of injection-induced mechanical deformation at the in salah co2 storage project. **International Journal of Greenhouse Gas Control**, Elsevier, v. 5, n. 2, p. 270–280, 2011. Cited in page 17.

36 RINALDI, A. P.; RUTQVIST, J. Modeling ground surface uplift during co2 sequestration: The case of in salah, algeria. **Energy Procedia**, Elsevier, v. 114, p. 3247–3256, 2017. Cited in page 17.

37 MENDES, C. A. T. **GeMA, a new framework for prototyping, development and integration of multiphysics and multiscale simulations in multidisciplinary groups**. Tese (Ph.D. thesis) — Pontifícia Universidade Católica do Rio de Janeiro (PUC-Rio), Rio de Janeiro, Brazil, 2016. Cited 2 times in pages 19 and 20.

38 MENDES, C. A.; GATTASS, M.; ROEHL, D. The gema framework–an innovative framework for the development of multiphysics and multiscale simulations. In: **VII European Congress on Computational Methods in Applied Sciences and Engineering**. [S.l.: s.n.], 2016. p. 5–10. Cited 2 times in pages 19 and 20.

39 JING, L.; HUDSON, J. A. Numerical methods in rock mechanics. **International Journal of Rock Mechanics and Mining Sciences**, v. 39, n. 4, p. 409–427, 2002. Cited in page 20.

40 RABCZUK, T. Computational methods for fracture in brittle and quasi-brittle solids: State-of-the-art review and future perspectives. **ISRN Applied Mathematics**, v. 2013, p. 1–38, 2013. Cited in page 20.

41 CHEN, Z.; HUAN, G.; MA, Y. **Computational Methods for Multiphase Flows in Porous Media**. Philadelphia: Society for Industrial and Applied Mathematics, 2006. v. 2. (Computational Science and Engineering, v. 2). Cited in page 20.

42 PEIRÓ, J.; SHERWIN, S. J. Finite difference, finite element and finite volume methods for partial differential equations. In: YIP, S. (Ed.). **Handbook of Materials Modeling**. Dordrecht: Springer, 2005. Vol. I: Methods and Models. Cited in page 20.

43 OLIVELLA, S.; GENS, A.; CARRERA, J.; ALONSO, E. Numerical formulation for a simulator (CODE_BRIGHT) for the coupled analysis of saline media. **Engineering Computations**, MCB UP Ltd, v. 13, n. 7, p. 87–112, 1996. Cited 2 times in pages 20 and 42.

44 KOLDITZ, O.; BAUER, S.; BILKE, L.; BÖTTCHER, N.; DELFS, J.-O.; FISCHER, T.; GÖRKE, U. J.; KALBACHER, T.; KOSAKOWSKI, G.; MCDERMOTT, C. et al. OpenGeoSys: An open-source initiative for numerical simulation of thermo-hydro-mechanical/chemical (THM/C) processes in porous media. **Environmental Earth Sciences**, Springer, v. 67, p. 589–599, 2012. Cited in page 20.

45 GIUDICELLI, G.; LINDSAY, A.; HARBOUR, L.; ICENHOUR, C.; LI, M.; HANSEL, J. E.; GERMAN, P.; BEHNE, P.; MARIN, O.; STOGNER, R. H. et al. 3.0-MOOSE: Enabling massively parallel multiphysics simulations. **SoftwareX**, Elsevier, v. 26, p. 101690, 2024. Cited in page 20.

46 MANZOLI, O. L.; BORGES, L. F.; RODRIGUES, E. A.; CLETO, P. R.; MAEDO, M. A.; BITENCOURT, L. A. A new discrete fracture approach based on the use of coupling finite elements for modeling fluid transport in naturally fractured porous media. **Computer Methods in Applied Mechanics and Engineering**, v. 386, p. 114112, 2021. ISSN 0045-7825. Cited in page 20.

47 CAMARGO, M.; CLETO, P. R.; MAEDO, M. A.; RODRIGUES, E. A.; BITENCOURT, L. A.; MANZOLI, O. L. Modeling the hydrodynamic behavior of fractures and barriers in porous media using coupling finite elements. **Journal of Petroleum Science and**

Engineering, v. 208, p. 109700, 2022. ISSN 0920-4105. Disponível em: https://www.sciencedirect.com/science/article/pii/S0920410521013280. Cited in page 20.

48 SCHäDLE, P.; ZULIAN, P.; VOGLER, D.; BHOPALAM, S. R.; NESTOLA, M. G.; EBIGBO, A.; KRAUSE, R.; SAAR, M. O. 3d non-conforming mesh model for flow in fractured porous media using lagrange multipliers. **Computers & Geosciences**, v. 132, p. 42–55, 2019. ISSN 0098-3004. Cited in page 20.

49 ZULIAN, P.; SCHäDLE, P.; KARAGYAUR, L.; NESTOLA, M. G. Comparison and application of non-conforming mesh models for flow in fractured porous media using dual lagrange multipliers. **Journal of Computational Physics**, v. 449, p. 110773, 2022. ISSN 0021-9991. Cited in page 20.

50 WU, J.-Y. A unified phase-field theory for the mechanics of damage and quasi-brittle failure. **Journal of the Mechanics and Physics of Solids**, Elsevier, v. 103, p. 72–99, 2017. Cited in page 20.

51 PAGGI, M.; REINOSO, J. Revisiting the problem of a crack impinging on an interface: a modeling framework for the interaction between the phase field approach for brittle fracture and the interface cohesive zone model. **Computer Methods in Applied Mechanics and Engineering**, Elsevier, v. 321, p. 145–172, 2017. Cited in page 20.

52 ZHOU, S.; ZHUANG, X.; RABCZUK, T. Phase-field modeling of fluid-driven dynamic cracking in porous media. **Computer Methods in Applied Mechanics and Engineering**, v. 350, p. 169–198, 2019. ISSN 0045-7825. Cited in page 20.

53 LIU, R.; ZHOU, S.; QIN, S.; CAO, S.; ZHUANG, X.; RABCZUK, T. A thermo-hydro-mechanical-chemical coupled phase field framework for modeling fractures in porous rocks: the dual-fracture model. **Acta Geotechnica**, Springer, v. 20, n. 10, p. 5443–5467, 2025. Cited in page 20.

54 MA, T.; ZHANG, K.; SHEN, W.; GUO, C.; XU, H. Discontinuous and continuous galerkin methods for compressible single-phase and two-phase flow in fractured porous media. **Advances in Water Resources**, Elsevier, v. 156, p. 104039, 2021. Cited in page 20.

55 MA, T.; JIANG, L.; SHEN, W.; CAO, W.; GUO, C.; NICK, H. M. Fully coupled hydro-mechanical modeling of two-phase flow in deformable fractured porous media with discontinuous and continuous galerkin method. **Computers and Geotechnics**, Elsevier, v. 164, p. 105823, 2023. Cited in page 20.

56 CERVERA, M.; BARBAT, G.; CHIUMENTI, M.; WU, J.-Y. A comparative review of xfem, mixed fem and phase-field models for quasi-brittle cracking. **Archives of Computational Methods in Engineering**, Springer, v. 29, n. 2, p. 1009–1083, 2022. Cited 2 times in pages 20 and 28.

57 FLEMISCH, B.; BERRE, I.; BOON, W.; FUMAGALLI, A.; SCHWENCK, N.; SCOTTI, A.; STEFANSSON, I.; TATOMIR, A. Benchmarks for single-phase flow in fractured porous media. **Advances in Water Resources**, Elsevier, v. 111, n. January 2017, p. 239–258, 2018. ISSN 03091708. Disponível em: https://doi.org/10.1016/j.advwatres.2017.10.036. Cited 3 times in pages 20, 21, and 22.

58 SEGURA, J. M.; CAROL, I. On zero-thickness interface elements for diffusion problems. **International Journal for Numerical and Analytical Methods in Geomechanics**, v. 28, n. 9, p. 947–962, 2004. ISSN 03639061. Cited 2 times in pages 20 and 21.

59 SEGURA, J. M.; CAROL, I. Coupled hm analysis using zero-thickness interface elements with double nodes. part i: Theoretical model. **International Journal for Numerical and Analytical Methods in Geomechanics**, v. 32, n. 18, p. 2083–2101, 2008. Cited 2 times in pages 20 and 21.

60 JING, L. A review of techniques, advances and outstanding issues in numerical modelling for rock mechanics and rock engineering. **International Journal of Rock Mechanics and Mining Sciences**, v. 40, n. 3, p. 283–353, 2003. Cited 2 times in pages 20 and 21.

61 NGUYEN, V. P.; LIAN, H.; RABCZUK, T.; BORDAS, S. Modelling hydraulic fractures in porous media using flow cohesive interface elements. **Engineering Geology**, v. 225, p. 68–82, 2017. ISSN 0013-7952. Cited 2 times in pages 20 and 21.

62 RUEDA, J.; MEJIA, C.; ROEHL, D.; PEREIRA, L. C. Hydro-mechanical modeling of hydraulic fracture propagation and its interactions with frictional natural fractures. **Computers and Geotechnics**, Elsevier, v. 111, p. 290–300, 2019. Cited 2 times in pages 20 and 21.

63 MEJIA, C.; RUEDA, J.; ROEHL, D. Numerical simulation of three-dimensional fracture interaction. **Computers and Geotechnics**, Elsevier, v. 122, p. 103528, 2020. Cited in page 20.

64 MANZOLI, O. L.; GAMINO, A. L.; RODRIGUES, E.; CLARO, G. Modeling of interfaces in two-dimensional problems using solid finite elements with high aspect ratio. **Computers & Structures**, Elsevier, v. 94, p. 70–82, 2012. Cited in page 21.

65 SÁNCHEZ, M.; MANZOLI, O. L.; GUIMARÃES, L. J. Modeling 3-d desiccation soil crack networks using a mesh fragmentation technique. **Computers and Geotechnics**, Elsevier, v. 62, p. 27–39, 2014. Cited in page 21.

66 MANZOLI, O. L.; CLETO, P. R.; SáNCHEZ, M.; GUIMARãES, L. J.; MAEDO, M. A. On the use of high aspect ratio finite elements to model hydraulic fracturing in deformable porous media. **Computer Methods in Applied Mechanics and Engineering**, v. 350, p. 57–80, 2019. ISSN 0045-7825. Cited in page 21.

67 FABBRI, H.; SáNCHEZ, M.; MAEDO, M.; CLETO, P.; MANZOLI, O. Modeling gas breakthrough and flow phenomena through engineered barrier systems using a discrete fracture approach. **Computers and Geotechnics**, v. 154, p. 105148, 2023. ISSN 0266-352X. Cited in page 21.

68 CORDERO, J. A. R.; SANCHEZ, E. C. M.; ROEHL, D. Hydromechanical modeling of unrestricted crack propagation in fractured formations using intrinsic cohesive zone model. **Engineering Fracture Mechanics**, v. 221, p. 106655, 2019. Cited 2 times in pages 21 and 22.

69 OLIVER, J.; CERVERA, M.; MANZOLI, O. Strong discontinuities and continuum plasticity models: the strong discontinuity approach. **International journal of plasticity**, Elsevier, v. 15, n. 3, p. 319–351, 1999. Cited in page 21.

70 OLIVER, J.; HUESPE, A. E. Continuum approach to material failure in strong discontinuity settings. **Computer methods in applied mechanics and engineering**, Elsevier, v. 193, n. 30-32, p. 3195–3220, 2004. Cited in page 21.

71 RAGUENEL, M.; LOPEZ, D.; BORGESE, C.; LI, W.-C. Use of locally refined unstructured meshes for co_2 storage flow and poromechanical simulations. In: SOCIETY OF PETROLEUM ENGINEERS. **Proceedings of the SPE Reservoir Simulation Conference 2025**. Galveston, Texas, USA: Society of Petroleum Engineers, 2025. p. D021S007R005. ISBN 979-8-3313-1960-1. Disponível em: https://doi.org/10.2118/223847-MS. Cited 2 times in pages 21 and 22.

72 LIMA, P.; SHAUER, N.; VILLEGAS, J. B.; DEVLOO, P. R. DFNMesh: Finite element meshing for discrete fracture matrix models. **Advances in Engineering Software**, Elsevier Ltd, v. 186, n. March, p. 103545, 2023. ISSN 18735339. Cited 2 times in pages 21 and 22.

73 HOLM, R.; KAUFMANN, R.; HEIMSUND, B. O.; ØIAN, E.; ESPEDAL, M. S. Meshing of domains with complex internal geometries. **Numerical Linear Algebra with Applications**, v. 13, n. 9, p. 717–731, 2006. ISSN 10705325. Cited in page 22.

74 CACACE, M.; BLÖCHER, G. MeshIt—a software for three dimensional volumetric meshing of complex faulted reservoirs. **Environmental Earth Sciences**, v. 74, n. 6, p. 5191–5209, 2015. ISSN 18666299. Cited in page 22.

75 BLESSENT, D.; THERRIEN, R.; MACQUARRIE, K. Coupling geological and numerical models to simulate groundwater flow and contaminant transport in fractured media. **Computers and Geosciences**, v. 35, n. 9, p. 1897–1906, 2009. ISSN 00983004. Cited in page 22.

76 LIAUDAT, J.; DIEUDONNÉ, A. C.; VARDON, P. J. Modelling gas fracturing in saturated clay samples using triple-node zero-thickness interface elements. **Computers and Geotechnics**, Elsevier Ltd, v. 154, n. November 2022, p. 105128, 2023. ISSN 18737633. Disponível em: https://doi.org/10.1016/j.compgeo.2022.105128. Cited in page 22.

77 CERFONTAINE, B.; DIEUDONNÉ, A. C.; RADU, J. P.; COLLIN, F.; CHARLIER, R. 3D zero-thickness coupled interface finite element: Formulation and application. **Computers and Geotechnics**, Elsevier Ltd, v. 69, p. 124–140, 2015. ISSN 18737633. Disponível em: http://dx.doi.org/10.1016/j.compgeo.2015.04.016. Cited in page 22.

78 CORDERO, J. A. R. **Reativação de falhas geológicas com modelos numéricos discretos e distribuído**. 137 p. Dissertação (M.Sc. dissertation) — Pontifícia Universidade Católica do Rio de Janeiro (PUC-Rio), Rio de Janeiro, Brazil, abr. 2013. Cited in page 22.

79 PEREIRA, F. L.; ROEHL, D.; LAQUINI, J. P.; OLIVEIRA, M. F. F.; COSTA, A. M. Fault reactivation case study for probabilistic assessment of carbon dioxide sequestration. **International Journal of Rock Mechanics and Mining Sciences**, Elsevier, v. 71, p. 310–319, 2014. Cited in page 22.

80 RUEDA, J.; NOREÑA, N.; OLIVEIRA, M.; ROEHL, D. Numerical models for detection of fault reactivation in oil and gas fields. In: ARMA. **ARMA US Rock Mechanics/Geomechanics Symposium**. [S.l.], 2014. p. ARMA–2014. Cited in page 22.

81 CASTAÑO, M. A. R. **Modelagens 2D e 3D para avaliação de reativação de falhas geológicas em reservatórios de petróleo**. 105 p. Dissertação (M.Sc. dissertation) — Pontifícia Universidade Católica do Rio de Janeiro (PUC-Rio), Rio de Janeiro, Brazil, dez. 2016. Cited in page 22.

82 QUEVEDO, R.; RAMIREZ, M.; ROEHL, D. 2d and 3d numerical modeling of fault reactivation. In: ARMA. **ARMA US Rock Mechanics/Geomechanics Symposium**. [S.l.], 2017. p. ARMA–2017. Cited in page 22.

83 RUEDA, J. A. C. **Failure Phenomena and Fluid Migration in Naturally Fractured Rock Formations**. Tese (Ph.D. thesis) — Pontifícia Universidade Católica do Rio de Janeiro (PUC-Rio), Rio de Janeiro, Brazil, 2021. Cited in page 22.

84 POUPLANA, I. de; OÑATE, E. Finite element modelling of fracture propagation in saturated media using quasi-zero-thickness interface elements. **Computers and Geotechnics**, Elsevier, v. 96, p. 103–117, 2018. Cited in page 22.

85 WU, Y. S.; QIN, G. A generalized numerical approach for modeling multiphase flow and transport in fractured porous media. **Communications in Computational Physics**, v. 6, n. 1, p. 85–108, 2009. ISSN 18152406. Cited in page 22.

86 VAEZI, I.; PARISIO, F.; YOSHIOKA, K.; ALCOLEA, A.; MEIER, P.; CARRERA, J.; OLIVELLA, S.; VILARRASA, V. Implicit hydromechanical representation of fractures using a continuum approach. **International Journal of Rock Mechanics and Mining Sciences**, Elsevier, v. 183, p. 105916, 2024. Cited 2 times in pages 22 and 24.

87 SÁNCHEZ-VILA, X.; GIRARDI, J. P.; CARRERA, J. A synthesis of approaches to upscaling of hydraulic conductivities. **Water Resources Research**, v. 31, n. 4, p. 867–882, 1995. Cited in page 22.

88 RENARD, P.; ABABOU, R. Equivalent permeability tensor of heterogeneous media: Upscaling methods and criteria (review and analyses). **Geosciences**, v. 12, n. 7, p. 269, 2022. Cited in page 22.

89 ODA, M. Permeability tensor for discontinuous rock masses. **Géotechnique**, v. 35, n. 4, p. 483–495, 1985. Cited in page 22.

90 ODA, M. An equivalent continuum model for coupled stress and fluid flow analysis in jointed rock masses. **Water Resources Research**, v. 22, n. 13, p. 1845–1856, 1986. Cited in page 22.

91 DURLOFSKY, L. J. Numerical calculation of equivalent grid block permeability tensors for heterogeneous porous media. **Water Resources Research**, v. 27, n. 5, p. 699–708, 1991. Cited in page 22.

92 BERKOWITZ, B. Characterizing flow and transport in fractured geological media: A review. **Advances in Water Resources**, v. 25, n. 8-12, p. 861–884, 2002. ISSN 03091708. Cited in page 22.

93 BARENBLATT, G. I.; ZHELTOV, I. P.; KOCHINA, I. N. Basic concepts in the theory of seepage of homogeneous liquids in fissured rocks. **Journal of Applied Mathematics and Mechanics**, v. 24, n. 5, p. 1286–1303, 1960. Cited in page 23.

94 WARREN, J. E.; ROOT, P. J. The behavior of naturally fractured reservoirs. **Society of Petroleum Engineers Journal**, v. 3, n. 3, p. 245–255, 1963. Cited in page 23.

95 Rueda Cordero, J. A.; Mejia Sanchez, E. C.; ROEHL, D. Integrated discrete fracture and dual porosity - Dual permeability models for fluid flow in deformable fractured media. **Journal of Petroleum Science and Engineering**, Elsevier B.V., v. 175, p. 644–653, 2019. ISSN 09204105. Cited in page 23.

96 RUEDA, J.; MEJIA, C.; NOREÑA, N.; ROEHL, D. A three-dimensional enhanced dual-porosity and dual-permeability approach for hydromechanical modeling of naturally fractured rocks. **International Journal for Numerical Methods in Engineering**, Wiley Online Library, v. 122, n. 7, p. 1663–1686, 2021. Cited in page 23.

97 PRUESS, K.; NARASIMHAN, T. N. A practical method for modeling fluid and heat flow in fractured porous media. **Society of Petroleum Engineers Journal**, v. 25, n. 1, p. 14–26, 1985. Cited in page 23.

98 WU, Y.-S.; DI, Y.; KANG, Z.; FAKCHAROENPHOL, P. A multiple-continuum model for simulating single-phase and multiphase flow in naturally fractured vuggy reservoirs. **Journal of Petroleum Science and Engineering**, v. 78, n. 1, p. 13–22, 2011. Cited in page 23.

99 KHALILI, N.; SELVADURAI, A. P. S. A fully coupled constitutive model for thermo-hydro-mechanical analysis in elastic media with double porosity. **Geophysical Research Letters**, v. 30, n. 24, p. 2243, 2003. Cited in page 23.

100 GELET, R.; LORET, B.; KHALILI, N. A thermo-hydro-mechanical coupled model in local thermal non-equilibrium for fractured HDR reservoir with double porosity. **Journal of Geophysical Research: Solid Earth**, v. 117, n. B7, p. B07207, 2012. Cited in page 23.

101 ANDRIANOV, N.; NICK, H. Machine learning of dual porosity model closures from discrete fracture simulations. **Advances in Water Resources**, Elsevier, v. 147, January 2021. Cited in page 24.

102 JAMEEI, A.; PIETRUSZCZAK, S. Embedded discontinuity approach for coupled hydromechanical analysis of fractured porous media. **International Journal for Numerical and Analytical Methods in Geomechanics**, Wiley Online Library, v. 44, n. 14, p. 1880–1902, 2020. Cited in page 24.

103 PIETRUSZCZAK, S.; JAMEEI, A. Assessment of stress-induced evolution of permeability tensor in rock mass containing discrete fracture network. **Computers and Geotechnics**, Elsevier, v. 174, p. 106580, 2024. Cited in page 24.

104 BABUšKA, I.; MELENK, J. M. The Partition of Unity Method. **International Journal for Numerical Methods in Engineering**, v. 40, n. 4, p. 727–758, 1997. ISSN 1097-0207. Cited in page 24.

105 DUARTE, C. A.; ODEN, J. T. An *h-p* adaptive method using clouds. **Computer Methods in Applied Mechanics and Engineering**, v. 139, n. 1, p. 237–262, 1996. ISSN 0045-7825. Cited in page 24.

106 MELENK, J. M.; BABUšKA, I. The partition of unity finite element method: Basic theory and applications. **Computer Methods in Applied Mechanics and Engineering**, v. 139, n. 1, p. 289–314, December 1996. ISSN 0045-7825. Disponível em: https://www.sciencedirect.com/science/article/pii/S0045782596010870. Cited in page 24.

107 MOëS, N.; DOLBOW, J.; BELYTSCHKO, T. A finite element method for crack growth without remeshing. **International Journal for Numerical Methods in Engineering**, v. 46, n. 1, p. 131–150, 1999. ISSN 1097-0207. Cited 2 times in pages 24 and 25.

108 BELYTSCHKO, T.; MOëS, N.; USUI, S.; PARIMI, C. Arbitrary discontinuities in finite elements. **International Journal for Numerical Methods in Engineering**, v. 50, n. 4, p. 993–1013, 2001. ISSN 1097-0207. Disponível em: https://onlinelibrary.wiley.com/doi/abs/10.1002/1097-0207%2820010210%2950%3A4%3C993%3A%3AAID-NME164%3E3.0.CO%3B2-M. Cited in page 24.

109 DOLBOW, J.; MOëS, N.; BELYTSCHKO, T. Discontinuous enrichment in finite elements with a partition of unity method. **Finite Elements in Analysis and Design**, v. 36, n. 3, p. 235–260, November 2000. ISSN 0168-874X. Cited in page 24.

110 DOLBOW, J.; MOëS, N.; BELYTSCHKO, T. An extended finite element method for modeling crack growth with frictional contact. **Computer Methods in Applied Mechanics and Engineering**, v. 190, n. 51, p. 6825–6846, October 2001. ISSN 0045-7825. Cited in page 25.

111 HIRMAND, M.; VAHAB, M.; KHOEI, A. R. An augmented Lagrangian contact formulation for frictional discontinuities with the extended finite element method. **Finite Elements in Analysis and Design**, v. 107, p. 28–43, December 2015. ISSN 0168-874X. Disponível em: https://www.sciencedirect.com/science/article/pii/S0168874X15001262. Cited 2 times in pages 25 and 26.

112 CRUSAT, L.; CAROL, I.; GAROLERA, D. XFEM formulation with sub-interpolation, and equivalence to zero-thickness interface elements. **International Journal for Numerical and Analytical Methods in Geomechanics**, v. 43, n. 1, p. 45–76, 2019. ISSN 1096-9853. Disponível em: https://onlinelibrary.wiley.com/doi/abs/10.1002/nag.2853. Cited in page 25.

113 KIM, T.; DOLBOW, J.; LAURSEN, T. A mortared finite element method for frictional contact on arbitrary interfaces. **Computational Mechanics**, v. 39, n. 3, p. 223–235, 2007. Cited in page 25.

114 SANDERS, J. D.; DOLBOW, J. E.; LAURSEN, T. A. On methods for stabilizing constraints over enriched interfaces in elasticity. **International Journal for Numerical Methods in Engineering**, v. 78, n. 9, p. 1009–1036, 2009. ISSN 1097-0207. Cited in page 25.

115 FUMAGALLI, A.; PASQUALE, L.; ZONCA, S.; MICHELETTI, S. An upscaling procedure for fractured reservoirs with embedded grids. **Water Resources Research**, v. 52, n. 8, p. 6506–6525, 2016. Cited in page 26.

116 FUMAGALLI, A.; KEILEGAVLEN, E.; SCIALÒ, S. Conforming, non-conforming and non-matching discretization couplings in discrete fracture network simulations. **Journal of Computational Physics**, Elsevier Inc., v. 376, p. 694–712, 2019. ISSN 10902716. Disponível em: https://doi.org/10.1016/j.jcp.2018.09.048. Cited in page 26.

117 KEILEGAVLEN, E.; BERGE, R.; FUMAGALLI, A.; STARNONI, M.; STEFANSSON, I.; VARELA, J.; BERRE, I. Porepy: an open-source software for simulation of multiphysics processes in fractured porous media. **Computational Geosciences**, v. 25, p. 1–23, 2021. Cited in page 26.

118 KHOEI, A. R.; HOSSEINI, N.; MOHAMMADNEJAD, T. Numerical modeling of two-phase fluid flow in deformable fractured porous media using the extended finite element method and an equivalent continuum model. **Advances in Water Resources**, Elsevier Ltd, v. 94, p. 510–528, 2015. ISSN

03091708. Disponível em: http://dx.doi.org/10.1016/j.advwatres.2016.02.017. Cited in page 26.

119 KHOEI, A. R.; VAHAB, M.; HIRMAND, M. An enriched–FEM technique for numerical simulation of interacting discontinuities in naturally fractured porous media. **Computer Methods in Applied Mechanics and Engineering**, Elsevier B.V., v. 331, p. 197–231, 2018. ISSN 00457825. Disponível em: https://doi.org/10.1016/j.cma.2017.11.016. Cited in page 26.

120 HOSSEINI, S. M.; KHOEI, A. R. Numerical simulation of proppant transport and tip screen-out in hydraulic fracturing with the extended finite element method. **International Journal of Rock Mechanics and Mining Sciences**, v. 128, p. 104247, 2020. Cited in page 26.

121 LIU, D.; ZHANG, J.; ARAGÓN, A. M.; SIMONE, A. The discontinuity-enriched finite element method for multiple intersecting discontinuities. **Computer Methods in Applied Mechanics and Engineering**, Elsevier, v. 433, p. 117432, 2025. Cited in page 27.

122 ZHANG, J.; YAN, Y.; DUARTE, C. A.; ARAGÓN, A. M. A discontinuity-enriched finite element method (de-fem) for modeling quasi-static fracture growth in brittle solids. **Computer Methods in Applied Mechanics and Engineering**, Elsevier, v. 435, p. 117585, 2025. Cited in page 27.

123 BOOM, S. J. van den; ZHANG, J.; KEULEN, F. van; ARAGÓN, A. M. A stable interface-enriched formulation for immersed domains with strong enforcement of essential boundary conditions. **International Journal for Numerical Methods in Engineering**, v. 120, n. 10, p. 1163–1183, 2019. ISSN 10970207. Cited in page 28.

124 COSTA, D. Dias-da; ALFAIATE, J.; SLUYS, L. J.; JúLIO, E. A comparative study on the modelling of discontinuous fracture by means of enriched nodal and element techniques and interface elements. **International Journal of Fracture**, v. 161, n. 1, p. 97–119, January 2010. ISSN 1573-2673. Cited 3 times in pages 28, 30, and 64.

125 BORJA, R. I. Assumed enhanced strain and the extended finite element methods: A unification of concepts. **Computer Methods in Applied Mechanics and Engineering**, v. 197, n. 33, p. 2789–2803, June 2008. ISSN 0045-7825. Cited 2 times in pages 28 and 30.

126 SIMO, J. C.; OLIVER, J.; ARMERO, F. An analysis of strong discontinuities induced by strain-softening in rate-independent inelastic solids. **Computational mechanics**, Springer, v. 12, n. 5, p. 277–296, 1993. Cited 4 times in pages 29, 30, 47, and 48.

127 OLIVER, J. Modelling strong discontinuities in solid mechanics via strain softening constitutive equations. part 1: Fundamentals. **International journal for numerical methods in engineering**, Wiley Online Library, v. 39, n. 21, p. 3575–3600, 1996. Cited 2 times in pages 29 and 47.

128 COSTA, D. Dias-da; ALFAIATE, J.; SLUYS, L.; JÚLIO, E. A discrete strong discontinuity approach. **Engineering Fracture Mechanics**, Elsevier, v. 76, n. 9, p. 1176–1201, 2009. Cited 4 times in pages 29, 31, 63, and 64.

129 IDELSOHN, S. R.; GIMENEZ, J. M.; MARTI, J.; NIGRO, N. M. Elemental enriched spaces for the treatment of weak and strong discontinuous fields. **Computer Methods in Applied Mechanics and Engineering**, v. 313, p. 535–559, 2017. ISSN 0045-7825. Cited 3 times in pages 29, 31, and 32.

130 DVORKIN, E. N.; CUITINO, A. M.; GIOIA, G. Finite elements with displacement interpolated embedded localization lines insensitive to mesh size and distortions. **International journal for numerical methods in engineering**, Wiley Online Library, v. 30, n. 3, p. 541–564, 1990. Cited in page 30.

131 DVORKIN, E. N.; ASSANELLI, A. P. 2d finite elements with displacement interpolated embedded localization lines: the analysis of fracture in frictional materials. **Computer methods in applied mechanics and engineering**, Elsevier, v. 90, n. 1-3, p. 829–844, 1991. Cited in page 30.

132 SIMO, J. C.; RIFAI, M. S. A class of mixed assumed strain methods and the method of incompatible modes. **International Journal for Numerical Methods in Engineering**, v. 29, n. 8, p. 1595–1638, 1990. Cited 3 times in pages 30, 48, and 49.

133 WELLS, G.; SLUYS, L. Three-dimensional embedded discontinuity model for brittle fracture. **International Journal of Solids and Structures**, Elsevier, v. 38, n. 5, p. 897–913, 2001. Cited in page 30.

134 LINDER, C.; ARMERO, F. Finite elements with embedded strong discontinuities for the modeling of failure in solids. **International Journal for Numerical Methods in Engineering**, Wiley Online Library, v. 72, n. 12, p. 1391–1433, 2007. Cited 3 times in pages 30, 44, and 57.

135 ARMERO, F.; KIM, J. Three-dimensional finite elements with embedded strong discontinuities to model material failure in the infinitesimal range. **International Journal for Numerical Methods in Engineering**, Wiley Online Library, v. 91, n. 12, p. 1291–1330, 2012. Cited 4 times in pages 30, 55, 57, and 156.

136 GASSER, T. C.; HOLZAPFEL, G. A. Geometrically non-linear and consistently linearized embedded strong discontinuity models for 3D problems with an application to the dissection analysis of soft biological tissues. **Computer Methods in Applied Mechanics and Engineering**, Elsevier, v. 192, n. 47-48, p. 5059–5098, 11 2003. ISSN 00457825. Cited 2 times in pages 30 and 34.

137 KIM, J.; ARMERO, F. Three-dimensional finite elements with embedded strong discontinuities for the analysis of solids at failure in the finite deformation range. **Computer Methods in Applied Mechanics and Engineering**, Elsevier, v. 317, p. 890–926, 2017. Cited in page 30.

138 JIRÁSEK, M. Comparative study on finite elements with embedded discontinuities. **Computer methods in applied mechanics and engineering**, Elsevier, v. 188, n. 1-3, p. 307–330, 2000. Cited 2 times in pages 30 and 34.

139 MOSLER, J.; MESCHKE, G. Embedded crack vs. smeared crack models: a comparison of elementwise discontinuous crack path approaches with emphasis on mesh bias. **Computer methods in applied mechanics and engineering**, Elsevier, v. 193, n. 30-32, p. 3351–3375, 2004. Cited in page 30.

140 ARMERO, F.; CALLARI, C. An analysis of strong discontinuities in a saturated poro-plastic solid. **International journal for numerical methods in engineering**, Wiley Online Library, v. 46, n. 10, p. 1673–1698, 1999. Cited 3 times in pages 30, 32, and 33.

141 CALLARI, C.; ARMERO, F. Finite element methods for the analysis of strong discontinuities in coupled poro-plastic media. **Computer Methods in Applied Mechanics and Engineering**, v. 191, n. 39, p. 4371–4400, 2002. Cited 3 times in pages 30, 32, and 33.

142 LU, M.; ZHANG, H.; ZHENG, Y.; ZHANG, L. A multiscale finite element method for the localization analysis of homogeneous and heterogeneous saturated porous media with embedded strong discontinuity model. **International Journal for Numerical Methods in Engineering**, Wiley Online Library, v. 112, n. 10, p. 1439–1472, 2017. Cited 3 times in pages 30, 32, and 33.

143 LARSSON, R.; RUNESSON, K.; STURE, S. Embedded localization band in undrained soil based on regularized strong discontinuity—theory and fe-analysis. **International Journal of Solids and Structures**, Elsevier, v. 33, n. 20-22, p. 3081–3101, 1996. Cited 3 times in pages 30, 32, and 33.

144 STEINMANN, P. A finite element formulation for strong discontinuities in fluid-saturated porous media. **Mechanics of Cohesive-frictional Materials: An International Journal on Experiments, Modelling and Computation of Materials and Structures**, Wiley Online Library, v. 4, n. 2, p. 133–152, 1999. Cited 3 times in pages 30, 32, and 33.

145 LARSSON, J.; LARSSON, R. Finite-element analysis of localization of deformation and fluid pressure in an elastoplastic porous medium. **International journal of solids and structures**, Elsevier, v. 37, n. 48-50, p. 7231–7257, 2000. Cited 3 times in pages 30, 32, and 33.

146 LARSSON, J.; LARSSON, R. Localization analysis of a fluid-saturated elastoplastic porous medium using regularized discontinuities. **Mechanics of Cohesive-frictional Materials: An International Journal on Experiments, Modelling and Computation of Materials and Structures**, Wiley Online Library, v. 5, n. 7, p. 565–582, 2000. Cited 3 times in pages 30, 32, and 33.

147 SUN, Y.; COLLIAT, J.-B.; SHAO, J. 3d enhanced finite element modeling (e-fem) in hydromechanical coupling: Applications in the fracking of porous media. **Computer Methods in Applied Mechanics and Engineering**, Elsevier, v. 448, p. 118501, 2026. Cited 2 times in pages 30 and 33.

148 LINDER, C.; ROSATO, D.; MIEHE, C. New finite elements with embedded strong discontinuities for the modeling of failure in electromechanical coupled solids. **Computer Methods in Applied Mechanics and Engineering**, Elsevier, v. 200, n. 1-4, p. 141–161, 2011. Cited in page 30.

149 LINDER, C.; ZHANG, X. Three-dimensional finite elements with embedded strong discontinuities to model failure in electromechanical coupled materials. **Computer Methods in Applied Mechanics and Engineering**, Elsevier, v. 273, p. 143–160, 2014. Cited in page 30.

150 COSTA, D. Dias-da; ALFAIATE, J.; SLUYS, L. J.; JÚLIO, E. Towards a generalization of a discrete strong discontinuity approach. **Computer Methods in Applied Mechanics and Engineering**, Elsevier, v. 198, n. 47-48, p. 3670–3681, 2009. Cited 2 times in pages 31 and 63.

151 DAMIRCHI, B. V.; CARVALHO, M. R.; JR., L. A. G. B.; MANZOLI, O. L.; COSTA, D. Dias-da. Transverse and longitudinal fluid flow modelling in fractured porous media with non-matching meshes. **International Journal for Numerical and Analytical Methods in Geomechanics**, v. 45, n. 1, p. 83–107, 2021. Cited 2 times in pages 31 and 32.

152 DAMIRCHI, B. V.; BITENCOURT, L. A.; MANZOLI, O. L.; COSTA, D. D. da. Coupled hydro-mechanical modelling of saturated fractured porous media with unified embedded finite element discretisations. **Computer Methods in Applied Mechanics and Engineering**, v. 393, p. 114804, 2022. ISSN 0045-7825. Cited 3 times in pages 31, 32, and 33.

153 CAVALCANTI, D.; MEJIA, C.; ROEHL, D.; POUPLANA, I. de; OÑATE, E. Hydromechanical embedded finite element for conductive and impermeable strong discontinuities in porous media. **Computers and Geotechnics**, Elsevier, v. 172, p. 106427, 2024. Cited in page 31.

154 CAVALCANTI, D.; MEJIA, C.; ROEHL, D.; POUPLANA, I. de; CASAS, G.; MARTHA, L. F. Embedded finite element formulation for fluid flow in fractured porous medium. **Computers and Geotechnics**, Elsevier, v. 171, p. 106384, 2024. Cited 2 times in pages 31 and 33.

155 IDELSOHN, S. R.; GIMENEZ, J. M.; NIGRO, N. M. Multifluid flows with weak and strong discontinuous interfaces using an elemental enriched space. **International Journal for Numerical Methods in Fluids**, Wiley Online Library, v. 86, n. 12, p. 750–769, 2018. Cited in page 32.

156 MEJIA, C.; ROEHL, D.; RUEDA, J.; QUEVEDO, R. A new approach for modeling three-dimensional fractured reservoirs with embedded complex

fracture networks. **Computers and Geotechnics**, Elsevier, v. 130, p. 103928, 2021. Cited in page 32.

157 BESERRA, L. B. d. S.; GUIMARÃES, L. J. d. N.; MANZOLI, O. L. Modelling of fluid flow in hydrocarbon reservoirs crossed by sealing faults using finite elements with embedded discontinuities in pressure field. In: **Proceedings of the 11th World Congress on Computational Mechanics (WCCM XI), 5th European Conference on Computational Mechanics (ECCM V), and 6th European Conference on Computational Fluid Dynamics (ECFD VI)**. Barcelona, Spain: [s.n.], 2014. Cited in page 33.

158 BESERRA, L. B. d. S. **Análise hidromecânica do fraturamento hidráulico via elementos finitos com descontinuidades fortes incorporadas**. Tese (Doutorado em Engenharia Civil) — Universidade Federal de Pernambuco, Recife, Brasil, 2015. In Portuguese. Cited in page 33.

159 ALVAREZ, L. L.; BESERRA, L.; GUIMARÃES, L.; MANZOLI, O. Reactivation of natural fractures network by hydraulic fracturing. In: EDP SCIENCES. **E3S Web of Conferences**. [S.l.], 2020. v. 205, p. 03001. Cited in page 33.

160 MACIEL, B.; ALVAREZ, L. L.; BELFORT, N. T.; GUIMARÃES, L. J. do N.; BESERRA, L. B. de S. Effectiveness of embedded discontinuities technique in capturing geomechanical behavior in naturally fractured reservoirs. **Journal of Petroleum Exploration and Production Technology**, Springer, v. 14, n. 3, p. 665–691, 2024. Cited in page 33.

161 MANZOLI, O. L.; SHING, P. B. A general technique to embed non-uniform discontinuities into standard solid finite elements. **Computers & Structures**, v. 84, n. 10-11, p. 742–757, 2006. Cited in page 33.

162 LIU, F.; SUN, W.; LI, M.; SHANG, X. A smoothed assumed enhanced strain method for frictional contact with constant strain elements. **Journal of Rock Mechanics and Geotechnical Engineering**, Elsevier, 2023. Cited in page 33.

163 COSTA, D. Dias-da; CARVALHO, M. R.; BYBORDIANI, M. A cracked zone clustering method for discrete fracture with minimal enhanced degrees of freedom. **Computer Methods in Applied Mechanics and Engineering**, v. 387, p. 114133, December 2021. ISSN 0045-7825. Disponível em: https://www.sciencedirect.com/science/article/pii/S0045782521004643. Cited in page 33.

164 JIRÁSEK, M.; ZIMMERMANN, T. Embedded crack model: I. basic formulation. **International journal for numerical methods in engineering**, Wiley Online Library, v. 50, n. 6, p. 1269–1290, 2001. Cited in page 34.

165 OLIVER, J.; HUESPE, A. E.; SAMANIEGO, E. A study on finite elements for capturing strong discontinuities. **International journal for**

numerical methods in engineering, Wiley Online Library, v. 56, n. 14, p. 2135–2161, 2003. Cited in page 34.

166 CAZES, F.; MESCHKE, G.; ZHOU, M.-M. Strong discontinuity approaches: An algorithm for robust performance and comparative assessment of accuracy. **International Journal of Solids and Structures**, Elsevier, v. 96, p. 355–379, 2016. Cited in page 34.

167 BORST, R. de; WELLS, G.; SLUYS, L. Some observations on embedded discontinuity models. **Engineering Computations**, v. 18, n. 1/2, p. 241–254, 2001. ISSN 0264-4401. Publisher: MCB UP Ltd. Cited in page 34.

168 SCHREFLER, B. A.; SIMONI, L.; XIKUI, L.; ZIENKIEWICZ, O. C. Mechanics of Partially Saturated Porous Media. In: **Numerical Methods and Constitutive Modelling in Geomechanics**. [S.l.]: Springer, Vienna, 1990. p. 169–209. ISBN 978-3-7091-2832-9. ISSN: 2309-3706. Cited in page 38.

169 BEAR, J. **Dynamics of fluids in porous media**. [S.l.]: Courier Corporation, 2013. Cited in page 39.

170 LEWIS, R. W.; SCHREFLER, B. A. **The finite element method in the static and dynamic deformation and consolidation of porous media**. [S.l.]: John Wiley & Sons, 1999. Cited in page 39.

171 WITHERSPOON, P. A.; WANG, J. S. Y.; IWAI, K.; GALE, J. E. Validity of cubic law for fluid flow in a deformable rock fracture. **Water Resources Research**, v. 16, n. 6, p. 1016–1024, 1980. Cited in page 40.

172 WELLS, G.; SLUYS, L. Application of embedded discontinuities for softening solids. **Engineering Fracture Mechanics**, v. 65, n. 2, p. 263–281, 2000. Cited in page 49.

173 WU, J.-Y.; LI, F.-B.; XU, S.-L. Extended embedded finite elements with continuous displacement jumps for the modeling of localized failure in solids. **Computer Methods in Applied Mechanics and Engineering**, Elsevier, v. 285, p. 346–378, 2015. Cited in page 57.

174 ARMERO, F.; EHRLICH, D. Finite element methods for the multi-scale modeling of softening hinge lines in plates at failure. **Computer methods in applied mechanics and engineering**, Elsevier, v. 195, n. 13-16, p. 1283–1324, 2006. Cited in page 57.

175 STANIĆ, A.; BRANK, B.; BRANCHERIE, D. Fracture of quasi-brittle solids by continuum and discrete-crack damage models and embedded discontinuity formulation. **Engineering fracture mechanics**, Elsevier, v. 227, p. 106924, 2020. Cited 2 times in pages 62 and 64.

176 DAY, R. A.; POTTS, D. M. Zero thickness interface elements—numerical stability and application. **International Journal for Numerical and Analytical Methods in Geomechanics**, v. 18, n. 10, p. 689–708, 1994. ISSN 1096-9853. Cited in page 64.

177 SCHELLEKENS, J. C. J.; BORST, R. D. On the numerical integration of interface elements. **International Journal for Numerical Methods in Engineering**, v. 36, n. 1, p. 43–66, 1993. ISSN 1097-0207. Cited in page 64.

178 SIMO, J. C.; HUGHES, T. J. **Computational inelasticity**. [S.l.]: Springer, 1998. Cited in page 153.

179 POTTS, D. M.; ZDRAVKOVIĆ, L. **Finite Element Analysis in Geotechnical Engineering: Theory**. London: Thomas Telford, 1999. ISBN 0727727532. Cited in page 155.

A
Publications included in the compendium

A.1
Paper 1

Embedded Finite Element formulation for fluid flow in fractured porous medium

Cavalcanti, D., Mejia, C., Roehl, D., de-Pouplana, I., Casas, G., & Martha, L. F.

Computers and Geotechnics, 171, 106384.(2024).
https://doi.org/10.1016/j.compgeo.2024.106384

Computers and Geotechnics 171 (2024) 106384

Contents lists available at ScienceDirect

Computers and Geotechnics

journal homepage: www.elsevier.com/locate/compgeo

Research paper

Embedded Finite Element formulation for fluid flow in fractured porous medium

Danilo Cavalcanti [a,b,c], Cristian Mejia [d], Deane Roehl [b,d,*], Ignasi de-Pouplana [e,a], Guillermo Casas [a], Luiz F. Martha [b,d]

[a] CIMNE – International Centre for Numerical Methods in Engineering, Spain
[b] Department of Civil and Environmental Engineering, Pontifical Catholic University of Rio de Janeiro, Brazil
[c] Universitat Politècnica de Catalunya (UPC), Spain
[d] Tecgraf Institute, Pontifical Catholic University of Rio de Janeiro, Brazil
[e] Department of Strength of Materials and Structural Engineering (RMEE), Universitat Politècnica de Catalunya (UPC), Spain

ARTICLE INFO

Keywords:
Embedded Finite Element Method (EFEM)
Fluid flow
Sealing discontinuities
Transient analysis

ABSTRACT

The presence of discontinuities, such as fractures or geological faults, can significantly influence the fluid flow in a porous medium. In general, the discontinuities can act as preferential flow paths. However, depending on their aperture and filling material, they can act as barriers to fluid flow. To model these different possibilities, this paper presents an embedded approach in the context of the finite element method to model the presence of discontinuities inside a porous medium in transient analyses. The formulation is attractive since it does not require the mesh used to discretize the porous medium to conform to the discontinuities. The derivation of the formulation is based on the Strong Discontinuity Approach by enriching the pressure field of the finite element with a Heaviside function. The enriched part of the pressure field is discretized based on the pressure jumps evaluated at the nodes where the discontinuity intersects the finite element. The discontinuity internal pressure is taken as an independent field, allowing the modeling of high pressures inside the discontinuity. A strategy to condense the discontinuity internal pressure degrees of freedom is presented. Numerical examples are presented showing the flexibility of the formulation to capture the influence of discontinuities on the fluid flow in porous medium. The results obtained with the proposed formulation are compared with interface element models, showing a good agreement between the two approaches.

1. Introduction

The extension fault in the Miocene section of the Gulf of Mexico plays an essential role in trapping large volumes of hydrocarbon accumulation in its reservoirs. Recently, this section was also evaluated as a site for large-scale and long-term CO_2 storage (Silva et al., 2023). The faults in this region have a fine-clay mineral filling material making them less permeable than the rock matrix and producing a barrier to fluid flow in the porous medium. Bond et al. (2013) analyze the In Salah field and also discuss that many fractures can become sealing over time due to cementation processes. Therefore, to understand field behavior it is important to, not only consider the presence of the discontinuities, but also their proper hydraulic constitutive behavior.

The discontinuities can be represented in the numerical model with different levels of accuracy and computational cost. The most simple and computationally efficient strategy is to use an equivalent continuum model (ECM). On the other hand, the most accurate but cumbersome and computationally intensive is to represent the discontinuities explicitly in the model, as done in a Discrete Fracture Model (DFM). The balance between accuracy and numerical efficiency can be reached with dual porosity models or embedded approaches.

In an ECM, the fractured medium is represented as a continuous medium with equivalent porosity and permeability properties, defined at a representative elementary volume (REV) (Wu and Qin, 2009). However, this representation is not always possible due to the non-existence of a REV (Berre et al., 2019; Berkowitz, 2002). Dual-porosity/dual permeability (DPDP) approaches superpose the system describing the rock matrix with a fracture network. The fracture network is characterized by a transfer function that limits the application of the DPDP approach to a regular set of fractures (Rueda Cordero et al., 2019a; Rueda et al., 2021). Recently, this limitation have been overcome by the use of Machine Learning techniques to determine the transfer function (Andrianov and Nick, 2021).

* Correspondence to: Rua Marques de São Vicente 225, 22451-000, RJ, Brazil.
E-mail addresses: dborges@cimne.upc.edu (D. Cavalcanti), crisms@tecgraf.puc-rio.br (C. Mejia), deane@tecgraf.puc-rio.br (D. Roehl).

https://doi.org/10.1016/j.compgeo.2024.106384
Received 27 November 2023; Received in revised form 25 March 2024; Accepted 24 April 2024
Available online 4 May 2024

A DFM can be created using zero-thickness interface elements or high-aspect-ratio elements (Flemisch et al., 2018; Fumagalli et al., 2019; Fadakar Alghalandis, 2017; Segura and Carol, 2008; Jing and Stephansson, 2007; Segura and Carol, 2004; Noorishad and Mehran, 1982; Nguyen et al., 2017; Rueda Cordero et al., 2019b; Mejia Sanchez et al., 2019, 2020; Manzoli et al., 2019; Fabbri et al., 2023). Recently, interface element formulations have been extended for multiphase flow problems (Liaudat et al., 2023; Cerfontaine et al., 2015). Despite being accurate, these approaches have the difficulty and disadvantage of requiring mesh conformity to the discontinuity, which imposes a challenge in the mesh generation in complex fracture networks (Lima et al., 2023; Holm et al., 2006; Cacace and Blöcher, 2015; Blessent et al., 2009).

The possibility to implicitly represent a discontinuity in the domain without needing a conforming mesh is the main advantage of approaches like the Extended Finite Element Method (XFEM) and embedded formulations. The XFEM allows incorporating discontinuities into the model without explicitly representing them in the mesh. This is achieved by enriching the discontinuous field using a local or global partition of unity (Belytschko et al., 2001; de Borst, 2017; Khoei, 2015,?; Khoei et al., 2018; Gutierrez Escobar et al., 2019; Xia et al., 2018, 2022; Cheng et al., 2022, 2023). However, a large degrees of freedom are added to the problem, and the method requires special integration procedures.

In embedded approaches, the discontinuity is implicitly represented in the mesh considering its orientation, length and properties. Different embedded approaches can be found in the literature (Olorode et al., 2020). Finite Volume formulations have been popular in solving fluid flow problems due to the local conservation property, and the Embedded Discrete Fracture Model (EDFM) is entirely developed in the context of Finite Volume discretization and a two-point flux approximation (Lee et al., 2001; Li and Lee, 2008; Moinfar et al., 2012; Fumagalli et al., 2016; Chai et al., 2018; Wang et al., 2019; Cusini et al., 2021). The original EDFM has a limitation of considering only discontinuities without a filling material, or with a highly permeable one, that will act as a conduit for the fluid flow. The Projection-based Embedded Discrete Fracture Model (pEDFM) extends the EDFM formulation to deal with discontinuities with lower permeability than the porous matrix (Ţene et al., 2017; Rao et al., 2020).

In the context of the Finite Element Method (FEM), the formulation can be developed using an idea similar to the XFEM, where the discontinuity is incorporated by enriching the pressure field. In both methods, the definition of the pressure field enrichment is highly related to the presence or absence of a filling material in the discontinuity. For a low-permeable filling material in the discontinuity, a jump occurs in the pressure field, incorporated through a Heaviside function-based enriched. In other cases, where the discontinuities act as a preferential flow path inside the porous medium, the pressure field is not discontinuous, only its gradient; therefore a distance function-based enrichment is used. In the literature, most works contemplate only the later case (Callari and Armero, 2002; Alfaiate et al., 2010; Benkemoun et al., 2015; Damirchi et al., 2022). Recently, Damirchi et al. (2021) presented an embedded finite element formulation capable of modeling longitudinal and transversal flow for steady-state single-phase fluid flow problems. To derive their formulation, they used a coupling finite element (Bitencourt et al., 2015) which introduces a coupling parameter to enforce the compatibility between the continuum mesh with the discontinuity mesh. In comparison with XFEM, the advantage of EFEM consists mainly in the reduced number of enrichment degrees of freedom. It is also worth mentioning that in the context of the finite element method local mass conservation can be achieved by mixed formulations (Durán et al., 2019).

In the context of FEM other approaches can implicitly represent a discontinuity inside the domain, such as phase field models (Zeng et al., 2020; Ehlers and Luo, 2017; Wilson and Landis, 2016; Zhou et al., 2019) coupling finite elements (CFE) (Manzoli et al., 2021), Lagrange multipliers (Zulian et al., 2022), and the combination of strategies such as dual porosity and EFEM (Alvarez et al., 2021). However, they are limited to modeling highly permeable discontinuities. To allow the behavior of discontinuities acting as barriers, Camargo et al. (2022) discretized the porous media and the discontinuities with different discretizations and coupled them using CFE. However, this approach requires the mesh of the porous media to conform to the discontinuity.

In this paper, an embedded finite element formulation is developed for transient problems. The formulation captures the discontinuities' influence on longitudinal and transversal flows, which allows modeling fractured porous media with sealed fractures acting as barriers. The method can be applied to problems with high-pressure gradients inside the discontinuity. The formulation can be easily combined with a static condensation technique to reduce the number of degrees of freedom.

The paper is organized as follows. Section 2 defines the enrichment of the pressure field and derives the weak form of the governing equation. Section 3 presents the spatial and time discretization of the problem. Section 4 presents an analogy of the embedded formulation with DFM composed of interface elements. Section 5 presents the numerical examples comparing the solutions obtained with the proposed embedded formulation with those of finite element models using interface element. Finally, Section 6 summarizes the main conclusions of the work.

2. Basic concepts

This section presents some basic concepts associated with the embedded finite element formulation based on the Strong Discontinuity Approach. First, the pressure field in the porous medium is defined to consider the discontinuity present in the domain. Then, the weak forms of the continuity equations are derived. It is assumed that the problem is governed by two independent fields: the pressure of the porous medium, $p(\mathbf{x},t)$, and the discontinuity internal pressure, $p_d(\mathbf{x},t)$.

For the following derivations, consider the problem presented in Fig. 1 with a domain Ω closed by a boundary Γ composed by the union of the boundaries Γ_p and Γ_q, associated with the essential and natural boundary conditions, respectively. The domain is crossed by a discontinuity, Γ_d, with aperture w, that separates it into two sub-domains, Ω^+ and Ω^-. Their definition is based on the normal vector to the discontinuity surface, $\mathbf{n}_d$, such that Ω^+ is the sub-region at which the normal vector $\mathbf{n}_d$ is pointing.

The boundary conditions associated with the pressure field of the porous medium are:

$$\begin{cases} \mathbf{v}\cdot\mathbf{n}_\Gamma = \bar{\bar{q}} \;, \mathbf{x}\in\Gamma_q \\ p = \bar{\bar{p}} \;, \mathbf{x}\in\Gamma_p \end{cases} \tag{1}$$

where $\mathbf{v}$ is the fluid relative velocity vector, $\bar{\bar{q}}$ is the flux associated with the natural boundary conditions and $\bar{\bar{p}}$ is the prescribed pressure at the boundary of the domain.

The boundary conditions associated with the pressure field inside the discontinuity are:

$$\begin{cases} \mathbf{v}_d\cdot\mathbf{n}_\Gamma = \bar{\bar{q}}_i \;, \mathbf{x}\in\Gamma_{dq} \\ p_d = \bar{\bar{p}}_d \;, \mathbf{x}\in\Gamma_{dp} \end{cases} \tag{2}$$

where $\mathbf{v}_d$ is the fluid relative velocity vector at the discontinuity in its local system, $\bar{\bar{q}}_i$ is the flux associated with the discontinuity natural boundary conditions and $\bar{\bar{p}}_d$ is the prescribed pressure at the discontinuity.

The compatibility of the fluid flow between the porous medium and the discontinuity is defined by:

$$[\![\mathbf{v}]\!]\cdot\mathbf{n}_d = -[\![\mathbf{v}_d]\!]\cdot\mathbf{n}_d = q_d \;, \mathbf{x}\in\Gamma_d \tag{3}$$

where q_d is the fluid flux through the discontinuity, and $[\![\mathbf{v}]\!]$ and $[\![\mathbf{v}_d]\!]$ are the jump of the relative velocity vector across the discontinuity.

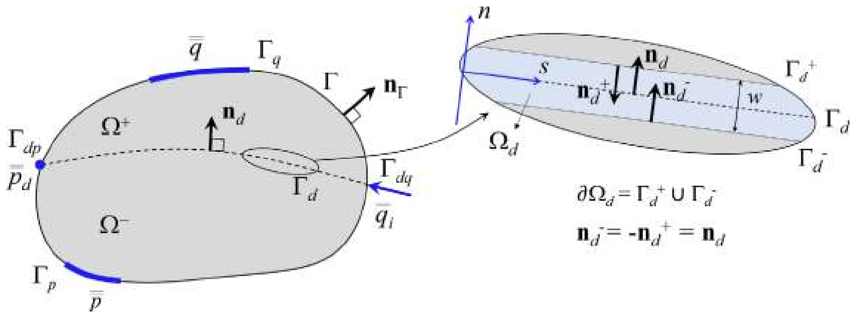

Fig. 1. Domain with the presence of a strong discontinuity.

2.1. Definition of the pressure field

To incorporate a discontinuity in the pressure field without representing it explicitly in the mesh, the embedded formulation requires the pressure field $p(\mathbf{x}, t)$ to be defined as

$$p(\mathbf{x}, t) = \hat{p}(\mathbf{x}, t) + \tilde{p}(\mathbf{x}, t) \tag{4}$$

where $\hat{p}(\mathbf{x}, t)$ is the regular part of the pressure field, $\tilde{p}(\mathbf{x}, t)$ is the enriched part of the pressure field, t is the time, and $\mathbf{x} \in \Omega$.

Different alternatives can be found in the literature to define the enriched part of the pressure field. One is to use a distance function (Alfaiate et al., 2010; Ranaivomanana and Benkemoun, 2017; Benkemoun et al., 2015)

$$\tilde{p}(\mathbf{x}, t) = \Theta(\mathbf{x})\, \mathcal{D}_{\Gamma_d}(\mathbf{x})\, [\![p(t)]\!] \tag{5}$$

where $[\![p(t)]\!]$ is the increment of the pressure field and $\mathcal{D}_{\Gamma_d}$ represents the distance function that is defined as:

$$\mathcal{D}_{\Gamma_d}(\mathbf{x}) = \left(\mathbf{x} - \mathbf{x}_{ref}\right) \cdot \mathbf{n}_d \tag{6}$$

where $\mathbf{x}_{ref}$ is a reference point associated with the discontinuity.

In Eq. (5), $\Theta(\mathbf{x})$ is a piece-wise constant function defined as

$$\Theta(\mathbf{x}) = \begin{cases} \frac{V^+}{V}, & \text{if } \mathbf{x} \in \Omega^+ \\ \frac{V^-}{V}, & \text{if } \mathbf{x} \in \Omega^- \end{cases} \tag{7}$$

where V is the total volume of the domain, V^+ is the volume of the sub-domain Ω^+ and V^- is the volume of the sub-domain Ω^-. This term is introduced in order for the formulation to be able to fulfill the patch test condition of a constant pressure gradient representation.

The enriched pressure field defined with a distance function, as in Eq. (5), is continuous and does not allow modeling the transversal flow through the discontinuity. Thus, a discontinuous function is adopted as a pressure field enrichment.

$$\tilde{p}(\mathbf{x}, t) = \mathcal{H}_{\Gamma_d}(\mathbf{x})\, [\![p(\mathbf{x}, t)]\!] \tag{8}$$

where $\mathcal{H}_{\Gamma_d}$ is a Heaviside function defined as

$$\mathcal{H}_{\Gamma_d} = \begin{cases} 1, & \text{if } \mathbf{x} \in \Omega^+ \\ 0, & \text{otherwise} \end{cases} \tag{9}$$

The definition of the total pressure field as in Eq. (4) makes it challenging to apply the essential boundary conditions along the boundary of the sub-domain Ω^+, since it would require a constraint to be applied to both regular and enriched pressure fields. To overcome this problem, the strategy proposed by Oliver (1996) in the context of enhancing a displacement field is adopted. Thus, the regularized pressure field is defined as

$$\bar{p}(\mathbf{x}) = \hat{p}(\mathbf{x}) + \varphi(\mathbf{x})\, [\![p(\mathbf{x}, t)]\!] \tag{10}$$

with $\varphi(\mathbf{x})$ being an auxiliary function as

$$\varphi(\mathbf{x}) = \begin{cases} 1 & \mathbf{x} \in \Gamma \in \Omega^+ \\ 0 & \mathbf{x} \in \Gamma \in \Omega^- \end{cases} \tag{11}$$

Then, by considering the discontinuous enrichment from Eq. (8), the total pressure field, Eq. (4), is rewritten as

$$p(\mathbf{x}, t) = \bar{p}(\mathbf{x}, t) + \left(\mathcal{H}_{\Gamma_d}(\mathbf{x}) - \varphi(\mathbf{x})\right) [\![p(\mathbf{x}, t)]\!] \tag{12}$$

The introduction of the auxiliary function in Eq. (12) makes the part associated with $\bar{p}(\mathbf{x}, t)$ zero along the entire boundary of the domain. Therefore, the regularized pressure field, $\bar{p}(\mathbf{x}, t)$, and the total pressure field, $p(\mathbf{x}, t)$ have the same values along Γ.

2.2. Fluid flow through the porous medium

Neglecting the deformability of the solid skeleton, the continuity equation that defines the fluid flow through the porous medium is

$$\frac{1}{M}\frac{\partial p}{\partial t} + \nabla \cdot \mathbf{v} = 0, \; \mathbf{x} \in \Omega \backslash \Gamma_d \tag{13}$$

where M is the Biot's modulus

$$M = \left(\frac{\alpha - \phi}{K_s} + \frac{\phi}{K_f}\right)^{-1} \tag{14}$$

where α is Biot's coefficient, ϕ is the porosity, K_s is the bulk modulus of the solid skeleton and K_f is the bulk modulus of the fluid.

The weak form of the continuity Eq. (13) is obtained by applying the Galerkin method followed by the Divergence theorem:

$$\int_{\Omega\backslash\Gamma_d} \delta p \left(\frac{1}{M}\frac{\partial p}{\partial t}\right) d\Omega + \int_{\Gamma} \delta p\, (\mathbf{v} \cdot \mathbf{n})\, d\Gamma - \int_{\Omega\backslash\Gamma_d} \nabla\delta p \cdot \mathbf{v}\, d\Omega = 0 \tag{15}$$

with δp being all admissible variations of the pressure field.

Decomposing the integral along the boundary, Γ, and applying the boundary conditions, Eq. (1), yields:

$$\int_{\Omega\backslash\Gamma_d} \delta p \left(\frac{1}{M}\frac{\partial p}{\partial t}\right) d\Omega + \int_{\Gamma_q} \delta p\, \bar{\bar{q}}\, d\Gamma - \int_{\Gamma_d} \delta p\, q_d\, d\Gamma - \int_{\Omega\backslash\Gamma_d} \nabla\delta p \cdot \mathbf{v}\, d\Omega = 0 \tag{16}$$

The fluid relative velocity is defined by Darcy's law, neglecting the gravity term:

$$\mathbf{v} = -\frac{\mathbf{k}}{\mu_f}\nabla p \tag{17}$$

where $\mathbf{k}$ is the permeability matrix and μ_f is the dynamic fluid viscosity.

The third part of Eq. (16) is responsible for the coupling between the fluid flow of the porous medium and the discontinuity. The fluid flux

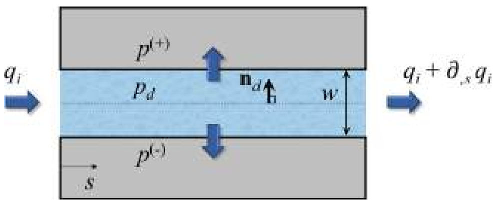

Fig. 2. Fluid flow pattern inside the discontinuity.

through the discontinuity, q_d, is defined by the leak-off model (Settari and Price, 1984):

$$q_d = c^{(+)}\left(p_d - p^{(+)}\right) + c^{(-)}\left(p_d - p^{(-)}\right) \tag{18}$$

where $c^{(+)}$ and $c^{(-)}$ are the leak-off parameters, and $p^{(+)}$ and $p^{(-)}$ are the pressures in the adjacent porous medium, as shown in Fig. 2.

2.3. Fluid flow inside the discontinuity

The continuity equation inside the discontinuity is

$$\frac{1}{M_d}\frac{\partial p_d}{\partial t} + \nabla_d \cdot \mathbf{v}_d = 0 \tag{19}$$

where M_d is the discontinuity Biot's modulus, and $\mathbf{v}_d$ and ∇_d are the fluid velocity vector and the Divergence operator defined at the discontinuity local system, respectively.

Following the same steps of the previous section, the weak form of the continuity equation of the fluid flow inside the discontinuity is

$$\int_{\Omega_d} \delta p_d \left(\frac{1}{M_d}\frac{\partial p_d}{\partial t}\right) d\Omega + \int_{\partial\Omega_d} \delta p_d \left(\mathbf{v}_d \cdot \mathbf{n}\right) d\Gamma + \int_{\Gamma_d} \delta p_d\, q_d\, d\Gamma - \int_{\Omega_d} \nabla\delta p_d \cdot \mathbf{v}_d\, d\Omega = 0 \tag{20}$$

with δp_d being all admissible variations of the discontinuity internal pressure field.

Assuming that the terms in Eq. (20) are constant in the normal direction, see Figs. 1, 2, and applying the boundary conditions, Eq. (2):

$$\int_{\Gamma_d} \delta p_d \frac{w}{M_d}\frac{\partial p_d}{\partial t}\, d\Omega + \int_{\Gamma_{dq}} \delta p_d\, \bar{\bar{q}}_i\, d\Gamma + \int_{\Gamma_d} \delta p_d\, q_d\, d\Gamma - \int_{\Gamma_d} \frac{\partial \delta p_d}{\partial s}\, w\, k_d\, \frac{\partial p_d}{\partial s}\, d\Omega = 0 \tag{21}$$

The discontinuity longitudinal permeability is defined by Witherspoon et al. (1980)

$$k_d = \frac{w^2}{12\,\mu_f} \tag{22}$$

3. Embedded finite element formulation

In this section, the weak forms of the continuity Eqs. (16) and (21) are spatially discretized using an embedded finite element method, and then the discretized system of first-order differential equations is solved using an implicit time integration scheme.

3.1. Definition of matrix mapping

Considering a linear quadrilateral finite element crossed by a discontinuity as shown in Fig. 3. The main idea of the proposed embedded finite element formulation is to evaluate the enriched pressure field, $\tilde{p}(\mathbf{x},t)$, Eq. (8), in terms of the jump in the pressure field across the discontinuity, evaluated along the discontinuity inside the element.

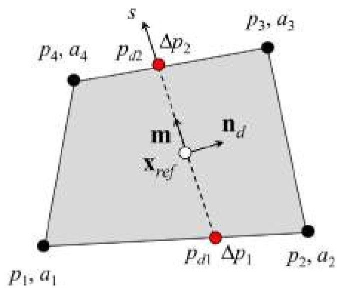

Fig. 3. Quadrilateral finite element with embedded discontinuity.

The jump of pressure field $[\![p(\mathbf{x},t)]\!]$ can be defined as,

$$[\![p(\mathbf{x},t)]\!] = \mathbf{M}_i(\mathbf{x})\,\Delta\mathbf{p}(t) \tag{23}$$

where $\mathbf{M}_i(\mathbf{x})$ is the matrix that transmits the jump of pressure from the discontinuity to the porous medium domain. To define this matrix, first, it is assumed that the jump in the pressure field can have a linear variation along the discontinuity tangential coordinate, s,

$$\Delta p(s,t) = \frac{\Delta p_1 + \Delta p_2}{2} + s\,\frac{\Delta p_2 - \Delta p_1}{l_d} \tag{24}$$

where l_d is the discontinuity length inside the element, and Δp_1 and Δp_2 are the jumps in the pressure field at the nodes where the discontinuity intersects the element.

Then, by assuming that the transmission of the jump in the pressure field that happens from the discontinuity to the continuum occurs completely in the normal direction,

$$\mathbf{M}_i(\mathbf{x}) = \left[\frac{1}{2} - \frac{\mathbf{m}\cdot(\mathbf{x}-\mathbf{x}_{ref})}{l_d} \quad \frac{1}{2} + \frac{\mathbf{m}\cdot(\mathbf{x}-\mathbf{x}_{ref})}{l_d}\right] \tag{25}$$

Finally, by evaluating Eq. (23) at the nodes of the element

$$\mathbf{a}(t) = \mathbf{M}\,\Delta\mathbf{p}(t) \tag{26}$$

where $\mathbf{a}(t)$ is the enrichment degrees of freedom defined at the nodes of the finite element. Therefore, matrix $\mathbf{M}$ transfers the jump in the pressure field from the discontinuity to the nodes of the finite element.

$$\mathbf{M} = \left[\mathbf{M}_i^T(\mathbf{x}_1) \quad \mathbf{M}_i^T(\mathbf{x}_2) \quad \dots \quad \mathbf{M}_i^T(\mathbf{x}_n)\right]^T \tag{27}$$

3.2. Spatial discretization

The total pressure field is discretized by considering that the regularized part is a function of the degrees of freedom $\mathbf{p}$, and the enriched part is a function of $\Delta\mathbf{p}$.

$$p(\mathbf{x},t) = \mathbf{N}(\mathbf{x})\,\mathbf{p}(t) + \tilde{\mathbf{N}}(\mathbf{x})\,\Delta\mathbf{p}(t) \tag{28}$$

The matrix $\mathbf{N}$ contains the standard finite-element shape functions. The matrix $\tilde{\mathbf{N}}$ contains the enriched shape functions, which, based on (8) and (12) and using (26), is defined as

$$\tilde{\mathbf{N}}(\mathbf{x}) = \mathbf{N}(\mathbf{x})\left(\mathcal{H}_{\Gamma_d}(\mathbf{x})\,\mathbf{I} - \mathbf{H}_d\right)\mathbf{M} \tag{29}$$

where $\mathbf{H}_d$ is a diagonal matrix with the Heaviside function evaluated at the nodes associated with each degree of freedom of the finite element.

The gradient of the pressure field $\nabla p(\mathbf{x},t)$ is

$$\nabla p(\mathbf{x},t) = \mathbf{B}(\mathbf{x})\,\mathbf{p}(t) + \tilde{\mathbf{B}}(\mathbf{x})\,\Delta\mathbf{p}(t), \quad \mathbf{x} \in \Omega\backslash\Gamma_d \tag{30}$$

where $\mathbf{B}(\mathbf{x}) = \nabla\mathbf{N}(\mathbf{x})$ and $\tilde{\mathbf{B}}(\mathbf{x}) = \nabla\tilde{\mathbf{N}}(\mathbf{x})$.

In Eq. (30), the gradient of the pressure field is defined only in the continuous part of the domain, since the continuity equation associated with the fluid flow through the porous medium is only defined over $\Omega \backslash \Gamma_d$.

Finally, the longitudinal flow in the discontinuity middle plane is taken as an independent field and discretized as,

$$p_d(s,t) = \mathbf{N}_d(s)\ \mathbf{p}_d(t) \tag{31}$$

where $\mathbf{N}_d(s)$ represents the shape functions for the discontinuity.

Substituting the discretized fields from Eqs. (28), (30) and (31) into (16) and (21) leads to the system,

$$\mathbf{S}\,\dot{\mathbb{P}} + \mathbf{H}\,\mathbb{P} = \mathbf{Q}(t) \tag{32}$$

where the degrees of freedom vector $\mathbb{P}$ is defined as

$$\mathbb{P} = \begin{bmatrix}\mathbf{p}(t)^T & \Delta\mathbf{p}(t)^T & \mathbf{p}(t)^T\end{bmatrix}^T \tag{33}$$

The compressibility matrix is

$$\mathbf{S} = \begin{bmatrix}\mathbf{S}_c & \mathbf{0}\\ \mathbf{0} & \mathbf{S}_d\end{bmatrix} \tag{34}$$

where $\mathbf{S}_c$ is the porous medium compressibility matrix

$$\mathbf{S}_c = \int_{\Omega\backslash\Gamma_d} \mathbf{N}_{aug}(\mathbf{x})^T \frac{1}{M} \mathbf{N}_{aug}(\mathbf{x})\, d\Omega \tag{35}$$

and $\mathbf{S}_d$ is the discontinuity compressibility matrix

$$\mathbf{S}_d = \int_{\Gamma_d} \mathbf{N}_d(\mathbf{x})^T \frac{w}{M_d} \mathbf{N}_d(\mathbf{x})\, d\Gamma \tag{36}$$

and the fluid-flow matrix is composed of two parts, one that is associated with the permeability of the porous medium and the discontinuity on its own, and the other associated with the coupling between the two:

$$\mathbf{H} = \begin{bmatrix}\mathbf{H}_c & \mathbf{0}\\ \mathbf{0} & \mathbf{H}_d\end{bmatrix} + \begin{bmatrix}\mathbf{L}_c & -\mathbf{L}_{cd}\\ -\mathbf{L}_{cd}{}^T & \mathbf{L}_d\end{bmatrix} \tag{37}$$

where $\mathbf{H}_c$ is the fluid-flow matrix of the porous medium,

$$\mathbf{H}_c = \int_{\Omega\backslash\Gamma_d} \mathbf{B}_{aug}(\mathbf{x})^T \frac{\mathbf{k}}{\mu_f} \mathbf{B}_{aug}(\mathbf{x})\, d\Omega \tag{38}$$

$\mathbf{H}_d$ is the fluid-flow matrix of the discontinuity,

$$\mathbf{H}_d = \int_{\Gamma_d} \frac{\partial \mathbf{N}_d{}^T(\mathbf{x})}{\partial s} \frac{w^3}{12\,\mu_f} \frac{\partial \mathbf{N}_d(\mathbf{x})}{\partial s}\, d\Gamma \tag{39}$$

and $\mathbf{L}_c$, $\mathbf{L}_d$ and $\mathbf{L}_{cd}$ are the fluid-flow matrices that promote the coupling between the porous medium and the discontinuity,

$$\mathbf{L}_c = \int_{\Gamma_d} \mathbf{N}_{aug}^{(+)}(\mathbf{x})^T c^{(+)}\, \mathbf{N}_{aug}^{(+)}(\mathbf{x})\, d\Gamma + \int_{\Gamma_d} \mathbf{N}_{aug}^{(-)}(\mathbf{x})^T c^{(-)}\, \mathbf{N}_{aug}^{(-)}(\mathbf{x})\, d\Gamma \tag{40}$$

$$\mathbf{L}_d = \int_{\Gamma_d} \mathbf{N}_d{}^T(\mathbf{x}) \left(c^{(+)} + c^{(-)}\right) \mathbf{N}_d(\mathbf{x})\, d\Gamma \tag{41}$$

$$\mathbf{L}_{cd} = \int_{\Gamma_d} \mathbf{N}_{aug}^{(+)}(\mathbf{x})^T c^{(+)}\, \mathbf{N}_d(\mathbf{x})\, d\Gamma + \int_{\Gamma_d} \mathbf{N}_{aug}^{(-)}(\mathbf{x})^T c^{(-)}\, \mathbf{N}_d(\mathbf{x})\, d\Gamma \tag{42}$$

The discharge vector is

$$\mathbf{Q}(t) = \begin{bmatrix}\mathbf{q}(t)^T & \Delta\mathbf{q}(t)^T & \mathbf{q}_f(t)^T\end{bmatrix}^T \tag{43}$$

The augmented vectors, $()_{aug}$, are defined as

$$\mathbf{N}_{aug}(\mathbf{x}) = \begin{bmatrix}\mathbf{N}(\mathbf{x}) & \mathbf{N}(\mathbf{x})\left(\mathcal{H}_{\Gamma_d}(\mathbf{x})\,\mathbf{I} - \mathbf{H}_d\right)\mathbf{M}\end{bmatrix} \tag{44}$$

$$\mathbf{N}_{aug}^{(+)}(\mathbf{x}) = \begin{bmatrix}\mathbf{N}(\mathbf{x}) & \mathbf{N}(\mathbf{x})\left(\mathbf{I} - \mathbf{H}_d\right)\mathbf{M}\end{bmatrix} \tag{45}$$

$$\mathbf{N}_{aug}^{(-)}(\mathbf{x}) = \begin{bmatrix}\mathbf{N}(\mathbf{x}) & -\mathbf{N}(\mathbf{x})\,\mathbf{H}_d\,\mathbf{M}\end{bmatrix} \tag{46}$$

$$\mathbf{B}_{aug}(\mathbf{x}) = \begin{bmatrix}\mathbf{B}(\mathbf{x}) & \mathbf{B}(\mathbf{x})\left(\mathcal{H}_{\Gamma_d}(\mathbf{x})\,\mathbf{I} - \mathbf{H}_d\right)\mathbf{M}\end{bmatrix} \tag{47}$$

In the compressibility and the fluid-flow matrices of the porous medium, defined in Eqs. (35) and (38), there is a part that is a discontinuous function due to the presence of the Heaviside function. Due to this discontinuity, all element matrices are computed using a sub-division of the element domain into triangles, which are obtained from a Delaunay triangulation of each sub-domain including its centroid. Each triangle is integrated with a usual Gauss quadrature, as illustrated in Fig. 4.

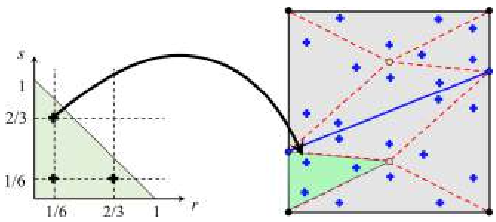

Fig. 4. Example of the definition of the numerical integration points using a sub-division of the domain.

Damirchi et al. (2021) highlighted the influence of the mapping matrix $\mathbf{M}$ on the numerical integration. This mapping matrix is used to transmit the pressure field jump along the discontinuity to the element nodes, as stated in Eq. (26). If the jump in the pressure field is transmitted to the porous medium, keeping the same pressure gradient field, then

$$\nabla p(\mathbf{x},t) = \nabla \hat{p}(\mathbf{x},t) \rightarrow \nabla \tilde{p}(\mathbf{x},t) = \mathcal{H}_{\Gamma_d}(\mathbf{x})\,\mathbf{B}(\mathbf{x})\,\mathbf{M}\,\Delta\mathbf{p}(t) = \mathbf{0},\ \ \mathbf{x} \in \Omega\backslash\Gamma_d \tag{48}$$

In the definition of the mapping matrix, Eq. (27), the condition in Eq. (48) is satisfied, implying that the fluid-flow matrix associated with the porous medium, Eq. (38), is continuous over the element domain. Therefore in steady-state problems, there is no need to perform the sub-division of the domain to compute the element matrices (Damirchi et al., 2021). But to perform a transient analysis, the compressibility matrix will require the sub-division for its integration.

3.3. Static condensation of pressure inside the discontinuity

The discontinuity pressure degrees of freedom can be defined as a function of the pressure field in the porous medium. This is done by performing a reduction of the space of variables. Then, the vector of degrees of freedom, Eq. (33), is redefined as:

$$\mathbb{P} = \mathbf{R}\,\mathbb{P}_R \tag{49}$$

with

$$\mathbf{R} = \begin{bmatrix}\mathbf{I}_{n_p\times n_p} & \mathbf{0}_{n_p\times n_{\Delta p}}\\ \mathbf{0}_{n_{\Delta p}\times n_p} & \mathbf{I}_{n_{\Delta p}\times n_{\Delta p}}\\ \mathbf{T}_{n_{p_d}\times n_p} & \tilde{\mathbf{T}}_{n_{p_d}\times n_{\Delta p}}\end{bmatrix} \tag{50}$$

$$\mathbb{P}_R = \left\{\mathbf{p}(t)^T \quad \Delta\mathbf{p}(t)^T\right\}^T \tag{51}$$

where $\mathbf{T}$ and $\tilde{\mathbf{T}}$ are the sub-condensation matrices. The sub-indices in Eq. (50) indicate the sizes of the matrices, with n_p, $n_{\Delta p}$ and n_{p_d} being the number of components of $\mathbf{p}$, $\Delta\mathbf{p}$ and $\mathbf{p}_d$, respectively.

Applying (49), the system (32) is rewritten using the reduced space of degrees of freedom

$$\mathbf{R}^T\,\mathbf{S}\,\mathbf{R}\,\dot{\mathbb{P}}_R + \mathbf{R}^T\,\mathbf{H}\,\mathbf{R}\,\mathbb{P}_R = \mathbf{R}^T\,\mathbf{Q}(t) \tag{52}$$

Mejia et al. (2021) proposed to statically condense the longitudinal pressure degrees of freedom, $\mathbf{p}_d$, as a linear combination of $\mathbf{p}$. Then, their sub-condensation matrix $\tilde{\mathbf{T}}$ is a zero matrix and $\mathbf{T}$ can be defined as:

$$\mathbf{T} = \begin{bmatrix}\mathbf{N}\left(\mathbf{x}_d^1\right)^T & \mathbf{N}\left(\mathbf{x}_d^2\right)^T\end{bmatrix}^T \tag{53}$$

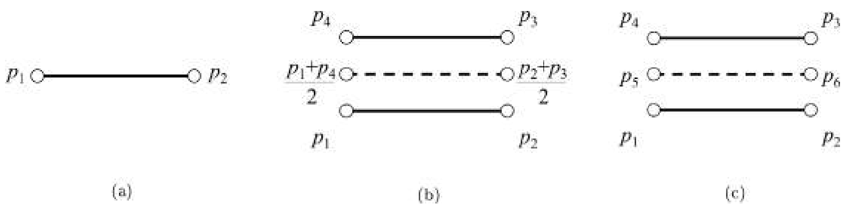

Fig. 5. Interface elements: (a) Single node; (b) Double node; (c) Triple node.

Damirchi et al. (2021) presented a condensation of longitudinal pressure degrees of freedom, setting its value inside the discontinuity to the mean of the pressures on the discontinuity top and bottom surfaces. Then, $\mathbf{T}$ is still defined by Eq. (53), but $\tilde{\mathbf{T}}$ is

$$\tilde{\mathbf{T}} = \left[\tilde{\mathbf{N}}^{mid} \left(\mathbf{x}_d^1 \right)^T \quad \tilde{\mathbf{N}}^{mid} \left(\mathbf{x}_d^2 \right)^T \right]^T \tag{54}$$

with

$$\tilde{\mathbf{N}}^{mid} (\mathbf{x}) = \mathbf{N} (\mathbf{x}) \left(\frac{1}{2} \mathbf{I} - \mathbf{H}_d \right) \mathbf{M} \tag{55}$$

This alternative is investigated later in a validation example.

3.4. Time discretization

To solve the discrete first-order differential equation system, Eq. (32), an implicit time integration scheme is used

$$\mathbb{P} \left(t_{n+1} \right) = \mathbb{P} \left(t_n \right) + \Delta t \, \dot{\mathbb{P}} \left(t_{n+1} \right) \tag{56}$$

where t_{n+1} corresponds to the current time, t_n to the previous one, and Δt is the time step.

Substituting Eq. (56) in (32) results in

$$(\mathbf{S} + \Delta t \, \mathbf{H}) \, \mathbb{P} \left(t_{n+1} \right) = \Delta t \, \mathbf{Q} + \mathbf{S} \, \mathbb{P} \left(t_n \right) \tag{57}$$

4. Analogy with DFM using interface elements

In this work, to validate the results obtained with the embedded approach, we compare them with solutions from a DFM using interface elements. Thus, we discuss the equivalence between the embedded approach and DFM across different categories of interface elements, shown in Fig. 5 (De Borst, 2018).

Single node interface elements, Fig. 5(a), can only model the longitudinal flow inside the discontinuity. Hence, they are similar to the embedded formulation using a distance function-based enrichment, Eq. (5).

Double node interface elements, Fig. 5(b), can model both longitudinal and transversal flow inside the discontinuity. In this element, the longitudinal pressure at the mid-plane nodes is not a degree of freedom. It is defined as a mean value of the pressure dofs of the top and bottom discontinuity surface nodes. Therefore, DFM using this interface element is similar to the embedded formulation presented in this work, using a discontinuous function-based enrichment, Eq. (8), and applying the static condensation of the longitudinal pressure dofs proposed by Damirchi et al. (2021).

Finally, triple node interface elements, Fig. 5(c), share many similarities with the double node elements but allow pressurizing the discontinuity since the longitudinal pressure in its mid-plane is an actual dof (De Borst, 2018). Then, the DFM using these elements will have similar behavior to the embedded formulation with a discontinuous function-based enrichment without statically condensing the longitudinal pressure dofs.

5. Numerical experiments

This section presents several benchmarks for single-phase fluid flow in fractured porous medium. For all benchmarks, unless otherwise specified, the hydraulic conductivity of the porous medium is 1.1574e−05 m/s, the fluid dynamic viscosity is 1.0e−6 kPa s, the fluid specific weight is 9.81 kPa/m, the solid skeleton bulk modulus is 1.0e9 kPa, the fluid bulk modulus is 2.0e6 kPa, the porosity is 0.3, Biot's coefficient is 0.6, and the discontinuity aperture is 1.0 mm. The longitudinal pressure degrees of freedom are assumed as global variables and not statically condensed.

The behavior of the embedded formulation was validated and evaluated by comparing the obtained results with solutions using a Discrete Fracture Model (DFM) with double and triple-node interface elements (Nguyen et al., 2017), implemented in the in-house code GeMA (Mendes et al., 2016; Mejia et al., 2020; Rueda et al., 2020). Following the analogy presented in Section 4, triple-node interface elements are used when the DFM is compared to EFEM without the static condensation of the discontinuity pressure dofs. Otherwise, double-node interface elements are used.

In domains with an internally embedded discontinuity as shown in Fig. 6, the nodes corresponding to the tips of the discontinuity must have null pressure jump $\Delta\mathbf{p}$.

Assuming these degrees of freedom as global variables, this boundary condition at the tips can easily be imposed.

In the following examples, the finite elements have a linear geometry and the discontinuities are defined by straight segments. Hence, to identify the nodes where each discontinuity intersects with the finite element mesh, we implemented the algorithm to detect intersections between line segments presented by Ericson (2005).

5.1. Domain with multiple non-intersecting parallel discontinuities

This example consists of a square 5.0 m domain with four 2.5 m long horizontal discontinuities, equally spaced and centered. Two scenarios for the boundary conditions are considered: a non-uniform pressure gradient and a nodal discharge at the center of the domain, as shown in Fig. 7.

Three regular meshes of linear quadrilateral elements were used for both the embedded approach and DFM. For the embedded approach, the number of sub-divisions of the edges was 16, 32, and 64. In the DFM meshes, finite elements crossed by a discontinuity were split into two, and an interface element was inserted between them.

Two parameter configurations are investigated for each scenario studied. In Case 1, all discontinuities have the same leak-off parameter equal to 1.0e−09 m/(kPa s). In Case 2, the discontinuities have different leak-off values. From bottom to top, the values of the leak-off parameter are 1.0e−03, 1.0e−05, 1.0e−07, and 1.0e−09 m/(kPa s).

First, are presented the solutions for the problem of a non-uniform pressure gradient, Fig. 7(a), at the final analysis time, 20.0 s. The simulation was performed assuming a time step of 0.1 s. Fig. 8 presents

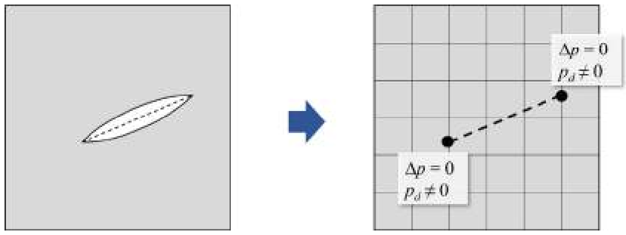

Fig. 6. Tip treatment.

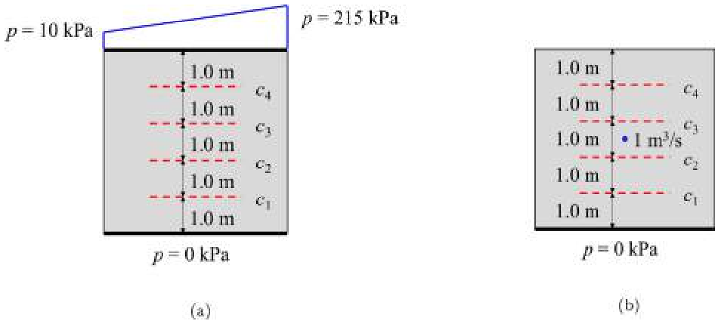

Fig. 7. Example 1: geometry and boundary conditions with (a) Non-uniform pressure at the top and (b) Nodal discharge at the center of the domain.

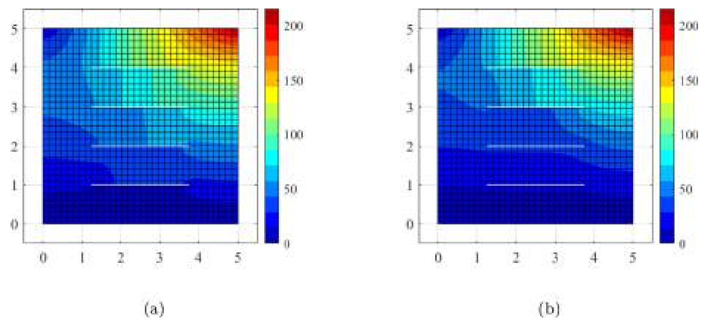

Fig. 8. Pore-pressure field (kPa) using the 32 × 32 mesh: (a) Case 1; (b) Case 2.

the pressure field from the embedded formulation using a 32 × 32 mesh for both leak-off assumptions.

Fig. 9 presents the pressure profiles defined along the y-axis at the middle of the domain and the relative difference with respect to the solution obtained with the DFM, for the three mesh refinements and the two cases.

The results shown in Figs. 8 and 9 demonstrate the influence of the leak-off parameter in the fluid flow through the porous medium. The pressure profiles (Fig. 9c) show that a higher jump in the pressure occurs for lower values of the leak-off parameter, showing that the formulation can model and control the transversal flow through a discontinuity. Also, it shows that for a higher leak-off, an imperceptible effect on the transversal flow is observed.

The relative differences of the pressure profile, in Figs. 9(b) and 9(d), show that the solutions using the embedded formulation agreed well with those obtained using a DFM for all three mesh refinement, with a relative difference lower than 0.5% in all cases. The residual relative difference between the two models is assumed to be related to the simplifications introduced in the embedded formulation, especially in the definition of the mapping matrix, Eq. (26).

Fig. 10 presents the pressure evolution at the center of the domain for the three meshes in both cases. It shows that the EFEM can capture a similar transient response as the DFM, with the results getting closer as the meshes are refined.

The solutions for the problem considering a fluid injection at the center point of the domain are now presented, Fig. 7(b), at the end of the analysis, after 20.0 s. Fig. 11 presents the pressure field from the embedded formulation using a 32 × 32 mesh, it shows that for Case 1, higher pressure is obtained since all discontinuities act as barriers for fluid flow.

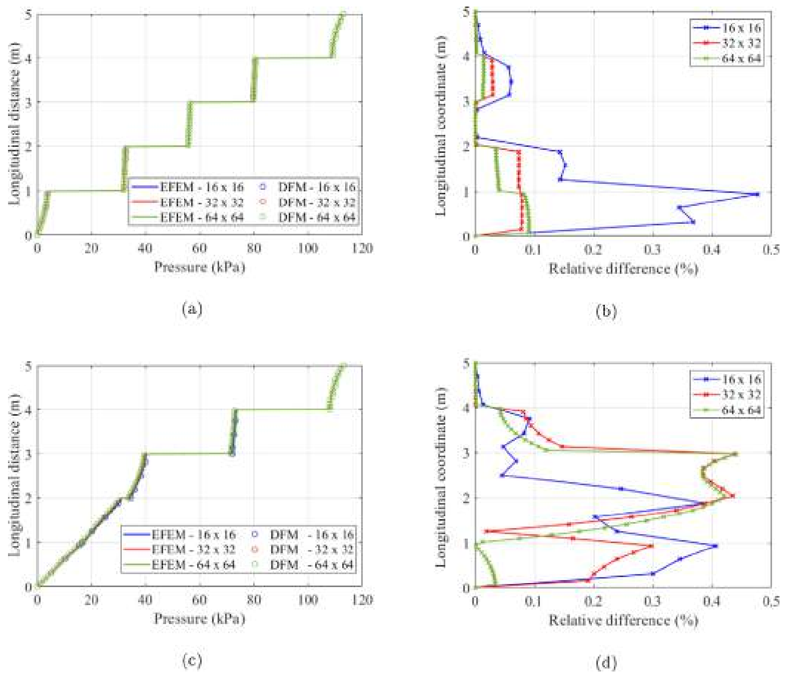

Fig. 9. Results for the problem with non-uniform pressure gradient: (a) Pressure field for Case 1; (b) Relative difference profile for Case 1; (c) Pressure field for Case 2; (d) Relative difference profile for Case 2.

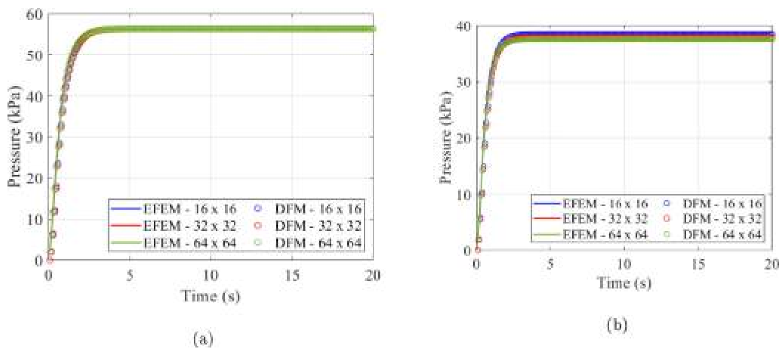

Fig. 10. Pressure evolution at the center of the domain: (a) Case 1, (b) Case 2.

Fig. 12 presents the pressure profiles defined along the y-axis at the middle of the domain and the relative difference with respect to the DFM solution, for the three mesh refinements and the two cases. In this problem, the relative differences along the pressure profile are higher in Case 2 for the coarser mesh but decrease for the more refined ones.

Fig. 13 presents the pressure evolution at the center of the domain for both cases using the three meshes. It shows a good agreement with the solution obtained with the DFM, and that the solutions of both methods get closer as the mesh is refined.

5.2. Injection at the discontinuity

In this example, a discharge is applied at the discontinuity mid-plane. The aim of this example is to show that this formulation can

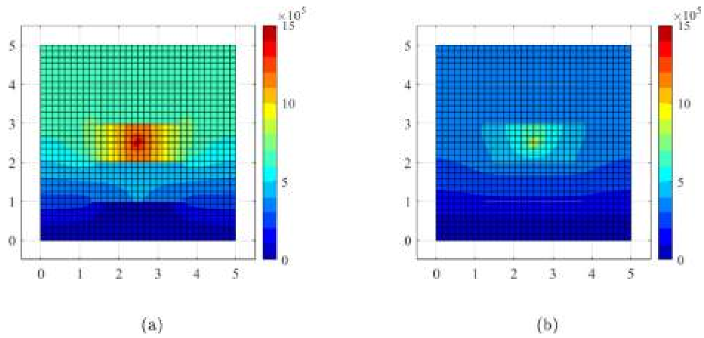

Fig. 11. Pore-pressure field (kPa) using the 32 × 32 mesh of (a) Case 1 and (b) Case 2.

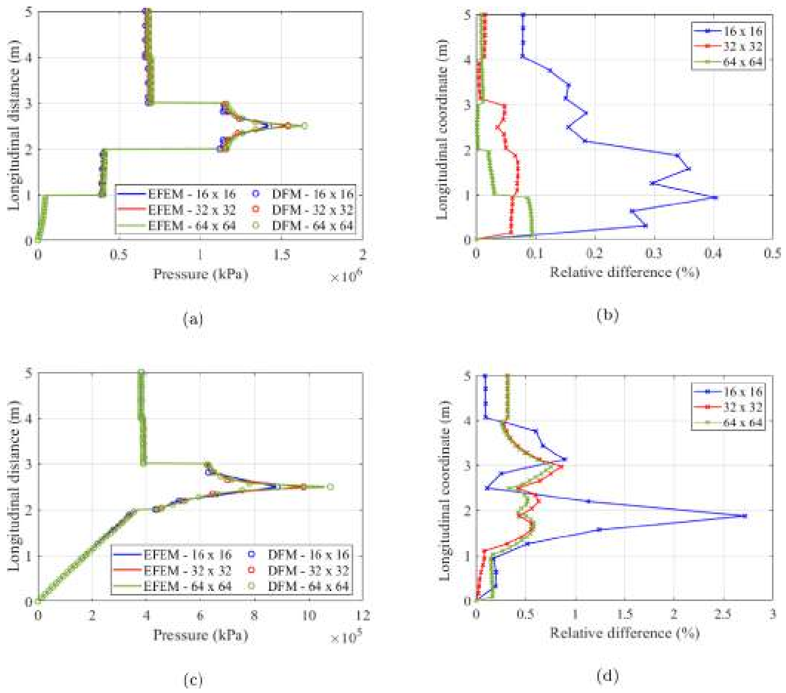

Fig. 12. Results for the problem with injection at the center: (a) Pressure field for Case 1, (b) Relative difference profile for Case 1, (c) Pressure field for Case 2, and (d) Relative difference profile for Case 2.

be easily used to model problems in which the discontinuity is pressurized, such as in a hydraulic fracture process. Since the pressures at the mid-plane nodes can be taken as independent degrees of freedom, applying a discharge at the discontinuity is simply done by assigning a Neumann boundary condition to this degree of freedom. Fig. 14 illustrates the problem geometry and boundary conditions, which consists of a rectangular domain with a discontinuity crossing it parallel to the x-axis. A discharge of 3 m^3/s is applied at the middle plane, and a null pressure condition is applied at the right edge.

Two regular meshes of linear quadrilateral elements were used for both embedded and DFM. For the embedded approach, the discretizations were 36 × 27 and 108 × 81. In the DFM meshes, the finite

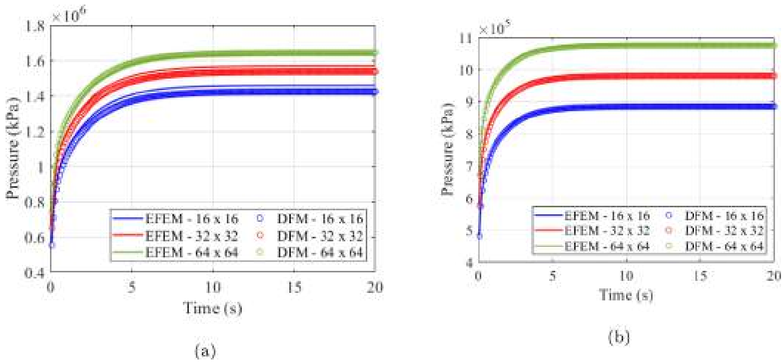

Fig. 13. Pressure evolution at the center of the domain: (a) Case 1, (b) Case 2.

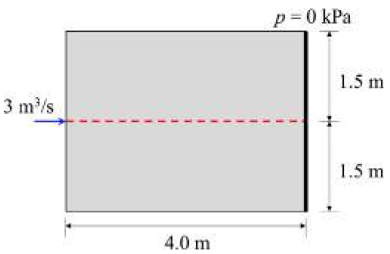

Fig. 14. Benchmark of fluid injection at the discontinuity.

elements crossed by a discontinuity were split into two and an interface element was added between them.

The problem was solved for two values of the leak-off parameter: 1.0e−01 and 1.0e−7 m/(kPa s). Fig. 15 presents the pressure field for both leak-off parameters at the end of the simulation of 1.0 s, which was performed considering a constant time step of 0.1 s.

Fig. 15 shows an evident influence of the leak-off parameter on controlling fluid leakage from the discontinuity to the continuum. In Fig. 15(a), due to the lower leak-off, the pressure field in the continuum does not increase as much as in the scenario with the higher leak-off, Fig. 15(b).

The comparison with the DFM with triple-node interface elements is shown in Fig. 16. The pressure and relative difference profiles are evaluated along the y-axis of the middle of the domain (x = 2 m).

The results for the scenario with a lower leak-off parameter in Figs. 16(a) and 16(b) show that there is a small difference in the behavior of both models. For the two mesh refinements, the relative difference between them did not change significantly, therefore, the difference is assumed to be from the formulation simplifications, especially in the definition of the mapping matrix, Eq. (26). For the scenario with a higher leak-off parameter presented in Figs. 16(c) and 16(d), the solutions obtained with both models are closer, and the relative difference decreases as the mesh is refined. The solutions for the second scenario were closer since the influence of the discontinuity in the transversal flow is smaller for a higher leak-off.

Fig. 17 presents the evolution of the discontinuity pressure at the injection node for the two leak-off values and discretizations. It shows a good agreement with the results obtained with the DFM, using triple-node interface elements. This reinforces that the relative difference observed in the pressure profile of the porous medium presented in Fig. 16, is related to the simplifications introduced in the embedded formulation related to how the pressure jump is transmitted from the discontinuity to the continuum.

5.3. Fluid flow through fractured dam foundation

This benchmark consists of a gravity dam over a fractured porous medium. The geometry, boundary conditions, and mesh used in the embedded approach are shown in Fig. 18. The hydraulic conductivity of the porous medium is 1.0e−7 m/s, and the specific weight of water is 10 kN/m^3. A steady-state analysis is performed.

Two fractured domains are considered. The first one was proposed by Segura and Carol (2004), in which the fractures inside the domain have a 45° angle with the horizontal axis and are uniformly distributed with a 1.0 m spacing. In the second one, 37 fractures were randomly placed inside the domain.

The DFM finite element mesh for the regular fracture domain is composed of 5249 nodes with 6048 linear triangular finite elements and 1008 triple-node interface elements. The mesh of the random fractured domain comprises 3297 nodes with 5252 linear triangular finite elements and 358 triple-node interface elements. The FE meshes are presented in Fig. 20.

The problem is first solved for the regular fracture domain, Fig. 19(a), for two leak-off values, a high leak-off, c = 1e−05 m/(kPa s), and a low leak-off, c = 1e−09 m/(kPa s), and for two aperture values, 0.01 mm and 0.1 mm. The pressure field obtained with the embedded approach for each scenario is presented in Fig. 21.

The pressure fields presented in Fig. 21 show that for the smaller aperture and higher leak-off, the presence of the fracture system did not influence the pressure field inside the domain. With a higher aperture, a change in the pressure distribution following the fracture's orientation is seen. For a lower leak-off parameter, the presence of the fractures has a higher impact on the pressure field distribution, for both values of aperture. For a higher aperture, the pressure distribution is less affected by the leak-off.

The influence of the fracture system on the pressure field can be better seen in Fig. 22 in which the pressure profiles are evaluated along the x-axis at mid height. It also presents the solutions by Segura and Carol (2004) and the relative difference of the solution obtained with the embedded formulation in relation to the solution using the DFM.

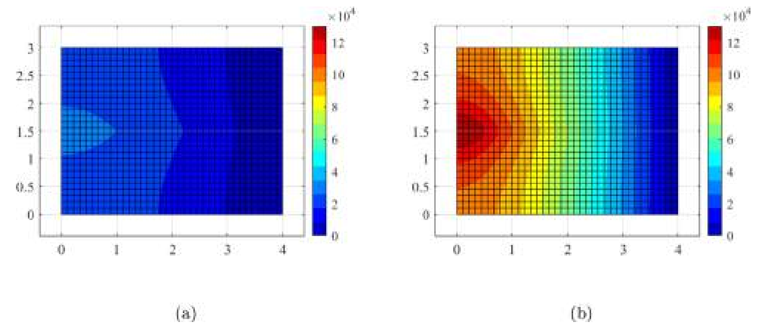

Fig. 15. Pore-pressure field (kPa) using the 36 × 27 mesh for (a) Lower leak-off, and (b) Higher leak-off.

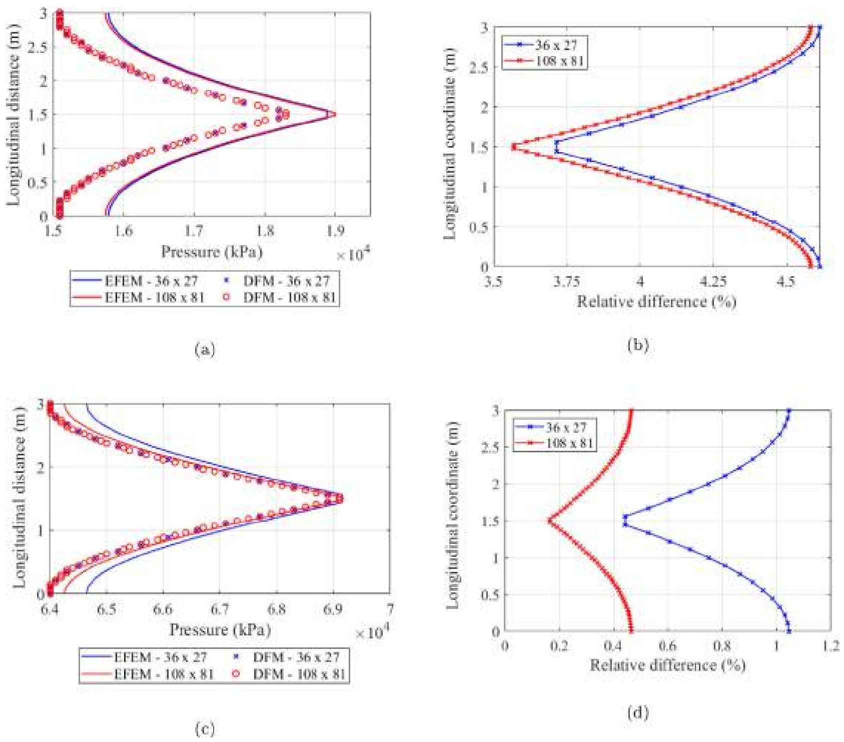

Fig. 16. Results for the problem with injection at the discontinuity: (a) Pressure field for lower leak-off; (b) Relative difference profile for lower leak-off; (c) Pressure field for higher leak-off; (d) Relative difference profile for higher leak-off.

For a higher leak-off parameter, Figs. 22(a) and 22(b) show good agreement between the solutions of the embedded approach and the DFM, with a maximum relative difference along the profile of approximately 0.6%. The pressure profiles in this case are also close to the ones presented by Segura and Carol (2004).

For a lower leak-off parameter, Figs. 22(c) and 22(d) show that there is a better agreement with the two approaches for a smaller aperture, with a maximum relative difference lower then 0.5%. With a larger aperture, the agreement between the two approaches is not as good, which is justified by the simplification introduced in the mapping matrix, Eq. (26), of the embedded formulation. Since the formulations

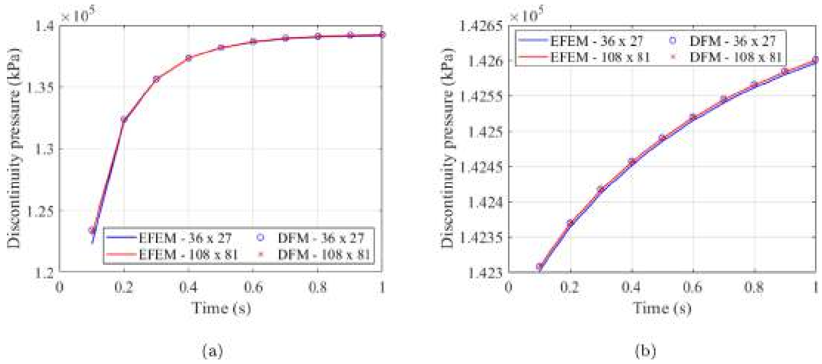

Fig. 17. Discontinuity pressure evolution at the injection node: (a) Case 1, (b) Case 2.

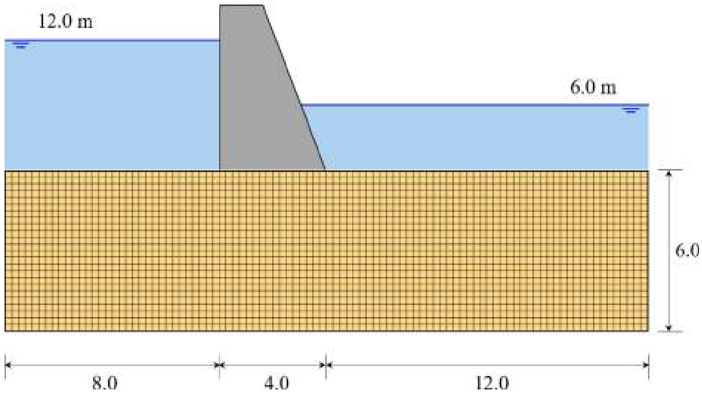

Fig. 18. Geometry, boundary conditions and finite element mesh used for the embedded approach of the fractured dam foundation.

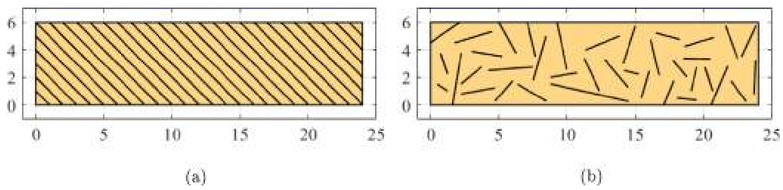

Fig. 19. Fracture domain with a (a) Regular and (b) Random distribution of fractures.

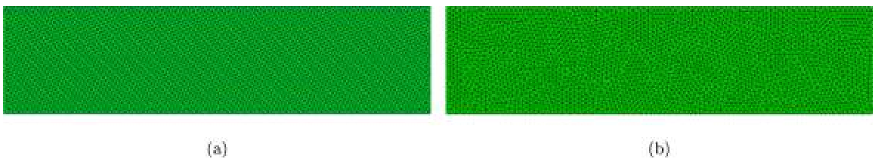

Fig. 20. Finite element mesh for the DFM: (a) Regular; (b) Random.

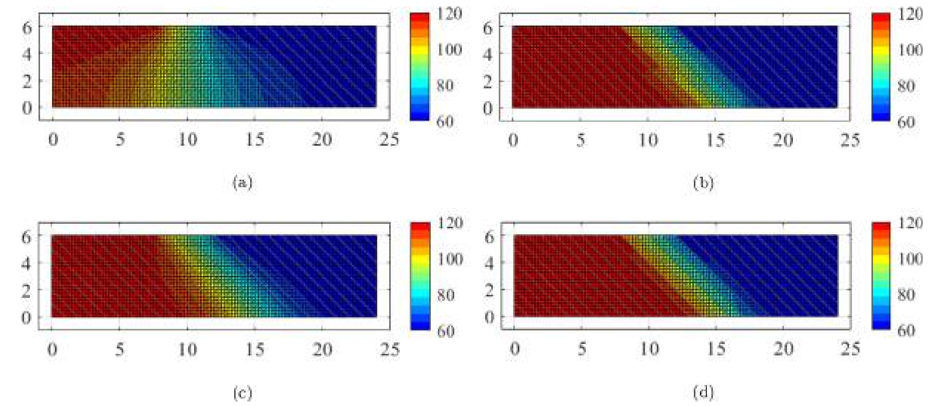

Fig. 21. Pore-pressure field (kPa) for the regular fracture domain: (a) w = 0.01 mm and c = 1e−05 m/(kPa s); (b) w = 0.01 mm and c = 1e−09 m/(kPa s); (c) w = 0.1 mm and c = 1e−05 m/(kPa s); (d) w = 0.1 mm and c = 1e−09 m/(kPa s).

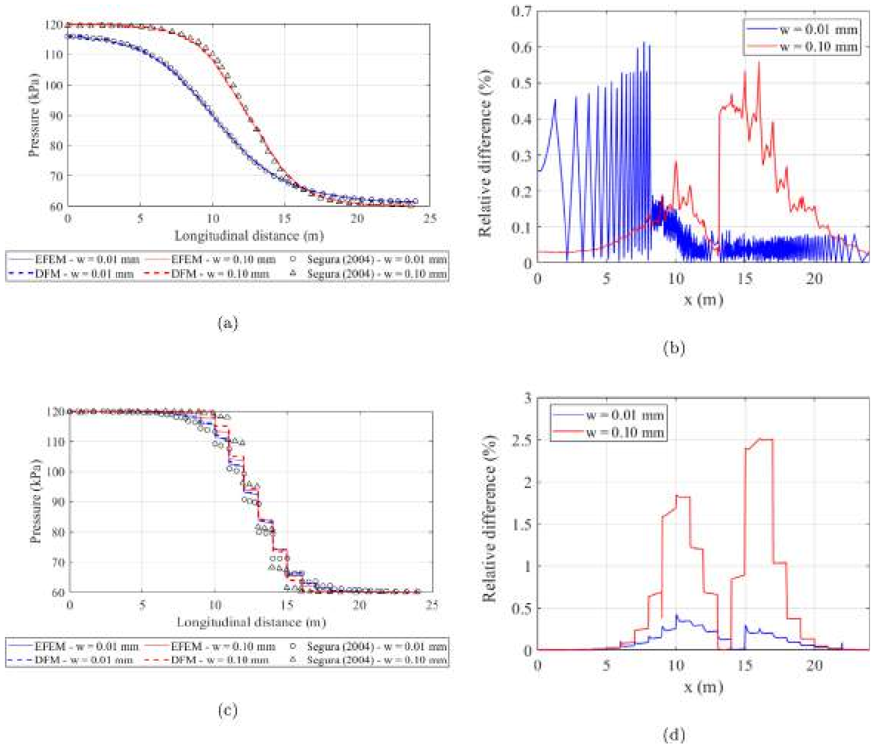

Fig. 22. Results for the regular fracture domain: (a) Pressure profiles for the higher leak-off value; (b) relative difference profile for the higher leak-off value; (c) Pressure profiles for the lower leak-off value; (d) relative difference profile for the lower leak-off value.

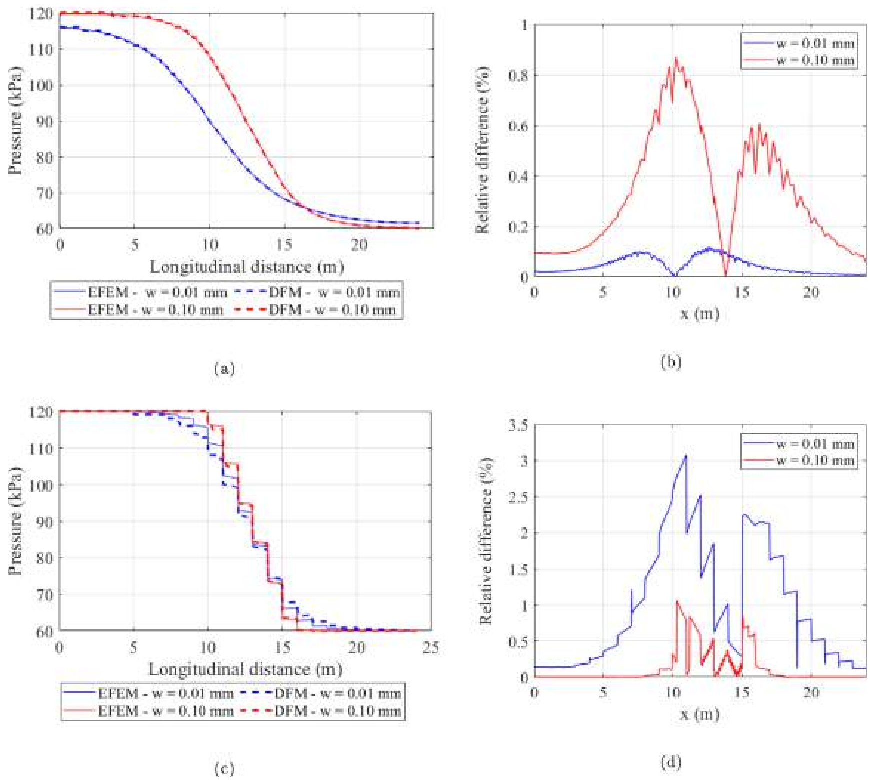

Fig. 23. Results for the regular fracture domain applying the static condensation: (a) Pressure profiles for the higher leak-off value; (b) relative difference profile for the higher leak-off value; (c) Pressure profiles for the lower leak-off value; (d) relative difference profile for the lower leak-off value.

are equivalent, the differences between our DFM solutions and those presented by Segura and Carol (2004) are assumed to be related to problem modeling.

The problem is now solved by applying the static condensation of the longitudinal degrees of freedom in the embedded approach and using double-node interface elements in the DFM.

The results obtained with the embedded formulation using the static condensation of the longitudinal pressure degrees of freedom presented in Fig. 23, showed a good agreement with the solutions of the DFM using double-node interface elements. This highlights the flexibility of this embedded formulation in achieving a similar behavior for different interface element formulations.

The same analyses were performed for the random fracture system, Fig. 19(b). The pressure fields obtained with the embedded approach are presented in Fig. 24. The static condensation of the longitudinal pressure dofs was not performed.

The pressure and relative difference profiles are shown in Fig. 25. A good agreement between the solutions using the embedded approach and the DFM for all scenarios can be seen.

6. Conclusions

This paper presented an embedded finite element formulation for fluid flow problems capable of modeling the influence of discontinuities on both longitudinal and transversal flow. The coupling between porous medium and discontinuity is achieved based on the derivation of the governing equations and constitutive modeling of the transversal flow through the discontinuity, without the need of introducing a coupling parameter.

The proposed embedded formulation performed well in steady-state and transient analyses, showing good agreement with models based on a DFM using interface elements. The formulation was capable of modeling the presence of discontinuities that act as barriers to fluid flow inside the porous medium. Also, the static condensation of the longitudinal pressure degrees of freedom allows the embedded formulation to represent the behavior of double interface elements.

The present embedded formulation is also capable of easily modeling the injection of fluid inside the discontinuities, making it attractive for problems such as hydraulic fracturing. Also, as shown by the foundation dam example, the embedded formulation does not require mesh conformity to the discontinuities. It was shown that with the same mesh discretization for the continuum, different fracture systems can be considered with results very close to the ones obtained with a DFM. Finally, the authors are currently investigating the extension of the proposed formulation to deal with multiple intersecting discontinuities.

CRediT authorship contribution statement

Danilo Cavalcanti: Writing – original draft, Validation, Conceptualization, Formal analysis, Investigation, Methodology, Software.

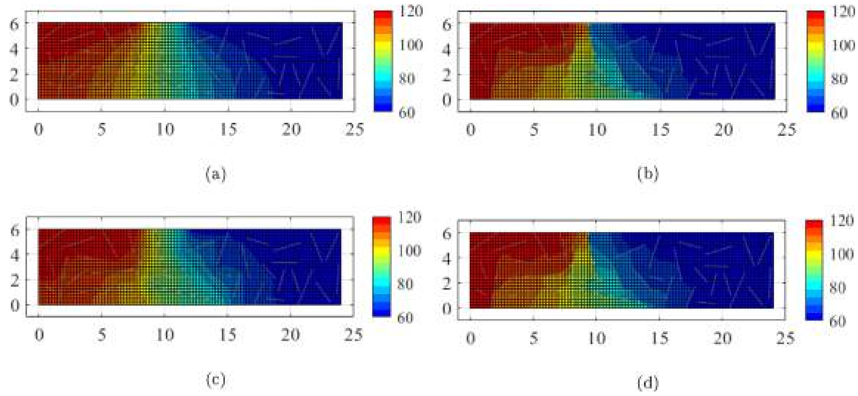

Fig. 24. Pore-pressure field (kPa) for the random fracture domain: (a) w = 0.01 mm and c = 1e−05 m/(kPa s); (b) w = 0.01 mm and c = 1e−09 m/(kPa s); (c) w = 0.1 mm and c = 1e−05 m/(kPa s); (d) w = 0.1 mm and c = 1e−09 m/(kPa s).

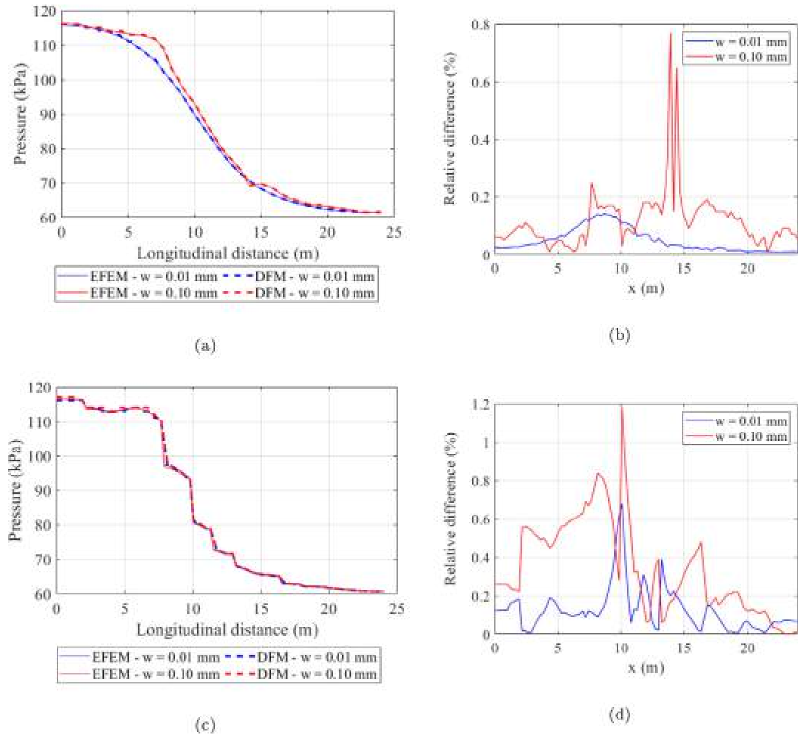

Fig. 25. Results for the random fracture domain: (a) Pressure profiles for the higher leak-off value; (b) relative difference profile for the higher leak-off value; (c) Pressure profiles for the lower leak-off value; (d) relative difference profile for the lower leak-off value.

Cristian Mejia: Formal analysis, Conceptualization, Methodology, Software, Supervision, Validation, Writing – review & editing. **Deane Roehl:** Writing – review & editing, Supervision, Resources, Project administration, Conceptualization. **Ignasi de-Pouplana:** Writing – review & editing, Supervision, Resources. **Guillermo Casas:** Writing – review & editing, Supervision, Resources. **Luiz F. Martha:** Writing – review & editing, Supervision.

Declaration of competing interest

All authors have participated in (a) conception and design, or analysis and interpretation of the data; (b) drafting the article or revising it critically for important intellectual content; and (c) approval of the final version.

This manuscript has not been submitted to, nor is under review at, another journal or other publishing venue.

The authors have no affiliation with any organization with a direct or indirect financial interest in the subject matter discussed in the manuscript.

Data availability

Data will be made available on request.

Acknowledgments

The authors acknowledge the financial support from the Brazilian National Council for Scientific and Technological Development (CNPq), Brazil Grants 309384/2019-2 and 308056/2022-1; Carlos Chagas Filho Foundation, Brazil for Supporting Research in the State of Rio de Janeiro (FAPERJ) Grants E-26/200.463/2023 and E-26/201.391/2021; and the grant TED2021-130510A-I00 funded by MCIN/AEI/10.13039/501100011033, Spain and by the "European Union NextGenerationEU/PRTR". This study was financed in part by the Coordenação de Aperfeiçoamento de Pessoal de Nível Superior - Brasil (CAPES) - Finance Code 001.

References

Alfaiate, J., Moonen, P., Sluys, L., Carmeliet, J., 2010. On the use of strong discontinuity formulations for the modeling of preferential moisture uptake in fractured porous media. Comput. Methods Appl. Mech. Engrg. 199, 2828–2839.

Alvarez, L.L., Guimarães, L.J.d.N., Gomes, I.F., Beserra, L., Pereira, L.C., de Miranda, T.S., Maciel, B., Barbosa, J.A., 2021. Impact of fracture topology on the fluid flow behavior of naturally fractured reservoirs. Energies 14 (17), http://dx.doi.org/10.3390/en14175488.

Andrianov, N., Nick, H., 2021. Machine learning of dual porosity model closures from discrete fracture simulations. Adv. Water Resour. 147, http://dx.doi.org/10.1016/j.advwatres.2020.103810.

Belytschko, T., Moës, N., Usui, S., Parimi, C., 2001. Arbitrary discontinuities in finite elements. Internat. J. Numer. Methods Engrg. 50 (4), 993–1013. http://dx.doi.org/10.1002/1097-0207(20010210)50:4<993::AID-NME164>3.0.CO;2-M.

Benkemoun, N., Gelet, R., Roubin, E., Colliat, B., 2015. Poroelastic two-phase material modeling: Theoretical formulation and embedded finite element method implementation. Int. J. Numer. Anal. Methods Geomech. 39, 1255–1275.

Berkowitz, B., 2002. Characterizing flow and transport in fractured geological media: A review. Adv. Water Resour. 25 (8–12), 861–884. http://dx.doi.org/10.1016/S0309-1708(02)00042-8.

Berre, I., Doster, F., Keilegavlen, E., 2019. Flow in fractured porous media: A review of conceptual models and discretization approaches. Transp. Porous Media 130 (1), 215–236. http://dx.doi.org/10.1007/s11242-018-1171-6, arXiv:1805.05701.

Bitencourt, L.A., Manzoli, O.L., Prazeres, P.G., Rodrigues, E.A., Bittencourt, T.N., 2015. A coupling technique for non-matching finite element meshes. Comput. Methods Appl. Mech. Engrg. 290, 19–44. http://dx.doi.org/10.1016/j.cma.2015.02.025.

Blessent, D., Therrien, R., MacQuarrie, K., 2009. Coupling geological and numerical models to simulate groundwater flow and contaminant transport in fractured media. Comput. Geosci. 35 (9), 1897–1906. http://dx.doi.org/10.1016/j.cageo.2008.12.008.

Bond, C.E., Wightman, R., Ringrose, P.S., 2013. The influence of fracture anisotropy on CO2 flow. Geophys. Res. Lett. 40 (7), 1284–1289. http://dx.doi.org/10.1002/grl.50313.

Cacace, M., Blöcher, G., 2015. MeshIt—a software for three dimensional volumetric meshing of complex faulted reservoirs. Environ. Earth Sci. 74 (6), 5191–5209. http://dx.doi.org/10.1007/s12665-015-4537-x.

Callari, C., Armero, F., 2002. Finite element methods for the analysis of strong discontinuities in coupled poro-plastic media. Comput. Methods Appl. Mech. Engrg. 191 (39), 4371–4400. http://dx.doi.org/10.1016/S0045-7825(02)00374-2.

Camargo, M., Cleto, P.R., Maedo, M.A., Rodrigues, E.A., Bitencourt, L.A., Manzoli, O.L., 2022. Modeling the hydrodynamic behavior of fractures and barriers in porous media using coupling finite elements. J. Pet. Sci. Eng. 208, 109700. http://dx.doi.org/10.1016/j.petrol.2021.109700, URL https://www.sciencedirect.com/science/article/pii/S0920410521013280.

Cerfontaine, B., Dieudonné, A.C., Radu, J.P., Collin, F., Charlier, R., 2015. 3D zero-thickness coupled interface finite element: Formulation and application. Comput. Geotech. 69, 124–140. http://dx.doi.org/10.1016/j.compgeo.2015.04.016.

Chai, Z., Yan, B., Killough, J., Wang, Y., 2018. An efficient method for fractured shale reservoir history matching: The embedded discrete fracture multi-continuum approach. J. Pet. Sci. Eng. 160, 170–181. http://dx.doi.org/10.1016/j.petrol.2017.10.055.

Cheng, L., Luo, Z., Xie, Y., Zhao, L., Wu, L., 2023. Numerical simulation and analysis of damage evolution and fracture activation in enhanced tight oil recovery using a THMD coupled model. Comput. Geotech. 155 (January), 105244. http://dx.doi.org/10.1016/j.compgeo.2023.105244.

Cheng, L., Luo, Z., Zhao, L., Xie, Y., 2022. Numerical analysis of fracture deformation and instability during CO2 geological sequestration using a THM-XFEM coupled model. Comput. Geotech. 145, http://dx.doi.org/10.1016/j.compgeo.2022.104664.

Cusini, M., White, J.A., Castelletto, N., Settgast, R.R., 2021. Simulation of coupled multiphase flow and geomechanics in porous media with embedded discrete fractures. Int. J. Numer. Anal. Methods Geomech. 45 (5), 563–584. http://dx.doi.org/10.1002/nag.3168.

Damirchi, B.V., Bitencourt, L.A., Manzoli, O.L., da Costa, D.D., 2022. Coupled hydro-mechanical modelling of saturated fractured porous media with unified embedded finite element discretisations. Comput. Methods Appl. Mech. Engrg. 393, 114804. http://dx.doi.org/10.1016/j.cma.2022.114804.

Damirchi, B.V., Carvalho, M.R., Bitencourt Jr., L.A.G., Manzoli, O.L., Dias-da Costa, D., 2021. Transverse and longitudinal fluid flow modelling in fractured porous media with non-matching meshes. Int. J. Numer. Anal. Methods Geomech. 45 (1), 83–107. http://dx.doi.org/10.1002/nag.3147.

de Borst, R., 2017. Fluid flow in fractured and fracturing porous media: A unified view. Mech. Res. Commun. 80, 47–57. http://dx.doi.org/10.1016/j.mechrescom.2016.05.004.

De Borst, R., 2018. Computational Methods for Fracture in Porous Media: Isogeometric and Extended Finite Element Methods. Elsevier.

Durán, O., Devloo, P.R., Gomes, S.M., Valentin, F., 2019. A multiscale hybrid method for Darcy's problems using mixed finite element local solvers. Comput. Methods Appl. Mech. Engrg. 354, 213–244. http://dx.doi.org/10.1016/j.cma.2019.05.013.

Ehlers, W., Luo, C., 2017. A phase-field approach embedded in the theory of porous media for the description of dynamic hydraulic fracturing. Comput. Methods Appl. Mech. Engrg. 315, 348–368. http://dx.doi.org/10.1016/j.cma.2016.10.045.

Ericson, C., 2005. Real-Time Collision Detection. CRC Press, p. 632. http://dx.doi.org/10.1201/b14581.

Fabbri, H., Sánchez, M., Maedo, M., Cleto, P., Manzoli, O., 2023. Modeling gas breakthrough and flow phenomena through engineered barrier systems using a discrete fracture approach. Comput. Geotech. 154, 105148. http://dx.doi.org/10.1016/j.compgeo.2022.105148.

Fadakar Alghalandis, Y., 2017. ADFNE: Open source software for discrete fracture network engineering, two and three dimensional applications. Comput. Geosci. 102 (February), 1–11. http://dx.doi.org/10.1016/j.cageo.2017.02.002.

Flemisch, B., Berre, I., Boon, W., Fumagalli, A., Schwenck, N., Scotti, A., Stefansson, I., Tatomir, A., 2018. Benchmarks for single-phase flow in fractured porous media. Adv. Water Resour. 111 (January 2017), 239–258. http://dx.doi.org/10.1016/j.advwatres.2017.10.036, arXiv:1701.01496.

Fumagalli, A., Keilegavlen, E., Scialò, S., 2019. Conforming, non-conforming and non-matching discretization couplings in discrete fracture network simulations. J. Comput. Phys. 376, 694–712. http://dx.doi.org/10.1016/j.jcp.2018.09.048.

Fumagalli, A., Pasquale, L., Zonca, S., Micheletti, S., 2016. An upscaling procedure for fractured reservoirs with embedded grids. Water Resour. Res. 52 (8), 6506–6525. http://dx.doi.org/10.1002/2015WR017729.

Gutierrez Escobar, R., Mejia Sanchez, E.C., Roehl, D., Romanel, C., 2019. Xfem modeling of stress shadowing in multiple hydraulic fractures in multi-layered formations. J. Nat. Gas Sci. Eng. 70 (June), 102950. http://dx.doi.org/10.1016/j.jngse.2019.102950.

Holm, R., Kaufmann, R., Heimsund, B.O., Øian, E., Espedal, M.S., 2006. Meshing of domains with complex internal geometries. Numer. Linear Algebra Appl. 13 (9), 717–731. http://dx.doi.org/10.1002/nla.505.

Jing, L., Stephansson, O., 2007. Discrete fracture network (DFN) method. Dev. Geotech. Eng. 85, 365–398. http://dx.doi.org/10.1016/S0165-1250(07)85010-3.

Khoei, A.M., 2015. Extended Finite Element Method: theory and applications. John Wiley & Sons.

Khoei, A.R., Vahab, M., Hirmand, M., 2018. An enriched–FEM technique for numerical simulation of interacting discontinuities in naturally fractured porous media. Comput. Methods Appl. Mech. Engrg. 331, 197–231. http://dx.doi.org/10.1016/j.cma.2017.11.016.

Lee, S.H., Lough, M.F., Jensen, C.L., 2001. Hierarchical modeling of flow in naturally fractured formations with multiple length scales conventional finite difference on the basis of their length (l f) relative to the finite difference grid size (/ g), fractures are classified as belonging to on. Water Resour. Res. 37 (3), 443–455.

Li, L., Lee, S.H., 2008. Efficient field-scale simulation of black oil in a naturally fractured reservoir through discrete fracture networks and homogenized media. SPE Res. Eval. Eng. 11 (4), 750–758. http://dx.doi.org/10.2118/103901-pa.

Liaudat, J., Dieudonné, A.C., Vardon, P.J., 2023. Modelling gas fracturing in saturated clay samples using triple-node zero-thickness interface elements. Comput. Geotech. 154 (November 2022), 105128. http://dx.doi.org/10.1016/j.compgeo.2022.105128.

Lima, P., Shauer, N., Villegas, J.B., Devloo, P.R., 2023. DFNMesh: Finite element meshing for discrete fracture matrix models. Adv. Eng. Softw. 186 (March), 103545. http://dx.doi.org/10.1016/j.advengsoft.2023.103545.

Manzoli, O.L., Borges, L.F., Rodrigues, E.A., Cleto, P.R., Maedo, M.A., Bitencourt, L.A., 2021. A new discrete fracture approach based on the use of coupling finite elements for modeling fluid transport in naturally fractured porous media. Comput. Methods Appl. Mech. Engrg. 386, 114112. http://dx.doi.org/10.1016/j.cma.2021.114112.

Manzoli, O.L., Cleto, P.R., Sánchez, M., Guimarães, L.J., Maedo, M.A., 2019. On the use of high aspect ratio finite elements to model hydraulic fracturing in deformable porous media. Comput. Methods Appl. Mech. Engrg. 350, 57–80. http://dx.doi.org/10.1016/j.cma.2019.03.006.

Mejia, C., Paullo Muñoz, L.F., Roehl, D., 2020. Discrete fracture propagation analysis using a robust combined continuation method. Int. J. Solids Struct. 193–194, 405–417. http://dx.doi.org/10.1016/j.ijsolstr.2020.02.002.

Mejia, C., Roehl, D., Rueda, J., Quevedo, R., 2021. A new approach for modeling three-dimensional fractured reservoirs with embedded complex fracture networks. Comput. Geotech. 130, 103928. http://dx.doi.org/10.1016/j.compgeo.2020.103928.

Mejia Sanchez, E.C., Quevedo, R., Roehl, D., 2019. Hydro-mechanical modelling of naturally fractured reservoirs. In: 53rd U.S. Rock Mechanics/Geomechanics Symposium. no. June.

Mejia Sanchez, E.C., Rueda Cordero, J.A., Roehl, D., 2020. Numerical simulation of three-dimensional fracture interaction. Comput. Geotech. 122 (March), 103528. http://dx.doi.org/10.1016/j.compgeo.2020.103528.

Mendes, C.A., Gattass, M., Roehl, D., 2016. The gema framework - an innovative framework for the development of multiphysics and multiscale simulations. In: ECCOMAS Congress 2016 - Proceedings of the 7th European Congress on Computational Methods in Applied Sciences and Engineering, vol. 4, (no. June), pp. 7886–7894. http://dx.doi.org/10.7712/100016.2383.6771.

Moinfar, A., Varavei, A., Sepehrnoori, K., Johns, R.T., 2012. Development of a novel and computationally-efficient discrete-fracture model to study IOR processes in naturally fractured reservoirs. In: Proceedings - SPE Symposium on Improved Oil Recovery, vol. 2, pp. 1277–1293. http://dx.doi.org/10.2118/154246-ms.

Nguyen, V.P., Lian, H., Rabczuk, T., Bordas, S., 2017. Modelling hydraulic fractures in porous media using flow cohesive interface elements. Eng. Geol. 225, 68–82. http://dx.doi.org/10.1016/j.enggeo.2017.04.010.

Noorishad, J., Mehran, M., 1982. An upstream finite element method for solution of transient transport equation in fractured porous media. Water Resour. Res. 18 (3), 588–596. http://dx.doi.org/10.1029/WR018i003p00588.

Oliver, J., 1996. Modelling strong discontinuities in solid mechanics via strain softening constitutive equations. Part 2: Numerical simulation. Internat. J. Numer. Methods Engrg. 39, 3601–3623.

Olorode, O., Wang, B., Rashid, H.U., 2020. Three-dimensional projection-based embedded discrete-fracture model for compositional simulation of fractured reservoirs. SPE J. 25 (4), 2143–2161. http://dx.doi.org/10.2118/201243-PA.

Ranaivomanana, H., Benkemoun, N., 2017. Numerical modelling of the healing process induced by carbonation of a single crack in concrete structures: Theoretical formulation and embedded finite element method implementation. Finite Elem. Anal. Des. 132, 42–51. http://dx.doi.org/10.1016/j.finel.2017.05.003.

Rao, X., Cheng, L., Cao, R., Jia, P., Liu, H., Du, X., 2020. A modified projection-based embedded discrete fracture model (pEDFM) for practical and accurate numerical simulation of fractured reservoir. J. Pet. Sci. Eng. 187 (November 2019), 106852. http://dx.doi.org/10.1016/j.petrol.2019.106852.

Rueda, J., Mejia, C., Noreña, N., Roehl, D., 2021. A three-dimensional enhanced dual-porosity and dual-permeability approach for hydromechanical modeling of naturally fractured rocks. Internat. J. Numer. Methods Engrg. 122 (7), 1663–1686. http://dx.doi.org/10.1002/nme.6594.

Rueda, J., Mejia, C., Quevedo, R., Roehl, D., 2020. Impacts of natural fractures on hydraulic fracturing treatment in all asymptotic propagation regimes. Comput. Methods Appl. Mech. Engrg. 371, 113296. http://dx.doi.org/10.1016/j.cma.2020.113296.

Rueda Cordero, J.A., Mejia Sanchez, E.C., Roehl, D., 2019a. Integrated discrete fracture and dual porosity - dual permeability models for fluid flow in deformable fractured media. J. Pet. Sci. Eng. 175, 644–653. http://dx.doi.org/10.1016/j.petrol.2018.12.053.

Rueda Cordero, J.A., Mejia Sanchez, E.C., Roehl, D., Pereira, L.C., 2019b. Hydro-mechanical modeling of hydraulic fracture propagation and its interactions with frictional natural fractures. Comput. Geotech. 111, 290–300. http://dx.doi.org/10.1016/j.compgeo.2019.03.020.

Segura, J.M., Carol, I., 2004. On zero-thickness interface elements for diffusion problems. Int. J. Numer. Anal. Methods Geomech. 28 (9), 947–962. http://dx.doi.org/10.1002/nag.358.

Segura, J.M., Carol, I., 2008. Coupled HM analysis using zero-thickness interface elements with double nodes. Part I: Theoretical model. Int. J. Numer. Anal. Methods Geomech. 32 (18), 2083–2101. http://dx.doi.org/10.1002/nag.735.

Settari, A., Price, H.S., 1984. Simulation of hydraulic fracturing in low-permeability reservoirs. Soc. Petrol. Eng. J. 24 (02), 141–152. http://dx.doi.org/10.2118/8939-PA.

Silva, J.A., Saló-Salgado, L., Patterson, J., Dasari, G.R., Juanes, R., 2023. Assessing the viability of CO2 storage in offshore formations of the Gulf of Mexico at a scale relevant for climate-change mitigation. Int. J. Greenh. Gas Control 126 (April), 103884. http://dx.doi.org/10.1016/j.ijggc.2023.103884.

Ţene, M., Bosma, S.B., Al Kobaisi, M.S., Hajibeygi, H., 2017. Projection-based embedded discrete fracture model (pEDFM). Adv. Water Resour. 105, 205–216. http://dx.doi.org/10.1016/j.advwatres.2017.05.009.

Wang, C., Ran, Q., Wu, Y.-S., 2019. Robust implementations of the 3D-EDFM algorithm for reservoir simulation with complicated hydraulic fractures. J. Pet. Sci. Eng. 181, 106229. http://dx.doi.org/10.1016/j.petrol.2019.106229.

Wilson, Z.A., Landis, C.M., 2016. Phase-field modeling of hydraulic fracture. J. Mech. Phys. Solids 96, 264–290. http://dx.doi.org/10.1016/j.jmps.2016.07.019.

Witherspoon, P.A., Wang, J.S.Y., Iwai, K., Gale, J.E., 1980. Validity of cubic law for fluid flow in a deformable rock fracture. Water Resour. Res. 16 (6), 1016–1024. http://dx.doi.org/10.1029/WR016i006p01016.

Wu, Y.S., Qin, G., 2009. A generalized numerical approach for modeling multiphase flow and transport in fractured porous media. Commun. Comput. Phys. 6 (1), 85–108. http://dx.doi.org/10.4208/cicp.2009.v6.p85.

Xia, Y., Jin, Y., Oswald, J., Chen, M., Chen, K., 2018. Extended finite element modeling of production from a reservoir embedded with an arbitrary fracture network. Internat. J. Numer. Methods Fluids 86 (5), 329–345. http://dx.doi.org/10.1002/fld.4421.

Xia, Y., Wei, S., Deng, Y., Jin, Y., 2022. A new enriched method for extended finite element modeling of fluid flow in fractured reservoirs. Comput. Geotech. 148, http://dx.doi.org/10.1016/j.compgeo.2022.104806.

Zeng, Q., Liu, W., Yao, J., Liu, J., 2020. A phase field based discrete fracture model (PFDFM) for fluid flow in fractured porous media. J. Pet. Sci. Eng. 191, 107191. http://dx.doi.org/10.1016/j.petrol.2020.107191.

Zhou, S., Zhuang, X., Rabczuk, T., 2019. Phase-field modeling of fluid-driven dynamic cracking in porous media. Comput. Methods Appl. Mech. Engrg. 350, 169–198. http://dx.doi.org/10.1016/j.cma.2019.03.001.

Zulian, P., Schädle, P., Karagyaur, L., Nestola, M.G., 2022. Comparison and application of non-conforming mesh models for flow in fractured porous media using dual Lagrange multipliers. J. Comput. Phys. 449, 110773. http://dx.doi.org/10.1016/j.jcp.2021.110773.

A.2
Paper 2

Hydromechanical embedded finite element for conductive and impermeable strong discontinuities in porous media

Cavalcanti, D., Mejia, C., Roehl, D., de-Pouplana, I., & Oñate, E.
Computers and Geotechnics, 172, 106427.(2024).
https://doi.org/10.1016/j.compgeo.2024.106427

Computers and Geotechnics 172 (2024) 106427

Contents lists available at ScienceDirect

Computers and Geotechnics

journal homepage: www.elsevier.com/locate/compgeo

Research Paper

Hydromechanical embedded finite element for conductive and impermeable strong discontinuities in porous media

Danilo Cavalcanti [a,b,c,*], Cristian Mejia [d], Deane Roehl [b,d], Ignasi de-Pouplana [a,e], Eugenio Oñate [a]

[a] *CIMNE – International Centre for Numerical Methods in Engineering, Spain*
[b] *Department of Civil and Environmental Engineering, Pontifical Catholic University of Rio de Janeiro, Brazil*
[c] *Universitat Politècnica de Catalunya (UPC), Spain*
[d] *Tecgraf Institute, Pontifical Catholic University of Rio de Janeiro, Brazil*
[e] *Department of Strength of Materials and Structural Engineering (RMEE), Universitat Politècnica de Catalunya (UPC), Spain*

A R T I C L E I N F O

Keywords:
Embedded finite element method (EFEM)
Strong discontinuity approach
Impermeable discontinuities
Geological fault reactivation
Geomechanics

A B S T R A C T

The pore pressure inside oil and gas reservoirs compartmentalized by sealing faults increases during injection processes. The rise in the pore pressure can induce fault reactivation, leading to hydraulic issues such as fluid leakage from the reservoir to other layers and seismicity. Therefore, it is essential to accurately model the mechanisms involved in this problem, primarily related to the presence of a strong discontinuity, a fault, inside the domain. Several numerical approaches can be used to represent the presence of discontinuities. The embedded finite element method (EFEM) has recently gained attention because it does not require the mesh to conform with the discontinuities, thus circumventing the typical mesh generation challenges of modeling faulted domains. The current EFEM formulations cannot properly model a hydromechanical problem such as fault reactivation, due to simplifications in their derivation. Hence, this work proposes a new fully coupled hydro-mechanical EFEM formulation based on the Strong Discontinuity Approach that can represent discontinuities acting as preferential flow paths or barriers for the fluid flow. The formulation is applied to a fault reactivation problem, showing the main reactivation mechanisms. This paper also discusses the presence of spurious oscillations along the discontinuities and their relations with the mesh discretization.

1. Introduction

The use of deep geological formations to store carbon dioxide (CO_2) is agreed to be feasible and important to limit the increase in the average atmospheric temperature (IPCC, 2021; Metz et al., 2005). In these sites, pre-existing discontinuities, such as geological faults, can play a significant role as a trapping mechanism for storing CO_2 (Pereira et al., 2014; Silva et al., 2023; Metz et al., 2005). In the risk assessment and monitoring of the injection and storage of CO_2, the risk of fault reactivation must be analyzed to guarantee that it will not escape to other rock strata and that no induced seismicity appears. Therefore, numerical simulations of such problems have been extensively studied in the literature (Cappa and Rutqvist, 2011; Chan and Zoback, 2007; Jha and Juanes, 2014; Pan et al., 2016; Pruess and Spycher, 2007; Quevedo et al., 2017; Rueda et al., 2014; Rutqvist et al., 2007, 2013, 2016; Serajian et al., 2016).

The complexity of simulating a fault reactivation problem requires an accurate method that can capture the reactivation mechanisms. Different numerical approaches have been proposed to represent discontinuities (Berre et al., 2019; Jing, 2003). In the context of the Finite Element Method, the most accurate and computationally cumbersome is the Discrete Fracture Method (DFM), which uses zero-thickness interface elements to model the behavior of the discontinuities (Day and Potts, 1994; de-Pouplana and Oñate, 2018; Nguyen et al., 2017; Segura and Carol, 2008a, 2008b). Despite its computational cost, one of the main difficulties associated with DFMs is the requirement of discontinuity-conforming meshes (Fadakar et al., 2017; Lima et al., 2023). In realistic problems, DFM imposes a huge challenge in mesh generation.

To avoid the need to explicitly represent the discontinuity in the

* Corresponding author at: Centre Internacional de Mètodes Numèrics a l'Enginyeria (CIMNE), 08034 Barcelona, Spain.
E-mail addresses: dborges@cimne.upc.edu (D. Cavalcanti), crisms@tecgraf.puc-rio.br (C. Mejia), deane@tecgraf.puc-rio.br (D. Roehl), ignasi.de.pouplana@upc.edu (I. de-Pouplana), onate@cimne.upc.edu (E. Oñate).

https://doi.org/10.1016/j.compgeo.2024.106427

Available online 21 May 2024

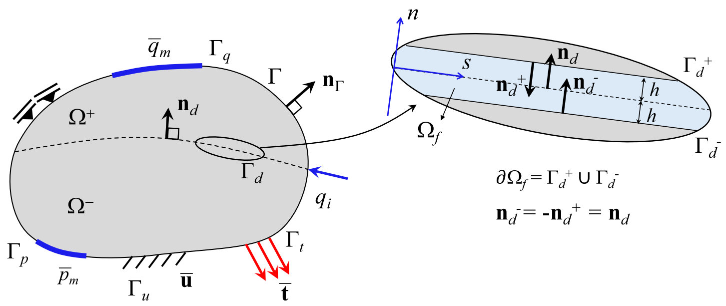

Fig. 1. Problem domain and boundary conditions.

mesh, enriched finite element formulations have gained attention due to their capability to implicitly represent the discontinuity in the domain. In the Extended Finite Element Method (XFEM), the primary fields of the problem, e.g., the displacement and the pore-pressure fields, are enriched with a discontinuous function using a global or local partition of unity (Belytschko et al., 2001; Crusat et al., 2019; De Borst et al., 2006; Khoei, 2015). Its application in geomechanics extends from fault reactivation problems (Hosseini et al., 2023; Liu, 2020; Prévost and Sukumar, 2016) to hydraulic fracturing problems (Cruz et al., 2018, 2019; Hosseini and Khoei, 2020; Khoei et al., 2015, 2016, 2018; Vahab et al., 2019). Similarly, the embedded finite element methods (EFEM) also implicitly incorporate a discontinuity by enriching the primary fields (Cazes et al., 2016; Damirchi et al., 2021; Jirásek, 2000). The difference between the two approaches is mainly the nature of the enrichment. The XFEM defines the enrichment degrees of freedom in a global sense at the nodes of the finite element mesh, meaning that the enrichment degrees of freedom at these nodes are shared by the elements connected to them. On the other hand, EFEM represents the discontinuity of the primary fields using the jumps that occur at the nodes of the intersection between the discontinuity and the finite element mesh (Cervera et al., 2022; Dias-Da-Costa et al., 2010; Wu, 2011). Therefore, the most straightforward advantage of EFEM over XFEM is the reduced number of enrichment degrees of freedom. In EFEM, if the jump degrees of freedom are taken as local variables, the enrichment degrees of freedom can be condensed by solving the governing equations associated with the discontinuity at an element level (Linder and Armero, 2007; Stanić et al., 2020). However, considering the jump degrees of freedom as global variables defined at the nodes of the discontinuity has the advantage of guaranteeing the continuity of the jump field along its extension (Bybordiani and Dias-da-Costa, 2021; Dias-da-Costa et al., 2009a, 2009b).

In the context of coupled hydromechanical problems, the existing embedded finite element formulations have limitations regarding their application in some practical reservoir simulations. For example, in a fault reactivation simulation, it is essential to model discontinuities that act as preferential paths or as barriers to the fluid flow. To meet the latter behavior, the pressure field needs to be enriched with a Heaviside function (Cavalcanti et al., 2024). Also, the enriched displacement field must include linear deformation modes to avoid stress locking (Linder and Armero, 2007). In the literature, none of the coupled hydromechanical embedded finite element formulations have such features (Armero and Callari, 1999; Benkemoun et al., 2015; Callari, 2004; Callari et al., 2010; Larsson et al., 1996; Lu et al., 2017). Recently, Damirchi et al. (2022) presented a hydromechanical embedded finite element formulation based on the strong discontinuity approach using a coupling finite element (Bitencourt et al., 2015) to assure compatibility between the continuum and discontinuity meshes. They applied the formulation to problems with discontinuities acting as a preferential path for fluid flow.

This paper proposes a fully coupled hydromechanical embedded finite element formulation, considering a strong discontinuity on both displacement and pore-pressure fields, for the transient behavior of deformable porous media. The present formulation allows the modeling of discontinuities that act as preferential paths or as barriers for the fluid flow in the porous media. In this formulation, no coupling finite element or coupling parameter is required. The paper is structured in the following sections. Section 2 presents the derivation of the weak form of the governing equations as well as the definition of the enrichment of the displacement and pore-pressure fields. Section 3 presents how the problem is solved with the proposed embedded finite element formulation. Section 4 presents two validation tests. Section 5 presents the application of the proposed formulation in solving a fault reactivation problem. Finally, Section 6 summarizes the main conclusions of the work.

2. Governing equations

A domain Ω crossed by discontinuity Γ_d is adopted for the following derivations, as shown in Fig. 1. It separates the model into two subdomains (Ω^+ and Ω^-) based on the normal vector to the discontinuity surface, $\mathbf{n}_d$, such that Ω^+ is the sub-region at which the normal vector $\mathbf{n}_d$ is pointing.

The boundary conditions associated with the displacement field, $\mathbf{u}(\mathbf{x}, t)$, are:

$$\boldsymbol{\sigma} \cdot \mathbf{n} = \overline{\mathbf{t}}, \mathbf{x} \in \Gamma_t \tag{1}$$

$$\mathbf{u} = \overline{\mathbf{u}}, \mathbf{x} \in \Gamma_u$$

$$\boldsymbol{\sigma} \cdot \mathbf{n}_d = \mathbf{t}_d, \mathbf{x} \in \Gamma_d$$

where $\boldsymbol{\sigma}$ is the Cauchy stress tensor, $\mathbf{t}$ is the traction vector on the boundary with normal $\mathbf{n}$ associated with the natural boundary conditions, $\overline{\mathbf{u}}$ is the prescribed displacement, $\mathbf{t}_d$ is the traction vector on the discontinuity boundary, with normal $\mathbf{n}_d$.

The boundary conditions associated with the pore-pressure field in the continuum porous media, $p_m(\mathbf{x}, t)$ are:

$$\mathbf{v}_m \cdot \mathbf{n} = \overline{q}_m, \mathbf{x} \in \Gamma_q \tag{2}$$

$$p_m = \overline{p}_m, \mathbf{x} \in \Gamma_p$$

$$[\![\mathbf{v}_m]\!] \cdot \mathbf{n}_d = q_d, \mathbf{x} \in \Gamma_d$$

where $\mathbf{v}_m$ is the fluid relative velocity vector, $\overline{q}_m$ is the flux associated with the natural boundary conditions, q_d is the flux through the discontinuity, $\overline{p}_m$ is the prescribed pressure associated with the essential boundary conditions, and $[\![\ ]\!]$ denotes the jump in the field along Γ_d.

2.1. Approximation of primary fields

The problem is governed by three independent fields: the displacement, $\mathbf{u}(\mathbf{x},t)$, the pore-pressure of the continuum porous media, $p_m(\mathbf{x},t)$, and the pore-pressure along the discontinuity surface, $p_f(\mathbf{x},t)$.

To incorporate a discontinuity into the domain without having it explicitly represented requires that $\mathbf{u}(\mathbf{x},t)$ and $p_m(\mathbf{x},t)$ be defined as presented for the following generic field $g(\mathbf{x})$ (Oliver, 1996):

$$g(\mathbf{x}) = \overline{g}(\mathbf{x}) + \left(\mathscr{H}_{\Gamma_d}(\mathbf{x}) - \varphi(\mathbf{x})\right)\widetilde{g}(\mathbf{x}) \tag{3}$$

where $\overline{g}(\mathbf{x})$ is the regularized part of the field, $\widetilde{g}(\mathbf{x})$ is the enrichment part of the field, $\mathscr{H}_{\Gamma_d}(\mathbf{x})$ is the Heaviside function, and $\varphi(\mathbf{x})$ is an auxiliary function defined, respectively, as

$$\overline{g}(\mathbf{x}) = \widehat{g}(\mathbf{x}) + \varphi(\mathbf{x})\widetilde{g}(\mathbf{x}) \tag{4}$$

$$\mathscr{H}_{\Gamma_d}(\mathbf{x}) = \begin{cases} 1, & \mathbf{x} \in \Omega^+ \\ 0, & \text{otherwise} \end{cases} \tag{5}$$

$$\varphi(\mathbf{x}) = \begin{cases} 1, & \mathbf{x} \in \Gamma \in \Omega^+ \\ 0, & \mathbf{x} \in \Gamma \in \Omega^- \end{cases} \tag{6}$$

with $\widehat{g}(\mathbf{x})$ being the regular part of the field.

Fig. 2 illustrates the composition of the generic field with a regularized enrichment.

2.2. Mechanical equilibrium problem

The differential equilibrium equation is:

$$\nabla\cdot\boldsymbol{\sigma} + \mathbf{b} = 0, \mathbf{x} \in \Omega \tag{7}$$

where $\mathbf{b}$ represents the body force per unit volume vector.

Applying the Galerkin method followed by the Divergence theorem:

$$-\int_\Omega \nabla^S\delta\mathbf{u} : \boldsymbol{\sigma} d\Omega + \int_{\partial\Omega} \delta\mathbf{u}\cdot(\boldsymbol{\sigma}\cdot\mathbf{n})d\Gamma + \int_\Omega \delta\mathbf{u}\cdot\mathbf{b}d\Omega = 0 \tag{8}$$

The integral along the boundary of the domain is decomposed as

$$\int_{\partial\Omega} \delta\mathbf{u}\cdot(\boldsymbol{\sigma}\cdot\mathbf{n})d\Gamma = \int_{\Gamma_t} \delta\mathbf{u}\cdot(\boldsymbol{\sigma}\cdot\mathbf{n})d\Gamma + \int_{\Gamma_d^-} \delta\mathbf{u}\cdot\left(\boldsymbol{\sigma}\cdot\mathbf{n}_d^-\right)d\Gamma + \int_{\Gamma_d^+} \delta\mathbf{u}\cdot\left(\boldsymbol{\sigma}\cdot\mathbf{n}_d^+\right)d\Gamma \tag{9}$$

and applying the boundary conditions, Eq. (1), and substituting Eq. (9) into Eq. (8)

$$\int_\Omega \nabla^S\delta\mathbf{u} : \boldsymbol{\sigma} d\Omega + \int_{\Gamma_d} \delta[\![\mathbf{u}]\!]\cdot\mathbf{t}_d\, d\Gamma - \int_{\Gamma_t} \delta\mathbf{u}\cdot\mathbf{t}\, d\Gamma - \int_\Omega \delta\mathbf{u}\cdot\mathbf{b}\, d\Omega = 0 \tag{10}$$

Finally, adopting Biot's stress decomposition (Biot and Blot, 1941; Biot and Willis, 1957).

$$\boldsymbol{\sigma} = \boldsymbol{\sigma}^{'} - \alpha p_m\, \mathbf{I} \tag{11}$$

$$\mathbf{t}_d = \mathbf{t}_d^{'} - \alpha_f\, p_f\, \mathbf{n}_d \tag{12}$$

where σ' is the effective stress tensor, $\mathbf{t}_d{}'$ is the effective cohesive stresse vector, and α and α_f are the Biot's coefficient of the porous media and the discontinuity, respectively.

Assuming that the continuum porous media is elastic, the effective stresses are

$$\boldsymbol{\sigma}^{'}(\boldsymbol{\varepsilon}) = \mathbf{D}\, \boldsymbol{\varepsilon} \tag{13}$$

where $\mathbf{D}$ is the elastic constitutive matrix.

A traction-separation elastic and an elastoplastic cohesive law governs the discontinuity behavior, $\mathbf{t}_d{}' = \mathbf{t}_d{}'([\![\mathbf{u}]\!])$. For the elastic cohesive model, the effective traction vector is

$$\mathbf{t}_d^{'}([\![\mathbf{u}]\!]) = \mathbf{T}_d\, \mathbf{R}_d[\![\mathbf{u}]\!] \tag{14}$$

where $\mathbf{R}_d$ is the rotation matrix from the global cartesian to the discontinuity local coordinate system, and $\mathbf{T}_d$ is the constitutive tensor

$$\mathbf{T}_d = \begin{bmatrix} k_s & 0 \\ 0 & k_n \end{bmatrix} \tag{15}$$

with k_N and k_S being the discontinuity normal and shear cohesive stiffness.To avoid the penetration of the two regions along the discontinuity, a penalty approach is used. The normal stiffness is defined based on the current opening of the discontinuity, $w = [\![u]\!]_n + w_0$, where $[\![u]\!]_n$ is the normal displacement jump and w_0 is the initial opening:

$$k_n = \begin{cases} k_n^0 & \text{, if } w > 0 \\ p\, k_n^0 & \text{, if } w \leq 0 \end{cases} \tag{16}$$

where k_n^0 is the initial normal stiffness, and p is the penalization coefficient, which is equal to 5 E/l_e, with E being the Young modulus and l_e the characteristic length (Hosseini et al., 2023).

For the elastoplastic cohesive model, an additive decomposition of the displacement jump vector is defined as

$$[\![\mathbf{u}]\!] = [\![\mathbf{u}]\!]^e + [\![\mathbf{u}]\!]^p \tag{17}$$

where $[\![\mathbf{u}]\!]^e$ and $[\![\mathbf{u}]\!]^p$ are the elastic and plastic parts of the displacement jump, respectively.

The yield criterion is a combination of the Mohr-Coulomb, f_{MC}, and a tension cut-off, f_{TC}, surface:

$$f_{MC} = |t_S| + t_N \tan\phi - c \tag{18}$$

$$f_{TC} = t_N - f_t \tag{19}$$

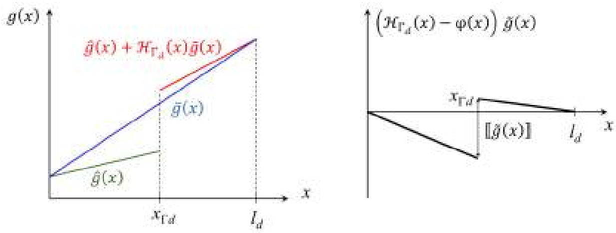

(a) (b)

Fig. 2. Behavior of a generic one-dimensional field with a strong embedded discontinuity: (a) regularized generic function and (b) discontinuous part of the generic field.

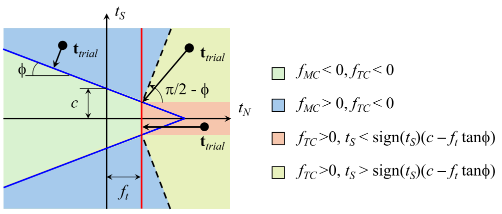

Fig. 3. Illustration of the return mapping of cohesive stresses to an admissible state. This representation is valid for $f_t < c\ /\ \tan\,\phi$.

where t_S and t_N are the shear and normal components of the cohesive traction vector, ϕ is the friction angle, c is the cohesion, and f_t is the tensile strength.

Fig. 3 presents the split of the cohesive stress space t_N - t_S based on the two yield surfaces and how an inadmissible trial elastic traction state is corrected considering these surfaces.

The plastic part of the displacement jump is computed using the flow rule combining the active surfaces. For instance, when both are active:

$$[\![\dot{\mathbf{u}}]\!]^p = \lambda_{MC}\frac{\partial g_{MC}}{\partial \mathbf{t}_d} + \lambda_{TC}\frac{\partial g_{TC}}{\partial \mathbf{t}_d} \tag{20}$$

where λ_{MC} and λ_{TC} are the plastic multipliers and g_{MC} and g_{TC} are the plastic potential surfaces of the Mohr-Coulomb and the tension cut-off yield criteria, respectively. The plastic potential surface for the tension cut-off equals its yield surface. For the Mohr-Coulomb, the plastic potential is

$$g_{MC} = |t_S| + t_N \tan\varphi - c \tag{21}$$

where φ is the dilatancy angle.

For more details on the cohesive stress integration algorithm and the definition of the tangent constitutive matrix, see Abreu et al. (2022) and Potts and Zdravkovic (1999).

2.3. Fluid flow through the porous media

The continuity equation of the continuum porous media is,

$$\alpha\ \nabla\cdot\dot{\mathbf{u}} + \frac{1}{M}\frac{\partial p_m}{\partial t} + \nabla\cdot\mathbf{v}_m = 0, \quad \mathbf{x}\in\Omega\backslash\Gamma_d \tag{22}$$

where M is Biot's modulus (Biot and Willis, 1957):

$$M = \left(\frac{\phi}{K_f} + \frac{\alpha - \phi}{K_s}\right)^{-1} \tag{23}$$

where ϕ is the porosity, and K_s and K_f are the bulk moduli of the solid skeleton and the fluid, respectively.

Applying the Galerkin method followed by the Divergence theorem gives:

$$\begin{aligned}&\int_{\Omega\backslash\Gamma_d}\delta p_m(\alpha\nabla\cdot\dot{\mathbf{u}})d\Omega + \int_{\Omega\backslash\Gamma_d}\delta p_m\left(\frac{1}{M}\frac{\partial p_m}{\partial t}\right)d\Omega + \int_{\partial\Omega}\delta p_m(\mathbf{v}_m\cdot\mathbf{n})d\Gamma\\&-\int_{\Omega\backslash\Gamma_d}\nabla\delta p_m\cdot\mathbf{v}_m d\Omega\\&=0\end{aligned} \tag{24}$$

Decomposing the integral along the boundary and applying the boundary conditions, eq. (2) yields:

$$\begin{aligned}&\int_{\Omega\backslash\Gamma_d}\delta p_m(\alpha\nabla\cdot\dot{\mathbf{u}})d\Omega + \int_{\Omega\backslash\Gamma_d}\delta p_m\left(\frac{1}{M}\frac{\partial p_m}{\partial t}\right)d\Omega + \int_{\Gamma_q}\delta p_m\ \overline{q}_m\ d\Gamma\\&-\int_{\Gamma_d}\nabla\delta p_m\ q_d\ d\Gamma - \int_{\Omega\backslash\Gamma_d}\nabla\delta p_m\cdot\mathbf{v}_m\ d\Omega\\&=0\end{aligned} \tag{25}$$

Neglecting gravity effects, Darcy's law governs the relative fluid velocity in the porous medium

$$\mathbf{v}_m = -\frac{\mathbf{k}_m}{\mu}\nabla p_m \tag{26}$$

where $\mathbf{k}_m$ is the intrinsic permeability matrix and μ is the dynamic fluid viscosity.

The fluid flow exchange between the discontinuity and the porous medium, q_d, can be decomposed into two parts:

$$q_d = q_d^{(+)} + q_d^{(-)} \tag{27}$$

with

$$q_d^{(+)} = c_T\left(p_f - p_m^{(+)}\right) \tag{28}$$

$$q_d^{(-)} = c_B\left(p_f - p_m^{(-)}\right) \tag{29}$$

where c_T and c_B are the leak-off parameters, which control the transversal flow through the discontinuity.

Finally, substituting Eqs. (26)–(29) into Eq. (25), provides the weak form of the continuity equation for the continuum porous medium:

$$\begin{aligned}&\int_{\Omega\backslash\Gamma_d}\delta p_m(\alpha\nabla\cdot\dot{\mathbf{u}})d\Omega + \int_{\Omega\backslash\Gamma_d}\delta p_m\left(\frac{1}{M}\frac{\partial p_m}{\partial t}\right)d\Omega + \int_{\Gamma_q}\delta p_m\ \overline{q}_m d\Gamma\\&-\int_{\Gamma_d}\nabla\delta p_m c_T\left(p_f - p_m^{(+)}\right)d\Gamma - \int_{\Gamma_d}\nabla\delta p_m\ c_B\left(p_f - p_m^{(-)}\right)d\Gamma\\&+\int_{\Omega\backslash\Gamma_d}\nabla\delta p_m\cdot\left(\frac{\mathbf{k}_m}{\mu}\nabla p_m\right)d\Omega\\&=0\end{aligned} \tag{30}$$

2.4. Fluid flow inside the discontinuity

The one-dimensional continuity equation of the discontinuity is

$$\alpha_f\nabla_d\cdot\dot{\mathbf{u}}_d + \frac{1}{M_f}\frac{\partial p_f}{\partial t} + \nabla_d\cdot\mathbf{v}_f = 0, \quad \mathbf{x}\in\Gamma_d \tag{31}$$

where M_f is Biot's modulus of the discontinuity. The divergence operator is defined at the discontinuity local system as

$$\nabla_d = \begin{bmatrix}\dfrac{\partial}{\partial s} & \dfrac{\partial}{\partial n}\end{bmatrix}^T \tag{32}$$

The derivation of the weak form of the continuity equation for the continuum porous media follows the steps of the previous section. The final integral form is the following:

$$\begin{aligned}&\int_{\Omega_f}\delta p_f\left(\alpha_f\nabla_d\cdot\dot{\mathbf{u}}_d\right)d\Omega + \int_{\Omega_f}\delta p_f\left(\frac{1}{M_f}\frac{\partial p_f}{\partial t}\right)d\Omega + \int_{\Gamma_d}\delta p_f\ q_d d\Gamma\\&-\int_{\Omega_f}\nabla_d\delta p_f\cdot\mathbf{v}_f d\Omega\\&=0\end{aligned} \tag{33}$$

The terms of Eq. (33) are assumed constant in the discontinuity normal direction, see Fig. 1, and, thus,can be simplified. The first term is rewritten as,

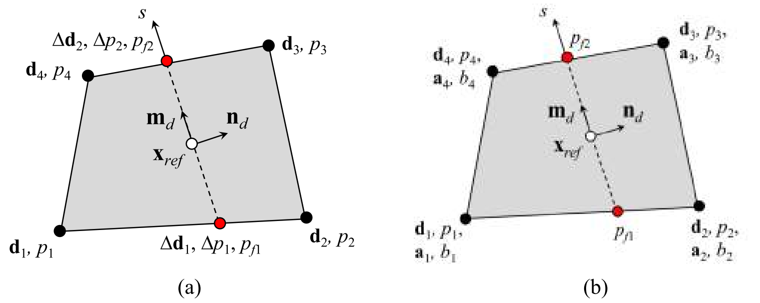

Fig. 4. Degrees of freedom in a quadrilateral element for (a) EFEM and (b) XFEM.

$$\begin{aligned}\int_{\Omega_f} \delta p_f \left(\alpha_f \nabla_d \cdot \dot{\mathbf{u}}_d\right) d\Omega &= \int_{\Gamma_d}\int_{-h}^{h} \delta p_f \left(\alpha_f \nabla_d \cdot \dot{\mathbf{u}}_d\right) dn\, d\Gamma \\ &= \int_{\Gamma_d} \delta p_f\ \alpha_f (2h)\frac{1}{2}\left(\frac{\partial \dot{u}_S}{\partial s}|_h + \frac{\partial \dot{u}_S}{\partial s}|_{-h}\right) d\Gamma \\ &+ \int_{\Gamma_d} \delta p_f \alpha_f [\![\dot{u}_N]\!] d\Gamma \end{aligned} \tag{34}$$

The second term in Eq. (33) is

$$\int_{\Omega_f} \delta p_f \left(\frac{1}{M_f}\frac{\partial p_f}{\partial t}\right) d\Omega = \int_{\Gamma_d}\int_{-h}^{h} \delta p_f \frac{1}{M_f}\frac{\partial p_f}{\partial t} dn\, d\Gamma = \int_{\Gamma_d} (2h)\delta p_f \frac{1}{M_f}\frac{\partial p_f}{\partial t} d\Gamma \tag{35}$$

The fourth term in Eq. (33) is:

$$\int_{\Omega_f} \nabla_d \delta p_f \cdot \mathbf{v}_f d\Omega = \int_{\Gamma_d}\int_{-h}^{h} \nabla_d \delta p_f \cdot \left(-\mathbf{k}_d \nabla_d p_f\right) dn d\Gamma = -\int_{\Gamma_d} w \frac{\partial \delta p_f}{\partial S} k_l \frac{\partial p_f}{\partial S} d\Gamma \tag{36}$$

where k_l is the discontinuity longitudinal permeability, which is defined by the cubic law as (Snow, 1965; Witherspoon et al., 1980)

$$k_l = \frac{w^2}{12\mu} \tag{37}$$

Finally, the weak form of the continuity equation results by substituting Eqs. (34)–(36) into Eq. (33):

$$\begin{aligned}&\int_{\Gamma_d} \delta p_f \alpha_f w \frac{1}{2}\left(\frac{\partial \dot{u}_S}{\partial s}|_h + \frac{\partial \dot{u}_S}{\partial s}|_{-h}\right) d\Gamma + \int_{\Gamma_d} \delta p_f \alpha_f [\![\dot{u}_N]\!] d\Gamma \\ &+ \int_{\Gamma_d} (2h)\delta p_f \frac{1}{M_f}\frac{\partial p_f}{\partial t} d\Gamma + \int_{\Gamma_d} \nabla \delta p_m c_T \left(p_f - p_m^{(+)}\right) d\Gamma \\ &+ \int_{\Gamma_d} \nabla \delta p_m c_B \left(p_f - p_m^{(-)}\right) d\Gamma + \int_{\Gamma_d} (2h)\frac{\partial \delta p_f}{\partial s} k_l \frac{\partial p_f}{\partial s} d\Gamma = 0\end{aligned} \tag{38}$$

3. Embedded finite element formulation

This section presents the embedded finite element discretization as a reduction of the enrichment variable used in an XFEM discretization. Fig. 4 presents the degrees of freedom (DOFs), based on both XFEM and EFEM, of a quadrilateral finite element crossed by a strong discontinuity with length l_d, a tangential unit vector $\mathbf{m}_d = [\cos\alpha\ \sin\alpha]^{\mathrm{T}}$, and a normal unit vector $\mathbf{n}_d = [-\sin\alpha\ \cos\alpha]^{\mathrm{T}}$.

In XFEM, the displacement and pore-pressure fields of the porous media are discretized as

$$\mathbf{u}(\mathbf{x}, t) = \mathbf{N}_u(\mathbf{x})\mathbf{d}(t) + \widetilde{\mathbf{N}}_u(\mathbf{x})\mathbf{a}(t) \tag{39}$$

$$p_m(\mathbf{x}, t) = \mathbf{N}_p(\mathbf{x})\mathbf{p}(t) + \widetilde{\mathbf{N}}_p(\mathbf{x})\mathbf{b}(t) \tag{40}$$

where, $\mathbf{d}$ and $\mathbf{a}$ are the standard and enrichment DOFs of the displacement field, $\mathbf{p}$ and $\mathbf{b}$ are the standard and enrichment DOFs of the pore pressure field in the porous media, $\mathbf{N}_\alpha$, $\alpha = u, p$, contains the standard shape functions of the finite element, and $\widetilde{\mathbf{N}}_\alpha$ contains the enrichment shape functions defined as:

$$\widetilde{\mathbf{N}}_\alpha(\mathbf{x}) = \mathbf{N}_\alpha(\mathbf{x})\left(\mathscr{H}_{\Gamma_d}(\mathbf{x})\mathbf{I} - \mathbf{H}_d^{(\alpha)}\right), \alpha = u, p \tag{41}$$

where $\mathbf{H}_d^{(\alpha)}$ is a diagonal matrix with the Heaviside function evaluated at the nodes associated with each degree of freedom of the finite element.

In the continuity equations, the discretization of the pore pressure field of the porous medium at a specific region of the domain, Ω^+ or Ω^-, is defined as

$$p_m^{(\pm)}(\mathbf{x}, t) = \mathbf{N}_p(\mathbf{x})\mathbf{p}(t) + \widetilde{\mathbf{N}}_p^{(\pm)}(\mathbf{x})\mathbf{b}(t) \tag{42}$$

where $\widetilde{\mathbf{N}}_p^{(+)}(\mathbf{x})$ is the matrix with the enhanced shape functions at Ω^+, with $\mathscr{H}_{\Gamma_d}(\mathbf{x}) = 1$, and $\widetilde{\mathbf{N}}_p^{(-)}(\mathbf{x})$ is the matrix with the enhanced shape functions at Ω^-, with $\mathscr{H}_{\Gamma_d}(\mathbf{x}) = 0$.

The pore pressure in the discontinuity mid-plane is:

$$p_f(s, t) = \mathbf{N}_f(s)\mathbf{p}_f(t) \tag{43}$$

where $\mathbf{p}_f$ is the pore pressure DOF vector at the discontinuity mid-plane and $\mathbf{N}_f$ is a vector containing Lagrange shape functions defined in terms of the tangential coordinate of the discontinuity, s.

The displacement jump along the discontinuity is

$$[\![\mathbf{u}]\!](s, t) = \mathbf{R}_d\ \mathbf{N}_d(s)\Delta\mathbf{d}(t) \tag{44}$$

where $\Delta\mathbf{d}$ is the vector with the discontinuity nodal displacement jumps and $\mathbf{N}_d$ is a matrix containing Lagrange shape functions defined in terms of the tangential coordinate of the discontinuity.

The symmetric part of the displacement field gradient in the continuous part of the domain is

$$\nabla^S \mathbf{u}(\mathbf{x}, t) = \mathbf{B}_u(\mathbf{x})\ \mathbf{d}(t) + \widetilde{\mathbf{B}}_u(\mathbf{x})\ \mathbf{a}(t), \quad \mathbf{x} \in \Omega \backslash \Gamma_d \tag{45}$$

where $\mathbf{B}_u(\mathbf{x}) = \partial \mathbf{N}_u(\mathbf{x})$ and $\widetilde{\mathbf{B}}_u(\mathbf{x}) = \partial \widetilde{\mathbf{N}}_u(\mathbf{x})$, with ∂ being the representation of the symmetric gradient operator in matrix form.

The divergent of the displacement field rate is

$$\nabla \cdot \dot{\mathbf{u}} = \mathbf{m}^T\left(\mathbf{B}_u(\mathbf{x})\dot{\mathbf{d}}(t) + \widetilde{\mathbf{B}}_u(\mathbf{x})\dot{\mathbf{a}}(t)\right), \quad \mathbf{x} \in \Omega \backslash \Gamma_d \tag{46}$$

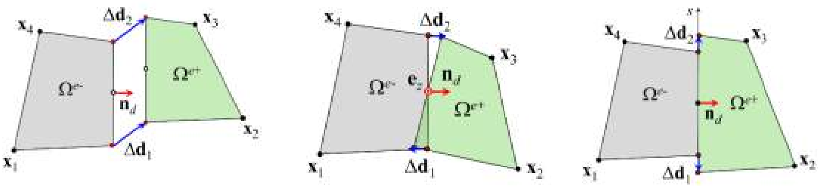

(a) (b) (c)

Fig. 5. Enrichment deformation modes: (a) Constant translation; (b) Small relative rotation; (c) Stretching.

with $\mathbf{m}^{\mathrm{T}} = [1\,1\,0]^{\mathrm{T}}$, for bidimensional problems.

The rate of the normal displacement jump is

$$[\![\dot{u}_N]\!](s,t) = \mathbf{n}_d{}^T \mathbf{N}_d(s) \Delta\dot{\mathbf{d}}(t) \tag{47}$$

The mean rate of the derivative of the shear displacement jump in the tangential direction is

$$\frac{1}{2}\left(\frac{\partial \dot{u}_S}{\partial s}|h + \frac{\partial \dot{u}_S}{\partial s}|-h\right) = \mathbf{r}_s\left(\mathbf{B}_u(\mathbf{x})\dot{\mathbf{d}}(t) + \widetilde{\mathbf{B}}_u^m(\mathbf{x})\dot{\mathbf{a}}(t)\right) \tag{48}$$

with $\mathbf{r}_s = [\cos^2\alpha \ \sin^2\alpha \ \sin\alpha\cos\alpha]$ and

$$\widetilde{\mathbf{B}}_u^m(\mathbf{x}) = \partial \mathbf{N}_u(\mathbf{x})\left(\frac{1}{2}\mathbf{I} - \mathbf{H}_d^{(u)}\right) \tag{49}$$

The gradient of the pore-pressure field of the porous media is:

$$\nabla p_m(\mathbf{x},t) = \mathbf{B}_p(\mathbf{x})\mathbf{d}(t) + \widetilde{\mathbf{B}}_p(\mathbf{x})\mathbf{b}(t), \quad \mathbf{x} \in \Omega \backslash \Gamma_d \tag{50}$$

where $\mathbf{B}_p(\mathbf{x}) = \nabla \mathbf{N}_p(\mathbf{x})$ and $\widetilde{\mathbf{B}}_p(\mathbf{x}) = \nabla \widetilde{\mathbf{N}}_p(\mathbf{x})$.

3.1. Mapping matrices

In the proposed EFEM, the enrichment part of displacement and pore-pressure field in the porous media are discretized using the displacement and pressure jumps at the intersection nodes between the discontinuity and the finite element borders, as illustrated in Fig. 4. In order to obtain such a discretization, we define a linear transformation that reduces the enrichment DOFs space to the jumps of each field, as:

$$\mathbf{a}(t) = \mathbb{M}_u \Delta\mathbf{d}(t) \tag{51}$$

$$\mathbf{b}(t) = \mathbb{M}_p \Delta\mathbf{p}(t) \tag{52}$$

To obtain $\mathbb{M}_u$, the jump of the displacement field is assumed to have a linear variation along the tangential coordinate, s. Then, the transmission of the displacement jump to the continuum is assumed to be a combination of three different deformation modes: a constant translation, a small relative rotation around the discontinuity reference point, and a stretching mode, as illustrated in Fig. 5 (Dias-da-Costa et al., 2009). The linear deformation modes are important to avoid stress-locking behavior (Linder and Armero, 2007).

The displacement mapping matrix of a node, $\mathbf{M}_u(\mathbf{x})$, can be written as a composition of two parts: the rigid-body deformation modes, $\mathbf{M}_u^{RB}(\mathbf{x})$, and the stretching modes, $\mathbf{M}_u^S(\mathbf{x})$.

$$\mathbf{M}_u(\mathbf{x}) = \mathbf{M}_u^{RB}(\mathbf{x}) + \mathbf{M}_u^S(\mathbf{x}) \tag{53}$$

with

$$\mathbf{M}_u^{RB}(\mathbf{x}) = \begin{bmatrix} \frac{1}{2} - \frac{\left(y - y_{ref}\right)\sin\alpha}{l_d} & \frac{\left(x - x_{ref}\right)\sin\alpha}{l_d} \\ \frac{\left(y - y_{ref}\right)\cos\alpha}{l_d} & \frac{1}{2} - \frac{\left(x - x_{ref}\right)\cos\alpha}{l_d} \\ \frac{1}{2} + \frac{\left(y - y_{ref}\right)\sin\alpha}{l_d} & -\frac{\left(x - x_{ref}\right)\sin\alpha}{l_d} \\ -\frac{\left(y - y_{ref}\right)\cos\alpha}{l_d} & \frac{1}{2} + \frac{\left(y - y_{ref}\right)\cos\alpha}{l_d} \end{bmatrix}^T \tag{54}$$

$$\mathbf{M}_u^S(\mathbf{x}) = \frac{s(\mathbf{x})}{l_d}\begin{bmatrix} -\cos^2\alpha & -\sin\alpha\cos\alpha \\ -\sin\alpha\cos\alpha & -\sin^2\alpha \\ \cos^2\alpha & \sin\alpha\cos\alpha \\ \sin\alpha\cos\alpha & \sin^2\alpha \end{bmatrix}^T \tag{55}$$

The mapping matrix of the pressure jump of a node, $\mathbf{M}_p(\mathbf{x})$, is defined assuming that the transmission to the continuum occurs entirely in the normal direction, i.e. (Damirchi et al., 2021):

$$\mathbf{M}_p(\mathbf{x}) = \left[\frac{1}{2} - \frac{s(\mathbf{x})}{l_d} \quad \frac{1}{2} + \frac{s(\mathbf{x})}{l_d}\right] \tag{56}$$

Finally, element mapping matrices are obtained by concatenating by rows the nodes mapping matrices evaluated at the nodes of the element, namely,

$$\mathbb{M}_\alpha = \left[\mathbf{M}_\alpha(\mathbf{x}_1)^T \quad \mathbf{M}_\alpha(\mathbf{x}_2)^T \quad \dots \quad \mathbf{M}_\alpha(\mathbf{x}_n)^T\right]^T, \alpha = u, p \tag{57}$$

3.2. Linearization and time integration

Substituting Eqs. (39)–(52) into the weak form of the equilibrium, Eq. (10), and both continuity equations, Eqs. (30) and (38), leads to the following residual vector,

$$\begin{Bmatrix} \mathbf{r}_U(t) \\ \mathbf{r}_P(t) \\ \mathbf{r}_{p_f}(t) \end{Bmatrix} = \begin{Bmatrix} \mathbf{F}_U^{int}(t) \\ 0_{n_P} \\ 0_{n_{p_f}} \end{Bmatrix} - \begin{Bmatrix} \mathbf{F}_U^{ext}(t) \\ \mathbf{F}_P^{ext}(t) \\ \mathbf{F}_{p_f}^{ext}(t) \end{Bmatrix} + \begin{bmatrix} 0_{n_U \times n_U} & -\mathbf{Q}^{\mathrm{T}} & -\mathbf{Q}_f{}^{\mathrm{T}} \\ 0_{n_P \times n_U} & \mathbf{H}_m + \mathbf{L}_m & -\mathbf{L}_{mf} \\ 0_{n_{p_f} \times n_U} & -\mathbf{L}_{mf}{}^T & \mathbf{H}_f + \mathbf{L}_f \end{bmatrix} \begin{Bmatrix} \mathbf{U}(t) \\ \mathbf{P}(t) \\ \mathbf{p}_f(t) \end{Bmatrix} + \begin{bmatrix} 0_{n_U \times n_U} & 0_{n_U \times n_P} & 0_{n_U \times n_{p_f}} \\ \mathbf{Q} & \mathbf{S}_m & 0_{n_P \times n_{p_f}} \\ \mathbf{E}_f + \mathbf{Q}_f & 0_{n_{p_f} \times n_P} & \mathbf{S}_f \end{bmatrix} \begin{Bmatrix} \dot{\mathbf{U}}(t) \\ \dot{\mathbf{P}}(t) \\ \dot{\mathbf{p}}_f(t) \end{Bmatrix} \tag{58}$$

where $\mathbf{U} = [\mathbf{d}^{\mathrm{T}}\ \Delta\mathbf{d}^{\mathrm{T}}]^{\mathrm{T}}$ is the set of displacement DOFs, $\mathbf{P} = [\mathbf{p}^{\mathrm{T}}\ \Delta\mathbf{p}^{\mathrm{T}}]^{\mathrm{T}}$ is the set of the continuum pore-pressure DOFs. The sub-indices in the zeros in eq. (58) indicate the size of the vector/matrix, with n_U, n_P and n_{pf} being the number of components of $\mathbf{U}$, $\mathbf{P}$, and $\mathbf{P}_f$, respectively. $\mathbf{F}_U^{ext}(t)$, $\mathbf{F}_P^{ext}(t)$ and $\mathbf{F}_{P_f}^{ext}(t)$ are the nodal external loads and fluid discharge, vectors; $\mathbf{F}_U^{int}$ is the internal force vector,

$$\mathbf{F}_U^{int} = \begin{Bmatrix} \int_{\Omega} \mathbf{B}_u{}^T \boldsymbol{\sigma}' d\Omega \\ \int_{\Omega\backslash\Gamma_d} \mathbb{M}_u{}^T \widetilde{\mathbf{B}}_u{}^T \boldsymbol{\sigma}' d\Omega + \int_{\Gamma_d} \mathbf{N}_d{}^T \mathbf{R}_d{}^T \mathbf{t}_d' d\Gamma \end{Bmatrix} \tag{59}$$

$\mathbf{H}_m$ is the fluid flow matrix of the porous medium,

$$\mathbf{H}_m = \begin{bmatrix} \int_{\Omega\backslash\Gamma_d} \mathbf{B}_p{}^T \frac{\mathbf{k}_m}{\mu} \mathbf{B}_p d\Omega & \int_{\Omega\backslash\Gamma_d} \mathbf{B}_p{}^T \frac{\mathbf{k}_m}{\mu} \widetilde{\mathbf{B}}_p \mathbb{M}_p d\Omega \\ \int_{\Omega\backslash\Gamma_d} \mathbb{M}_p{}^T \widetilde{\mathbf{B}}_p{}^T \frac{\mathbf{k}_m}{\mu} \mathbf{B}_p d\Omega & \int_{\Omega\backslash\Gamma_d} \mathbb{M}_p{}^T \widetilde{\mathbf{B}}_p{}^T \frac{\mathbf{k}_m}{\mu} \widetilde{\mathbf{B}}_p \mathbb{M}_p d\Omega \end{bmatrix} \tag{60}$$

$\mathbf{H}_f$ is the fluid flow matrix of the discontinuity,

$$\mathbf{H}_f = \int_{\Gamma_d} w \frac{\partial \mathbf{N}_f{}^T}{\partial s} k_l \frac{\partial \mathbf{N}_f}{\partial s} d\Gamma \tag{61}$$

$\mathbf{L}_m, \mathbf{L}_{mf}$ and $\mathbf{L}_f$ are the matrices that couple the flow between the porous medium and the discontinuity,

$$\mathbf{L}_m = \mathbf{L}_m^{(+)} + \mathbf{L}_m^{(-)} \tag{62}$$

$$\mathbf{L}_m^{(\pm)} = \begin{bmatrix} \int_{\Gamma_d} \mathbf{N}_p{}^T c_{T/B}\ \mathbf{N}_p\ d\Omega & \int_{\Gamma_d} \mathbf{N}_p{}^T c_{T/B}\ \widetilde{\mathbf{N}}_p^{(+)} \mathbb{M}_p\ d\Omega \\ \int_{\Gamma_d} \mathbb{M}_p{}^T \widetilde{\mathbf{N}}_p^{(+)T} c_{T/B}\ \mathbf{N}_p\ d\Omega & \int_{\Gamma_d} \mathbb{M}_p{}^T \widetilde{\mathbf{N}}_p{}^T c_{T/B}\ \widetilde{\mathbf{N}_p}^{(+)} \mathbb{M}_p\ d\Omega \end{bmatrix} \tag{63}$$

$$\mathbf{L}_{mf} = \begin{bmatrix} \int_{\Gamma_d} \mathbf{N}_p{}^T (c_T + c_B) \mathbf{N}_f\ d\Omega \\ \int_{\Gamma_d} \mathbb{M}_p{}^T \widetilde{\mathbf{N}}_p^{(+)T} c_T\ \mathbf{N}_f\ d\Omega + \int_{\Gamma_d} \mathbb{M}_p{}^T \widetilde{\mathbf{N}}_p^{(-)T} c_B\ \mathbf{N}_f\ d\Omega \end{bmatrix} \tag{64}$$

$$\mathbf{L}_f = \int_{\Gamma_d} \mathbf{N}_f{}^T (c_T + c_B) \mathbf{N}_f d\Gamma \tag{65}$$

$\mathbf{S}_m$ is the compressibility matrix of the porous medium,

$$\mathbf{S}_m = \begin{bmatrix} \int_{\Omega\backslash\Gamma_d} \mathbf{N}_p{}^T \frac{1}{M} \mathbf{N}_p d\Omega & \int_{\Omega\backslash\Gamma_d} \mathbf{N}_p{}^T \frac{1}{M} \widetilde{\mathbf{N}}_p \mathbb{M}_p d\Omega \\ \int_{\Omega\backslash\Gamma_d} \mathbb{M}_p{}^T \widetilde{\mathbf{N}}_p{}^T \frac{1}{M} \mathbf{N}_p d\Omega & \int_{\Omega\backslash\Gamma_d} \mathbb{M}_p{}^T \widetilde{\mathbf{N}}_p{}^T \frac{1}{M} \widetilde{\mathbf{N}}_p \mathbb{M}_p d\Omega \end{bmatrix} \tag{66}$$

$\mathbf{S}_f$ is the compressibility matrix of the discontinuity,

$$\mathbf{S}_f = \int_{\Gamma_d} \mathbf{N}_f{}^T \frac{w}{M_f} \mathbf{N}_f d\Gamma \tag{67}$$

$\mathbf{Q}$ is the hydromechanical coupling matrix of the porous medium,

$$\mathbf{Q}^{\mathrm{T}} = \begin{bmatrix} \int_{\Omega\backslash\Gamma_d} \mathbf{B}_u{}^T \mathbf{m}\, \alpha\, \mathbf{N}_p d\Omega & \int_{\Omega\backslash\Gamma_d} \mathbf{B}_u{}^T \mathbf{m}\, \alpha\, \widetilde{\mathbf{N}}_p \mathbb{M}_p d\Omega \\ \int_{\Omega\backslash\Gamma_d} \mathbb{M}_u{}^T \widetilde{\mathbf{B}}_u{}^T \mathbf{m}\, \alpha\, \mathbf{N}_p d\Omega & \int_{\Omega\backslash\Gamma_d} \mathbb{M}_u{}^T \widetilde{\mathbf{B}}_u{}^T \mathbf{m}\, \alpha\, \widetilde{\mathbf{N}}_p \mathbb{M}_p d\Omega \end{bmatrix} \tag{68}$$

$\mathbf{Q}_f$ and $\mathbf{E}_f$ are the hydromechanical coupling matrix of the discontinuity,

$$\mathbf{Q}_f{}^{\mathrm{T}} = \begin{bmatrix} 0_{n_d \times n_{pf}} \\ \int_{\Gamma_d} \mathbf{N}_d{}^T \alpha_f \mathbf{n}_d \mathbf{N}_f d\Gamma \end{bmatrix} \tag{69}$$

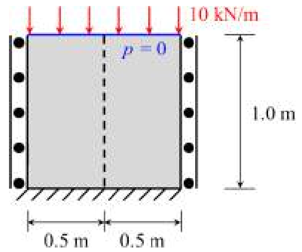

Fig. 6. Geometry and boundary conditions of consolidation in discontinuous block.

$$\mathbf{E}_f = \left[\int_{\Gamma_d} w \mathbf{N}_f{}^T \alpha_f \mathbf{r}_s \mathbf{B}_u d\Gamma \quad \int_{\Gamma_d} w \mathbf{N}_f{}^T \alpha_f \mathbf{r}_s \widetilde{\mathbf{B}}_u^m \mathbb{M}_u d\Gamma \right] \tag{70}$$

where n_d is the number of components of standard displacement DOFs $\mathbf{d}$.

Using a fully implicit time integration scheme and then linearizing the system results in

$$\begin{Bmatrix} \mathbf{r}_U \\ \mathbf{r}_P \\ \mathbf{r}_{P_f} \end{Bmatrix}_{n+1}^{i+1} = \mathbf{J}_{n+1}^{i+1} \begin{Bmatrix} \delta\mathbf{U} \\ \delta\mathbf{P} \\ \delta\mathbf{p}_f \end{Bmatrix}_{n+1}^{i+1} + \begin{Bmatrix} \mathbf{r}_U \\ \mathbf{r}_P \\ \mathbf{r}_{P_f} \end{Bmatrix}_{n+1}^{i} \tag{71}$$

with

$$\mathbf{J}_{n+1}^{i+1} = \begin{bmatrix} \mathbf{K} & -\mathbf{Q}^{\mathrm{T}} & -\mathbf{Q}_f{}^{\mathrm{T}} \\ \frac{1}{\Delta t}\mathbf{Q} & \frac{1}{\Delta t}\mathbf{S}_m + \mathbf{H}_m + \mathbf{L}_m & -\mathbf{L}_{mf} \\ \frac{1}{\Delta t}(\mathbf{Q}_f + \mathbf{E}_f) & -\mathbf{L}_{mf}{}^T & \frac{1}{\Delta t}\mathbf{S}_f + \mathbf{H}_f + \mathbf{L}_f \end{bmatrix} \tag{72}$$

where $\mathbf{K}$ is the tangent stiffness matrix:

$$\mathbf{K} = \begin{bmatrix} \int_{\Omega} \mathbf{B}_u{}^T \mathbf{D} \mathbf{B}_u d\Omega & \int_{\Omega} \mathbf{B}_u{}^T \mathbf{D} \mathbf{B}_u \mathbb{M}_u d\Omega \\ \int_{\Omega\backslash\Gamma_d} \mathbb{M}_u{}^T \widetilde{\mathbf{B}}_u{}^T \mathbf{D} \mathbf{B}_u d\Omega & \int_{\Omega\backslash\Gamma_d} \mathbb{M}_u{}^T \widetilde{\mathbf{B}}_u{}^T \mathbf{D} \widetilde{\mathbf{B}}_u \mathbb{M}_u d\Omega + \int_{\Gamma_d} \mathbf{N}_d{}^T \mathbf{R}_d{}^T \mathbf{T}_d \mathbf{R}_d \mathbf{N}_d d\Gamma \end{bmatrix} \tag{73}$$

The numerical integration of the matrices and vectors defined over the continuum porous media domain presented in eqs. (59) - (73) is performed by applying a sub-division of the element domain into triangular sub-domains, a common practice in XFEM (Khoei, 2015). This is required due to the presence of the Heaviside function in sub-matrices associated with the enrichment DOFs (Dias-da-Costa et al., 2009). The matrices and vectors defined over the discontinuity domain are integrated using a two-node trapezoidal rule (Dias-Da-Costa et al., 2010).

The enrichment DOFs $\Delta\mathbf{d}$, $\Delta\mathbf{p}$, and $\mathbf{p}_f$, are all considered global degrees of freedom. Therefore, they are not statically condensed.

4. Validation tests

The solution obtained with the embedded formulation here proposed is compared with that obtained using a discrete fracture model with triple-node interface elements implemented in the in-house computational framework GeMA (Mejia et al., 2020; Mendes et al., 2016; Rueda et al., 2020).

Despite the formulation being flexible and allowing different leak-off parameters at each side of the discontinuity, c_T and c_B, in the following examples, they are assumed to have the same value c, and are referred to as the leak-off parameter.

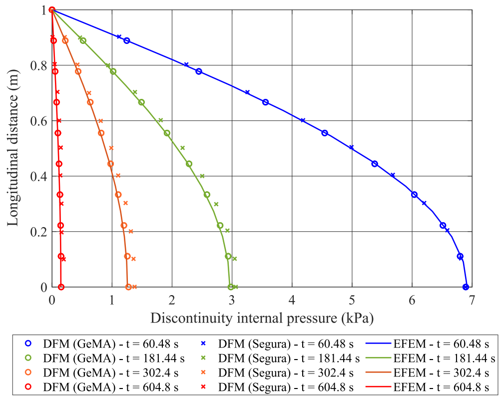

Fig. 7. Pore-pressure profile at the discontinuity mid-plane for different times.

4.1. Consolidation of a block crossed by a discontinuity

Segura and Carol initially solved this consolidation problem (Segura and Carol, 2008) using fully coupled HM interface elements. The geometry and boundary conditions are summarized in Fig. 6. The displacement jumps in the discontinuity are fixed for comparison with the reference solution. The model properties are Young's modulus of 1.0 MPa, Poisson's ratio of 0.3, normal cohesive stiffness of 2.0e04 kPa/m, shear cohesive stiffness of 1.0e03 kPa/m, discontinuity opening of 2.4038e-04 m, hydraulic conductivity of 1.1574e-05 m/s, fluid dynamic viscosity of 1.0e-06 kPa s, and leak-off parameters of 1.0 m/(kPa s).

The domain was discretized with a regular finite element mesh of 11 x 11 linear quadrilaterals. A transient analysis was performed with a fixed time step of 0.5 s.

Fig. 7 presents the EFEM results for the pore pressure profile at the discontinuity mid-plane at different times. It also includes the solutions proposed by Segura and Carol (Segura and Carol, 2008).

The numerical results show that the EFEM captures the influence of the discontinuity in the consolidation process and demonstrates good agreement with the solution obtained using the DFM, as illustrated in Fig. 7.

4.2. Consolidation of a block with an inclined internal discontinuity

This benchmark is inspired by the model proposed by Lamb et al. (2013) using XFEM and considering permeable and cohesionless discontinuities. Here, the problem is adapted considering a stress-dependent discontinuity crossing the domain. The influence of the discontinuity on transversal flow is investigated. The discontinuity longitudinal permeability, Eq. (37), is updated during the analysis.

The geometry and boundary conditions are presented in Fig. 8(a). The nodal displacement jump in the x-direction at the lateral borders is zero. The finite element mesh of the DFM used for validation is presented in Fig. 8(b), which has 2703 nodes, 2500 linear quadrilateral finite elements, and 50 triple-node interface elements (Nguyen et al., 2017; Rueda et al., 2020).

The mechanical properties are Young's modulus of 40.0 MPa and Poisson ratio of 0.3. The discontinuity cohesive material is elastic with normal and shear cohesive stiffness of 5.0e03 kPa/m and an initial opening of 1.063e-03 m. The hydraulic conductivity is 1.0e−08 m/s, the fluid dynamic viscosity is 1.0e−06 kPa·s, the compressibility of both the fluid and the solid grains are neglected.

The domain was discretized with a structured mesh of 50 × 50 linear quadrilateral finite elements. A transient analysis was performed during 100 days, using a fixed time-step of 1 day.

Fig. 9 shows the pressure evolution over time at the node with coordinates (0.0,8.0) for EFEM and DFM models considering two leak-off parameter values, a high leak-off, $c = 1.0$ m/(kPa s), and a low leak-off, $c = 1.0e{-}15$ m/(kPa s). The result for a model without discontinuity is

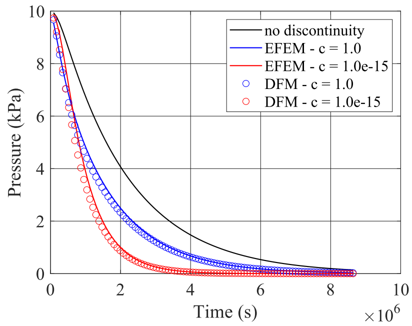

Fig. 9. Pressure evolution over time at the left bottom node.

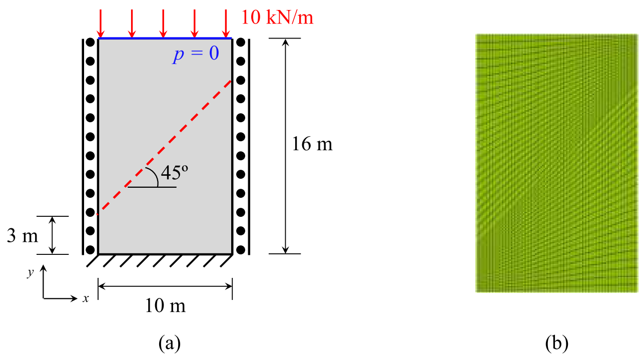

Fig. 8. Consolidation of a block with inclined discontinuity (a) Geometry and boundary conditions (Adapted from Lamb et al. (2013), (b) Finite element mesh used in the DFM.

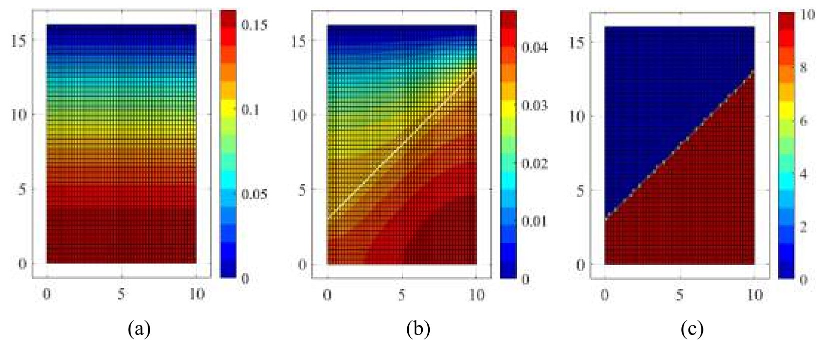

Fig. 10. EFEM model pressure field (kPa) for (a) domain without discontinuity, (b) and (c) block with inclined discontinuity with $c = 1.0$ and $c = 1.0\text{e}{-15}$ m/(kPa s), respectively.

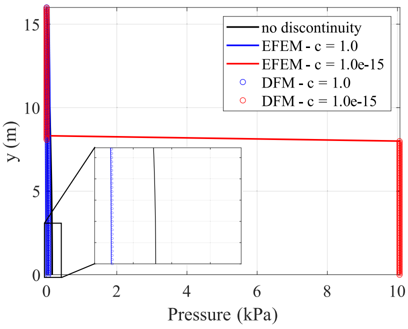

Fig. 11. Pressure profile along at $x = 5$.

also shown for comparison.

The results in Fig. 9 show good agreement between the EFEM and the DFM solutions, and how the discontinuity can affect the consolidation process. The discontinuity with a high leak-off parameter acts as a preferential path for fluid flow, allowing the pressure to decrease at a higher rate than the model without discontinuity. On the other hand, the discontinuity with a low leak-off parameter acts as a barrier for transversal fluid flow through the porous media. In this case, the pressure drop happens at an even higher rate. To better understand the influence of the discontinuity leak-off parameters over the pressure distribution, Fig. 10 shows the pressure field for the models without and with the discontinuity using EFEM, and Fig. 11 shows their pressure profile along the y-coordinate at $x = 5$ m. The values correspond to the final time step.

Fig. 10 shows how the discontinuity with different values of leak-off parameter influences the pressure distribution. In Fig. 10(b) a preferential path of fluid flow can be observed, following the direction of the discontinuity. In Fig. 10(c), since the discontinuity is acting as a barrier for the fluid flow, the pressure field on the bottom part of the domain does not dissipate.

Fig. 11 allows visualizing the pressure jump across the discontinuity for the low leak-off parameter scenario.

The influence of the discontinuity with different leak-off values on the displacement field is also analyzed, and the profiles along the y-coordinate at $x = 5$ m are shown in Fig. 12.

Fig. 12 shows that the discontinuity significantly impacts the displacement field components and that it is strongly affected by the leak-off parameter. The results showed an excellent agreement with the solutions from the DFM.

The cohesive stresses along the discontinuity are compared with solutions using a DFM (see Fig. 13). The results show spurious oscillations on the cohesive stresses along the discontinuity using the EFEM. The literature reports this behavior in association with XFEM, occurring when the discontinuity runs skewed to the mesh (Crusat et al., 2019; Moës et al., 2006; Sanders et al., 2009). Since the EFEM, as presented here, can be seen as a particular case of XFEM, it is assumed that the

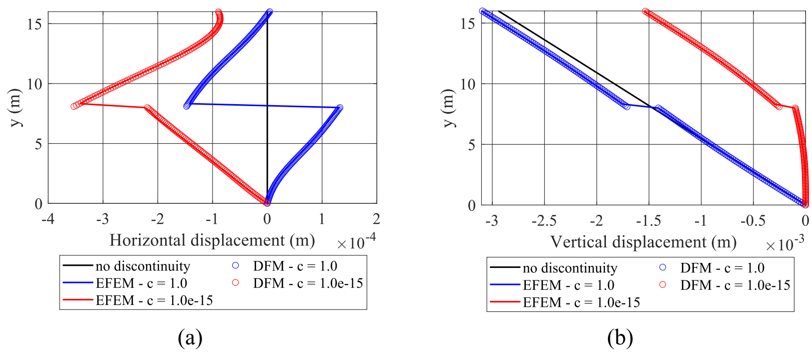

Fig. 12. Displacement along the y-coordinate at $x = 5$: (a) horizontal and (b) vertical components.

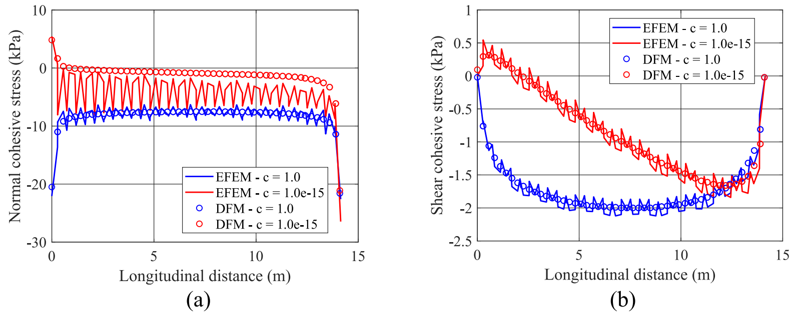

Fig. 13. Cohesive stresses along the fault: (a) normal cohesive stress and (b) shear cohesive stress.

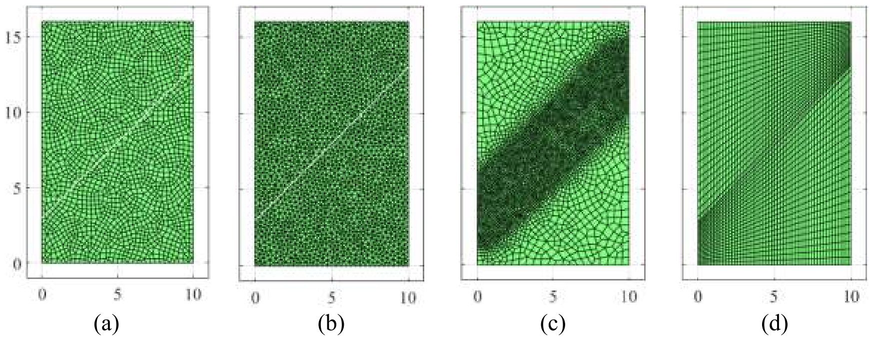

Fig. 14. Model discretization (a) uniform unstructured quadrilateral mesh (USQ), (b) uniform unstructured triangular mesh (UST), (c) unstructured quadrilateral mesh with refinement close to the discontinuity (USQR), (d) structured aligned with the discontinuity (SA50).

causes of the oscillations are the same. Despite these spurious oscillations in the cohesive stresses, the results of the displacement and pressure fields agree well with the solutions obtained with a DFM.

Finally, to analyze the effect of spatial discretization, the consolidation problem with a low leak-off parameter was solved using six different finite element meshes: two regular structured meshes with different levels of refinement, 50 × 50 (S50) and 100 × 100 (S100); one uniform unstructured quadrilateral mesh (USQ); one uniform unstructured triangular mesh (UST); one unstructured mesh refined at the region close to the discontinuity (USQR); and one non-regular 50 × 50 structured mesh that aligns to the discontinuity (SA50). Fig. 14 presents the non-uniform and unstructured meshes.

Fig. 15 presents the results for the displacements, cohesive stresses, and pressure for the six finite element meshes.

From the displacement (Fig. 15 (a) and (b)) and pressure (Fig. 15 (e)) profiles along $x = 5$ m and the pressure evolution over time (Fig. 15 (f)), the results show that they are not mesh-dependent. Meanwhile, the adopted mesh can strongly affect the cohesive stresses along the discontinuity. The unstructured mesh with triangular elements reported major spurious oscillations. This is expected since linear triangular finite elements have a constant strain and stress field and, hence, a poorer representation. The oscillations in the cohesive shear stresses tend to reduce with mesh refinement. However, the cohesive normal stresses for the unstructured quadrilateral mesh with a high refinement close to the discontinuity still presented high oscillations at some points. The points of higher oscillations occur when the discontinuity crosses the finite element very close to one of its vertices. Finally, the oscillations are eliminated with the use of a mesh that is aligned with the discontinuity.

5. Fault reactivation problem

The fault reactivation problem analyzed here is based on the one studied by Cappa and Rutqvist (2011). The geometry, boundary conditions and DFM mesh are presented in Fig. 16. It consists of a reservoir sealed by two caprock layers crossed by a fault. The fluid is injected with a volumetric discharge of 2.0e-5 m^3/s. The nodal displacements and pressure jumps at the bottom edge of the model are zero. The origin of the cartesian system is located at the left bottom node of the model, as indicated in Fig. 16. The initial pressure at the top of the reservoir corresponds to a water level located at $y = 2500$ m, and an atmospheric pressure of 100 kPa acts at the ground surface.

All layers have the following common properties: Young's modulus of 10 GPa, Poisson's ratio of 0.25, fluid dynamic viscosity of 5.98e-7 kPa.s, fluid bulk modulus of 2.2e6 kPa, Biot coefficient of 1, saturated rock specific weight of 22.6 kPa/m, water specific weight of 10 kPa/m, and incompressible solid grains. Other parameters adopted for each layer are summarized in Table 1.

To avoid numerical instabilities due to the very low permeability of the caprock layers, the pressure degrees of freedom of the elements located internally in the caprock layers are fixed at the hydrostatic value.

The fault segment in the aquifers is taken as elastic, and in the reservoir and caprock layers as elastoplastic, following the Mohr-Coulomb criterion with tension cut-off. The normal and shear stiffnesses are 5.0e9 kPa/m, the initial opening is 1.0e-7 m, the friction angle is 25°, the dilatancy angle is 20°, and the cohesion and the tensile strength are zero.

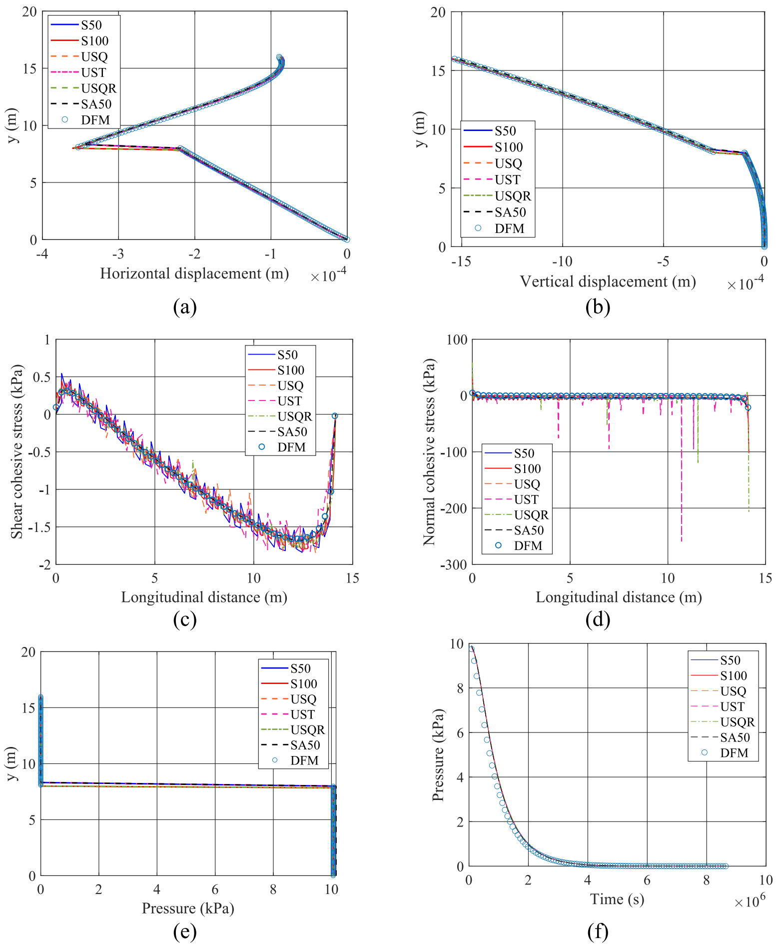

Fig. 15. Results of the consolidation problem using different meshes: (a) horizontal displacement profile at $x = 5$ m, (b) vertical displacement profile at $x = 5$ m, (c) shear cohesive stress along the discontinuity, (d) normal cohesive stress along the discontinuity, (e) pressure profile at $x = 5$ m, (f) pressure at the right bottom node over time.

D. Cavalcanti et al. Computers and Geotechnics 172 (2024) 106427

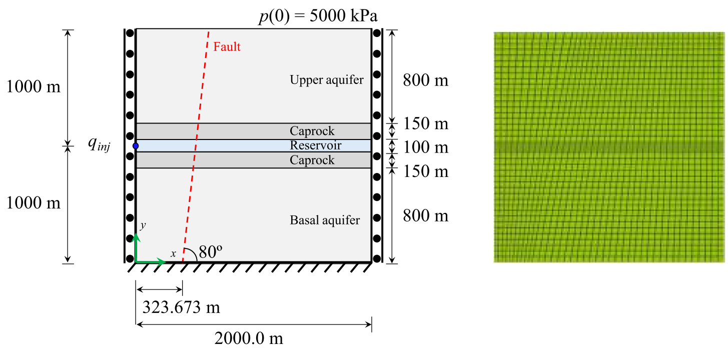

(a) (b)

Fig. 16. Fault reactivation problem: (a) Geometry and boundary conditions (adapted from Cappa and Rutqvist (2011); (b) DFM mesh.

Table 1
Hydraulic properties of each layer.

Properties	Basal aquifer	Caprock	Reservoir	Upper aquifer
Intrinsic permeability (m^2)	1.0e−16	1.0e−19	1.0e−13	1.0e−14
Porosity	0.01	0.01	0.1	0.01

The pore-pressure field is initialized with a hydrostatic gradient of 10.0 kPa/m, and the vertical effective stress is initialized considering the self-weight with a resultant gradient of 12.6 kPa/m, as shown in Fig. 17. The horizontal effective stresses are initialized by $\sigma'_x = K_0\,\sigma'_y$, with K_0 being the Earth-pressure coefficient.

The initial cohesive stresses along the discontinuity are computed by rotating the stress vector following the direction of the discontinuity:

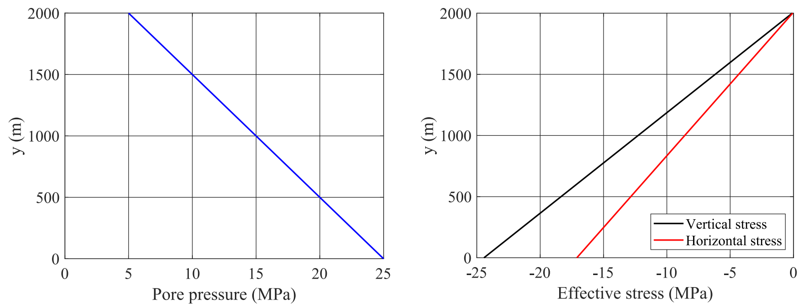

(a) (b)

Fig. 17. Initial conditions for the fault reactivation problem: (a) Pore-pressure; (b) Effective stresses.

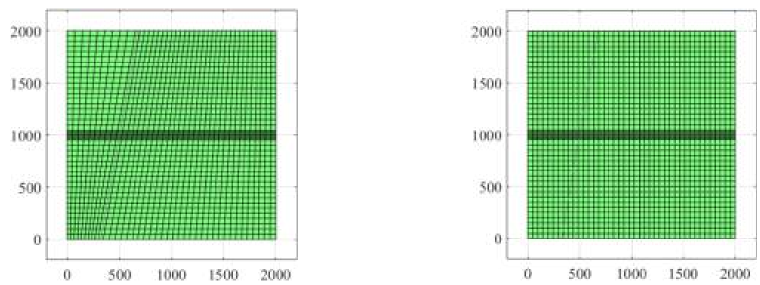

(a) (b)

Fig. 18. Mesh discretization with (a) aligned structured, (b) regular structured, and (c) refined regular structured mesh used in the EFEM.

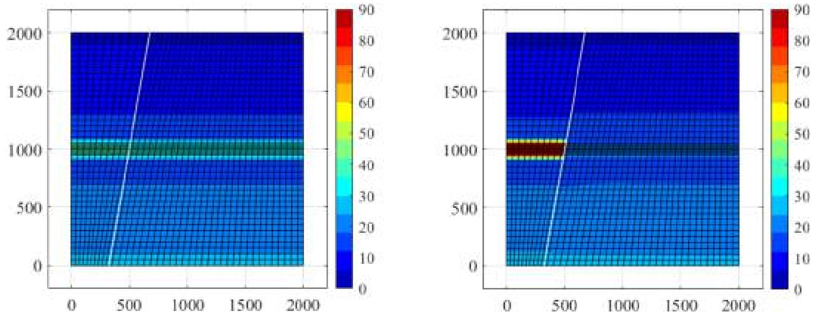

(a) (b)

Fig. 19. Pressure field, in MPa, with (a) $c = 1.0\text{e}{-9}$ m/(kPa s) and (b) $c = 1.0\text{e}{-12}$ m/(kPa s).

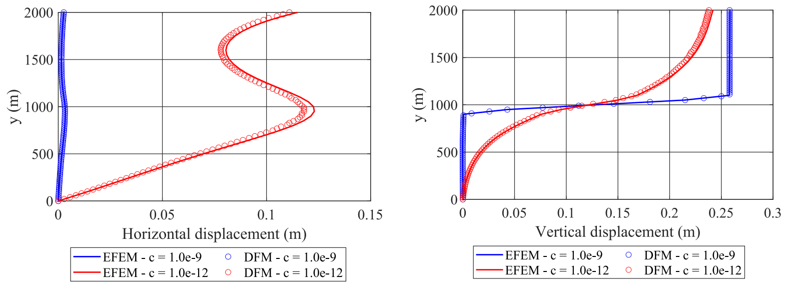

(a) (b)

Fig. 20. Displacement along the y-coordinate at $x = 1000$ m: (a) horizontal and (b) vertical components.

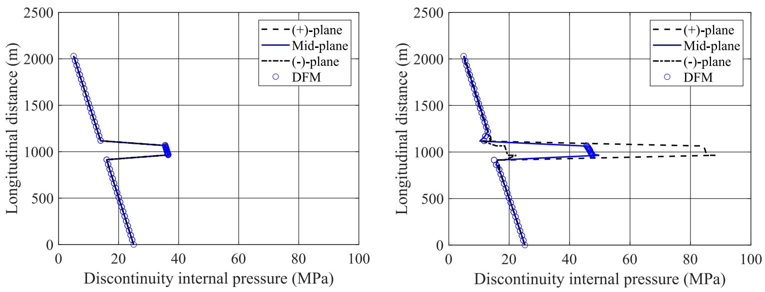

(a) (b)

Fig. 21. Fault internal pressure in comparison with the pore pressure at the adjacent faces of the fault for leak-off: (a) 1.0e−9 and (b) 1.0e−12 m/(kPa s).

$$\begin{Bmatrix} t_s' \\ t_n' \end{Bmatrix} = \begin{bmatrix} -\sin\alpha\cos\alpha & \sin\alpha\cos\alpha \\ \sin^2\alpha & \cos^2\alpha \end{bmatrix} \begin{Bmatrix} K_0\,\sigma_y' \\ \sigma_y' \end{Bmatrix} \tag{74}$$

Appendix A presents how these initial conditions are incorporated into the numerical model

A simulation was performed for 365 days. The initial time step is 1000 s and is adapted during the analysis limited by a maximum value of 1 day. Two finite element meshes are tested, one structured aligned with the discontinuity and one regular structured, as shown in Fig. 18.

The problem is solved with two values for the leak-off parameter, 1.0e-9 and 1.0e-12 m/(kPa s). Fig. 19 shows the pressure field at the end of the analysis using EFEM with the aligned mesh, presented in Fig. 18 (a).

First, results using EFEM with the aligned mesh, presented in Fig. 18 (a), are compared with those using the DFM. The displacement profiles along the y-coordinate at $x = 1000$ m are shown in Fig. 20 for two leak-off parameters, 1.0e-9 and 1.0e-12 m/(kPa s). The results show a good agreement between the EFEM and DFM solutions, and it evidence that the change in the leak-off parameter strongly affects the displacement field.

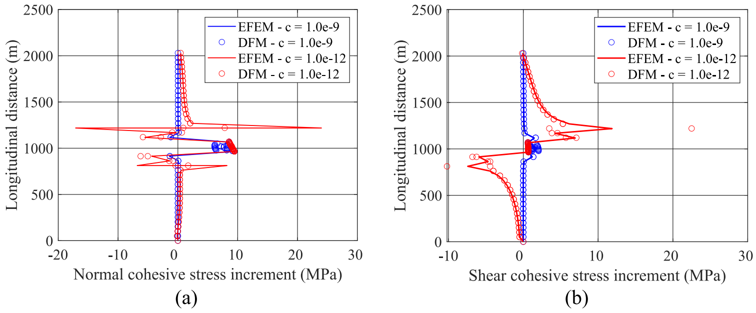

Fig. 22. Comparison of (a) the normal and (b) the shear stresses along the fault at the end of the simulation.

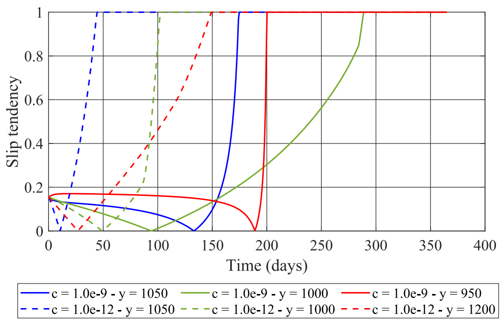

Fig. 23. Slip tendency evolution using EFEM with the aligned mesh.

Fig. 21 shows the fault internal pressure along its length in comparison with the pressure at the fault adjacent faces. The results show that EFEM captured a similar pressure build-up as the DFM, for both values of leak-off parameter.

Fig. 21 (a) shows that for the higher leak-off parameter, 1.0e- 9 m/(kPa s), the pore pressure inside and at the fault adjacent planes are approximately the same. However, for a lower leak-off parameter, 1.0e-12 m/(kPa s), the results show that there is a pressure jump across the fault and the internal pressure is an intermediate value concerning the pressure in the adjacent planes. Hosseini et al. (2023) and Jha and Juanes (2014) discuss that to be closer to safety in assessing fault reactivation, the pore pressure inside the discontinuity should be imposed as the maximum value regarding the adjacent planes. This could be accomplished through the present embedded formulation by imposing a constraint on the definition of the pressure field inside the discontinuity.

The increments in the cohesive stresses for the two leak-off parameters at the end of the analysis are presented in Fig. 22. The results show that the normal cohesive stress increment is higher for the lower leak-off parameter, which is related to a higher pore-pressure build-up observed in Fig. 21. Higher shear cohesive stresses at the layers outside the reservoir are also observed for a lower leak-off value.

To assess the fault reactivation, as performed by Quevedo et al. (2017), a slip tendency (*ST*) parameter, Eq. (75), was evaluated at three points along the fault. The results are shown in Fig. 23. The points of the fault are labeled based on their *y*-coordinate.

$$ST = \frac{|t_s|}{t_N \tan\phi + c} \tag{75}$$

Fig. 23 shows that the leak-off parameter strongly influences the reactivation of the fault. For a lower leak-off parameter, since there is a higher pore-pressure build-up, the reactivation happens earlier. It also shows that the first point in the reservoir, in both cases, to reactivate is the one located at the edge with the upper caprock layer.

Finally, the influence of the mesh in EFEM is evaluated by comparing the cohesive stress increments and the slip tendency parameter evolution along the fault for the two meshes shown in Fig. 18, for a leak-off parameter of 1.0e-9 m/(kPa s). The results in Fig. 25 show that the spurious oscillations in the cohesive stresses along the fault, observed in

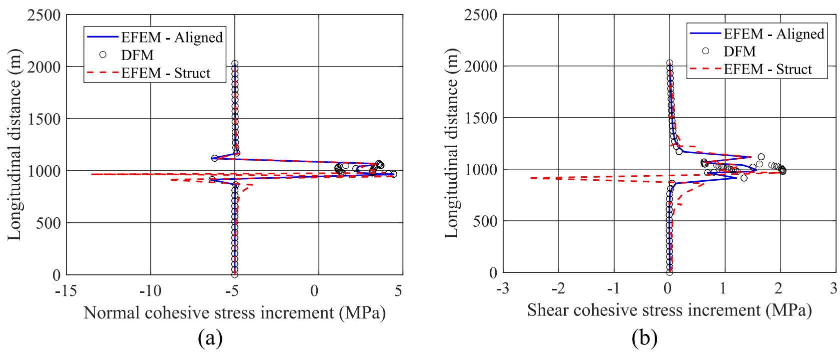

Fig. 24. (a) Normal and (b) shear cohesive stresses along the fault with EFEM and $c = 1.0\text{e}{-9}$ m/(kPa s).

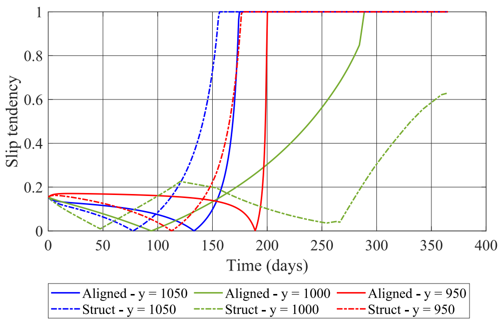

Fig. 25. Slip tendency parameter evolution for a fault with c = 1.0e-9 m/(kPa s).

Fig. 24 and discussed in the previous example, impact the fault reactivation analysis. Given that an elastoplastic cohesive model is used, for a same mesh discretization, the spurious oscillations in the cohesive stresses can indicate that the fault is pre-maturely reactivated. We have observed, by performing further tests, that using furtther refined meshes reduces this problem.

6. Conclusions

This paper presented a fully coupled embedded finite element method (EFEM) capable of modeling discontinuities that act as both preferential paths or barriers for fluid flow in permeable porous media. The coupling between the porous media and the discontinuity is achieved by deriving the weak form of the governing equations and the constitutive model.

The results obtained with the proposed EFEM were successfully verified using a discrete fracture finite element model with triple-node interface elements and were in good agreement with the reference solution.

This work also discussed the spurious oscillations of the cohesive stresses along the discontinuities associated with the mesh discretization when using the EFEM. These oscillations depend on the finite element mesh, happening when the discontinuity crosses the finite element close to one of its vertices. This issue is well reported in the XFEM literature but not that much in the EFEM one. We observed that these oscillations did not affect the global behavior of the model when the cohesive material is linear elastic.

Finally, the proposed EFEM was used to model fault reactivation problems, capturing the principal reactivation mechanisms. The results show that the spurious oscillations in the cohesive stresses can affect the evaluation of the fault reactivation since in this problem it was adopted an elastoplastic cohesive material model. The authors observed that this problem can be mitigated by using more refined meshes, but will further investigate ways to completely avoid it in future works.

CRediT authorship contribution statement

Danilo Cavalcanti: . **Cristian Mejia:** . **Deane Roehl:** Writing – review & editing, Supervision, Project administration, Methodology, Funding acquisition, Formal analysis, Conceptualization. **Ignasi de-Pouplana:** . **Eugenio Oñate:** Writing – review & editing, Supervision, Project administration, Funding acquisition.

Declaration of competing interest

The authors declare that they have no known competing financial interests or personal relationships that could have appeared to influence the work reported in this paper.

Data availability

Data will be made available on request.

Acknowledgments

The authors acknowledge the financial support from the Brazilian National Council for Scientific and Technological Development (CNPq) Grants 309384/2019-2 and 308056/2022-1; Carlos Chagas Filho Foundation for Supporting Research in the State of Rio de Janeiro (FAPERJ) Grants E-26/200.463/2023 and E-26/201.391/2021; the grant TED2021-130510A-I00 funded by MCIN/AEI/10.13039/501100011033 and by the "European Union NextGenerationEU/PRTR"; and the Severo Ochoa Programme through the Grant CEX2018-000797-S funded by MCIN/AEI/10.13039/501100011033. This study was financed in part by the Coordenação de Aperfeiçoamento de Pessoal de Nível Superior - Brasil (CAPES) - Finance Code 001.

Appendix A. Geostatic state

The initial stress state and hydrostatic pressure are defined in transient analysis by adding the geostatic contribution to the external solicitation vectors $\mathbf{F}_U^{ext}(t)$, $\mathbf{F}_P^{ext}(t)$ and $\mathbf{F}_{p_f}^{ext}(t)$. The vector associated with the displacement degrees of freedom is computed as:

$$\mathbf{F}_U^{Geo} = \left\{ \begin{array}{c} \int_\Omega \mathbf{B}_u{}^T(\boldsymbol{\sigma}' - \alpha\,\mathbf{m}\,p)d\Omega \\ \int_{\Omega\backslash\Gamma_d} \mathbb{M}_u{}^T \widetilde{\mathbf{B}}_u{}^T(\boldsymbol{\sigma}' - \alpha\,\mathbf{m}\,p)d\Omega + \int_{\Gamma_d} \mathbf{N}_d{}^T\mathbf{R}_d{}^T\left(\mathbf{t}_d' - \alpha_f\,\mathbf{n}_d\,p_f\right)d\Gamma \end{array} \right\} \tag{76}$$

with $\boldsymbol{\sigma}'$ and $\mathbf{t}_d'$ being the initial stress and cohesive stress tensors, respectively, and the pressures p and p_f correspond to the initial hydrostatic state.

The vectors associated with the pressure DOFs are:

$$\mathbf{F}_P^{Geo} = (\mathbf{H}_m + \mathbf{L}_m)\mathbf{P} - \mathbf{L}_{mf}\ \mathbf{p}_f \tag{77}$$

$$\mathbf{F}_{p_f}^{Geo} = -\mathbf{L}_{mf}\ \mathbf{P} + \left(\mathbf{H}_f + \mathbf{L}_f\right)\mathbf{p}_f \tag{78}$$

References

Abreu, R., Mejia, C., Roehl, D., 2022. A comprehensive implicit substepping integration scheme for multisurface plasticity. Int. J. Numer. Methods Eng. 123, 5–40. https://doi.org/10.1002/nme.6826.

Armero, F., Callari, C., 1999. An analysis of strong discontinuities in a saturated poro-plastic solid. Int. J. Numer. Methods Eng. 46, 1673–1698. https://doi.org/10.1002/(SICI)1097-0207(19991210)46:10<1673::AID-NME719>3.0.CO;2-S.

Belytschko, T., Moës, N., Usui, S., Parimi, C., 2001. Arbitrary discontinuities in finite elements. Int. J. Numer. Meth. Engng. 50, 993–1013. https://doi.org/10.1002/1097-0207(20010210)50:4<993::AID-NME164>3.0.CO;2-M.

Benkemoun, N., Gelet, R., Roubin, E., Colliat, J.B., 2015. Poroelastic two-phase material modeling: theoretical formulation and embedded finite element method implementation. Int. J. Numer. Anal. Methods Geomech. 39, 1255–1275. https://doi.org/10.1002/nag.2351.

Berre, I., Doster, F., Keilegavlen, E., 2019. Flow in fractured porous media: a review of conceptual models and discretization approaches. Transp. Porous Media. 130, 215–236. https://doi.org/10.1007/s11242-018-1171-6.

Biot, M.A., Blot, M.A., 1941. General theory of three dimensional consolidation general theory of three-dimensional consolidation. J. Appl. Phys. 12, 155–164. https://doi.org/10.1115/1.4011606.

Biot, M.A., Willis, D.G., 1957. The elastic coefficients of the theory of consolidation. J. Appl. Mech. 24, 594–601. https://doi.org/10.1115/1.4011606.

Bitencourt, L.A.G., Manzoli, O.L., Prazeres, P.G.C., Rodrigues, E.A., Bittencourt, T.N., 2015. A coupling technique for non-matching finite element meshes. Comput. Methods Appl. Mech. Eng. 290, 19–44. https://doi.org/10.1016/j.cma.2015.02.025.

Bybordiani, M., Dias-da-Costa, D., 2021. A consistent finite element approach for dynamic crack propagation with explicit time integration. Comput. Methods Appl. Mech. Eng. 376 https://doi.org/10.1016/j.cma.2020.113652.

Callari, C., 2004. Coupled numerical analysis of strain localization induced by shallow tunnels in saturated soils. Comput. Geotech. 31, 193–207. https://doi.org/10.1016/j.compgeo.2004.01.004.

Callari, C., Armero, F., Abati, A., 2010. Strong discontinuities in partially saturated poroplastic solids. Comput. Methods Appl. Mech. Eng. 199, 1513–1535. https://doi.org/10.1016/j.cma.2010.01.002.

Cappa, F., Rutqvist, J., 2011. Modeling of coupled deformation and permeability evolution during fault reactivation induced by deep underground injection of CO2. Int. J. Greenh. Gas Control. 5, 336–346. https://doi.org/10.1016/j.ijggc.2010.08.005.

Cavalcanti, D., Mejia, C., Roehl, D., De-Pouplana, I., Casas, G., Martha, L.F., 2024. Embedded finite element formulation for fluid flow in fractured porous media. Comput. Geotech. 171 https://doi.org/10.1016/j.compgeo.2024.106384.

Cazes, F., Meschke, G., Zhou, M.M., 2016. Strong discontinuity approaches: an algorithm for robust performance and comparative assessment of accuracy. Int. J. Solids Struct. 96, 355–379. https://doi.org/10.1016/j.ijsolstr.2016.05.016.

Cervera, M., Barbat, G.B., Chiumenti, M., Wu, J.Y., 2022. A comparative review of XFEM, mixed FEM and phase-field models for quasi-brittle cracking. Arch. Comput. Methods Eng. 29, 1009–1083. https://doi.org/10.1007/s11831-021-09604-8.

Chan, A.W., Zoback, M.D., 2007. The role of hydrocarbon production on land subsidence and fault reactivation in the Louisiana coastal zone. J. Coast. Res. 23, 771–786. https://doi.org/10.2112/05-0553.

Crusat, L., Carol, I., Garolera, D., 2019. XFEM formulation with sub-interpolation, and equivalence to zero-thickness interface elements. Int. J. Numer. Anal. Methods Geomech. 43, 45–76. https://doi.org/10.1002/nag.2853.

Cruz, F., Roehl, D., Vargas, E. do A., 2018. An XFEM element to model intersections between hydraulic and natural fractures in porous rocks. Int. J. Rock Mech. Min. Sci. 112, 385–397. https://doi.org/10.1016/j.ijrmms.2018.10.001.

Cruz, F., Roehl, D., Vargas, E. do A., 2019. An XFEM implementation in Abaqus to model intersections between fractures in porous rocks. Comput. Geotech. 112, 135–146. https://doi.org/10.1016/j.compgeo.2019.04.014.

Damirchi, B.V., Carvalho, M.R., Bitencourt, L.A.G., Manzoli, O.L., Dias-da-Costa, D., 2021. Transverse and longitudinal fluid flow modelling in fractured porous media with non-matching meshes. Int. J. Numer. Anal. Methods Geomech. 45, 83–107. https://doi.org/10.1002/nag.3147.

Damirchi, B.V., Bitencourt, L.A.G., Manzoli, O.L., Dias-da-Costa, D., 2022. Coupled hydro-mechanical modelling of saturated fractured porous media with unified embedded finite element discretisations. Comput. Methods Appl. Mech. Eng. 393 https://doi.org/10.1016/j.cma.2022.114804.

Day, R.A., Potts, D.M., 1994. Zero thickness interface elements—numerical stability and application. Int. J. Numer. Anal. Methods Geomech. 18, 689–708. https://doi.org/10.1002/nag.1610181003.

De Borst, R., Réthoré, J., Abellan, M.A., 2006. A numerical approach for arbitrary cracks in a fluid-saturated medium. Arch. Appl. Mech. 75, 595–606. https://doi.org/10.1007/s00419-006-0023-y.

de-Pouplana, I., Oñate, E., 2018. Finite element modelling of fracture propagation in saturated media using quasi-zero-thickness interface elements. Comput. Geotech. 96, 103–117. https://doi.org/10.1016/j.compgeo.2017.10.016.

Dias-da-Costa, D., Alfaiate, J., Sluys, L.J., Júlio, E., 2009. A discrete strong discontinuity approach. Eng. Fract. Mech. 76, 1176–1201. https://doi.org/10.1016/j.engfracmech.2009.01.011.

Dias-da-Costa, D., Alfaiate, J., Sluys, L.J., Júlio, E., 2009. Towards a generalization of a discrete strong discontinuity approach. Comput. Methods Appl. Mech. Eng. 198, 3670–3681. https://doi.org/10.1016/j.cma.2009.07.013.

Dias-Da-Costa, D., Alfaiate, J., Sluys, L.J., Júlio, E., 2010. A comparative study on the modelling of discontinuous fracture by means of enriched nodal and element techniques and interface elements. Int. J. Fract. 161, 97–119. https://doi.org/10.1007/s10704-009-9432-6.

Fadakar, Y., Alghalandis, Adfne, 2017. Open source software for discrete fracture network engineering, two and three dimensional applications. Comput. Geosci. 102, 1–11. https://doi.org/10.1016/j.cageo.2017.02.002.

Hosseini, N., Khoei, A.R., 2020. Numerical simulation of proppant transport and tip screen-out in hydraulic fracturing with the extended finite element method. Int. J. Rock Mech. Min. Sci. 128, 104247 https://doi.org/10.1016/j.ijrmms.2020.104247.

Hosseini, N., Priest, J.A., Eaton, D.W., 2023. Extended-FEM analysis of injection-induced slip on a fault with rate-and-state friction: insights into parameters that control induced seismicity. Rock Mech. Rock Eng. 56, 4229–4250. https://doi.org/10.1007/s00603-023-03283-6.

Intergovernmental Panel on Climate Change, Climate Change 2021 – The Physical Science Basis, 2021. https://doi.org/10.1017/9781009157896.

Jha, B., Juanes, R., 2014. Coupled modeling of multiphase flow and fault poromechanics during geologic CO2 storage. Energy Proc. 63, 3313–3329. https://doi.org/10.1016/j.egypro.2014.11.360.

Jing, L., 2003. A review of techniques, advances and outstanding issues in numerical modelling for rock mechanics and rock engineering. Int. J. Rock Mech. Min. Sci. 40, 283–353. https://doi.org/10.1016/S1365-1609(03)00013-3.

Jirásek, M., 2000. Comparative study on finite elements with embedded discontinuities. Comput. Methods Appl. Mech. Eng. 188, 307–330. https://doi.org/10.1016/S0045-7825(99)00154-1.

Khoei, A.R., 2015. Extended Finite Element Method: Theory and Applications. John Wiley and Sons.

Khoei, A.R., Hirmand, M., Vahab, M., Bazargan, M., 2015. An enriched FEM technique for modeling hydraulically driven cohesive fracture propagation in impermeable media with frictional natural faults: numerical and experimental investigations. Int. J. Numer. Methods Eng. 104, 439–468. https://doi.org/10.1002/nme.4944.

Khoei, A.R., Vahab, M., Hirmand, M., 2016. Modeling the interaction between fluid-driven fracture and natural fault using an enriched-FEM technique. Int. J. Fract. 197, 1–24. https://doi.org/10.1007/s10704-015-0051-0.

Khoei, A.R., Vahab, M., Hirmand, M., 2018. An enriched–FEM technique for numerical simulation of interacting discontinuities in naturally fractured porous media. Comput. Methods Appl. Mech. Eng. 331, 197–231. https://doi.org/10.1016/j.cma.2017.11.016.

Lamb, A.R., Gorman, G.J., Elsworth, D., 2013. A fracture mapping and extended finite element scheme for coupled deformation and fluid flow in fractured porous media. Int. J. Numer. Anal. Methods Geomech. 37, 2916–2936. https://doi.org/10.1002/nag.2168.

Larsson, R., Runesson, K., Sture, S., 1996. Embedded localization band in undrained soil based on regularized strong discontinuity - theory and fe-analysis. Int. J. Solids Struct. 33, 3081–3101.

Lima, P., Shauer, N., Villegas, J.B., Devloo, P.R.B., 2023. DFNMesh: Finite element meshing for discrete fracture matrix models. Adv. Eng. Softw. 186, 103545 https://doi.org/10.1016/j.advengsoft.2023.103545.

Linder, C., Armero, F., 2007. Finite elements with embedded strong discontinuities for the modeling of failure in solids. Int. J. Numer. Methods Eng. 72, 1391–1433. https://doi.org/10.1002/nme.2042.

Liu, D., 2020. A numerical method for analyzing fault slip tendency under fluid injection with XFEM. Acta Geotech. 15, 325–345. https://doi.org/10.1007/s11440-019-00814-w.

Lu, M., Zhang, H., Zheng, Y., Zhang, L., 2017. A multiscale finite element method for the localization analysis of homogeneous and heterogeneous saturated porous media with embedded strong discontinuity model. Int. J. Numer. Methods Eng. 112, 1439–1472. https://doi.org/10.1002/nme.5564.

Mejia, C., Paullo Muñoz, L.F., Roehl, D., 2020. Discrete fracture propagation analysis using a robust combined continuation method. Int. J. Solids Struct. 193–194, 405–417. https://doi.org/10.1016/J.IJSOLSTR.2020.02.002.

Mendes, C.A.T., Gattass, M., Roehl, D., 2016. The GeMA framework - An innovative framework for the development of multiphysics and multiscale simulations. ECCOMAS Congr. 2016 - Proc. 7th Eur. Congr. Comput. Methods Appl. Sci. Eng. 4, 7886–7894. https://doi.org/10.7712/100016.2383.6771.

Metz, B., Davidson, O., de Coninck, H., Loos, M., Meyer, L., 2005. IPCC special report on carbon dioxide capture and storage, New York. https://doi.org/10.3866/pku.dxhx202208007.

Moës, N., Béchet, E., Tourbier, M., 2006. Imposing Dirichlet boundary conditions in the extended finite element method. Int. J. Numer. Methods Eng. 67, 1641–1669. https://doi.org/10.1002/nme.1675.

Nguyen, V.P., Lian, H., Rabczuk, T., Bordas, S., 2017. Modelling hydraulic fractures in porous media using flow cohesive interface elements. Eng. Geol. 225, 68–82. https://doi.org/10.1016/j.enggeo.2017.04.010.

Oliver, J., 1996. Modelling strong discontinuities in solid mechanics via strain softening constitutive equations. Part 2: Numerical simulation. Int. J. Numer. Methods Eng. 39, 3601–3623.

Pan, P., Wu, Z., Feng, X., Yan, F., 2016. Geomechanical modeling of CO2 geological storage: a review. J. Rock Mech. Geotech. Eng. 8, 936–947. https://doi.org/10.1016/j.jrmge.2016.10.002.

Pereira, F.L.G., Roehl, D., Paulo Laquini, J., Oliveira, M.F.F., Costa, A.M., 2014. Fault reactivation case study for probabilistic assessment of carbon dioxide sequestration. Int. J. Rock Mech. Min. Sci. 71, 310–319. https://doi.org/10.1016/j.ijrmms.2014.08.003.

Potts, D.M., Zdravkovic, L., 1999. Finite Element Analysis in Geotechnical Engineering: Theory. Thomas Telford Publishing.

Prévost, J.H., Sukumar, N., 2016. Faults simulations for three-dimensional reservoir-geomechanical models with the extended finite element method. J. Mech. Phys. Solids. 86, 1–18. https://doi.org/10.1016/j.jmps.2015.09.014.

Pruess, K., Spycher, N., 2007. ECO2N - a fluid property module for the TOUGH2 code for studies of CO2 storage in saline aquifers. Energy Convers. Manag. 48, 1761–1767. https://doi.org/10.1016/j.enconman.2007.01.016.

Quevedo, R., Ramirez, M., Roehl, D., 2017. 2D and 3D numerical modeling of fault reactivation. 51st US Rock Mech / Geomech. Symp. 2017 (4), 2247–2252.

Rueda, J., Mejia, C., Quevedo, R., Roehl, D., 2020. Impacts of natural fractures on hydraulic fracturing treatment in all asymptotic propagation regimes. Comput. Methods Appl. Mech. Eng. 371 https://doi.org/10.1016/j.cma.2020.113296.

Rueda, J.C., Noreña, N.V., Oliveira, M.F.F., Roehi, D., 2014. Numerical models for detection of fault reactivation in oil and gas fields. 48th US Rock Mech./Geomech. Symp. 2014 (2), 1132–1139.

Rutqvist, J., Birkholzer, J., Cappa, F., Tsang, C.F., 2007. Estimating maximum sustainable injection pressure during geological sequestration of CO2 using coupled fluid flow and geomechanical fault-slip analysis. Energy Convers. Manag. 48, 1798–1807. https://doi.org/10.1016/J.ENCONMAN.2007.01.021.

Rutqvist, J., Cappa, F., Mazzoldi, A., Rinaldi, A., 2013. Geomechanical modeling of fault responses and the potential for notable seismic events during underground CO2 injection. Energy Proc. 37, 4774–4784. https://doi.org/10.1016/j.egypro.2013.06.387.

Rutqvist, J., Rinaldi, A.P., Cappa, F., Jeanne, P., Mazzoldi, A., Urpi, L., Guglielmi, Y., Vilarrasa, V., 2016. Fault activation and induced seismicity in geological carbon storage – lessons learned from recent modeling studies. J. Rock Mech. Geotech. Eng. 8, 789–804. https://doi.org/10.1016/j.jrmge.2016.09.001.

Sanders, J.D., Dolbow, J.E., Laursen, T.A., 2009. On methods for stabilizing constraints over enriched interfaces in elasticity. Int. J. Numer. Methods Eng. 78, 1009–1036. https://doi.org/10.1002/nme.2514.

Segura, J.M., Carol, I., 2008. Coupled HM analysis using zero-thickness interface elements with double nodes. Part I: Theoretical model. Int. J. Numer. Anal. Methods Geomech. 32, 2083–2101. https://doi.org/10.1002/nag.

Segura, J.M., Carol, I., 2008. Coupled HM analysis using zero-thickness interface elements with double nodes—Part II: Verification and application. Int. J. Numer. Anal. Methods Geomech. 32, 2103–2123. https://doi.org/10.1002/nag.

Serajian, V., Diessl, J., Bruno, M.S., Hermansson, L.C., Hatland, J., Risanger, M., Torsvik, M., 2016. 3D geomechanical modeling and fault reactivation risk analysis for a well at Brage oilfield, Norway. Soc. Pet. Eng. - SPE Eur. Featur. 78th EAGE Conf. Exhib. 1–16. https://doi.org/10.2118/180197-ms.

Silva, J.A., Saló-Salgado, L., Patterson, J., Dasari, G.R., Juanes, R., 2023. Assessing the viability of CO2 storage in offshore formations of the Gulf of Mexico at a scale relevant for climate-change mitigation. Int. J. Greenh. Gas Control. 126, 103884 https://doi.org/10.1016/j.ijggc.2023.103884.

Snow, D.T., 1965. A Parallel Plate Model of Fractured Permeable Media. University of California.

Stanić, A., Brank, B., Brancherie, D., 2020. Fracture of quasi-brittle solids by continuum and discrete-crack damage models and embedded discontinuity formulation. Eng. Fract. Mech. 227 https://doi.org/10.1016/j.engfracmech.2020.106924.

Vahab, M., Khoei, A.R., Khalili, N., 2019. An X-FEM technique in modeling hydro-fracture interaction with naturally-cemented faults. Eng. Fract. Mech. 212, 269–290. https://doi.org/10.1016/j.engfracmech.2019.03.020.

Witherspoon, P.A., Wang, J.S.Y., Iwai, K., Gale, J.E., 1980. Validity of Cubic Law for fluid flow in a deformable rock fracture. Water Resour. Res. 16, 1016–1024. https://doi.org/10.1029/WR016i006p01016.

Wu, J.Y., 2011. Unified analysis of enriched finite elements for modeling cohesive cracks. Comput. Methods Appl. Mech. Eng. 200, 3031–3050. https://doi.org/10.1016/j.cma.2011.05.008.

A.3
Paper 3

Behavior of cohesive stresses in embedded finite elements based on the strong discontinuity approach

Cavalcanti, D., Mejia, C., Souza C., Mendes, C. A., de-Pouplana, I., Casas, G. & Roehl, D.

Finite Elements in Analysis and Design, 253, 104485.(2025).
https://doi.org/10.1016/j.finel.2025.104485

Finite Elements in Analysis and Design 253 (2026) 104485

Contents lists available at ScienceDirect

Finite Elements in Analysis & Design

journal homepage: www.elsevier.com/locate/finel

Behavior of cohesive stresses in embedded finite elements based on the strong discontinuity approach

Danilo Cavalcanti [a,b,c,*], Cristian Mejia [d], Caio Souza [d], Carlos A. Mendes [d], Ignasi de-Pouplana [e,a], Guillermo Casas [a], Deane Roehl [c,d]

[a] *Centre Internacional de Mètodes Numèrics en Enginyeria (CIMNE), Barcelona, Spain*
[b] *Universitat Politècnica de Catalunya - BarcelonaTech (UPC), Spain*
[c] *Department of Civil and Environmental Engineering, Pontifical Catholic University of Rio de Janeiro, Brazil*
[d] *Tecgraf Institute, Pontifical Catholic University of Rio de Janeiro, Brazil*
[e] *Department of Strength of Materials and Structural Engineering, Universitat Politècnica de Catalunya - BarcelonaTech (UPC), Spain*

ARTICLE INFO

Keywords:
Embedded Finite Element Method (E-FEM)
Strong Discontinuity Approach (SDA)
Enhanced Assumed Strain (EAS)
Spurious oscillations

ABSTRACT

Embedded finite element formulations have gained increased attention for modeling strong discontinuities in solid mechanics problems, as they eliminate the need for mesh conformity required by discrete fracture models. While several such formulations have been extensively studied, particularly regarding strategies to mitigate stress locking, less is understood about the causes and possible remedies to the spurious stress oscillations along cohesive discontinuities. In this work, we employ the Enhanced Assumed Strain framework to derive two of the most popular formulation types: the Kinematically Optimal Symmetric (KOS) and the Statically and Kinematically Optimal Nonsymmetric (SKON). We investigate their performance in a broad range of scenarios, including stick and slip contact conditions, in both two and three dimensions, using linear and quadratic finite elements. Our results show that the SKON formulation consistently yields smoother cohesive stress fields by enforcing local equilibrium in a strong sense. While spurious oscillations are effectively eliminated under stick conditions, small-amplitude oscillations may persist under slip conditions; however, they are significantly reduced compared to the KOS formulation. Finally, we demonstrate the application of the SKON formulation to a fault reactivation problem, confirming its capability to accurately capture stress evolution and assess fault reactivation risk.

1. Introduction

In computational mechanics, accurately modeling pre-existing strong discontinuities, such as fractures and geological faults, is essential for reliably predicting structural behavior. The complexity of this modeling increases significantly due to the cohesive characteristics and contact behavior inherent to these discontinuities. Based on the Finite Element Method (FEM), different approaches have been developed to accurately simulate these discontinuities [1]. Among the FEM-based methods, the discrete fracture model (DFM) provides the most accurate representation of these discontinuities using interface elements [2–8] or high-aspect-ratio elements [9,10]. However, it poses a challenge during mesh generation, as the mesh must conform to the discontinuity surface [11,12]. Meanwhile, formulations such as the Extended/Generalized Finite Element Method (XFEM/GFEM) [13–17], and Embedded Finite Element Method (E-FEM) [18–20] have gained prominence because they can capture discontinuities without

* Correspondence to: Edifici C1, Campus Nord UPC, 08034 Barcelona, Spain.
E-mail address: dborges@cimne.upc.edu (D. Cavalcanti).

https://doi.org/10.1016/j.finel.2025.104485
Received 26 July 2025; Received in revised form 11 November 2025; Accepted 14 November 2025
Available online 18 November 2025

requiring mesh conformity. An alternative methodology is phase-field methods, which represent cracks as diffused interfaces via an energy functional with a length scale and can couple with cohesive zones [21,22]. In this work, we focus on E-FEM. The main difference between E-FEM and XFEM lies in the nature of the enrichment field [23–25]. XFEM follows the Partition of Unity [13,26] to discretize the enrichment part of the field, with the enrichment degrees of freedom (dofs) being defined at the nodes of the mesh and are considered global variables. In E-FEM, the enrichment field has a lower continuity order, which allows the enrichment dofs to be condensed at element level.

Since the pioneer works of Dvorkin et al. [27,28], Simo and Rifai [29] and Simo et al. [30], several finite element formulations with embedded strong discontinuities have been proposed in the literature [18,20,31–33]. Jirasek [34] presented a comprehensive study on the different types of embedded finite element formulations, assuming constant strain finite elements with embedded discontinuities with a constant displacement jump. He classifies them into three groups: Statically Optimal Symmetric (SOS), Kinematically Optimal Symmetric (KOS), and Statically and Kinematically Optimal Nonsymmetric (SKON).

The SOS formulation is fully variationally consistent with the Hu–Washizu functional [35] and guarantees traction continuity across the discontinuities [36–38]. However, because of its poor kinematic behavior, spurious stress transfers occur, leading to stress locking and a low reported use in the literature. Nevertheless, it has been shown that eight-node quadrilateral elements are stable [39]. The KOS formulation resolves the stress locking instability by considering the rigid body deformation modes introduced by the discontinuity in the definition of the element kinematics. However, this formulation is inconsistent with the Hu–Washizu principle, and the traction continuity condition is not guaranteed [20,32,40–43]. Improved versions of this formulation have been proposed to guarantee traction continuity across the discontinuity [42,44]. Finally, the SKON group combines the advantages of the SOS and KOS groups [18,19,45–47], having a consistent kinematic behavior and assuring the traction continuity condition [30], which is achieved through a Petrov–Galerkin method.

Multiple authors have reviewed and compared various groups of embedded formulations [23,34,42,48–51]. Their primary focus was on how these formulations affect the overall behavior of the model, particularly regarding stress-locking issues, and their impact on the load–displacement response. While this issue is by now well understood and there are several formulations that effectively address it, there remains a need for further investigation into how the type of formulation influences the local behavior of the discontinuity fields, specifically the displacement jump and cohesive tractions. It has been reported that cohesive tractions at the discontinuity can experience spurious oscillations [52], which can significantly degrade the accuracy of embedded formulations based on the Strong Discontinuity Approach (SDA), especially in problems where cohesive stresses play a significant role, such as in fault reactivation analyses.

Recently, combining a clustering method with a KOS formulation has been shown to alleviate spurious traction oscillations [53]. Following a similar approach, a non-local method was proposed using a KOS formulation for constant strain finite elements, such as linear triangular, to solve spurious oscillations [41].

It is important to note that, in the context of XFEM, the issue of spurious traction oscillations has been subject to investigation [54,55], and various approaches have been proposed to address this problem. One approach involves stabilizing the functional associated with the variational problem using methods such as Nitsche's method [56–59], the Polynomial Pressure Projection [60], or other stabilization techniques [61–63]. Another approach is to change the space of the discretized variables using sub-interpolation schemes [64,65] or adopting reduced Lagrange multiplier spaces [66–68]. Due to differences in the definition of the enrichment field between XFEM and E-FEM, the stabilization techniques developed for XFEM cannot be directly applied to E-FEM. However, they still provide useful insights into the causes of the spurious traction oscillations.

Besides SDA-based embedded formulations, other FEM-based methods allow the implicit incorporation of discontinuities. Idelsohn et al. [69] proposed an enriched FEM that handles both weak and strong discontinuities. Their approach involves subdividing elements into triangles or tetrahedra that conform precisely to the discontinuity surface, allowing the enrichment space to be discretized using these sub-elements. In the strong-discontinuity case, nodes located on the surface are duplicated so that the two sides carry independent displacements. They treat their enrichment degrees of freedom as local variables and apply a static condensation to eliminate them. To improve the continuity of the enriched space, they include inter-element forces in the weak form. Another approach is the Discontinuity Enriched FEM (DE-FEM) [70]. Like the method by Idelsohn et al. [69], it relies on element subdivision, but differs in two key respects: the enrichment DOFs correspond directly to displacement jumps and are treated as global variables. This method has proven effective in eliminating spurious traction oscillations and in handling material interfaces, immersed boundaries [71], and discontinuity intersections in two- and three-dimensional problems [72].

It is important to note that spurious oscillations in cohesive tractions are not unique to embedded or XFEM-type approaches; they also appear with standard interface elements. Appropriate interface quadrature can significantly reduce or eliminate such oscillations [73,74]. Yet oscillations may still persist in cases involving highly anisotropic cohesive laws or when large penalty stiffness values are used for contact enforcement. In such situations, mixed Augmented-Lagrangian schemes with quadratic displacement and linear Lagrange multiplier interpolation alleviate the oscillations [75]. More recently, Nitsche-based stabilized formulations have proven effective in eliminating them altogether [76,77].

Unlike earlier studies on E-FEM that mainly compared variants through global load–displacement curves using constant strain elements [23,34,42,48–51], we target the *local* behavior of cohesive tractions along embedded discontinuities for both KOS and SKON formulations. We also explore the use of various finite elements with linear and quadratic interpolation. Besides, we highlight that in the literature using E-FEM, the issue of spurious-traction oscillations has been addressed only for the KOS version [41,53], while the influence of SKON remains largely unexplored, aside from early evidence of oscillations in continuum stress fields [78]. To close this gap, we evaluate the performance of both KOS and SKON by analyzing the behavior of the cohesive traction through a series of tests, including two- and three-dimensional problems in different contact conditions. The comparisons are restricted to

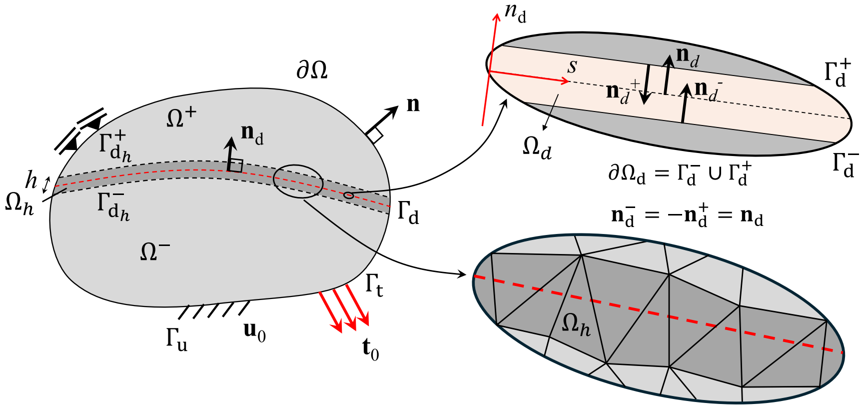

Fig. 1. Domain with the presence of a strong discontinuity.

SDA-based embedded formulations whose enrichment DOFs are element-local and can be statically condensed; methods that retain global enrichment variables lie beyond the present scope.

The paper is structured as follows. Section 2 presents the derivation of the weak form of the governing equations. Section 3 presents the finite element discretization. Section 4 presents some numerical examples. Finally, Section 5 summarizes the main conclusions of the work.

2. Governing equations

Consider the problem presented in Fig. 1 with a domain $\Omega \in \mathbb{R}^n$ (n = 2, 3) closed by a boundary $\partial\Omega$, with $\partial\Omega = \Gamma_u \cup \Gamma_t$ ($\Gamma_u \cap \Gamma_t = \emptyset$). The boundary Γ_u is associated with the essential boundary conditions and Γ_t with the natural boundary conditions. The domain is crossed by a discontinuity Ω_d, which divides it into two subdomains Ω^+ and Ω^-. Their definition is based on the normal vector to the discontinuity, $\mathbf{n}_d$, such that Ω^+ is the subregion at which the vector $\mathbf{n}_d$ points.

2.1. Strong form

Considering small displacements and strains, and neglecting the inertial effects, the boundary value problem is governed by

$$\nabla \cdot \boldsymbol{\sigma} + \mathbf{b} = \mathbf{0}, \ \mathbf{x} \in \Omega \backslash \Omega_d, \tag{1}$$

$$\boldsymbol{\varepsilon} = \nabla^s \mathbf{u}, \ \mathbf{x} \in \Omega \backslash \Omega_d, \tag{2}$$

$$\boldsymbol{\sigma} = \boldsymbol{\Sigma}(\boldsymbol{\varepsilon}), \ \mathbf{x} \in \Omega \backslash \Omega_d, \tag{3}$$

where $\boldsymbol{\sigma}$ is the Cauchy stress tensor, $\mathbf{b}$ is the body force vector, $\boldsymbol{\varepsilon}$ is the strain tensor, $\mathbf{u}$ is the displacement vector, ∇ denotes the nabla operator, and the superscript $()^s$ indicates the symmetric part of a second-order tensor. The operator $\boldsymbol{\Sigma}(\cdot)$ denotes the constitutive relation, which for elastic materials is defined as

$$\boldsymbol{\Sigma}(\boldsymbol{\varepsilon}) = \frac{\partial \Psi(\boldsymbol{\varepsilon}, \boldsymbol{\Sigma}(\boldsymbol{\varepsilon}))}{\partial \boldsymbol{\varepsilon}}, \tag{4}$$

where Ψ is the elastic strain energy density function.

The field boundary conditions are

$$\mathbf{u} = \mathbf{u}_0, \ \mathbf{x} \in \Gamma_u, \tag{5}$$

$$\mathbf{t} = \mathbf{t}_0, \ \mathbf{x} \in \Gamma_t, \tag{6}$$

with $\mathbf{t} = \boldsymbol{\sigma} \cdot \mathbf{n}$, where $\mathbf{n}$ is the outward unit normal vector to the boundary of the domain $\partial\Omega$.

Finally, along the discontinuity, the cohesive stresses, $\mathbf{t}_d$, must be in equilibrium with the tractions on each side of the discontinuity:

$$\boldsymbol{\sigma}^+ \cdot \mathbf{n}_d^+ = -\boldsymbol{\sigma}^- \cdot \mathbf{n}_d^- = -\mathbf{t}_d, \ \mathbf{x} \in \Gamma_d, \tag{7}$$

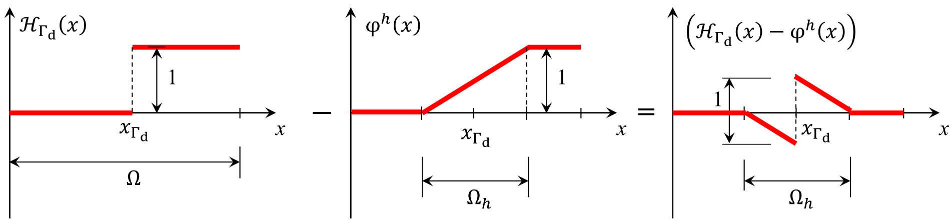

Fig. 2. Construction of the unit jump function in a one-dimensional problem with an embedded strong discontinuity.
Source: Adapted from [49].

We consider a smooth discontinuity surface. Therefore, we can assume that $\mathbf{n}_d^- = -\mathbf{n}_d^+ = \mathbf{n}_d$. The cohesive stresses are determined by a cohesive law, with $\mathbf{t}_d = \mathbf{t}_d([\![\mathbf{u}]\!])$, with $[\![\mathbf{u}]\!]$ being the displacement jump at the discontinuity surface, defined on Γ_d, as

$$[\![\mathbf{u}]\!] = \mathbf{u}^+ - \mathbf{u}^-. \tag{8}$$

2.2. Strong discontinuity kinematics

To incorporate the kinematics of a strong discontinuity, the displacement field is defined as

$$\mathbf{u}(\mathbf{x}) = \hat{\mathbf{u}}(\mathbf{x}) + \left(\mathscr{H}_{\Gamma_d}(\mathbf{x}) - \varphi^h(\mathbf{x})\right)\tilde{\mathbf{u}}(\mathbf{x}), \tag{9}$$

where $\hat{\mathbf{u}}$ is the regular part of the displacement field, $\tilde{\mathbf{u}}$ is the enhanced part of the displacement field, $\mathscr{H}_{\Gamma_d}$ is the Heaviside function,

$$\mathscr{H}_{\Gamma_d}(\mathbf{x}) = \begin{cases} 1, & \mathbf{x} \in \Omega^+ \\ 0, & \mathbf{x} \in \Omega^- \end{cases}, \tag{10}$$

and φ^h is an arbitrary auxiliary continuous function that needs to obey

$$\varphi^h(\mathbf{x}) = \begin{cases} 1, & \mathbf{x} \in \Omega^+ \backslash \Omega_h \\ 0, & \mathbf{x} \in \Omega^- \backslash \Omega_h \end{cases}, \tag{11}$$

with Ω_h being a subdomain of Ω surrounding the discontinuity surface Γ_d, see Fig. 1. The purpose of $\varphi^h(\mathbf{x})$ is illustrated in Fig. 2, which shows that subtracting $\mathscr{H}_{\Gamma_d}(\mathbf{x})$ by φ^h makes it zero outside the support Ω_h.

In Eq. (9), the admissible affine set of total displacement field $\mathscr{U}$ is

$$\mathscr{U} = \left\{\mathbf{u} \mid \mathbf{u} = \hat{\mathbf{u}} + \left(\mathscr{H}_{\Gamma_d} - \varphi^h\right)\tilde{\mathbf{u}},\ \hat{\mathbf{u}} \in \hat{\mathscr{U}},\ \tilde{\mathbf{u}} \in \tilde{\mathscr{U}}\right\}, \tag{12}$$

with

$$\hat{\mathscr{U}} = \left\{\hat{\mathbf{u}} \mid \hat{\mathbf{u}} \in \left[H^1(\Omega)\right]^n, \hat{\mathbf{u}}\big|_{\Gamma_u} = \mathbf{u}_0\right\}, \tag{13}$$

$$\tilde{\mathscr{U}} = \left\{\tilde{\mathbf{u}} \mid \tilde{\mathbf{u}} \in \left[L^2(\Omega)\right]^n\right\}, \tag{14}$$

where L^2 denotes the space of square-integrable real functions.

$$L^2(\Omega) = \left\{g \mid \int_\Omega g^2\, d\Omega < \infty\right\}, \tag{15}$$

and H^1 is the Hilbert functional space

$$H^1(\Omega) = \left\{g \mid g \in L^2(\Omega), \nabla g \in \left[L^2(\Omega)\right]^d\right\}, \text{with } d = \dim \Omega. \tag{16}$$

Therefore, the enhanced displacement field is defined in a space with a lower continuity requirement than the regular displacement field.

Substituting the displacement field, Eq. (9), into the compatibility equation, Eq. (2), we obtain

$$\boldsymbol{\varepsilon}(\mathbf{x}) = \nabla^s\hat{\mathbf{u}}(\mathbf{x}) + \tilde{\boldsymbol{\varepsilon}}(\mathbf{x}), \tag{17}$$

where

$$\tilde{\boldsymbol{\varepsilon}}(\mathbf{x}) = \tilde{\boldsymbol{\varepsilon}}_b(\mathbf{x}) + \delta_{\Gamma_d}(\mathbf{x})\left([\![\mathbf{u}]\!](\mathbf{x}) \otimes \mathbf{n}_d(\mathbf{x})\right)^s, \tag{18}$$

where δ_{Γ_d} is the Dirac's delta defined at the discontinuity and $\widetilde{\boldsymbol{\varepsilon}}_b$ the bounded part of the enhanced strain field, given by

$$\widetilde{\boldsymbol{\varepsilon}}_b(\mathbf{x}) = \left(\mathscr{H}_{\Gamma_d}(\mathbf{x}) - \varphi^h(\mathbf{x})\right) \nabla^s \widetilde{\mathbf{u}}(\mathbf{x}) - \nabla^s \varphi^h(\mathbf{x}) \otimes \widetilde{\mathbf{u}}(\mathbf{x}). \tag{19}$$

We assume that the enriched displacement field is composed only of rigid-body deformation modes, which implies that $\nabla^s \widetilde{\mathbf{u}}(\mathbf{x}) = \mathbf{0}$. Then, the bounded part of the enhanced strain tensor can be simplified to [32,41]

$$\widetilde{\boldsymbol{\varepsilon}}_b(\mathbf{x}) = -\nabla^s \varphi^h(\mathbf{x}) \otimes \widetilde{\mathbf{u}}(\mathbf{x}). \tag{20}$$

2.3. Weak form

There are different approaches to derive the weak form of the governing equations associated with this problem, including the Variational Multiscale Method [23,47,79,80], the Enhanced Assumed Strain (EAS) method [18,29,81,82], and even plasticity-like frameworks [83]. Cazes et al. [50] present the derivation of a constant strain triangular element with an embedded strong discontinuity with constant displacement jump using all three approaches. Here, we adopt the EAS approach to derive the weak form of the governing equations.

In the EAS method the strain field is decomposed into a compatible, $\nabla^s \mathbf{u}$, and an incompatible part, $\bar{\boldsymbol{\varepsilon}}$,

$$\boldsymbol{\varepsilon}(\mathbf{x}) = \nabla^s \mathbf{u}(\mathbf{x}) + \bar{\boldsymbol{\varepsilon}}(\mathbf{x}). \tag{21}$$

Comparing the format of the strain tensor defined by the EAS method, Eq. (21), with the strain tensor including the kinematics of a strong discontinuity, Eq. (17), leads to $\bar{\boldsymbol{\varepsilon}}(\mathbf{x}) = \widetilde{\boldsymbol{\varepsilon}}(\mathbf{x})$. Hence, the effect of a strong discontinuity can be incorporated directly into the strain field as an incompatible strain mode [18].

In the EAS formulation, the weak form of the governing equations is derived from the Hu–Washizu functional, which considers the displacement, strain, and stress fields as independent [35].

$$\Pi(\mathbf{u}, \boldsymbol{\varepsilon}, \boldsymbol{\sigma}) = \int_\Omega \Psi(\boldsymbol{\varepsilon}, \boldsymbol{\Sigma}(\boldsymbol{\varepsilon}))\, d\Omega - \int_{\Gamma_t} \mathbf{t} \cdot \mathbf{u}\, d\Gamma - \int_\Omega \mathbf{b} \cdot \mathbf{u}\, d\Omega - \int_\Omega \boldsymbol{\sigma} : (\boldsymbol{\varepsilon} - \nabla^s \mathbf{u})\, d\Omega. \tag{22}$$

The stationary condition of this functional corresponds to an integral weak imposition of the linear momentum balance, Eq. (1), and an integral imposition of the compatibility, Eq. (2), and constitutive, Eq. (3), equations, as

$$\int_\Omega \nabla^s \mathbf{v} : \boldsymbol{\sigma}\, d\Omega - \int_{\Gamma_t} \mathbf{v} \cdot \mathbf{t}\, d\Gamma - \int_\Omega \mathbf{v} \cdot \mathbf{b}\, d\Omega = 0, \quad \text{for} \quad \mathbf{v} \in \mathscr{V}, \tag{23}$$

$$\int_\Omega \boldsymbol{\tau} : (\boldsymbol{\varepsilon} - \nabla^s \mathbf{u})\, d\Omega = 0, \quad \text{for} \quad \boldsymbol{\tau} \in \mathscr{S}, \tag{24}$$

$$\int_\Omega \boldsymbol{\gamma} : (\boldsymbol{\Sigma}(\boldsymbol{\varepsilon}) - \boldsymbol{\sigma})\, d\Omega = 0, \quad \text{for} \quad \boldsymbol{\gamma} \in \mathscr{E}, \tag{25}$$

where $\mathbf{v} \in \mathscr{V}$, $\boldsymbol{\tau} \in \mathscr{S}$ and $\boldsymbol{\gamma} \in \mathscr{E}$ are, respectively, the admissible variations of the displacement, stress and strain fields, where $\mathscr{S} = \mathscr{E} = \left[L^2(\Omega)\right]^{n \times n}$ and $\mathscr{V} = \left\{ \mathbf{v} \mid \mathbf{v} \in \left[H^1(\Omega)\right]^n, \mathbf{v}\big|_{\Gamma_u} = \mathbf{0} \right\}$.

As done in Eq. (21) for the strain field, its admissible variation, $\boldsymbol{\gamma}$, is also decomposed into a compatible and an incompatible part as

$$\boldsymbol{\gamma} = \nabla^s \mathbf{v} + \widetilde{\boldsymbol{\gamma}}, \tag{26}$$

with $\widetilde{\boldsymbol{\gamma}}$ being the admissible variation of the enhanced strains.

Substituting the strain decomposition, Eqs. (21) and (26), into Eqs. (23), (24) and (25), the Euler equations associated with the Hu–Washizu functional can be re-written as:

$$\int_\Omega \nabla^s \mathbf{v} : \boldsymbol{\Sigma}(\boldsymbol{\varepsilon})\, d\Omega - \int_{\Gamma_t} \mathbf{v} \cdot \mathbf{t}\, d\Gamma - \int_\Omega \mathbf{v} \cdot \mathbf{b}\, d\Omega = 0, \tag{27}$$

$$\int_\Omega \widetilde{\boldsymbol{\gamma}} : (\boldsymbol{\Sigma}(\boldsymbol{\varepsilon}) - \boldsymbol{\sigma})\, d\Omega = 0, \tag{28}$$

$$\int_\Omega \boldsymbol{\tau} : \widetilde{\boldsymbol{\varepsilon}}\, d\Omega = 0. \tag{29}$$

Eq. (29) enforces L^2-orthogonality of the incompatible strains to the admissible stresses, so they perform no virtual work. Consequently, it implies that $\boldsymbol{\sigma}$ depends only on the regular strain field.

Based on Eq. (18), the enhanced strain field and its admissible variation are further decomposed into a bounded, $\widetilde{\boldsymbol{\varepsilon}}_b$, and a discontinuous part, $\delta_{\Gamma_d}\left([\![\mathbf{u}]\!] \otimes \mathbf{n}_d\right)^S$ belonging to the space $\widetilde{\mathscr{E}}$ defined as [18]

$$\widetilde{\mathscr{E}} = \left\{ \widetilde{\boldsymbol{\varepsilon}} = \widetilde{\boldsymbol{\varepsilon}}_b + \delta_{\Gamma_d}\left(\mathbf{u}_d \otimes \mathbf{n}_d\right)^S \mid \widetilde{\boldsymbol{\varepsilon}}_b \in \mathscr{E}, \mathbf{u}_d \in \mathscr{U}_d \right\}, \tag{30}$$

where $\mathscr{U}_d = \left[L^2(\Omega)\right]^n$.

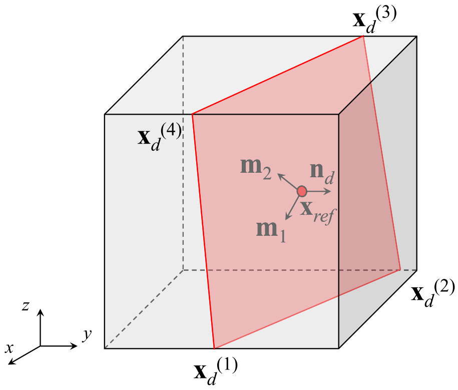

Fig. 3. Hexahedral finite element with embedded strong discontinuity.

Applying the enhanced strain decomposition into Eqs. (28) and (29),

$$\int_\Omega \tilde{\boldsymbol{\gamma}}_\mathrm{b} : (\boldsymbol{\Sigma}(\boldsymbol{\varepsilon}) - \boldsymbol{\sigma})\, d\Omega + \int_\Omega \delta_{\Gamma_\mathrm{d}} \left(\mathbf{v}_\mathrm{d} \otimes \mathbf{n}_\mathrm{d}\right)^\mathrm{S} : (\boldsymbol{\Sigma}(\boldsymbol{\varepsilon}) - \boldsymbol{\sigma})\, d\Omega = 0, \tag{31}$$

$$\int_\Omega \boldsymbol{\tau} : \tilde{\boldsymbol{\varepsilon}}_\mathrm{b}\, d\Omega + \int_\Omega \delta_{\Gamma_\mathrm{d}} \boldsymbol{\tau} : \left(\mathbf{u}_\mathrm{d} \otimes \mathbf{n}_\mathrm{d}\right)^\mathrm{S}\, d\Omega = 0. \tag{32}$$

Using Dirac's delta property and re-writing the tensor double-contraction,

$$\int_\Omega \tilde{\boldsymbol{\gamma}}_\mathrm{b} : (\boldsymbol{\Sigma}(\boldsymbol{\varepsilon}) - \boldsymbol{\sigma})\, d\Omega + \int_{\Gamma_\mathrm{d}} \mathbf{v}_\mathrm{d} \cdot \left((\boldsymbol{\Sigma}(\boldsymbol{\varepsilon}) - \boldsymbol{\sigma}) \cdot \mathbf{n}_\mathrm{d}\right) d\Gamma = 0, \tag{33}$$

$$\int_\Omega \boldsymbol{\tau} : \tilde{\boldsymbol{\varepsilon}}_\mathrm{b}\, d\Omega + \int_{\Gamma_\mathrm{d}} \left(\boldsymbol{\tau} \cdot \mathbf{n}_\mathrm{d}\right) \cdot \mathbf{u}_\mathrm{d}\, d\Gamma = 0. \tag{34}$$

By choosing the space $\mathcal{S}$ as L^2-orthogonal to $\tilde{\mathcal{E}}$, the problem composed by Eqs. (27), (33), (34) is reduced to [29]: *Find* $\mathbf{u} \in \mathcal{U}$ *such that for all* $\mathbf{v} \in \mathcal{V}$ *and* $\tilde{\boldsymbol{\gamma}} \in \tilde{\mathcal{E}}$*, it holds that*

$$\begin{cases} \displaystyle\int_\Omega \nabla^\mathrm{s}\mathbf{v} : \boldsymbol{\Sigma}(\boldsymbol{\varepsilon})\, d\Omega - \int_{\Gamma_t} \mathbf{v} \cdot \mathbf{t}\, d\Gamma - \int_\Omega \mathbf{v} \cdot \mathbf{b}\, d\Omega = 0, \\ \displaystyle\int_\Omega \tilde{\boldsymbol{\gamma}}_\mathrm{b} : \boldsymbol{\Sigma}(\boldsymbol{\varepsilon})\, d\Omega + \int_{\Gamma_\mathrm{d}} \mathbf{v}_\mathrm{d} \cdot \mathbf{t}_\mathrm{d}\left(\mathbf{u}_\mathrm{d}\right) d\Gamma = 0. \end{cases} \tag{35}$$

In (35), we have $\mathbf{t}_\mathrm{d}\left(\mathbf{u}_\mathrm{d}\right) = \boldsymbol{\Sigma}(\boldsymbol{\varepsilon}) \cdot \mathbf{n}_\mathrm{d}$, from the traction continuity condition in Eq. (7). Eq. (34) is not present in the system (35) since it becomes trivial with the orthogonality assumption.

Finally, from Eq. (33), the orthogonality condition imposes that

$$\int_\Omega \tilde{\boldsymbol{\gamma}}_\mathrm{b} : \boldsymbol{\sigma}\, d\Omega = -\int_{\Gamma_\mathrm{d}} \mathbf{v}_\mathrm{d} \cdot \left(\boldsymbol{\sigma} \cdot \mathbf{n}_\mathrm{d}\right) d\Gamma, \tag{36}$$

which will later be used to define the discretization of $\tilde{\boldsymbol{\gamma}}_\mathrm{b}$.

3. Finite element discretization

This section covers the discretization of the system described in Eq. (35) through a finite element approach. To maintain generality, we will consider a three-dimensional domain, as it can later be easily simplified to a two-dimensional one. For the sake of notation simplicity, we assume that the domain Ω consists of a single finite element, denoted as e.

3.1. Geometric characterization of the embedded discontinuity

In finite element, the discontinuity can be characterized by its centroid, $\mathbf{x}_\mathrm{ref}$, and its orientation vectors, as shown in Fig. 3. We consider the discontinuity to be a straight plane inside the element.

The discontinuity normal vector is determined by

$$\mathbf{n}_{\mathrm{d}} = \frac{\left(\mathbf{x}_{\mathrm{d}}^{(1)} - \mathbf{x}_{\mathrm{ref}}\right) \times \left(\mathbf{x}_{\mathrm{d}}^{(2)} - \mathbf{x}_{\mathrm{ref}}\right)}{\left\| \left(\mathbf{x}_{\mathrm{d}}^{(1)} - \mathbf{x}_{\mathrm{ref}}\right) \times \left(\mathbf{x}_{\mathrm{d}}^{(2)} - \mathbf{x}_{\mathrm{ref}}\right) \right\|}, \tag{37}$$

and the tangential vector $\mathbf{m}_1$ by

$$\mathbf{m}_1 = \frac{\left(\mathbf{x}_{\mathrm{d}}^{(1)} - \mathbf{x}_{\mathrm{ref}}\right)}{\left\| \left(\mathbf{x}_{\mathrm{d}}^{(1)} - \mathbf{x}_{\mathrm{ref}}\right) \right\|}. \tag{38}$$

The second tangential vector is then obtained by

$$\mathbf{m}_2 = \mathbf{n}_{\mathrm{d}} \times \mathbf{m}_1. \tag{39}$$

Along each tangential axis, a relative coordinate is defined as

$$s_i = \left(\mathbf{x}_{\mathrm{d}} - \mathbf{x}_{\mathrm{ref}}\right) \cdot \mathbf{m}_i, \quad i = 1, 2. \tag{40}$$

3.2. Regular fields

The regular part of the displacement field, Eq. (9), is approximated using the standard finite element shape function matrix, $\mathbf{N}(\mathbf{x})$, as

$$\hat{\mathbf{u}}^h(\mathbf{x}) = \mathbf{N}(\mathbf{x})\, \mathbf{d}, \tag{41}$$

where $\mathbf{d}$ represents the regular degrees of freedom (dofs).

The approximation of admissible variation of the displacement field, $\mathbf{v}^h$, and its symmetric gradient are, respectively,

$$\mathbf{v}^h(\mathbf{x}) = \mathbf{N}(\mathbf{x})\, \boldsymbol{\eta}, \tag{42}$$

$$\nabla^{\mathrm{S}} \mathbf{v}^h(\mathbf{x}) = \mathbf{B}(\mathbf{x})\, \boldsymbol{\eta}, \tag{43}$$

where $\mathbf{B}(\mathbf{x})$ is the standard finite element strain–displacement matrix and $\boldsymbol{\eta}$ represents the dofs associated with the variation of the displacement field.

3.3. Enrichment deformation modes

The displacement jump along the discontinuity in the discontinuity local coordinate system, $\mathbf{u}_{\mathrm{d}}^h$, is defined in terms of the enriched dofs, $\boldsymbol{\alpha}$, as

$$\mathbf{u}_{\mathrm{d}}^h(s_1, s_2) = \mathbf{N}_{\mathrm{d}}(s_1, s_2)\, \boldsymbol{\alpha}. \tag{44}$$

For a constant displacement jump, $\mathbf{N}_{\mathrm{d}}(s_1, s_2) = \mathbf{I}$ and $\boldsymbol{\alpha} = \left[\alpha_0^{m_1} \;\; \alpha_0^{m_2} \;\; \alpha_0^{n}\right]^{\top}$. While for a displacement jump with the normal component having linear variations along s_1 and s_2, they are

$$\mathbf{N}_{\mathrm{d}}(s_1, s_2) = \begin{bmatrix} 1 & 0 & 0 & 0 & 0 \\ 0 & 1 & 0 & 0 & 0 \\ 0 & 0 & 1 & s_1 & s_2 \end{bmatrix}, \tag{45}$$

$$\boldsymbol{\alpha} = \left[\alpha_0^{m_1} \quad \alpha_0^{m_2} \quad \alpha_0^{n} \quad \alpha_1^{n} \quad \alpha_2^{n}\right]^{\top}. \tag{46}$$

The admissible variation of the displacement jump, $\mathbf{v}_{\mathrm{d}}^h$, is approximated as

$$\mathbf{v}_{\mathrm{d}}^h(s_1, s_2) = \mathbf{N}_{\mathrm{d}}(s_1, s_2)\, \boldsymbol{\beta}, \tag{47}$$

where $\boldsymbol{\beta}$ represents the admissible variation of the enriched dofs.

The enhanced part of the displacement field, Eq. (9), is defined based on the discontinuity jump field, with each enriched dof being associated with an enhanced deformation mode[1] [45]:

$$\tilde{\mathbf{u}}^h(\mathbf{x}) = \underbrace{\alpha_0^{m_1}\, \mathbf{m}_1 + \alpha_0^{m_2}\, \mathbf{m}_2 + \alpha_0^{n}\, \mathbf{n}_{\mathrm{d}}}_{\text{Relative translation modes}} + \underbrace{\alpha_1^{n}\, \left(\mathbf{n}_{\mathrm{d}}\, \mathbf{m}_1{}^{\top} - \mathbf{m}_1\, \mathbf{n}_{\mathrm{d}}{}^{\top}\right) \Delta\mathbf{x} + \alpha_2^{n}\, \left(\mathbf{m}_2\, \mathbf{n}_{\mathrm{d}}{}^{\top} - \mathbf{n}_{\mathrm{d}}\, \mathbf{m}_2{}^{\top}\right) \Delta\mathbf{x}}_{\text{Relative rotation modes}}, \tag{48}$$

where $\Delta\mathbf{x} = \mathbf{x} - \mathbf{x}_{\mathrm{ref}}$.

[1] The derivation of these enhanced modes is presented as supplementary material using a Matlab LiveScript.

The auxiliary function φ^h, used in Eq. (9), is defined as [18,45,47]

$$\varphi^h(\mathbf{x}) = \sum_{i=1}^{n^+} \mathbf{N}^{(i)}(\mathbf{x}). \tag{49}$$

where n^+ corresponds to the number of nodes in Ω^+.

Finally, the enhanced part of the strain field, Eq. (20), is

$$\tilde{\varepsilon}_\mathrm{b}^h(\mathbf{x}) = \tilde{\mathbf{B}}(\mathbf{x})\boldsymbol{\alpha}, \tag{50}$$

with

$$\tilde{\mathbf{B}}(\mathbf{x}) = -\sum_{i\in\Omega^+} \begin{bmatrix} \left(\mathbf{B}^{(i)}(\mathbf{x})\mathbf{m}_1\right)^\top \\ \left(\mathbf{B}^{(i)}(\mathbf{x})\mathbf{m}_2\right)^\top \\ \left(\mathbf{B}^{(i)}(\mathbf{x})\mathbf{n}_\mathrm{d}\right)^\top \\ \left(\mathbf{B}^{(i)}(\mathbf{x})\left(\mathbf{n}_\mathrm{d}\,{\mathbf{m}_1}^\top - \mathbf{m}_1\,{\mathbf{n}_\mathrm{d}}^\top\right)\left(\mathbf{x}^{(i)} - \mathbf{x}_\mathrm{ref}\right)\right)^\top \\ \left(\mathbf{B}^{(i)}(\mathbf{x})\left(\mathbf{m}_2\,{\mathbf{n}_\mathrm{d}}^\top - \mathbf{n}_\mathrm{d}\,{\mathbf{m}_2}^\top\right)\left(\mathbf{x}^{(i)} - \mathbf{x}_\mathrm{ref}\right)\right)^\top \end{bmatrix}^\top. \tag{51}$$

Then the strain field, (17), is discretized as

$$\boldsymbol{\varepsilon}^h(\mathbf{x}) = \mathbf{B}(\mathbf{x})\,\mathbf{d} + \tilde{\mathbf{B}}(\mathbf{x})\,\boldsymbol{\alpha},\;\; \mathbf{x}\in\Omega\backslash\Gamma_\mathrm{d}. \tag{52}$$

3.4. Stress projection matrix

In Voigt notation, the strain tensor is represented by $\boldsymbol{\varepsilon}^h = \{\varepsilon_{xx}, \varepsilon_{yy}, \varepsilon_{zz}, 2\varepsilon_{xy}, 2\varepsilon_{yz}, 2\varepsilon_{xz}\}^\top$ and the stress tensor is $\boldsymbol{\sigma}^h = \{\sigma_{xx}, \sigma_{yy}, \sigma_{zz}, \sigma_{xy}, \sigma_{yz}, \sigma_{xz}\}^\top$. Then, a projection matrix $\mathbf{P}$ is defined as

$$\mathbf{P} = \begin{bmatrix} n_x & 0 & 0 & n_y & 0 & n_z \\ 0 & n_y & 0 & n_x & n_z & 0 \\ 0 & 0 & n_z & 0 & n_y & n_x \end{bmatrix}^\top, \tag{53}$$

such that

$$\left(\mathbf{v}_\mathrm{d}\otimes\mathbf{n}_\mathrm{d}\right)^\mathrm{S} = \mathbf{P}\,\boldsymbol{\Lambda}\mathbf{v}_\mathrm{d}^h, \tag{54a}$$

$$\boldsymbol{\sigma}\cdot\mathbf{n}_\mathrm{d} = \boldsymbol{\Lambda}^\top\mathbf{P}^\top\,\boldsymbol{\sigma}^h, \tag{54b}$$

where the discontinuity orientation matrix $\boldsymbol{\Lambda} = [\mathbf{m}_1\;\mathbf{m}_2\;\mathbf{n}_\mathrm{d}]$ is introduced because the enriched dofs are defined in the discontinuity local coordinate system, see Eq. (47). It acts as a rotation matrix of the displacement jumps and the traction vector.

The discretization of the admissible variation in the bounded part of the enhanced strain field, $\tilde{\boldsymbol{\gamma}}_\mathrm{b}^h$, is

$$\tilde{\boldsymbol{\gamma}}_\mathrm{b}^h(\mathbf{x}) = \mathbf{G}(\mathbf{x})\,\boldsymbol{\beta}. \tag{55}$$

In the Kinematically Optimal Symmetric (KOS) versions of embedded finite element formulation, matrix $\mathbf{G}$ is equal to $\tilde{\mathbf{B}}$, Eq. (51). In the Statically and Kinematically Optimal Nonsymmetric (SKON) versions, $\mathbf{G}$ is defined based on the orthogonality condition, Eq. (36), as

$$\boldsymbol{\beta}^\top\int_\Omega \mathbf{G}^\top\,\boldsymbol{\sigma}^h\,d\Omega = -\boldsymbol{\beta}^\top\int_{\Gamma_\mathrm{d}} \mathbf{N}_\mathrm{d}^\top\,\boldsymbol{\Lambda}^\top\,\mathbf{P}^\top\,\boldsymbol{\sigma}^h\,d\Gamma. \tag{56}$$

Substituting Eq. (47) and having $\mathbf{G} = \left[\mathbf{G}_0\;\mathbf{G}_1\;\mathbf{G}_2\right]$, Eq. (56) can be restated as

$$\left[\boldsymbol{\beta}_0\quad\boldsymbol{\beta}_1\quad\boldsymbol{\beta}_2\right]\left(\int_\Omega \left[\mathbf{G}_0\quad\mathbf{G}_1\quad\mathbf{G}_2\right]^\top\boldsymbol{\sigma}^h\,d\Omega + \int_{\Gamma_\mathrm{d}}\left[\mathbf{P}\boldsymbol{\Lambda}\quad s_1\,\mathbf{P}\,\mathbf{n}_\mathrm{d}\quad s_2\,\mathbf{P}\,\mathbf{n}_\mathrm{d}\right]^\top\boldsymbol{\sigma}^h\,d\Gamma\right) = 0. \tag{57}$$

It assumes that the matrices inside the integrals are proportional to each other through a polynomial function $g_k(\mathbf{x})$, $k = 0,1,2$, [23,45,47,84]:

$$\mathbf{G}(\mathbf{x}) = \left[-g_0(\mathbf{x})\,\mathbf{P}\boldsymbol{\Lambda}\quad -g_1(\mathbf{x})\,\mathbf{P}\,\mathbf{n}_\mathrm{d}\quad -g_2(\mathbf{x})\,\mathbf{P}\,\mathbf{n}_\mathrm{d}\right]^\top. \tag{58}$$

The polynomial $g_k(\mathbf{x})$ is assumed to have an order that matches the polynomial approximation of the discrete stress field $\boldsymbol{\sigma}^h(\mathbf{x})$ [46],

$$g_k(\mathbf{x}) = \mathbf{p}(\mathbf{x})^\top\left[c_0^{(k)}\quad c_1^{(k)}\quad c_2^{(k)}\quad c_3^{(k)}\right]^\top = \mathbf{p}(\mathbf{x})^\top\,\mathbf{c}_k, \tag{59}$$

$$\boldsymbol{\sigma}^h(\mathbf{x}) = \mathbf{p}(\mathbf{x})^\top\left[\boldsymbol{\sigma}_0\quad\boldsymbol{\sigma}_1\quad\boldsymbol{\sigma}_2\quad\boldsymbol{\sigma}_3\right]^\top = \mathbf{p}(\mathbf{x})^\top\,\mathbf{S}, \tag{60}$$

where $\mathbf{p}(\mathbf{x})$ is the polynomial basis. Its definition depends on the finite element used; for example, for linear hexahedral elements, $\mathbf{p}(\mathbf{x}) = \begin{bmatrix} 1 & x & y & z \end{bmatrix}^{\top}$.

Substituting Eqs. (58), (59) and (60) into Eq. (57), leads to

$$\begin{bmatrix} \mathbf{c}_0 & \mathbf{c}_1 & \mathbf{c}_2 \end{bmatrix} = \left(\int_{\Omega} \mathbf{p}\,\mathbf{p}^{\top}\, d\Omega \right)^{-1} \begin{bmatrix} \int_{\Gamma_{\mathrm{d}}} \mathbf{p}\, d\Gamma & \int_{\Gamma_{\mathrm{d}}} s_1\, \mathbf{p}\, d\Gamma & \int_{\Gamma_{\mathrm{d}}} s_2\, \mathbf{p}\, d\Gamma \end{bmatrix}. \tag{61}$$

Another condition required in the discretization of the enhanced strain field, $\tilde{\boldsymbol{\gamma}}^h_{\mathrm{b}}$, comes from the generalized patch test, which requires the finite element to accurately represent a uniform stress field [34]. Therefore, the enhanced strains must be orthogonal to any uniform stress field, $\boldsymbol{\sigma}_{\mathrm{c}}$ [81]; that is

$$0 = \int_{\Omega} \boldsymbol{\sigma}_{\mathrm{c}}^{\top}\, \tilde{\boldsymbol{\gamma}}^h_{\mathrm{b}}(\mathbf{x})\, d\Omega = \boldsymbol{\sigma}_{\mathrm{c}}^{\top} \int_{\Omega} \mathbf{G}(\mathbf{x})\, d\Omega\, \boldsymbol{\beta}. \tag{62}$$

Since this must be valid for all admissible variations $\boldsymbol{\beta}$, we conclude that

$$\int_{\Omega} \mathbf{G}(\mathbf{x})\, d\Omega = \mathbf{0}. \tag{63}$$

This is known as the zero-mean condition. In the SKON formulation, this is naturally achieved. An alternative that can be found in the literature, but is not explored in this work, is to subtract from the enhanced strain field the mean value of each component of the matrix $\tilde{\mathbf{B}}(\mathbf{x})$ [34,81,85,86]:

$$\mathbf{G}(\mathbf{x}) = \tilde{\mathbf{B}}(\mathbf{x}) - \frac{\int_{\Omega} \tilde{\mathbf{B}}(\mathbf{x})\, d\Omega}{\int_{\Omega} \mathbf{x}\, d\Omega}. \tag{64}$$

3.5. Solution scheme

The residual vectors of the system are obtained by applying the discretization into the system in Eq. (35)

$$\begin{cases} \mathbf{r}_{\mathrm{c}}(\mathbf{d}, \boldsymbol{\alpha}) = \int_{\Omega} \mathbf{B}^{\top} \boldsymbol{\Sigma}(\mathbf{d}, \boldsymbol{\alpha})\, d\Omega - \int_{\Gamma_t} \mathbf{N}^{\top} \mathbf{t}\, d\Gamma - \int_{\Omega} \mathbf{N}^{\top} \mathbf{b}\, d\Omega = \mathbf{0}, \ \forall\, \boldsymbol{\eta} \neq \mathbf{0}, \\ \mathbf{r}_{\mathrm{d}}(\mathbf{d}, \boldsymbol{\alpha}) = \int_{\Omega} \mathbf{G}^{\top} \boldsymbol{\Sigma}(\mathbf{d}, \boldsymbol{\alpha})\, d\Omega + \int_{\Gamma_{\mathrm{d}}} \mathbf{N}_{\mathrm{d}}^{\top}\, \mathbf{t}_{\mathrm{d}}(\boldsymbol{\alpha})\, d\Gamma = \mathbf{0}, \ \forall\, \boldsymbol{\beta} \neq \mathbf{0}. \end{cases} \tag{65}$$

where the subscripts “c” and “d” in the residual vectors stand for “continuum” and “discontinuity”, respectively.

The system is solved using an incremental-iterative strategy

$$\begin{bmatrix} \mathbf{K}_{\mathrm{cc}} & \mathbf{K}_{\mathrm{cd}} \\ \mathbf{K}_{\mathrm{dc}} & \mathbf{K}_{\mathrm{dd}} \end{bmatrix}^{i}_{n+1} \begin{bmatrix} \delta\mathbf{d} \\ \delta\boldsymbol{\alpha} \end{bmatrix}^{i}_{n+1} = - \begin{bmatrix} \mathbf{r}_{\mathrm{c}} \\ \mathbf{r}_{\mathrm{d}} \end{bmatrix}^{i}_{n+1}, \tag{66}$$

with

$$\mathbf{K}_{\mathrm{cc}} = \int_{\Omega} \mathbf{B}^{\top} \mathbf{D}\, \mathbf{B}\, d\Omega, \tag{67}$$

$$\mathbf{K}_{\mathrm{cd}} = \int_{\Omega} \mathbf{B}^{\top} \mathbf{D}\, \tilde{\mathbf{B}}\, d\Omega, \tag{68}$$

$$\mathbf{K}_{\mathrm{dc}} = \int_{\Omega} \mathbf{G}^{\top} \mathbf{D}\, \mathbf{B}\, d\Omega, \tag{69}$$

$$\mathbf{K}_{\mathrm{dd}} = \int_{\Omega} \mathbf{G}^{\top} \mathbf{D}\, \tilde{\mathbf{B}}\, d\Omega + \int_{\Gamma_{\mathrm{d}}} \mathbf{N}_{\mathrm{d}}^{\top} \mathbf{T}_{\mathrm{d}}\, \mathbf{N}_{\mathrm{d}}\, d\Gamma, \tag{70}$$

where $\mathbf{D}$ denotes the bulk tangent constitutive matrix and $\mathbf{T}_{\mathrm{d}}$ the tangent cohesive matrix on the discontinuity. For a linear-elastic cohesive law,

$$\mathbf{T}_{\mathrm{d}} = \begin{bmatrix} k_{\mathrm{s}} & 0 & 0 \\ 0 & k_{\mathrm{s}} & 0 \\ 0 & 0 & k_{\mathrm{n}} \end{bmatrix}, \tag{71}$$

with k_{s} and k_{n} being the elastic shear and normal cohesive stiffnesses, respectively.

Due to the local nature of the enhanced degrees of freedom, $\boldsymbol{\alpha}$, which are associated with the enrichment space $\tilde{\mathscr{E}}$ defined in Eq. (30), these degrees of freedom can be statically condensed at the element level [45,47,87,88]. This condensation is achieved using a local–global operator split approach [89], in which the equilibrium equations associated with $\boldsymbol{\alpha}$ are solved locally within each enriched element. During this process, the residual vector $\mathbf{r}_{\mathrm{d}}$ is treated as a function of $\boldsymbol{\alpha}$, i.e., $\mathbf{r}_{\mathrm{d}} = \mathbf{r}_{\mathrm{d}}(\boldsymbol{\alpha})$, while the regular degrees of freedom $\mathbf{d}$ are kept fixed at their current iteration value, $\mathbf{d}^i_{n+1}$.

Since $\mathbf{r}_{\mathrm{d}}$ is zero, the solution of the second equation in the system (65) is

$$\delta\boldsymbol{\alpha}^{i+1}_{n+1} = -\left({\mathbf{K}_{\mathrm{dd}}}^{i}_{n+1} \right)^{-1} {\mathbf{K}_{\mathrm{dc}}}^{i}_{n+1}\, \delta\mathbf{d}^{i+1}_{n+1}. \tag{72}$$

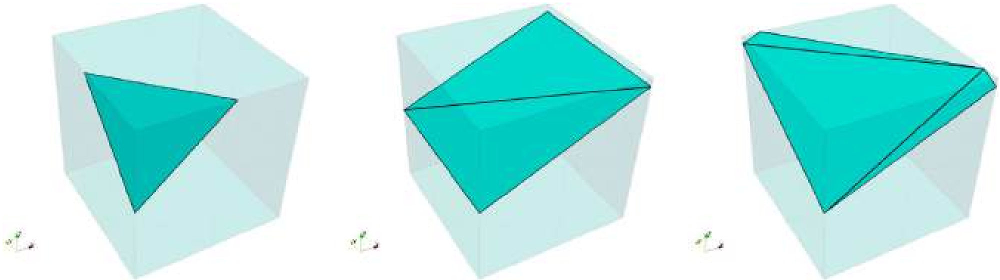

Fig. 4. Triangulation of the discontinuity surface inside the finite element in different intersection scenarios.

Substituting in the first equation,

$$\bar{\mathbf{K}}_{n+1}^{i}\,\delta\mathbf{d}_{n+1}^{i+1} = -\mathbf{r}_{\mathrm{c},n+1}^{i}\,, \tag{73}$$

with $\bar{\mathbf{K}}_{n+1}^{i}$ being the tangent stiffness matrix containing the condensed contribution of the enrichment,

$$\bar{\mathbf{K}}_{n+1}^{i} = \mathbf{K}_{\mathrm{cc}}{}_{n+1}^{i} - \mathbf{K}_{\mathrm{cd}}{}_{n+1}^{i}\left(\mathbf{K}_{\mathrm{dd}}{}_{n+1}^{i}\right)^{-1}\mathbf{K}_{\mathrm{dc}}{}_{n+1}^{i}\,. \tag{74}$$

3.6. Numerical integration

In the definition of the enhanced strain field, as presented in Eq. (20), a simplification is made by considering only rigid-body modes. This simplification enables using a regular quadrature rule to evaluate the integrals defined on the continuum [32].

To compute the contribution of the discontinuity cohesive forces, defined by the integrals over the discontinuity surface in Eqs. (65) and (72), the integration points of the discontinuity surface inside an element are defined based on triangulation, as illustrated in Fig. 4. In each triangle, the integration points are defined following a first-order Newton–Cotes rule [24,73,90]. The per-element triangulation is performed using Dynamic Programming optimization [91] with a pre-defined criterion for optimal triangles.

4. Numerical examples

In this section, we compare the KOS and SKON-embedded formulations in several numerical experiments. The examples considered are classical benchmark problems commonly used in the literature to evaluate the stability of cohesive stresses across embedded interfaces. Patch tests that assess the global behavior of these formulations can be found in [23,45,47,50]. The SOS formulation is excluded from this comparison, as it suffers from stress locking and is infrequently used in practice.

In contact mechanics, stick and slip conditions define two limiting regimes into which problems are typically classified. Under stick conditions, there are no relative displacements between the discontinuity surfaces $[\![\mathbf{u}]\!] = \mathbf{0}$; while under slip relative displacements are present, $[\![\mathbf{u}]\!] \neq \mathbf{0}$ [60,67]. The selected examples cover both cases.

Unless otherwise specified, the continuum is composed of a linear elastic material with Young's modulus of 10 GPa and Poisson's ratio of 0.3. The discontinuity is modeled with a linear isotropic cohesive material with a cohesive stiffness of 1.0e7 GPa/m. This high stiffness serves as a penalty parameter to avoid overlapping between the two regions separated by the discontinuity. Finally, the example in Section 4.6 explores the use of the SKON formulation in a fault reactivation problem.

In all examples, when a discontinuity intersects an internal mesh node, a small perturbation is applied to the node coordinates, as motivated by Idelsohn et al. [69]. The magnitude of the perturbation is equal to 0.1% of the mean characteristic length of the elements connected to the node and is applied following the normal vector of the discontinuity surface.

The computational implementation was performed in the in-house multiphysics framework GeMA (Geo Modeling Analysis)[2] [92]. It has been successfully applied to a wide range of problems, such as hydraulic fracturing [7,8,93–96], fluid flow and hydromechanical simulations in naturally fractured reservoirs [97–100], salt geomechanics [101–103], and others. For the examples presented in this work, we employ the interface element available in GeMA [104] to construct a discrete fracture model (DFM) with a similar mesh refinement, serving as a reference solution.

4.1. Horizontal fracture under uniform tension

This example assesses the ability of the formulation to transmit a uniform stress across an interface [61,76,105]. The geometry and boundary conditions are shown in Fig. 5

[2] https://web.tecgraf.puc-rio.br/gema/

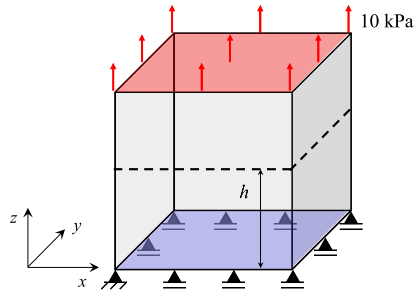

Fig. 5. Geometry and boundary conditions of a 1 × 1 × 1 m block with horizontal discontinuity surface under uniform tension.

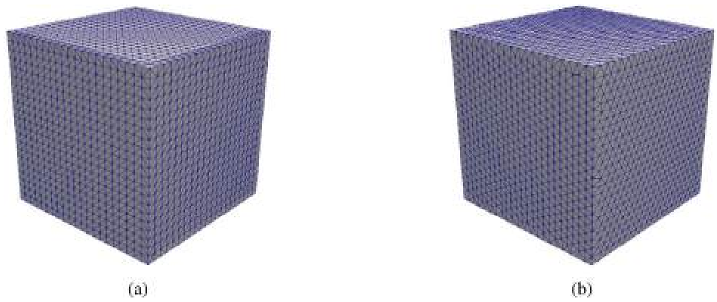

Fig. 6. Discretization with linear tetrahedral elements: (a) Continuum structured mesh (10648 nodes and 55566 elements); (b) Unstructured mesh (17158 nodes and 92312 elements).

Table 1
Discrete L^2 relative error of the normal cohesive traction for structured and unstructured meshes (z = 0.50 m).

Cohesive stiffness (GPa/m)	Structured		Unstructured	
	KOS	SKON	KOS	SKON
1.0E6	1.4553E−03	3.0503E−13	4.0703E−03	1.6679E−12
1.0E9	2.6661E−01	1.1648E−11	1.8689E+00	6.7425E−12
1.0E12	3.3325E−01	6.8231E−12	6.3140E+01	7.5093e−12
1.0E15	3.3333E−01	7.9905E−12	7.7657E+01	7.1787E−12

Two finite element meshes with linear tetrahedral elements were adopted, one structured and one unstructured, as shown in Fig. 6.

Following Ghosh et al. [76], we assess the discrete L^2 relative error of the normal traction, Eq. (75), for different values of cohesive stiffnesses

$$\text{Error} = \frac{\sqrt{\sum_{i=1}^{N_{\text{IP}}}\left(t_{\text{n}}^{(i)} - \bar{t}_{\text{n}}^{(i)}\right)^2}}{\sqrt{\sum_{i=1}^{N_{\text{IP}}}\left(\bar{t}_{\text{n}}^{(i)}\right)^2}}, \tag{75}$$

where N_{IP} is the total number of integration points along the interface, $t_{\text{n}}^{(i)}$ is the normal cohesive stress, and $\bar{t}_{\text{n}}$ is the reference value at the integration point i. For this problem, the normal cohesive stress along the interface is constant and equal to the pressure load applied at the top face, 10 kPa.

First, the discontinuity is set at z = 0.5 m. For each mesh, we solve the problem using both KOS and SKON with four values of cohesive stiffness: 1.0e6, 1.0e9, 1.0e12, and 1.0e15 GPa/m. Table 1 reports the relative error. Fig. 7 shows the normal cohesive traction along the interface for the case with 1.0e9 GPa/m.

The results in Fig. 7 and in Table 1 show that SKON recovers the uniform cohesive traction to round-off level (errors ∼ 10^{-11}–10^{-12}) on both meshes for all stiffnesses. In contrast, KOS does not transmit a uniform normal traction and its error depends on mesh and stiffness. The unstructured mesh shows the largest degradation as the stiffness increases. This superior behavior of the

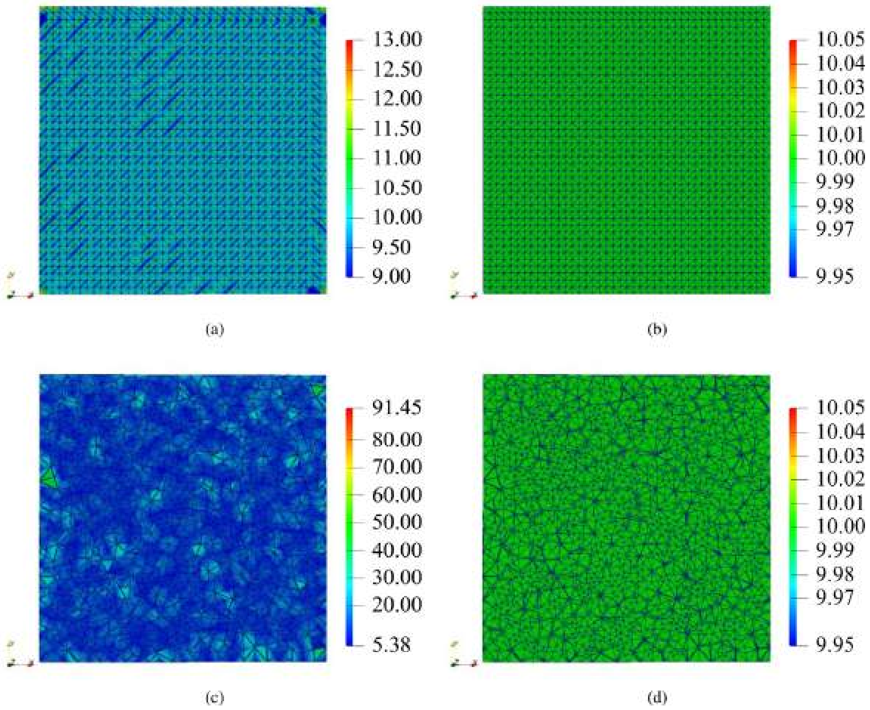

Fig. 7. Normal cohesive traction (kPa) along the plane at $z = 0.50$ m: (a) Structured mesh with KOS formulation; (b) Structured mesh with SKON formulation;(c) Unstructured mesh with KOS formulation; (d) Unstructured mesh with SKON formulation.

Table 2
Discrete L^2 relative error of the normal cohesive traction for structured and unstructured meshes ($z = 0.51$ m).

Cohesive stiffness (GPa/m)	Structured		Unstructured	
	KOS	SKON	KOS	SKON
1.0E6	2.8792e−02	3.0483e−13	4.1872e−03	1.9495e−11
1.0E9	8.5379e−01	1.1834e−11	1.8797e+00	4.6797e−11
1.0E12	1.4963e+00	1.1435e−11	9.2162e+00	9.0025e−12
1.0E15	1.4975e+00	7.9905e−12	9.2830e+00	8.9734e−12

SKON formulation is due to the strong enforcement of the orthogonality condition, Eq. (36), and its fulfillment of the zero mean condition, Eq. (63), both of which are violated by the KOS formulation.

To test dependence on the relative position of the discontinuity inside elements, we repeat the analysis with the horizontal discontinuity at $z = 0.51$ m using the same meshes and stiffness values. Fig. 8 shows the normal cohesive traction along the interface for the case with 1.0e9 GPa/m. Table 2 reports the discrete errors. SKON's error remains at round-off level on both meshes. KOS errors increase notably relative to the $z = 0.50$ m case, especially on the structured mesh, confirming sensitivity to interface placement. This also explains the higher amplitudes observed in the KOS formulation for both discontinuity placements using the unstructured mesh.

Across all tests, the difference in total execution time between the KOS and SKON formulations remained below 1%. Therefore, the SKON formulation could be used without any significant increase in computational expense.

4.2. Horizontal fracture subjected to compression under a stick condition

This example has been used in both XFEM [60,61] and E-FEM [41] literature. Geometry and boundary conditions are shown in Fig. 9(a). The clamped supports produce a non-uniform compression state.

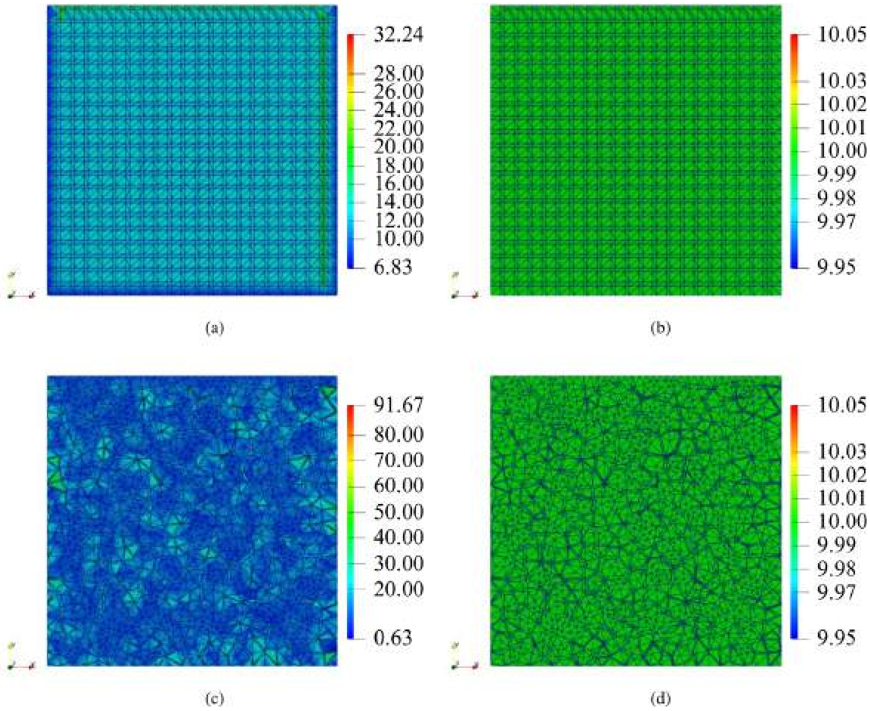

Fig. 8. Normal cohesive stress (kPa) in the discontinuity surface located at $z = 0.51$ m: (a) Structured mesh with KOS formulation; (b) Structured mesh with SKON formulation; (c) Unstructured mesh with KOS formulation; (d) Unstructured mesh with SKON formulation.

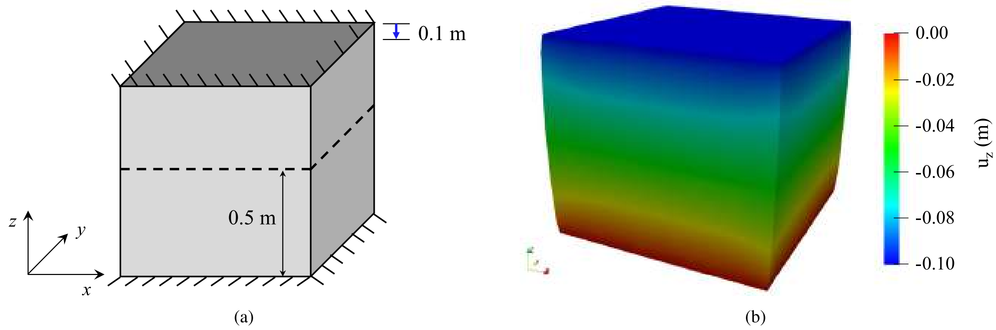

Fig. 9. Block of $1 \times 1 \times 1$ m with horizontal discontinuity surface: (a) Geometry and boundary conditions; (b) z-component of the displacement field displayed in the deformed configuration.

The same finite element meshes used in the previous example (Fig. 6) were adopted. For each mesh discretization, the problem was solved with both KOS and SKON embedded formulations. The normal cohesive stress field over the discontinuity plane is presented in Fig. 10. It is observed that for both discretizations, the SKON formulation provided a smooth normal cohesive stress field. On the other hand, the KOS formulation has led to spurious oscillations, which are amplified by the unstructured mesh.

Fig. 11 presents the normal cohesive stress profile along the middle of the discontinuity plane and compares the solutions with those obtained with the DFM.

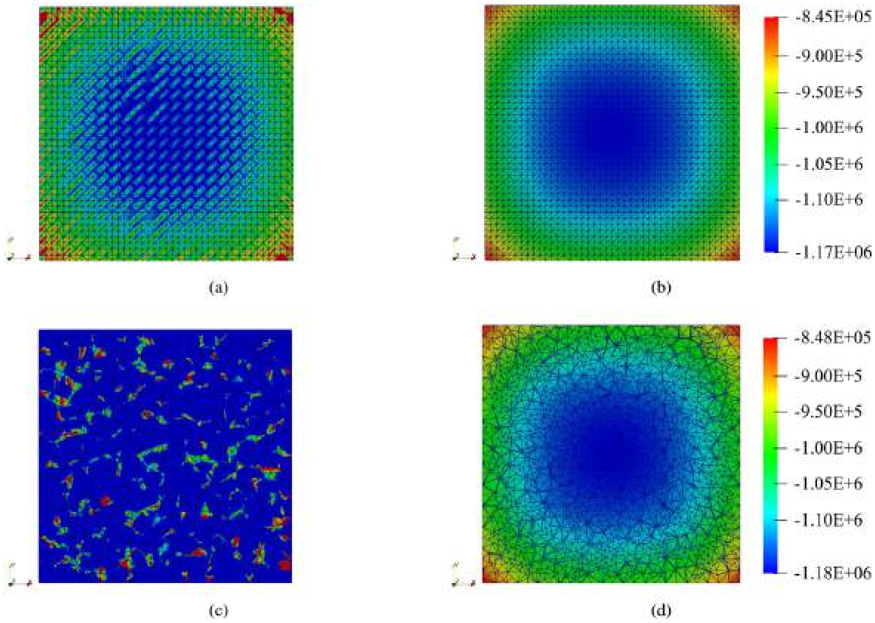

Fig. 10. Normal cohesive stress (kPa): (a) Structured mesh with KOS formulation; (b) Structured mesh with SKON formulation;(c) Unstructured mesh with KOS formulation; (d) Unstructured mesh with SKON formulation.

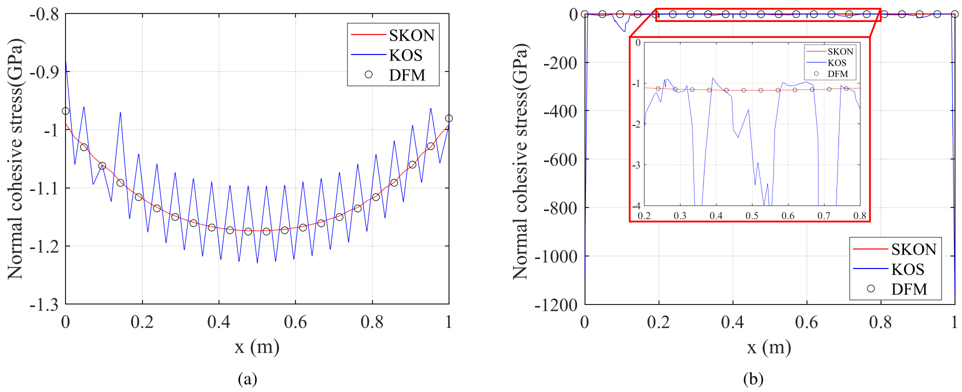

Fig. 11. Normal cohesive stress profile along x at y = 0.5 m: (a) Structured mesh; (b) Unstructured mesh.

Fig. 11 shows that SKON recovers the non-uniform compressive stress and matches the DFM reference. By contrast, KOS exhibits spurious oscillations, as in Section 4.1. Their larger amplitude on the unstructured mesh reflects KOS's sensitivity to the discontinuity position within elements.

4.3. Horizontal fracture subjected to compression and shear under a stick condition

The geometry and boundary conditions are shown in Fig. 12(a) [57,63]. A plane strain condition is assumed. Four finite element types are tested: linear and quadratic triangular and quadrilateral elements, following the discretizations shown in Figs. 12(b) and 12(c).

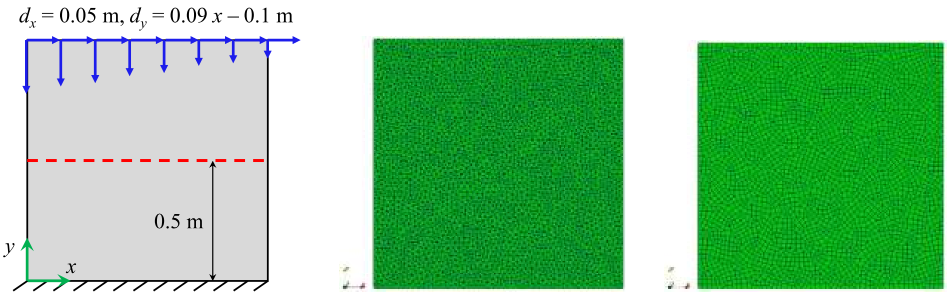

(a) (b) (c)

Fig. 12. Square domain of 1 × 1 m with a horizontal fracture under combined shear and compression: (a) Geometry and boundary conditions; (b) Triangular mesh with 6828 elements, 3413 nodes for linear interpolation (tri3), and 13,449 nodes for quadratic interpolation (tri6); (c) Quadrilateral mesh with 3391 elements, 3288 nodes for linear interpolation (quad4), and 9762 nodes for quadratic interpolation (quad8).

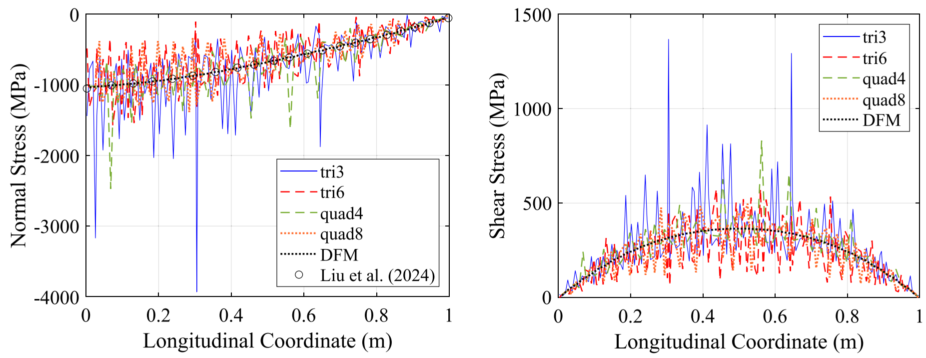

(a) (b)

Fig. 13. Cohesive stresses along the discontinuity with the KOS formulation: (a) Normal cohesive stress and (b) Shear cohesive stress.

Table 3
Discrete L^2 relative error of the normal and shear stresses along horizontal fracture subjected to compression and shear under a stick condition.

Element type	Normal stress		Shear stress	
	KOS	SKON	KOS	SKON
tri3	1.114405E+00	1.954446E−02	1.070511E+00	1.953698E−02
tri6	6.528774E−01	6.520195E−03	6.618904E−01	6.219319E−03
quad4	5.115037E−01	1.250764E−02	4.173368E−01	1.178531E−02
quad8	4.351861E−01	5.868543E−03	4.117455E−01	5.496001E−03

Figs. 16 and 17 show the normal and shear cohesive stresses along the discontinuity using both KOS and SKON formulations for all four element types, respectively. For the normal component, we also include the solution reported by Liu et al. [41], which uses a non-local (smoothed) KOS embedded formulation. A reference solution is once again generated using a DFM with interface elements and a structured mesh composed of linear quadrilateral elements with a size of 0.02 m. Table 3 reports the discrete relative errors.

The results in Fig. 13 and Table 3 indicate that the KOS formulation produces spurious oscillations for all element types, with the largest errors observed for the linear triangular element. In contrast, Fig. 14 demonstrates that the SKON formulation effectively mitigates these oscillations for all tested elements. While both linear (tri3, quad4) and quadratic (tri6, quad8) finite elements yield cohesive stresses that closely match the reference DFM solution, quadratic elements provide slightly smoother stress profiles. Overall, the consistency between the E-FEM results and the reference DFM solution confirms the accuracy and robustness of the SKON formulation for reliably modeling cohesive stress distributions under stick conditions.

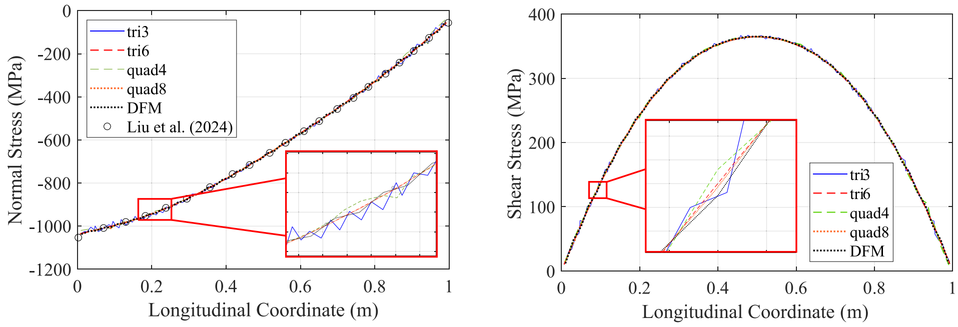

(a) (b)

Fig. 14. Cohesive stresses along the discontinuity with the SKON formulation: (a) Normal cohesive stress and (b) Shear cohesive stress.

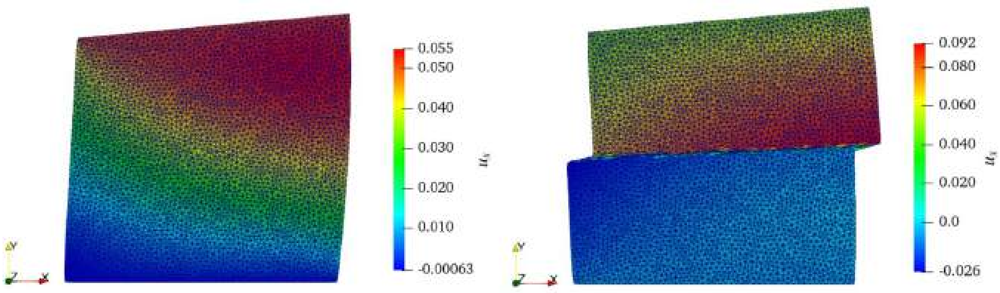

(a) (b)

Fig. 15. Horizontal displacement component in the deformed configuration: (a) k_s = 1.0e7 GPa and (b) k_s=1.0e−3 GPa.

The SKON results for the normal cohesive stress, Fig. 14(a), closely match the non-local KOS solution reported by Liu et al. [41]. Thus, under stick conditions, SKON achieves a comparable level of traction smoothness while eliminating the additional computational cost associated with non-local regularization.

4.4. Horizontal fracture subjected to compression and shear under a slip condition

The geometry, boundary conditions, and finite element meshes are identical to those used in the example presented in Section 4.3. To induce a slip condition, the shear cohesive stiffness is reduced to 1.0e−3 GPa/m, as shown in Fig. 15. Therefore, the tangent cohesive constitutive matrix, $\mathbf{T}_d$, presented in Eq. (70), is anisotropic.

Figs. 16 and 17 show the normal and shear cohesive stresses along the discontinuity using both KOS and SKON formulations for all four element types, respectively. The same DFM used in Section 4.3 acts as the reference solution. Table 4 reports the discrete relative errors.

As in the case where the stick condition is imposed, here too the SKON formulation yields smooth cohesive stress distributions, while the KOS presented high amplitude spurious oscillations. Observe that the use of linear interpolation finite elements increases very slightly the level of noise in the shear cohesive stresses, which corresponds to the component associated with the low cohesive stiffness. However, the amplitude of this noise is negligible. Once again, employing quadratic finite elements eliminates even this noise, leading to smoother solutions that match the DFM result.

Using linear quadrilateral elements, we conducted a mesh-convergence study. Besides the mesh in Fig. 12(c) (3391 elements), three additional meshes with 1000, 13155, and 51837 elements were analyzed. Table 5 reports the discrete L^2-relative error with

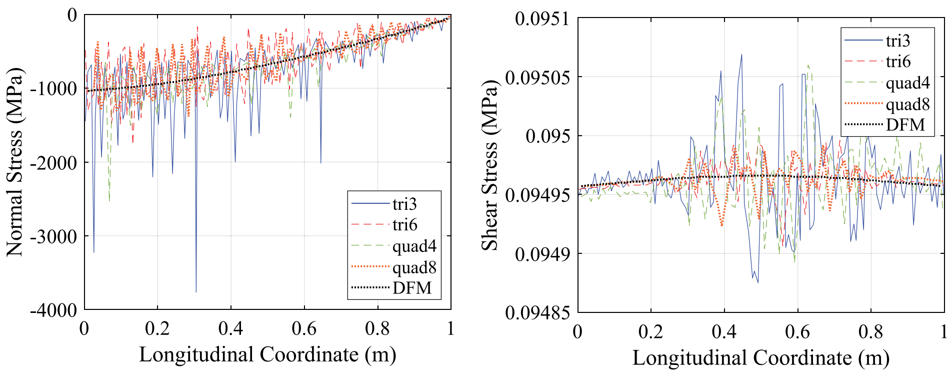

(a) (b)

Fig. 16. Cohesive stresses along the discontinuity with the KOS formulation: (a) Normal cohesive stress; (b) Shear cohesive stress.

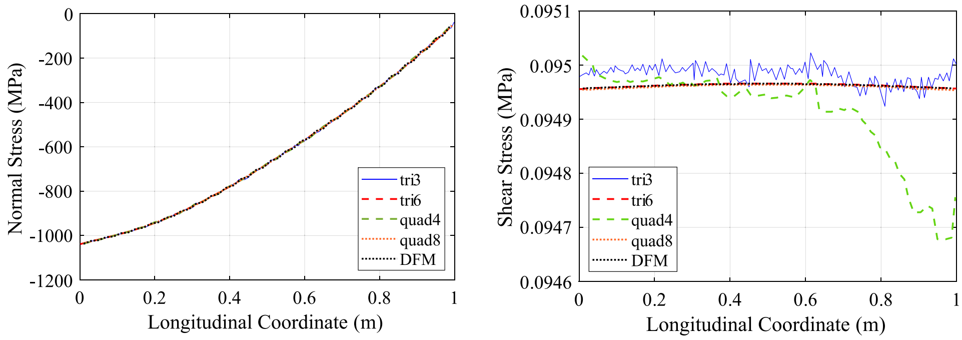

(a) (b)

Fig. 17. Cohesive stresses along the discontinuity with the SKON formulation: (a) Normal cohesive stress; (b) Shear cohesive stress.

Table 4
Discrete L^2 relative error of the normal and shear stresses along horizontal fracture subjected to compression and shear under a slip condition.

Element type	Normal stress		Shear stress	
	KOS	SKON	KOS	SKON
tri3	1.113040E+00	9.879368E−03	5.763900E−04	4.246665E−04
tri6	6.463622E−01	6.665083E−03	1.979567E−04	8.711183E−06
quad4	4.599423E−01	2.455538E−03	3.852615E−04	6.228178E−04
quad8	4.220712E−01	5.871546E−03	1.481302E−04	2.669716E−05

respect to the DFM solution. The SKON normal-traction error decreases monotonically with refinement, whereas the KOS normal-traction error increases. For shear tractions, KOS errors decrease with refinement, and SKON shows a non-monotone but overall decreasing trend, reaching a similar magnitude at the finest mesh. It is worth noticing, however, that in this example, the behavior of the shear tractions is several orders smaller, making them less informative for assessing oscillations.

4.5. Inclined fracture subjected to compression under a slip condition

This problem is used in the literature to assess the capability of the formulation to represent frictional sliding based on Coulomb's

Table 5
Mesh-convergence for quad4 elements. Discrete L^2-relative error of fracture-normal and shear tractions, evaluated along a horizontal fracture subjected to combined compression and shear under a slip condition.

Number of elements	Normal stress		Shear stress	
	KOS	SKON	KOS	SKON
1000	1.485834E−01	2.911571E−03	2.336703E−04	1.724564E−04
3391	4.599423E−01	2.455538E−03	3.852615E−04	6.228178E−04
13155	3.541351E−01	1.397399E−03	1.385180E−04	2.812501E−04
51837	4.245659E−01	1.208483E−03	1.007622E−04	1.116127E−04

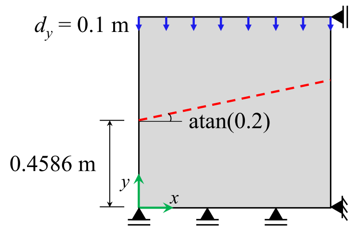

Fig. 18. Geometry and boundary conditions of 1 × 1 m domain with an inclined fracture [57].

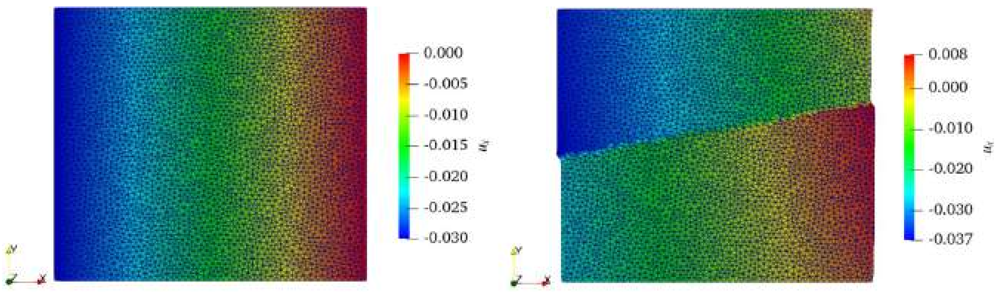

(a) (b)

Fig. 19. Horizontal displacement component in the deformed configuration: (a) μ = 0.21 and (b) μ = 0.19.

law [41,57,63,106,107]. The geometry and boundary conditions are presented in Fig. 18. The same meshes from Section 4.3 are used.

Here, the Young modulus is 1 GPa, the Poisson ratio is 0.3, and both the normal and shear cohesive stiffness values are set to 1.0e7 GPa/m. Plane stress conditions are assumed. An elastoplastic cohesive model based on the Mohr–Coulomb yield criteria is adopted [52,108]. Two values of the friction coefficient, μ, are considered, one lower and one higher than the fracture inclination. As expected, Fig. 19 shows that the discontinuity remains in the stick condition for $\mu = 0.21$, and it reaches a slip condition with $\mu = 0.19$.

We highlight that both SKON and KOS formulations accurately capture this global behavior. Fig. 20 shows that the horizontal displacement fields over the continuum are identical for both formulations in both cases.

Despite being capable of properly representing the global behavior, the KOS formulation leads to spurious oscillations even when the model is in the stick condition ($\mu = 0.21$), as shown in Fig. 21. In contrast, the SKON formulation accurately captures the constant stress state along the discontinuity.

However, under the slip condition, the SKON formulation no longer produces a smooth cohesive stress field along the discontinuity. Fig. 22 illustrates the cohesive stress distribution obtained using different finite element types. In this case, the use of higher-order interpolation elements proves insufficient to eliminate the oscillations, which indicates that they result from missing kinematic modes associated with the discontinuity. Nevertheless, it is important to highlight that the amplitude of these oscillations remains significantly smaller than those observed with the KOS formulation.

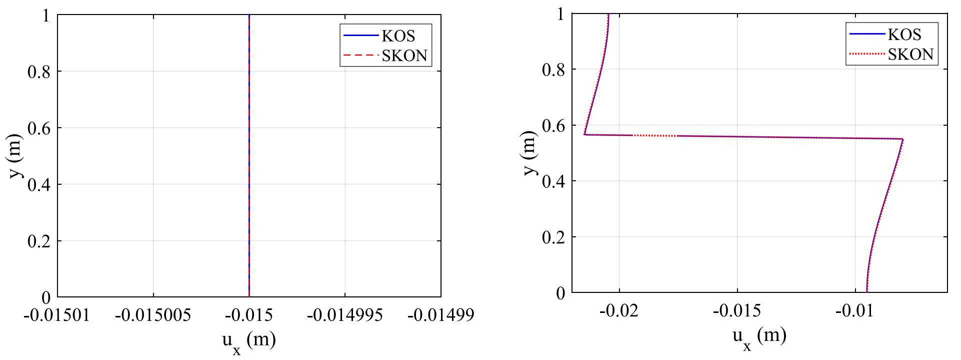

(a) (b)

Fig. 20. Horizontal displacement profile over the continuum mesh along y at $x = 0.5$ m: (a) $\mu = 0.21$ and (b) $\mu = 0.19$. Solutions using linear triangular finite elements.

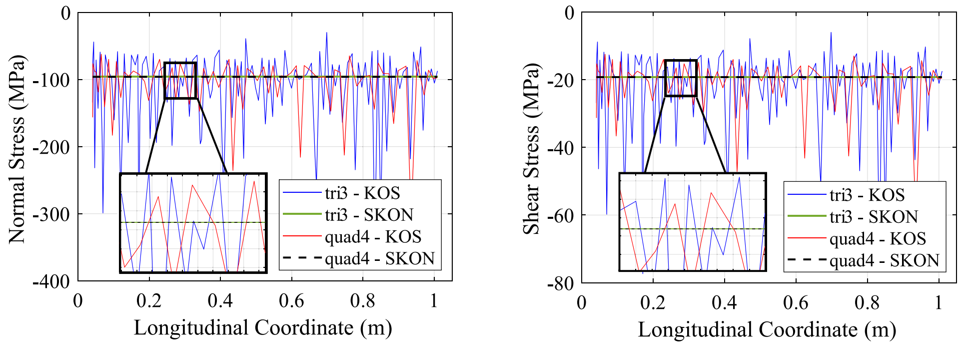

(a) (b)

Fig. 21. Cohesive stresses along the discontinuity in the stick condition ($\mu = 0.21$): (a) normal cohesive stress; (b) shear cohesive stress.

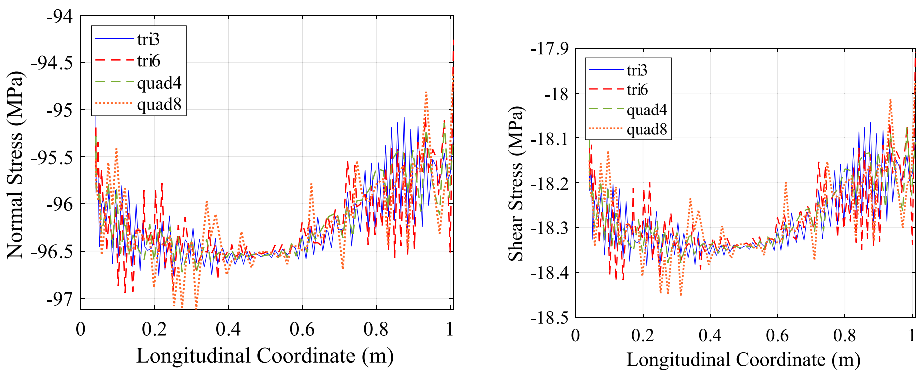

(a) (b)

Fig. 22. Cohesive stresses along the discontinuity under the slip condition for the SKON formulation ($\mu = 0.19$): (a) normal cohesive stress and (b) shear cohesive stress.

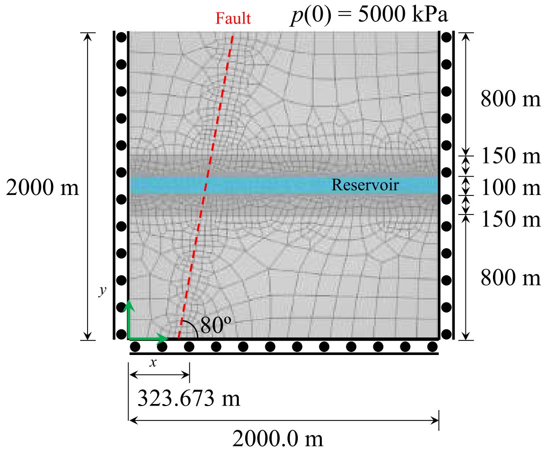

Fig. 23. Fault reactivation problem [109]: Geometry, boundary conditions, and finite element mesh used in the DFM.

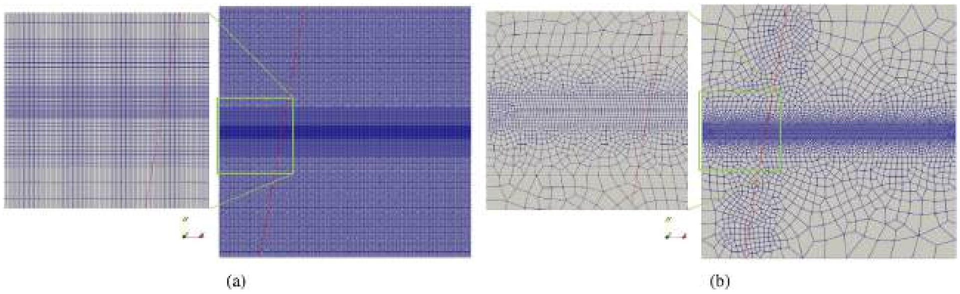

Fig. 24. Finite element meshes: (a) Structured; (b) Unstructured.

4.6. Fault reactivation assessment

This study investigates a fault reactivation model based on the one analyzed by Cappa and Rutqvist [109]. Cavalcanti et al. [52] addressed this problem using a fully coupled hydromechanical embedded finite element formulation and reported that due to spurious oscillations in the cohesive stresses, the fault could prematurely reactivate. In this previous study, the KOS formulation was used. Therefore, in this work, we investigate the application of the SKON formulation to the same problem. The geometry, boundary conditions, and finite element mesh used in the reference DFM are presented in Fig. 23.

The continuum model is assumed linear elastic, with a Young modulus equal to 10 GPa and a Poisson ratio equal to 0.25. The fault is elastoplastic, with a cohesive stiffness equal to 5.0 GPa/m, friction angle equal to 25°, dilatancy angle equal to 20°, and zero cohesion. The simulation consists of applying a total pore pressure increment of 15 MPa over the course of 5 years on the left side of the reservoir with respect to the fault. The pore pressure and stresses are initialized considering a hydrostatic state, with the specific water weight equal to 10 kN/m^3, the solid specific weight equal to 22.7 kN/m^3, and the Earth pressure coefficient equal to 0.7. The pore pressure field acts on the finite element model as an equivalent external force vector, as presented in Appendix A.

Two finite element meshes using linear quadrilateral finite elements are used, one structured and one unstructured, as shown in Fig. 24.

Fig. 25 shows the normal and shear cohesive stresses along the fault using E-FEM with both meshes and compares them with the solution obtained using the DFM.

The results in Fig. 25 show excellent agreement with the reference solution and no spurious oscillations with both meshes.

We also analyze the evolution of the slip tendency parameter (ST), Eq. (76), at the fault point on the top of the reservoir layer. Fig. 26 shows that a similar trajectory is obtained by the two E-FEM meshes and the DFM. In the three of them, the reactivation at this point of the fault is reached for the same pore pressure increment.

$$ST = \frac{|\mathbf{t}_{\mathrm{d}} \cdot \mathbf{m}|}{(\mathbf{t}_{\mathrm{d}} \cdot \mathbf{n}_{\mathrm{d}})\tan(25°)} \tag{76}$$

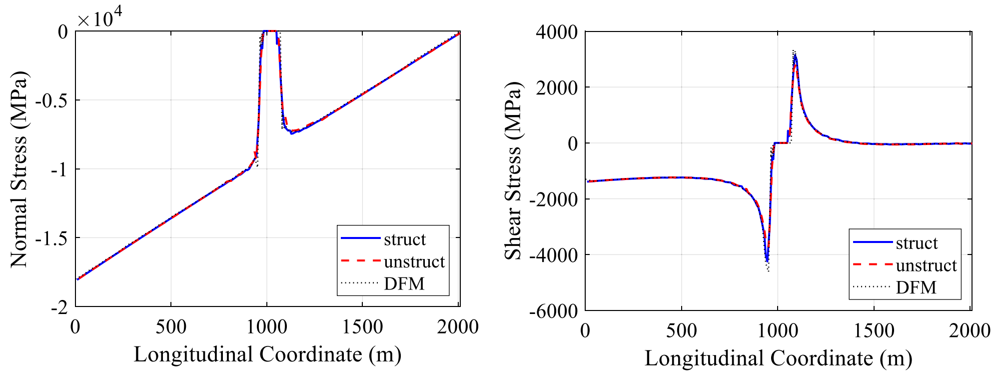

(a) (b)

Fig. 25. Cohesive stresses along the fault: (a) normal cohesive stress; (b) shear cohesive stress.

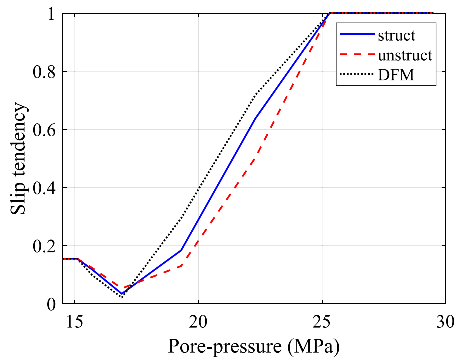

Fig. 26. Slip tendency evolution.

5. Conclusions

This work presented a series of numerical experiments to assess the behavior of the cohesive stresses at discontinuities using embedded finite element formulations based on the Strong Discontinuity Approach. The examples explore the use of different types of finite element and cover both stick and slip contact conditions. Based on the results obtained, we reach the following conclusions:

- The SKON formulation provides a smoother cohesive stress field by enforcing the local equilibrium of the discontinuity in a strong sense.
- Under stick conditions, the SKON formulation consistently produces a smooth cohesive-stress field for all finite-element types tested, on both structured and unstructured meshes.
- Under slip conditions governed by a frictional contact law, SKON may exhibit small-amplitude oscillations that persist even with higher-order bulk interpolation. This behavior is consistent with previous observations for conventional interface elements, where anisotropic cohesive laws or strong penalty enforcement can induce similar artifacts [76]. In this regard, a non-local formulation may serve as an effective alternative [41].
- The SKON formulation proves to be a viable approach for modeling stress changes and assessing fault reactivation risk induced by injection processes, without requiring special mesh configurations, as previously reported for the KOS formulation by Cavalcanti et al. [52].
- For problems involving lower-order discontinuities, such as material interfaces, the boundary conditions are identical to those of a strong discontinuity under a stick condition. Therefore, the SKON-based formulation is sufficient to guarantee a smooth cohesive stress field.

Future work will extend the present comparison of SDA-based E-FEM formulations to convergence analyses of the nonlinear solution scheme for large-scale, application-driven 3D non-linear problems. It will also assess additional deformation modes that admit discontinuous bulk strains inside the element (weak discontinuities) as an alternative to further reduce the small oscillations observed for SKON under the slip condition.

CRediT authorship contribution statement

Danilo Cavalcanti: Writing – review & editing, Writing – original draft, Validation, Software, Methodology, Formal analysis, Conceptualization. **Cristian Mejia:** Writing – review & editing, Supervision, Software, Methodology, Formal analysis. **Caio Souza:** Writing – review & editing, Validation, Software. **Carlos A. Mendes:** Writing – review & editing, Validation, Software, Project administration. **Ignasi de-Pouplana:** Writing – review & editing, Supervision, Project administration. **Guillermo Casas:** Writing – review & editing, Supervision. **Deane Roehl:** Writing – review & editing, Supervision, Project administration, Methodology, Formal analysis, Conceptualization.

Declaration of competing interest

The authors have no affiliation with any organization with a direct or indirect financial interest in the subject matter discussed in the manuscript.

Acknowledgments

This research was carried out in association with the ongoing R&D project "Risk assessment of geological fault reactivation by CO_2 injection" (PUC-Rio/ ExxonMobil Exploração Brasil Ltda./ ANP) sponsored by ExxonMobil Exploração Brasil Ltda. under the ANP R&D levy regulation and ANP project number 23449-2. The authors acknowledge the financial support of the Brazilian National Council for Scientific and Technological Development (CNPq) Grants 315077/2023-9 and 308056/2022-1; Carlos Chagas Filho Foundation for Supporting Research in the State of Rio de Janeiro (FAPERJ) Grants E-26/200.463/2023 and E-26/201.391/2021. This study was financed in part by the Coordenação de Aperfeiçoamento de Pessoal de Nível Superior - Brasil (CAPES) - Finance Code 001.

Appendix A

To incorporate the hydromechanical forces due to the presence of a pore pressure field in the domain, we consider a saturated porous media and apply Biot's stress decomposition [110,111],

$$\boldsymbol{\Sigma}(\mathbf{d},\boldsymbol{\alpha}) = \boldsymbol{\Sigma}'(\mathbf{d},\boldsymbol{\alpha}) - p\,\mathbf{I}, \tag{77}$$

$$\mathbf{t}_{\mathrm{d}}(\boldsymbol{\alpha}) = \mathbf{t}'_{\mathrm{d}}(\boldsymbol{\alpha}) - p_{\mathrm{d}}\,\mathbf{n}_{\mathrm{d}}, \tag{78}$$

where p is the pore pressure field in the continuum domain and p_{d} is the pore pressure field within the discontinuity. These pore pressure fields are discretized as follows

$$p(\mathbf{x}) = \mathbf{N}_{\mathrm{p}}(\mathbf{x})\;\mathbf{p}, \tag{79}$$

$$p_{\mathrm{d}}(\mathbf{x}) = \mathbf{N}_{\mathrm{p}}^{\mathrm{d}}(\mathbf{x})\;\mathbf{p}_{\mathrm{d}}. \tag{80}$$

where $\mathbf{N}_{\mathrm{p}}(\mathbf{x})$ is the row vector of shape functions associated with the pore pressure field in the bulk domain, and $\mathbf{N}_{\mathrm{p}}^{\mathrm{d}}(\mathbf{x})$ is the row vector of shape functions defined on the discontinuity surface.

Substituting Eqs. (77)–(80) into the system (65) leads to

$$\begin{cases} \mathbf{r}_{\mathrm{c}} = \int_{\Omega} \mathbf{B}^{\top}\boldsymbol{\Sigma}'\,d\Omega - \int_{\Omega} \mathbf{B}^{\top}\mathbf{m}\,\mathbf{N}_{\mathrm{p}}\,d\Omega\,\mathbf{p} - \int_{\Gamma_t} \mathbf{N}^{\top}\mathbf{t}\,d\Gamma - \int_{\Omega} \mathbf{N}^{\top}\mathbf{b}\,d\Omega \\ \mathbf{r}_{\mathrm{d}} = \int_{\Omega} \mathbf{G}^{\top}\boldsymbol{\Sigma}'\,d\Omega - \int_{\Omega} \mathbf{G}^{\top}\mathbf{m}\,\mathbf{N}_{\mathrm{p}}\,d\Omega\,\mathbf{p} + \int_{\Gamma_{\mathrm{d}}} \mathbf{N}_{\mathrm{d}}^{\top}\mathbf{t}'_{\mathrm{d}}\,d\Gamma - \int_{\Gamma_{\mathrm{d}}} \mathbf{N}_{\mathrm{d}}^{\top}\mathbf{n}_{\mathrm{d}}\,\mathbf{N}_{\mathrm{p}}^{\mathrm{d}}\,d\Gamma\,\mathbf{p}_{\mathrm{d}} \end{cases} \tag{81}$$

Appendix B. Supplementary data

Supplementary material related to this article can be found online at https://doi.org/10.1016/j.finel.2025.104485.

Data availability

Data will be made available on request.

References

[1] M. Cervera, G. Barbat, M. Chiumenti, J.-Y. Wu, A comparative review of XFEM, mixed FEM and phase-field models for quasi-brittle cracking, Arch. Comput. Methods Eng. 29 (2) (2022) 1009–1083.

[2] B. Flemisch, I. Berre, W. Boon, A. Fumagalli, N. Schwenck, A. Scotti, I. Stefansson, A. Tatomir, Benchmarks for single-phase flow in fractured porous media, Adv. Water Resour. 111 (January 2017) (2018) 239–258, http://dx.doi.org/10.1016/j.advwatres.2017.10.036.

[3] A. Fumagalli, E. Keilegavlen, S. Scialò, Conforming, non-conforming and non-matching discretization couplings in discrete fracture network simulations, J. Comput. Phys. 376 (2019) 694–712, http://dx.doi.org/10.1016/j.jcp.2018.09.048.

[4] J.M. Segura, I. Carol, Coupled HM analysis using zero-thickness interface elements with double nodes. Part I: Theoretical model, Int. J. Numer. Anal. Methods Geomech. 32 (18) (2008) 2083–2101, http://dx.doi.org/10.1002/nag.735.

[5] L. Jing, O. Stephansson, Discrete Fracture Network (DFN) Method, Dev. Geotech. Eng. 85 (2007) 365–398, http://dx.doi.org/10.1016/S0165-1250(07)85010-3.

[6] V.P. Nguyen, H. Lian, T. Rabczuk, S. Bordas, Modelling hydraulic fractures in porous media using flow cohesive interface elements, Eng. Geol. 225 (2017) 68–82, http://dx.doi.org/10.1016/j.enggeo.2017.04.010.

[7] J. Rueda, C. Mejia, D. Roehl, L.C. Pereira, Hydro-mechanical modeling of hydraulic fracture propagation and its interactions with frictional natural fractures, Comput. Geotech. 111 (2019) 290–300.

[8] C. Mejia, J. Rueda, D. Roehl, Numerical simulation of three-dimensional fracture interaction, Comput. Geotech. 122 (2020) 103528.

[9] O.L. Manzoli, P.R. Cleto, M. Sánchez, L.J. Guimarães, M.A. Maedo, On the use of high aspect ratio finite elements to model hydraulic fracturing in deformable porous media, Comput. Methods Appl. Mech. Engrg. 350 (2019) 57–80, http://dx.doi.org/10.1016/j.cma.2019.03.006.

[10] H. Fabbri, M. Sánchez, M. Maedo, P. Cleto, O. Manzoli, Modeling gas breakthrough and flow phenomena through engineered barrier systems using a discrete fracture approach, Comput. Geotech. 154 (2023) 105148, http://dx.doi.org/10.1016/j.compgeo.2022.105148.

[11] P. Lima, N. Shauer, J.B. Villegas, P.R. Devloo, DFNMesh: Finite element meshing for discrete fracture matrix models, Adv. Eng. Softw. 186 (March) (2023) 103545, http://dx.doi.org/10.1016/j.advengsoft.2023.103545.

[12] V.P. Nguyen, An open source program to generate zero-thickness cohesive interface elements, Adv. Eng. Softw. 74 (2014) 27–39, http://dx.doi.org/10.1016/j.advengsoft.2014.04.002.

[13] I. Babuška, J.M. Melenk, The Partition of Unity Method, Internat. J. Numer. Methods Engrg. 40 (4) (1997) 727–758, http://dx.doi.org/10.1002/(SICI)1097-0207(19970228)40:4<727::AID-NME86>3.0.CO;2-N.

[14] C.A. Duarte, J.T. Oden, An *h-p* adaptive method using clouds, Comput. Methods Appl. Mech. Engrg. 139 (1) (1996) 237–262, http://dx.doi.org/10.1016/S0045-7825(96)01085-7.

[15] N. Moës, J. Dolbow, T. Belytschko, A finite element method for crack growth without remeshing, Internat. J. Numer. Methods Engrg. 46 (1) (1999) 131–150, http://dx.doi.org/10.1002/(SICI)1097-0207(19990910)46:1<131::AID-NME726>3.0.CO;2-J.

[16] T. Belytschko, N. Moës, S. Usui, C. Parimi, Arbitrary discontinuities in finite elements, Internat. J. Numer. Methods Engrg. 50 (4) (2001) 993–1013, http://dx.doi.org/10.1002/1097-0207(20010210)50:4<993::AID-NME164>3.0.CO;2-M, URL https://onlinelibrary.wiley.com/doi/abs/10.1002/1097-0207%2820010210%2950%3A4%3C993%3A%3AAID-NME164%3E3.0.CO%3B2-M.

[17] J. Dolbow, N. Moës, T. Belytschko, Discontinuous enrichment in finite elements with a partition of unity method, Finite Elem. Anal. Des. 36 (3) (2000) 235–260, http://dx.doi.org/10.1016/S0168-874X(00)00035-4, Robert J. Melosh Medal Competition, Duke University, Durham NC, USA, March 1999.

[18] G. Wells, L. Sluys, Application of embedded discontinuities for softening solids, Eng. Fract. Mech. 65 (2) (2000) 263–281, http://dx.doi.org/10.1016/S0013-7944(99)00120-4.

[19] J. Oliver, I.F. Dias, A.E. Huespe, Crack-path field and strain-injection techniques in computational modeling of propagating material failure, Comput. Methods Appl. Mech. Engrg. 274 (2014) 289–348, http://dx.doi.org/10.1016/j.cma.2014.01.008.

[20] H.R. Lotfi, P.B. Shing, Embedded representation of fracture in concrete with mixed finite elements, Internat. J. Numer. Methods Engrg. 38 (1995) 1307–1325.

[21] J.-Y. Wu, A unified phase-field theory for the mechanics of damage and quasi-brittle failure, J. Mech. Phys. Solids 103 (2017) 72–99.

[22] M. Paggi, J. Reinoso, Revisiting the problem of a crack impinging on an interface: a modeling framework for the interaction between the phase field approach for brittle fracture and the interface cohesive zone model, Comput. Methods Appl. Mech. Engrg. 321 (2017) 145–172.

[23] J.-Y. Wu, Unified analysis of enriched finite elements for modeling cohesive cracks, Comput. Methods Appl. Mech. Engrg. 200 (45–46) (2011) 3031–3050.

[24] D. Dias-da Costa, J. Alfaiate, L.J. Sluys, E. Júlio, A comparative study on the modelling of discontinuous fracture by means of enriched nodal and element techniques and interface elements, Int. J. Fract. 161 (1) (2010) 97–119, http://dx.doi.org/10.1007/s10704-009-9432-6.

[25] R.I. Borja, Assumed enhanced strain and the extended finite element methods: A unification of concepts, Comput. Methods Appl. Mech. Engrg. 197 (33) (2008) 2789–2803, http://dx.doi.org/10.1016/j.cma.2008.01.019.

[26] J.M. Melenk, I. Babuška, The partition of unity finite element method: Basic theory and applications, Comput. Methods Appl. Mech. Engrg. 139 (1) (1996) 289–314, http://dx.doi.org/10.1016/S0045-7825(96)01087-0, URL https://www.sciencedirect.com/science/article/pii/S0045782596010870.

[27] E.N. Dvorkin, A.M. Cuitino, G. Gioia, Finite elements with displacement interpolated embedded localization lines insensitive to mesh size and distortions, Internat. J. Numer. Methods Engrg. 30 (3) (1990) 541–564.

[28] E.N. Dvorkin, A.P. Assanelli, 2D finite elements with displacement interpolated embedded localization lines: the analysis of fracture in frictional materials, Comput. Methods Appl. Mech. Engrg. 90 (1–3) (1991) 829–844.

[29] J.C. Simo, M.S. Rifai, A class of mixed assumed strain methods and the method of incompatible modes, Internat. J. Numer. Methods Engrg. 29 (8) (1990) 1595–1638, http://dx.doi.org/10.1002/nme.1620290802.

[30] J.C. Simo, J. Oliver, F. Armero, An analysis of strong discontinuities induced by strain-softening in rate-independent inelastic solids, Comput. Mech. 12 (5) (1993) 277–296.

[31] J. Oliver, Modelling strong discontinuities in solid mechanics via strain softening constitutive equations. Part 1: Fundamentals, Internat. J. Numer. Methods Engrg. 39 (21) (1996) 3575–3600.

[32] D. Dias-da Costa, J. Alfaiate, L. Sluys, E. Júlio, A discrete strong discontinuity approach, Eng. Fract. Mech. 76 (9) (2009) 1176–1201.

[33] P.M.A. Areias, J.M.A. César de Sá, C.A. Conceição António, J.a.S.a.O. Carneiro, V.M.P. Teixeira, Strong displacement discontinuities and Lagrange multipliers in the analysis of finite displacement fracture problems, Comput. Mech. 35 (1) (2004) 54–71, http://dx.doi.org/10.1007/s00466-004-0603-z.

[34] M. Jirásek, Comparative study on finite elements with embedded discontinuities, Comput. Methods Appl. Mech. Engrg. 188 (1–3) (2000) 307–330.

[35] C. Pionke, G. Wempner, Finite elements via the Hu-Washizu theorem - convergence and error, in: G.Z. Voyiadjis, L.C. Bank, L.J. Jacob (Eds.), Mechanics of Materials and Structures, in: Studies in Applied Mechanics, vol. 35, Elsevier, 1994, pp. 123–142, http://dx.doi.org/10.1016/B978-0-444-89918-7.50013-7.

[36] T. Belytschko, J. Fish, B.E. Engelmann, A finite element with embedded localization zones, Comput. Methods Appl. Mech. Engrg. 70 (1) (1988) 59–89, http://dx.doi.org/10.1016/0045-7825(88)90180-6, URL https://www.sciencedirect.com/science/article/pii/0045782588901806.

[37] R. Larsson, K. Runesson, Element-embedded localization band based on regularized displacement discontinuity, J. Eng. Mech. 122 (5) (1996) 402–411, http://dx.doi.org/10.1061/(ASCE)0733-9399(1996)122:5(402).

[38] Y. Zhang, X. Zhuang, Cracking elements: A self-propagating Strong Discontinuity embedded Approach for quasi-brittle fracture, Finite Elem. Anal. Des. 144 (2018) 84–100, http://dx.doi.org/10.1016/j.finel.2017.10.007.

[39] Y. Zhang, R. Lackner, M. Zeiml, H.A. Mang, Strong discontinuity embedded approach with standard SOS formulation: Element formulation, energy-based crack-tracking strategy, and validations, Comput. Methods Appl. Mech. Engrg. 287 (2015) 335–366, http://dx.doi.org/10.1016/j.cma.2015.02.001.
[40] J. Alfaiate, A. Simone, L.J. Sluys, Non-homogeneous displacement jumps in strong embedded discontinuities, Int. J. Solids Struct. 40 (21) (2003) 5799–5817, http://dx.doi.org/10.1016/S0020-7683(03)00372-X.
[41] F. Liu, W. Sun, M. Li, X. Shang, A smoothed assumed enhanced strain method for frictional contact with constant strain elements, J. Rock Mech. Geotech. Eng. (2023).
[42] T.C. Gasser, G.A. Holzapfel, Geometrically non-linear and consistently linearized embedded strong discontinuity models for 3D problems with an application to the dissection analysis of soft biological tissues, Comput. Methods Appl. Mech. Engrg. 192 (47–48) (2003) 5059–5098, http://dx.doi.org/10.1016/j.cma.2003.06.001.
[43] D. Dias-da Costa, J. Alfaiate, L. Sluys, P. Areias, E. Júlio, An embedded formulation with conforming finite elements to capture strong discontinuities, Internat. J. Numer. Methods Engrg. 93 (2) (2013) 224–244, http://dx.doi.org/10.1002/nme.4393.
[44] G. Juárez-Luna, G. Ayala, Improvement of some features of finite elements with embedded discontinuities, Eng. Fract. Mech. 118 (2014) 31–48, http://dx.doi.org/10.1016/j.engfracmech.2014.02.002.
[45] F. Armero, J. Kim, Three-dimensional finite elements with embedded strong discontinuities to model material failure in the infinitesimal range, Internat. J. Numer. Methods Engrg. 91 (12) (2012) 1291–1330.
[46] F. Armero, D. Ehrlich, Finite element methods for the multi-scale modeling of softening hinge lines in plates at failure, Comput. Methods Appl. Mech. Engrg. 195 (13–16) (2006) 1283–1324.
[47] C. Linder, F. Armero, Finite elements with embedded strong discontinuities for the modeling of failure in solids, Internat. J. Numer. Methods Engrg. 72 (12) (2007) 1391–1433.
[48] M. Jirásek, T. Zimmermann, Embedded crack model: I. Basic formulation, Internat. J. Numer. Methods Engrg. 50 (6) (2001) 1269–1290.
[49] J. Oliver, A.E. Huespe, E. Samaniego, A study on finite elements for capturing strong discontinuities, Internat. J. Numer. Methods Engrg. 56 (14) (2003) 2135–2161.
[50] F. Cazes, G. Meschke, M.-M. Zhou, Strong discontinuity approaches: An algorithm for robust performance and comparative assessment of accuracy, Int. J. Solids Struct. 96 (2016) 355–379.
[51] R. de Borst, G. Wells, L. Sluys, Some observations on embedded discontinuity models, Eng. Comput. 18 (1/2) (2001) 241–254, http://dx.doi.org/10.1108/02644400110365897, Publisher: MCB UP Ltd.
[52] D. Cavalcanti, C. Mejia, D. Roehl, I. de Pouplana, E. Oñate, Hydromechanical embedded finite element for conductive and impermeable strong discontinuities in porous media, Comput. Geotech. 172 (2024) 106427.
[53] D. Dias-da Costa, M.R. Carvalho, M. Bybordiani, A cracked zone clustering method for discrete fracture with minimal enhanced degrees of freedom, Comput. Methods Appl. Mech. Engrg. 387 (2021) 114133, http://dx.doi.org/10.1016/j.cma.2021.114133, URL https://www.sciencedirect.com/science/article/pii/S0045782521004643.
[54] A. Simone, Partition of unity-based discontinuous elements for interface phenomena: computational issues, Commun. Numer. Methods Eng. 20 (6) (2004) 465–478, http://dx.doi.org/10.1002/cnm.688.
[55] A. Ahmed, L. Sluys, Anomalous behavior of bilinear quadrilateral finite elements for modeling cohesive cracks with XFEM/GFEM, Internat. J. Numer. Methods Engrg. 94 (5) (2013) 454–472, http://dx.doi.org/10.1002/nme.4456.
[56] J.D. Sanders, J.E. Dolbow, T.A. Laursen, On methods for stabilizing constraints over enriched interfaces in elasticity, Internat. J. Numer. Methods Engrg. 78 (9) (2009) 1009–1036, http://dx.doi.org/10.1002/nme.2514.
[57] C. Annavarapu, M. Hautefeuille, J.E. Dolbow, A nitsche stabilized finite element method for frictional sliding on embedded interfaces. Part I: single interface, Comput. Methods Appl. Mech. Engrg. 268 (2014) 417–436.
[58] E.T. Coon, B.E. Shaw, M. Spiegelman, A Nitsche-extended finite element method for earthquake rupture on complex fault systems, Comput. Methods Appl. Mech. Engrg. 200 (41–44) (2011) 2859–2870, http://dx.doi.org/10.1016/j.cma.2011.05.005.
[59] C. Annavarapu, M. Hautefeuille, J.E. Dolbow, A robust Nitsche's formulation for interface problems, Comput. Methods Appl. Mech. Engrg. 225–228 (2012) 44–54, http://dx.doi.org/10.1016/j.cma.2012.03.008.
[60] F. Liu, R.I. Borja, Stabilized low-order finite elements for frictional contact with the extended finite element method, Comput. Methods Appl. Mech. Engrg. 199 (37–40) (2010) 2456–2471.
[61] S. Sadaba, I. Romero, C. Gonzalez, J. Llorca, A stable X-FEM in cohesive transition from closed to open crack, Internat. J. Numer. Methods Engrg. 101 (7) (2015) 540–570.
[62] R.E. Erkmen, D. Dias-da Costa, Stabilization of the extended finite element method for stiff embedded interfaces and inclusions, Internat. J. Numer. Methods Engrg. 122 (24) (2021) 7378–7408, http://dx.doi.org/10.1002/nme.6834, URL https://onlinelibrary.wiley.com/doi/abs/10.1002/nme.6834.
[63] Y. Zhao, J. Choo, Y. Jiang, M. Li, C. Jiang, K. Soga, A barrier method for frictional contact on embedded interfaces, Comput. Methods Appl. Mech. Engrg. 393 (2022) 114820, http://dx.doi.org/10.1016/j.cma.2022.114820.
[64] L. Crusat, I. Carol, D. Garolera, XFEM formulation with sub-interpolation, and equivalence to zero-thickness interface elements, Int. J. Numer. Anal. Methods Geomech. 43 (1) (2019) 45–76, http://dx.doi.org/10.1002/nag.2853, URL https://onlinelibrary.wiley.com/doi/abs/10.1002/nag.2853.
[65] A. Latifaghili, M. Bybordiani, R.E. Erkmen, D. Dias-da Costa, An extended finite element method with polygonal enrichment shape functions for crack propagation and stiff interface problems, Internat. J. Numer. Methods Engrg. 123 (6) (2022) 1432–1455, http://dx.doi.org/10.1002/nme.6901, URL https://onlinelibrary.wiley.com/doi/abs/10.1002/nme.6901.
[66] É. Béchet, N. Moës, B. Wohlmuth, A stable Lagrange multiplier space for stiff interface conditions within the extended finite element method, Internat. J. Numer. Methods Engrg. 78 (8) (2009) 931–954, http://dx.doi.org/10.1002/nme.2515, URL https://onlinelibrary.wiley.com/doi/abs/10.1002/nme.2515.
[67] M. Hirmand, M. Vahab, A.R. Khoei, An augmented Lagrangian contact formulation for frictional discontinuities with the extended finite element method, Finite Elem. Anal. Des. 107 (2015) 28–43, http://dx.doi.org/10.1016/j.finel.2015.08.003, URL https://www.sciencedirect.com/science/article/pii/S0168874X15001262.
[68] A.R. Khoei, M. Vahab, M. Hirmand, An enriched–FEM technique for numerical simulation of interacting discontinuities in naturally fractured porous media, Comput. Methods Appl. Mech. Engrg. 331 (2018) 197–231, http://dx.doi.org/10.1016/j.cma.2017.11.016, URL https://www.sciencedirect.com/science/article/pii/S0045782517307181.
[69] S.R. Idelsohn, J.M. Gimenez, J. Marti, N.M. Nigro, Elemental enriched spaces for the treatment of weak and strong discontinuous fields, Comput. Methods Appl. Mech. Engrg. 313 (2017) 535–559, http://dx.doi.org/10.1016/j.cma.2016.09.048.
[70] A.M. Aragón, A. Simone, The Discontinuity-Enriched Finite Element Method, Internat. J. Numer. Methods Engrg. 112 (11) (2017) 1589–1613, http://dx.doi.org/10.1002/nme.5570.
[71] S.J. van den Boom, J. Zhang, F. van Keulen, A.M. Aragón, A stable interface-enriched formulation for immersed domains with strong enforcement of essential boundary conditions, Internat. J. Numer. Methods Engrg. 120 (10) (2019) 1163–1183, http://dx.doi.org/10.1002/nme.6139.
[72] J. Zhang, S.J. van den Boom, F. van Keulen, A.M. Aragón, A stable discontinuity-enriched finite element method for 3-D problems containing weak and strong discontinuities, Comput. Methods Appl. Mech. Engrg. 355 (2019) 1097–1123, http://dx.doi.org/10.1016/j.cma.2019.05.018.
[73] J.C.J. Schellekens, R. De Borst, On the numerical integration of interface elements, Internat. J. Numer. Methods Engrg. 36 (1) (1993) 43–66, http://dx.doi.org/10.1002/nme.1620360104.

[74] R. De Borst, Numerical aspects of cohesive-zone models, Eng. Fract. Mech. 70 (14) (2003) 1743–1757.
[75] E. Lorentz, A mixed interface finite element for cohesive zone models, Comput. Methods Appl. Mech. Engrg. 198 (2) (2008) 302–317.
[76] G. Ghosh, R. Duddu, C. Annavarapu, A stabilized finite element method for enforcing stiff anisotropic cohesive laws using interface elements, Comput. Methods Appl. Mech. Engrg. 348 (2019) 1013–1038.
[77] G. Ghosh, R. Duddu, C. Annavarapu, On the robustness of the stabilized finite element method for delamination analysis of composites using cohesive elements, Int. J. Comput. Methods Eng. Sci. Mech. 22 (6) (2021) 538–558.
[78] O.L. Manzoli, P.B. Shing, A general technique to embed non-uniform discontinuities into standard solid finite elements, Comput. Struct. 84 (10–11) (2006) 742–757, http://dx.doi.org/10.1016/j.compstruc.2005.10.009.
[79] T.J.R. Hughes, Multiscale phenomena: Green's functions, the Dirichlet-to-Neumann formulation, subgrid scale models, bubbles and the origins of stabilized methods, Comput. Methods Appl. Mech. Engrg. 127 (1) (1995) 387–401, http://dx.doi.org/10.1016/0045-7825(95)00844-9.
[80] T.J.R. Hughes, G.R. Feijóo, L. Mazzei, J.-B. Quincy, The variational multiscale method—a paradigm for computational mechanics, Comput. Methods Appl. Mech. Engrg. 166 (1) (1998) 3–24, http://dx.doi.org/10.1016/S0045-7825(98)00079-6, Advances in Stabilized Methods in Computational Mechanics.
[81] A. Ibrahimbegovic, Nonlinear Solid Mechanics: Theoretical Formulations and Finite Element Solution Methods, vol. 160, Springer Science & Business Media, 2009.
[82] E. Roubin, A. Vallade, N. Benkemoun, J.-B. Colliat, Multi-scale failure of heterogeneous materials: A double kinematics enhancement for Embedded Finite Element Method, Int. J. Solids Struct. 52 (2015) 180–196, http://dx.doi.org/10.1016/j.ijsolstr.2014.10.001.
[83] R.I. Borja, A finite element model for strain localization analysis of strongly discontinuous fields based on standard Galerkin approximation, Comput. Methods Appl. Mech. Engrg. 190 (11) (2000) 1529–1549, http://dx.doi.org/10.1016/S0045-7825(00)00176-6.
[84] J.-Y. Wu, F.-B. Li, S.-L. Xu, Extended embedded finite elements with continuous displacement jumps for the modeling of localized failure in solids, Comput. Methods Appl. Mech. Engrg. 285 (2015) 346–378.
[85] A. Stanić, B. Brank, A. Ibrahimbegovic, H.G. Matthies, Crack propagation simulation without crack tracking algorithm: Embedded discontinuity formulation with incompatible modes, Comput. Methods Appl. Mech. Engrg. 386 (2021) 114090, http://dx.doi.org/10.1016/j.cma.2021.114090.
[86] J. Dujc, B. Brank, A. Ibrahimbegovic, Stress-hybrid quadrilateral finite element with embedded strong discontinuity for failure analysis of plane stress solids, Internat. J. Numer. Methods Engrg. 94 (12) (2013) 1075–1098, http://dx.doi.org/10.1002/nme.4475.
[87] J.-C. Simo, F. Armero, Geometrically non-linear enhanced strain mixed methods and the method of incompatible modes, Internat. J. Numer. Methods Engrg. 33 (7) (1992) 1413–1449.
[88] F. Armero, K. Garikipati, An analysis of strong discontinuities in multiplicative finite strain plasticity and their relation with the numerical simulation of strain localization in solids, Int. J. Solids Struct. 33 (20–22) (1996) 2863–2885.
[89] A. Stanić, B. Brank, D. Brancherie, Fracture of quasi-brittle solids by continuum and discrete-crack damage models and embedded discontinuity formulation, Eng. Fract. Mech. 227 (2020) 106924.
[90] R.A. Day, D.M. Potts, Zero thickness interface elements—numerical stability and application, Int. J. Numer. Anal. Methods Geomech. 18 (10) (1994) 689–708, http://dx.doi.org/10.1002/nag.1610181003.
[91] J. Kleinberg, E. Tardos, Algorithm Design, Pearson Education India, 2006.
[92] C.A. Mendes, M. Gattass, D. Roehl, The GeMA framework–an innovative framework for the development of multiphysics and multiscale simulations, in: VII European Congress on Computational Methods in Applied Sciences and Engineering, 2016, pp. 5–10.
[93] R.G. Escobar, C. Mejia, D. Roehl, C. Romanel, Xfem modeling of stress shadowing in multiple hydraulic fractures in multi-layered formations, J. Nat. Gas Sci. Eng. 70 (2019) 102950.
[94] L.F.P. Munoz, C. Mejia, J. Rueda, D. Roehl, Pseudo-coupled hydraulic fracturing analysis with displacement discontinuity and finite element methods, Eng. Fract. Mech. 274 (2022) 108774.
[95] J. Rueda, C. Mejia, D. Roehl, 3D unrestricted fluid-driven fracture propagation based on coupled hydromechanical interface elements, Eng. Fract. Mech. 272 (2022) 108680.
[96] J. Rueda, C. Mejia, D. Roehl, Hydromechanical simulation of fracture propagation and reservoir production with multiscale fractures, Rock Mech. Rock Eng. 56 (3) (2023) 1883–1907.
[97] J. Rueda, C. Mejia, D. Roehl, Integrated discrete fracture and dual porosity-dual permeability models for fluid flow in deformable fractured media, J. Pet. Sci. Eng. 175 (2019) 644–653.
[98] J. Rueda, C. Mejia, N. Noreña, D. Roehl, A three-dimensional enhanced dual-porosity and dual-permeability approach for hydromechanical modeling of naturally fractured rocks, Internat. J. Numer. Methods Engrg. 122 (7) (2021) 1663–1686.
[99] C. Mejia, D. Roehl, J. Rueda, R. Quevedo, A new approach for modeling three-dimensional fractured reservoirs with embedded complex fracture networks, Comput. Geotech. 130 (2021) 103928.
[100] C. Mejia, D. Roehl, J. Rueda, F. Fonseca, Geomechanical effects of natural fractures on fluid flow in a pre-salt field, J. Nat. Gas Sci. Eng. 107 (2022) 104772.
[101] P.A. Firme, D. Roehl, C. Mejia, C. Romanel, Geomechanics of salt towards natural barriers for the abandonment of pre-salt wells in Brazil, Geoenergy Sci. Eng. 228 (2023) 211849.
[102] W. Dias, D. Roehl, C. Mejia, P. Sotomayor, Cavern integrity for underground hydrogen storage in the Brazilian pre-salt fields, Int. J. Hydrog. Energy 48 (69) (2023) 26853–26869.
[103] P.A. Firme, D. Roehl, C. Mejia, C. Romanel, An assessment of the salt caprock creep impact on pre-salt reservoir geomechanics, Geomech. Energy Environ (2024) 100588.
[104] C. Mejia, L.F. Paullo Muñoz, D. Roehl, Discrete fracture propagation analysis using a robust combined continuation method, Int. J. Solids Struct. 193–194 (2020) 405–417, http://dx.doi.org/10.1016/J.IJSOLSTR.2020.02.002.
[105] M. Paggi, P. Wriggers, Node-to-segment and node-to-surface interface finite elements for fracture mechanics, Comput. Methods Appl. Mech. Engrg. 300 (2016) 540–560.
[106] J. Dolbow, N. Moës, T. Belytschko, An extended finite element method for modeling crack growth with frictional contact, Comput. Methods Appl. Mech. Engrg. 190 (51) (2001) 6825–6846, http://dx.doi.org/10.1016/S0045-7825(01)00260-2.
[107] T. Kim, J. Dolbow, T. Laursen, A mortared finite element method for frictional contact on arbitrary interfaces, Comput. Mech. 39 (3) (2007) 223–235, http://dx.doi.org/10.1007/s00466-005-0019-4.
[108] D.M. Potts, L. Zdravković, T.I. Addenbrooke, K.G. Higgins, N. Kovačević, Finite Element Analysis in Geotechnical Engineering: Application, vol. 2, Thomas Telford London, 2001.
[109] F. Cappa, J. Rutqvist, Modeling of coupled deformation and permeability evolution during fault reactivation induced by deep underground injection of CO2, Int. J. Greenh. Gas Control. 5 (2) (2011) 336–346, http://dx.doi.org/10.1016/j.ijggc.2010.08.005.
[110] M.A. Biot, D.G. Willis, The Elastic Coefficients of the Theory of Consolidation, J. Appl. Mech. 24 (4) (1957) 594–601, http://dx.doi.org/10.1115/1.4011606.
[111] M.A. Biot, M.A. Blot, General theory of three dimensional consolidation general theory of three-dimensional consolidation, J. Appl. Phys. 12 (2) (1941) 155–164, http://dx.doi.org/10.1115/1.4011606.

B
Elastoplastic cohesive law

This appendix summarizes the elastoplastic cohesive law adopted in this work and its return-mapping algorithm. The formulation closely follows classical small-strain plasticity, with the cohesive traction vector $\mathbf{t}_\mathrm{d}$ playing the role of a stress vector and the displacement jump $[\![\mathbf{u}]\!]$ playing the role of a strain-like measure.

B.1
Elastic law and yield functions

For a linear-elastic law, the cohesive tractions are

$$\mathbf{t}_\mathrm{d} = \mathbf{T}_\mathrm{d}^\mathrm{el}\,[\![\mathbf{u}]\!], \tag{B-1}$$

where

$$\mathbf{T}_\mathrm{d}^\mathrm{el} = \begin{bmatrix} k_\mathrm{s1} & 0 & 0 \\ 0 & k_\mathrm{s2} & 0 \\ 0 & 0 & k_\mathrm{n} \end{bmatrix}, \tag{B-2}$$

with k_s1, k_s2 and k_n being the elastic shear and normal cohesive stiffnesses, respectively.

The adopted yield criterion is a combination of the Mohr–Coulomb surface, f_MC,

$$f_\mathrm{MC} = |t_\mathrm{sr}| + t_\mathrm{n}\,\tan\phi - c, \tag{B-3}$$

and a tension cut-off, f_TC,

$$f_\mathrm{TC} = t_\mathrm{n} - f_\mathrm{t}, \tag{B-4}$$

where ϕ is the friction angle, c is the cohesion, f_t is the tensile strength, and t_sr is the resultant shear cohesive traction. For 2D problems t_sr coincides with the tangential component of the traction vector, while for 3D it is given by

$$t_\mathrm{sr} = \sqrt{{t_\mathrm{s1}}^2 + {t_\mathrm{s2}}^2}. \tag{B-5}$$

The present model does not include any hardening, so the yield functions do not depend on internal variables.

The traction space $t_\mathrm{n} - t_\mathrm{sr}$ is split into four regions:

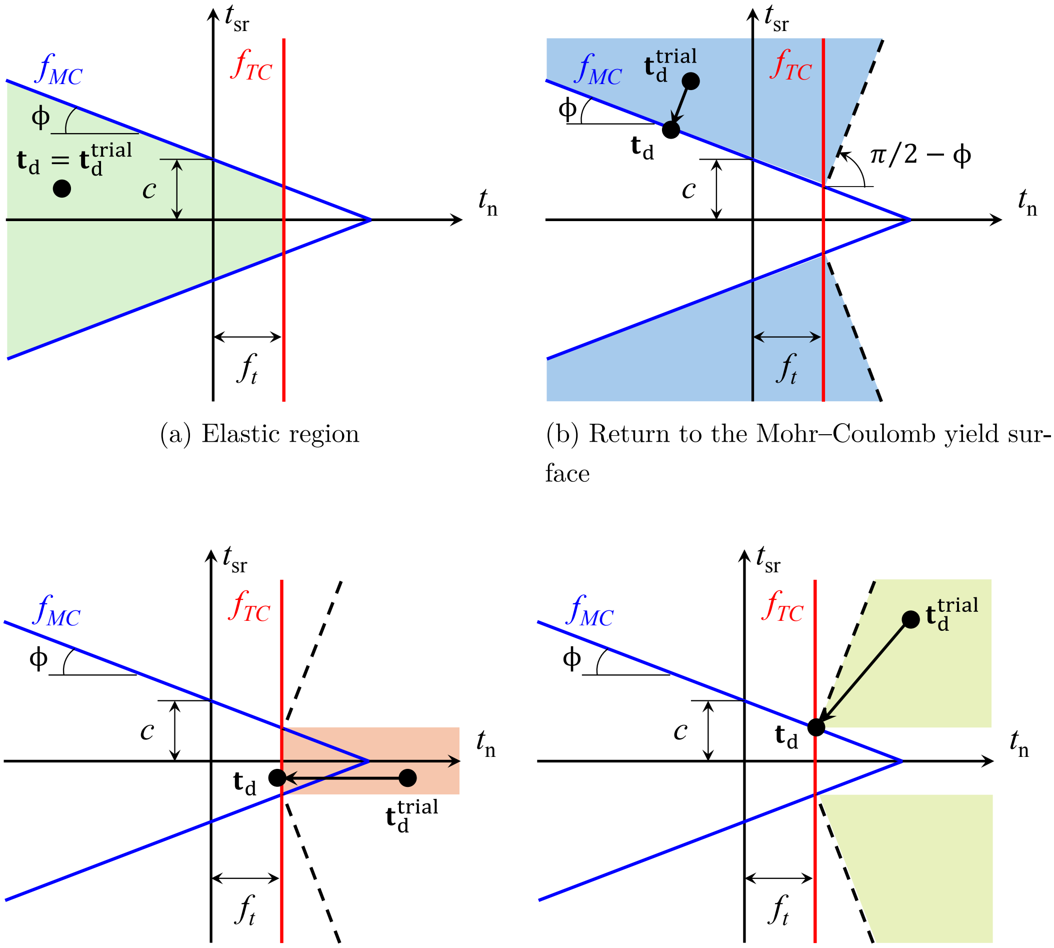

(a) Elastic region

(b) Return to the Mohr–Coulomb yield surface

(c) Return to the tension-cutoff surface

(d) Return to the intersection

Figure B.1: Return mapping to an admissible state: (a) Elastic region, (b) return to the Mohr–Coulomb yield surface, (c) return to the tension-cutoff surface, (d) return to the intersection between the two surfaces.

The plastic potential associated with the tension cut-off is taken equal to its yield surface, $g_{\mathrm{TC}} = f_{\mathrm{TC}}$. For the Mohr–Coulomb surface, to account for dilatancy, the plastic potential is chosen as

$$g_{\mathrm{MC}} = |t_{\mathrm{sr}}| + t_{\mathrm{n}} \tan\varphi - c, \tag{B-6}$$

where φ is the dilatancy angle. The model is associative for the tension cut-off and non-associative for the Mohr–Coulomb branch when $\varphi \neq \phi$.

Assuming small displacements and small strains, the displacement jump vector is additively decomposed into an elastic part, $[\![\mathbf{u}]\!]^{\mathrm{e}}$, and a plastic part, $[\![\mathbf{u}]\!]^{\mathrm{p}}$, as

$$[\![\mathbf{u}]\!] = [\![\mathbf{u}]\!]^{\mathrm{e}} + [\![\mathbf{u}]\!]^{\mathrm{p}}. \tag{B-7}$$

The cohesive traction depends only on the elastic part of the displacement jump and is given by

$$\mathbf{t}_{\mathrm{d}} = \mathbf{T}^{\mathrm{el}}_{\mathrm{d}} \left([\![\mathbf{u}]\!] - [\![\mathbf{u}]\!]^{\mathrm{p}} \right). \tag{B-8}$$

B.2 Return to a single surface

For a single active surface (either Mohr–Coulomb or tension cut-off), the evolution of the plastic part of the displacement jump is governed by the non-associative flow rule

$$[\![\dot{\mathbf{u}}]\!]^{\mathrm{p}} = \dot{\lambda} \, \frac{\partial g}{\partial \mathbf{t}_{\mathrm{d}}}, \tag{B-9}$$

where $\dot{\lambda}$ is the plastic multiplier rate and g is the active plastic potential. The loading–unloading conditions are expressed by the Karush–Kuhn–Tucker relations

$$\dot{\lambda} \geq 0, \qquad f \leq 0, \qquad \dot{\lambda} \, f = 0, \tag{B-10}$$

with f denoting the active yield function (either Mohr–Coulomb or tension cut-off).

Using a backward-Euler time integration, the updated plastic part of the displacement jump is

$$[\![\mathbf{u}]\!]^{\mathrm{p}}_{(n+1)} = [\![\mathbf{u}]\!]^{\mathrm{p}}_{(n)} + \Delta\lambda_{(n+1)} \, \frac{\partial g_{(n+1)}}{\partial \mathbf{t}_{\mathrm{d}}}, \tag{B-11}$$

where $\Delta\lambda_{(n+1)}$ is the increment of the plastic multiplier in the current step and the gradient is evaluated at $\mathbf{t}_{\mathrm{d}(n+1)}$.

The elastic predictor (trial state) for the cohesive traction is computed as

$$\mathbf{t}^{\mathrm{trial}}_{\mathrm{d}} = \mathbf{T}^{\mathrm{el}}_{\mathrm{d}} \left([\![\mathbf{u}]\!]_{(n+1)} - [\![\mathbf{u}]\!]^{\mathrm{p}}_{(n)} \right), \tag{B-12}$$

and the corresponding trial value of the active yield function is $f^{\mathrm{trial}} = f(\mathbf{t}^{\mathrm{trial}}_{\mathrm{d}})$. If $f^{\mathrm{trial}} \leq 0$, the step is elastic and $\Delta\lambda_{(n+1)} = 0$. Otherwise, a plastic correction is required and a return mapping to the yield surface is performed.

For a plastic step, inserting (B-11) into (B-8) gives the updated traction as

$$\mathbf{t}_{\mathrm{d}(n+1)} = \mathbf{t}^{\mathrm{trial}}_{\mathrm{d}} - \Delta\lambda_{(n+1)} \, \mathbf{T}^{\mathrm{el}}_{\mathrm{d}} \, \frac{\partial g_{(n+1)}}{\partial \mathbf{t}_{\mathrm{d}}}. \tag{B-13}$$

For perfect plasticity, a closed-form expression for the plastic multiplier increment $\Delta\lambda_{(n+1)}$ can be obtained by linearizing the consistency condition around the trial state,

$$f_{(n+1)} \approx f^{\mathrm{trial}} + \left(\frac{\partial f_{(n+1)}}{\partial \mathbf{t}_{\mathrm{d}}}\right)^{\top} \left(\mathbf{t}_{\mathrm{d}(n+1)} - \mathbf{t}_{\mathrm{d}}^{\mathrm{trial}}\right) = 0, \tag{B-14}$$

and substituting the plastic correction, which leads to

$$\Delta\lambda_{(n+1)} = \frac{f^{\mathrm{trial}}}{\left(\dfrac{\partial f_{(n+1)}}{\partial \mathbf{t}_{\mathrm{d}}}\right)^{\top} \mathbf{T}_{\mathrm{d}}^{\mathrm{el}} \dfrac{\partial g_{(n+1)}}{\partial \mathbf{t}_{\mathrm{d}}}}. \tag{B-15}$$

This expression is the cohesive analogue of the classical closed-form return-mapping formula for perfect plasticity.

B.2.1
Consistent tangent for a single surface

The consistent (algorithmic) tangent is defined by

$$d\mathbf{t}_{\mathrm{d}(n+1)} = \mathbf{T}_{\mathrm{d}}^{\mathrm{ep}}\, d[\![\mathbf{u}]\!]_{(n+1)}, \tag{B-16}$$

and is obtained by linearizing the fully discrete update, in analogy with small-strain plasticity [178].

Starting from the backward-Euler flow rule (B-11), and recalling that $\partial g_{(n+1)}/\partial \mathbf{t}_{\mathrm{d}}$ depends on $\mathbf{t}_{\mathrm{d}(n+1)}$, its differential reads

$$d[\![\mathbf{u}]\!]^{\mathrm{p}}_{(n+1)} = \Delta\lambda_{(n+1)} \frac{\partial^2 g_{(n+1)}}{\partial \mathbf{t}_{\mathrm{d}}^2}\, d\mathbf{t}_{\mathrm{d}(n+1)} + d\Delta\lambda_{(n+1)} \frac{\partial g_{(n+1)}}{\partial \mathbf{t}_{\mathrm{d}}}, \tag{B-17}$$

where $\partial^2 g_{(n+1)}/\partial \mathbf{t}_{\mathrm{d}}^2$ is the Hessian of the plastic potential at $\mathbf{t}_{\mathrm{d}(n+1)}$.

Differentiating the cohesive law (B-8) at step $(n+1)$ gives

$$d\mathbf{t}_{\mathrm{d}(n+1)} = \mathbf{T}_{\mathrm{d}}^{\mathrm{el}} \left(d[\![\mathbf{u}]\!]_{(n+1)} - d[\![\mathbf{u}]\!]^{\mathrm{p}}_{(n+1)}\right). \tag{B-18}$$

Substituting (B-17) into (B-18) and rearranging terms leads to

$$\left[\left(\mathbf{T}_{\mathrm{d}}^{\mathrm{el}}\right)^{-1} + \Delta\lambda_{(n+1)} \frac{\partial^2 g_{(n+1)}}{\partial \mathbf{t}_{\mathrm{d}}^2}\right] d\mathbf{t}_{\mathrm{d}(n+1)} = d[\![\mathbf{u}]\!]_{(n+1)} - d\Delta\lambda_{(n+1)} \frac{\partial g_{(n+1)}}{\partial \mathbf{t}_{\mathrm{d}}}. \tag{B-19}$$

The algorithmic cohesive moduli are then introduced as

$$\boldsymbol{\Xi}_{\mathrm{d}(n+1)} = \left(\left(\mathbf{T}_{\mathrm{d}}^{\mathrm{el}}\right)^{-1} + \Delta\lambda_{(n+1)} \frac{\partial^2 g_{(n+1)}}{\partial \mathbf{t}_{\mathrm{d}}^2}\right)^{-1}, \tag{B-20}$$

so that

$$d\mathbf{t}_{\mathrm{d}(n+1)} = \boldsymbol{\Xi}_{\mathrm{d}(n+1)} \left(d[\![\mathbf{u}]\!]_{(n+1)} - d\Delta\lambda_{(n+1)} \frac{\partial g_{(n+1)}}{\partial \mathbf{t}_{\mathrm{d}}}\right). \tag{B-21}$$

The consistency condition at the end of the step, $f_{(n+1)} = f(\mathbf{t}_{\mathrm{d}(n+1)}) = 0$, implies

$$df_{(n+1)} = \left(\frac{\partial f_{(n+1)}}{\partial \mathbf{t}_{\mathrm{d}}}\right)^{\top} d\mathbf{t}_{\mathrm{d}(n+1)} = 0. \tag{B-22}$$

Substituting (B-21) and solving for $d\Delta\lambda_{(n+1)}$ gives

$$d\Delta\lambda_{(n+1)} = \frac{\left(\frac{\partial f_{(n+1)}}{\partial \mathbf{t}_{\mathrm{d}}}\right)^{\top} \boldsymbol{\Xi}_{\mathrm{d}(n+1)} d[\![\mathbf{u}]\!]_{(n+1)}}{\left(\frac{\partial f_{(n+1)}}{\partial \mathbf{t}_{\mathrm{d}}}\right)^{\top} \boldsymbol{\Xi}_{\mathrm{d}(n+1)} \frac{\partial g_{(n+1)}}{\partial \mathbf{t}_{\mathrm{d}}}}. \tag{B-23}$$

Inserting this result back into (B-21) yields

$$d\mathbf{t}_{\mathrm{d}(n+1)} = \left[\boldsymbol{\Xi}_{\mathrm{d}(n+1)} - \frac{\boldsymbol{\Xi}_{\mathrm{d}(n+1)} \frac{\partial g_{(n+1)}}{\partial \mathbf{t}_{\mathrm{d}}} \left(\frac{\partial f_{(n+1)}}{\partial \mathbf{t}_{\mathrm{d}}}\right)^{\top} \boldsymbol{\Xi}_{\mathrm{d}(n+1)}}{\left(\frac{\partial f_{(n+1)}}{\partial \mathbf{t}_{\mathrm{d}}}\right)^{\top} \boldsymbol{\Xi}_{\mathrm{d}(n+1)} \frac{\partial g_{(n+1)}}{\partial \mathbf{t}_{\mathrm{d}}}}\right] d[\![\mathbf{u}]\!]_{(n+1)}. \tag{B-24}$$

Therefore, the cohesive algorithmic tangent matrix associated with the return to a single surface is

$$\mathbf{T}_{\mathrm{d}}^{\mathrm{ep}} = \boldsymbol{\Xi}_{\mathrm{d}(n+1)} - \frac{\boldsymbol{\Xi}_{\mathrm{d}(n+1)} \frac{\partial g_{(n+1)}}{\partial \mathbf{t}_{\mathrm{d}}} \left(\frac{\partial f_{(n+1)}}{\partial \mathbf{t}_{\mathrm{d}}}\right)^{\top} \boldsymbol{\Xi}_{\mathrm{d}(n+1)}}{\left(\frac{\partial f_{(n+1)}}{\partial \mathbf{t}_{\mathrm{d}}}\right)^{\top} \boldsymbol{\Xi}_{\mathrm{d}(n+1)} \frac{\partial g_{(n+1)}}{\partial \mathbf{t}_{\mathrm{d}}}}. \tag{B-25}$$

In the elastic regime ($f^{\mathrm{trial}} \leq 0$), no plastic correction occurs and $\mathbf{T}_{\mathrm{d}}^{\mathrm{ep}} = \mathbf{T}_{\mathrm{d}}^{\mathrm{el}}$.

For completeness, the gradients of the yield and plastic potential functions with respect to the cohesive traction vector for the Mohr–Coulomb are

$$\frac{\partial f_{\mathrm{MC}}}{\partial \mathbf{t}_{\mathrm{d}}} = \begin{bmatrix} \frac{t_{\mathrm{s1}}}{t_{\mathrm{sr}}} \\ \frac{t_{\mathrm{s2}}}{t_{\mathrm{sr}}} \\ \tan\phi \end{bmatrix}, \qquad \frac{\partial g_{\mathrm{MC}}}{\partial \mathbf{t}_{\mathrm{d}}} = \begin{bmatrix} \frac{t_{\mathrm{s1}}}{t_{\mathrm{sr}}} \\ \frac{t_{\mathrm{s2}}}{t_{\mathrm{sr}}} \\ \tan\varphi \end{bmatrix}, \tag{B-26}$$

and for the tension cut-off are

$$\frac{\partial f_{\mathrm{TC}}}{\partial \mathbf{t}_{\mathrm{d}}} = \frac{\partial g_{\mathrm{TC}}}{\partial \mathbf{t}_{\mathrm{d}}} = \begin{bmatrix} 0 \\ 0 \\ 1 \end{bmatrix}. \tag{B-27}$$

The Hessian matrix of the plastic potential surfaces are

$$\frac{\partial^2 g_{\mathrm{MC}}}{\partial \mathbf{t}_{\mathrm{d}}^2} = \begin{bmatrix} \frac{t_{\mathrm{s2}}^2}{t_{\mathrm{sr}}^3} & -\frac{t_{\mathrm{s1}} t_{\mathrm{s2}}}{t_{\mathrm{sr}}^3} & 0 \\ -\frac{t_{\mathrm{s1}} t_{\mathrm{s2}}}{t_{\mathrm{sr}}^3} & \frac{t_{\mathrm{s1}}^2}{t_{\mathrm{sr}}^3} & 0 \\ 0 & 0 & 0 \end{bmatrix}, \qquad \frac{\partial^2 g_{\mathrm{TC}}}{\partial \mathbf{t}_{\mathrm{d}}^2} = \begin{bmatrix} 0 & 0 & 0 \\ 0 & 0 & 0 \\ 0 & 0 & 0 \end{bmatrix}. \tag{B-28}$$

In 2D problems, the expressions above reduce by dropping the second shear component.

B.3
Return to the intersection

When both the Mohr–Coulomb and the tension cut-off surfaces are active at the end of the increment, the plastic correction involves two plastic multipliers. The flow rule at the intersection is written as [179]

$$[\![\dot{\mathbf{u}}]\!]^{\mathrm{p}} = \dot{\lambda}_{\mathrm{MC}} \frac{\partial g_{\mathrm{MC}}}{\partial \mathbf{t}_{\mathrm{d}}} + \dot{\lambda}_{\mathrm{TC}} \frac{\partial g_{\mathrm{TC}}}{\partial \mathbf{t}_{\mathrm{d}}}, \tag{B-29}$$

with $\dot{\lambda}_{\mathrm{MC}}$ and $\dot{\lambda}_{\mathrm{TC}}$ denoting the plastic multiplier rates associated with each surface. At the intersection, both yield functions are active, $f_{\mathrm{MC}} = 0$ and $f_{\mathrm{TC}} = 0$, and both plastic multipliers are nonzero.

Using a backward-Euler integration, the plastic part of the displacement jump is updated as

$$[\![\mathbf{u}]\!]^{\mathrm{p}}_{(n+1)} = [\![\mathbf{u}]\!]^{\mathrm{p}}_{(n)} + \Delta\lambda_{\mathrm{MC}(n+1)} \frac{\partial g_{\mathrm{MC}(n+1)}}{\partial \mathbf{t}_{\mathrm{d}}} + \Delta\lambda_{\mathrm{TC}(n+1)} \frac{\partial g_{\mathrm{TC}(n+1)}}{\partial \mathbf{t}_{\mathrm{d}}}, \tag{B-30}$$

where $\Delta\lambda_{\mathrm{MC}(n+1)}$ and $\Delta\lambda_{\mathrm{TC}(n+1)}$ are the plastic multiplier increments in the current step. In terms of the elastic predictor $\mathbf{t}_{\mathrm{d}}^{\mathrm{trial}}$, the updated traction reads

$$\mathbf{t}_{\mathrm{d}(n+1)} = \mathbf{t}_{\mathrm{d}}^{\mathrm{trial}} - \mathbf{T}_{\mathrm{d}}^{\mathrm{el}} \left(\Delta\lambda_{\mathrm{MC}(n+1)} \frac{\partial g_{\mathrm{MC}(n+1)}}{\partial \mathbf{t}_{\mathrm{d}}} + \Delta\lambda_{\mathrm{TC}(n+1)} \frac{\partial g_{\mathrm{TC}(n+1)}}{\partial \mathbf{t}_{\mathrm{d}}} \right). \tag{B-31}$$

For perfect plasticity, the plastic multiplier increments are obtained from the two consistency conditions linearized around the trial state,

$$f_{\alpha}^{\mathrm{trial}} = f_{\alpha}(\mathbf{t}_{\mathrm{d}}^{\mathrm{trial}}), \qquad \alpha \in \{\mathrm{MC}, \mathrm{TC}\}, \tag{B-32}$$

which leads to the following 2×2 system:

$$\begin{bmatrix} \left(\dfrac{\partial f_{\mathrm{MC}}}{\partial \mathbf{t}_{\mathrm{d}}}\right)^{\top} \mathbf{T}_{\mathrm{d}}^{\mathrm{el}} \dfrac{\partial g_{\mathrm{MC}}}{\partial \mathbf{t}_{\mathrm{d}}} & \left(\dfrac{\partial f_{\mathrm{MC}}}{\partial \mathbf{t}_{\mathrm{d}}}\right)^{\top} \mathbf{T}_{\mathrm{d}}^{\mathrm{el}} \dfrac{\partial g_{\mathrm{TC}}}{\partial \mathbf{t}_{\mathrm{d}}} \\ \left(\dfrac{\partial f_{\mathrm{TC}}}{\partial \mathbf{t}_{\mathrm{d}}}\right)^{\top} \mathbf{T}_{\mathrm{d}}^{\mathrm{el}} \dfrac{\partial g_{\mathrm{MC}}}{\partial \mathbf{t}_{\mathrm{d}}} & \left(\dfrac{\partial f_{\mathrm{TC}}}{\partial \mathbf{t}_{\mathrm{d}}}\right)^{\top} \mathbf{T}_{\mathrm{d}}^{\mathrm{el}} \dfrac{\partial g_{\mathrm{TC}}}{\partial \mathbf{t}_{\mathrm{d}}} \end{bmatrix}_{(n+1)} \begin{bmatrix} \Delta\lambda_{\mathrm{MC}(n+1)} \\ \Delta\lambda_{\mathrm{TC}(n+1)} \end{bmatrix} = \begin{bmatrix} f_{\mathrm{MC}}^{\mathrm{trial}} \\ f_{\mathrm{TC}}^{\mathrm{trial}} \end{bmatrix}, \tag{B-33}$$

whose solution provides the plastic multiplier increments associated with the return to the intersection. The structure of the corresponding consistent tangent follows the general multi-surface plasticity framework and can be derived by linearizing the discrete update in a similar manner to the single-surface case.

C
Enhanced deformation modes

This appendix presents the derivation of the enhanced deformation modes considering a three-dimensional model and a displacement jump that is linear in the in-plane local coordinates of the discontinuity surface, following Armero and Kim [135].

C.1
Enrichment degrees of freedom

The displacement jump along the discontinuity in the discontinuity local coordinate system, $\{\mathbf{m}_1,\, \mathbf{m}_2,\, \mathbf{n}_\mathrm{d}\}$, is defined as

$$\mathbf{u}^h_\mathrm{d}(s_1, s_2) = \begin{bmatrix} u^{m_1}_\mathrm{d} \\ u^{m_2}_\mathrm{d} \\ u^{n}_\mathrm{d} \end{bmatrix} = \begin{bmatrix} \alpha^{m_1}_0 + s_1\, \alpha^{m_1}_1 + s_2\, \alpha^{m_1}_2 \\ \alpha^{m_2}_0 + s_1\, \alpha^{m_2}_1 + s_2\, \alpha^{m_2}_2 \\ \alpha^{n}_0 + s_1\, \alpha^{n}_1 + s_2\, \alpha^{n}_2 \end{bmatrix} \tag{C-1}$$

For $\mathbf{x} \in \Gamma_\mathrm{d}$, the local coordinates are $s_i(\mathbf{x}) = \mathbf{m}_i \cdot (\mathbf{x} - \mathbf{x}_\mathrm{ref})$, $i = 1, 2$.

C.2
Deformation modes

In the following, the deformation modes associated with each enriched DOF, $\boldsymbol{\alpha}_u$, are presented.

For the derivations, some vector identities are used:

$$\begin{aligned} (\mathbf{a} \times \mathbf{b}) \times \mathbf{c} &= (\mathbf{a} \cdot \mathbf{c})\, \mathbf{b} - (\mathbf{b} \cdot \mathbf{c})\, \mathbf{a}, \\ \left(\mathbf{a}\, \mathbf{b}^\top\right) \mathbf{c} &= (\mathbf{b} \cdot \mathbf{c})\, \mathbf{a}. \end{aligned}$$

C.2.1
Relative translation modes

The relative translation part of the enhanced displacement is written as

$$\tilde{\mathbf{u}}^h_\mathrm{tr}(\mathbf{x}) = \alpha^{m_1}_0\, \mathbf{m}_1 + \alpha^{m_2}_0\, \mathbf{m}_2 + \alpha^{n}_0\, \mathbf{n}_\mathrm{d}. \tag{C-2}$$

This expression corresponds to a constant jump field, independent of $\mathbf{x}$. The coefficients $\alpha^{m_1}_0$, $\alpha^{m_2}_0$ and α^{n}_0 control, respectively, the tangential translation along $\mathbf{m}_1$, the tangential translation along $\mathbf{m}_2$, and the normal opening/closure across the discontinuity, as illustrated in Fig. C.1.

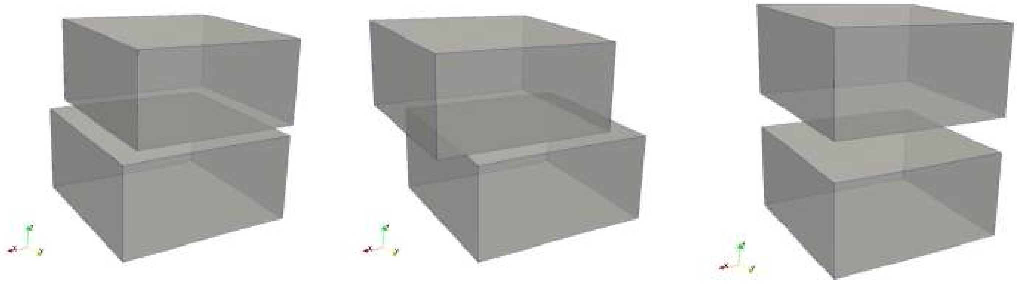

(a) $\alpha_0^{m_1}$ (b) $\alpha_0^{m_2}$ (c) α_0^{n}

Figure C.1: Constant relative translation deformation modes

C.2.2
Rotation around $\mathbf{m}_1$

The mode associated with α_2^n represents a rigid-body rotation around axis $\mathbf{m}_1$, as shown in Fig. C.2. It is defined as

$$\begin{aligned}\tilde{\mathbf{u}}_{\mathrm{r}1}^h(\mathbf{x}) &= \alpha_2^n \; (\mathbf{m}_1 \times \Delta\mathbf{x}) \\ &= \alpha_2^n \; ((\mathbf{m}_2 \times \mathbf{n}_\mathrm{d}) \times \Delta\mathbf{x}) \\ &= \alpha_2^n \; ((\mathbf{m}_2 \cdot \Delta\mathbf{x})\, \mathbf{n}_\mathrm{d} - (\mathbf{n}_\mathrm{d} \cdot \Delta\mathbf{x})\, \mathbf{m}_2) \\ &= \alpha_2^n \left(\mathbf{n}_\mathrm{d}\, \mathbf{m}_2{}^\top - \mathbf{m}_2\, \mathbf{n}_\mathrm{d}{}^\top \right) \Delta\mathbf{x},\end{aligned} \tag{C-3}$$

where $\Delta\mathbf{x} = \mathbf{x} - \mathbf{x}_{\mathrm{ref}}$.

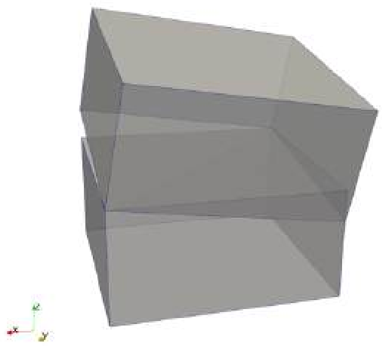

Figure C.2: Rotation around in-plane vector $\mathbf{m}_1$

C.2.3
Rotation around $\mathbf{m}_2$

The mode associated with α_1^n represents a rigid-body type rotation around $\mathbf{m}_2$, as shown in Fig. C.3. The sign is chosen so that, for $\mathbf{x} \in \Gamma_\mathrm{d}$, the induced normal jump has slope α_1^n with respect to s_1, consistent with the parametrization $u_\mathrm{d}^n = \alpha_0^n + s_1\, \alpha_1^n + s_2\, \alpha_2^n$:

$$\begin{aligned}\tilde{\mathbf{u}}^h_{\mathrm{r2}}(\mathbf{x}) &= -\alpha_1^n\ (\mathbf{m}_2 \times \Delta\mathbf{x}) \\ &= -\alpha_1^n\ ((\mathbf{n}_\mathrm{d} \times \mathbf{m}_1) \times \Delta\mathbf{x}) \\ &= -\alpha_1^n\ ((\mathbf{n}_\mathrm{d} \cdot \Delta\mathbf{x})\,\mathbf{m}_1 - (\mathbf{m}_1 \cdot \Delta\mathbf{x})\,\mathbf{n}_\mathrm{d}) \\ &= -\alpha_1^n\ \left(\mathbf{m}_1\,{\mathbf{n}_\mathrm{d}}^\top - \mathbf{n}_\mathrm{d}\,{\mathbf{m}_1}^\top\right)\Delta\mathbf{x}.\end{aligned} \tag{C-4}$$

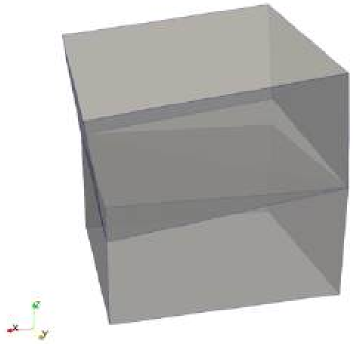

Figure C.3: Rotation around in-plane vector $\mathbf{m}_2$

C.2.4 Stretching

The modes associated with $\alpha_1^{m_1}$ and $\alpha_2^{m_2}$ correspond to relative stretching modes along the two tangential directions, as illustrated in Fig. C.4, and are defined by

$$\begin{aligned}\tilde{\mathbf{u}}^h_{\mathrm{st}}(\mathbf{x}) &= \alpha_1^{m_1}\ (\mathbf{m}_1 \cdot \Delta\mathbf{x})\,\mathbf{m}_1 + \alpha_2^{m_2}\ (\mathbf{m}_2 \cdot \Delta\mathbf{x})\,\mathbf{m}_2 \\ &= \alpha_1^{m_1}\ \left(\mathbf{m}_1\,{\mathbf{m}_1}^\top\right)\Delta\mathbf{x} + \alpha_2^{m_2}\ \left(\mathbf{m}_2\,{\mathbf{m}_2}^\top\right)\Delta\mathbf{x}.\end{aligned} \tag{C-5}$$

(a) $\alpha_1^{m_1}$ (b) $\alpha_2^{m_2}$

Figure C.4: Stretching deformation modes

C.2.5
In plane shear and rotation around the normal vector

The enriched DOFs $\alpha_1^{m_2}$ and $\alpha_2^{m_1}$ generate mixed in-plane modes, that couple the directions $\mathbf{m}_1$ and $\mathbf{m}_2$. They are defined as

The enriched DOFs $\alpha_1^{m_2}$ and $\alpha_2^{m_1}$ define a rotation around the normal vector. However, it is not a pure rotation; it consists of a pure rotation with an in-plane shear.

$$
\begin{aligned}
\tilde{\mathbf{u}}^h_{\text{mix}}(\mathbf{x}) &= \alpha_1^{m_2}\ (\mathbf{m}_2 \cdot \Delta\mathbf{x})\ \mathbf{m}_1 + \alpha_2^{m_1}\ (\mathbf{m}_1 \cdot \Delta\mathbf{x})\ \mathbf{m}_2 \\
&= \alpha_1^{m_2} \left(\mathbf{m}_1\, \mathbf{m}_2{}^{\top}\right) \Delta\mathbf{x} + \alpha_2^{m_1} \left(\mathbf{m}_2\, \mathbf{m}_1{}^{\top}\right) \Delta\mathbf{x}
\end{aligned}
\tag{C-6}
$$

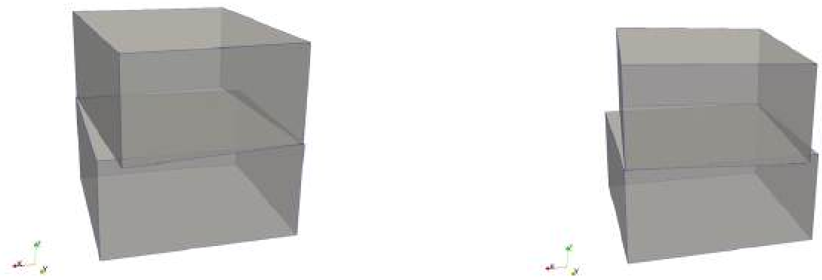

(a) $\alpha_1^{m_2}$ (b) $\alpha_2^{m_1}$

Figure C.5: In plane shear and rotation around the normal vector deformation modes

Decomposing the dyads into symmetric and antisymmetric parts yields an additive split into an in-plane shear component and a rigid rotation about $\mathbf{n}_\text{d}$:

$$
\tilde{\mathbf{u}}^h_{\text{mix}}(\mathbf{x}) = \tilde{\mathbf{u}}^h_{\text{nrot}}(\mathbf{x}) + \tilde{\mathbf{u}}^h_{\text{shear}}(\mathbf{x}) \tag{C-7}
$$

where

$$
\tilde{\mathbf{u}}^h_{\text{shear}}(\mathbf{x}) = (\alpha_1^{m_2} + \alpha_2^{m_1})\,\frac{1}{2}\left(\mathbf{m}_2\,\mathbf{m}_1{}^{\top} + \mathbf{m}_2\,\mathbf{m}_1{}^{\top}\right)\Delta\mathbf{x}, \tag{C-8}
$$

$$
\tilde{\mathbf{u}}^h_{\text{nrot}}(\mathbf{x}) = (\alpha_1^{m_2} - \alpha_2^{m_1})\,\frac{1}{2}\left(\mathbf{m}_2\,\mathbf{m}_1{}^{\top} - \mathbf{m}_2\,\mathbf{m}_1{}^{\top}\right)\Delta\mathbf{x} \tag{C-9}
$$

D
Discretized weak form

This appendix defines the sub-matrices appearing in the discrete residual vectors of the governing equations after applying the finite-element approximation of the displacement and pore-pressure fields introduced in Sec. 4.6.

$$
\begin{bmatrix} \mathbf{r}_\mathrm{u}(t_{n+1}) \\ \mathbf{r}_{\alpha_\mathrm{u}}(t_{n+1}) \\ \mathbf{r}_\mathrm{p}(t_{n+1}) \\ \mathbf{r}_{\alpha_\mathrm{p}}(t_{n+1}) \\ \mathbf{r}_{\mathrm{p_d}}(t_{n+1}) \end{bmatrix} = \begin{bmatrix} \mathbf{f}^\mathrm{i}_\mathrm{u}(t_{n+1}) \\ \mathbf{f}^\mathrm{i}_{\alpha_\mathrm{u}}(t_{n+1}) \\ \mathbf{f}^\mathrm{i}_\mathrm{p}(t_{n+1}) \\ \mathbf{f}^\mathrm{i}_{\alpha_\mathrm{p}}(t_{n+1}) \\ \mathbf{f}^\mathrm{i}_{\mathrm{p_d}}(t_{n+1}) \end{bmatrix} - \begin{bmatrix} \mathbf{f}^\mathrm{e}_\mathrm{u}(t_{n+1}) \\ \mathbf{f}^\mathrm{e}_{\alpha_\mathrm{u}}(t_{n+1}) \\ \mathbf{f}^\mathrm{e}_\mathrm{p}(t_{n+1}) \\ \mathbf{f}^\mathrm{e}_{\alpha_\mathrm{p}}(t_{n+1}) \\ \mathbf{f}^\mathrm{e}_{\mathrm{p_d}}(t_{n+1}) \end{bmatrix}
$$
$$
+ \begin{bmatrix} \mathbf{0} & \mathbf{0} & -\mathbf{Q}_{\mathrm{pu}}{}^\top & -\mathbf{Q}_{\alpha_\mathrm{p}\mathrm{u}}{}^\top & \mathbf{0} \\ \mathbf{0} & \mathbf{0} & -\mathbf{Q}_{\alpha_\mathrm{u}\mathrm{p}} & -\mathbf{Q}_{\alpha_\mathrm{u}\alpha_\mathrm{p}} & -\mathbf{Q}_{\alpha_\mathrm{u}\mathrm{p_d}} \\ \mathbf{0} & \mathbf{0} & \mathbf{H}_{\mathrm{pp}} + \mathbf{L}_{\mathrm{pp}} & \mathbf{H}_{\mathrm{p}\alpha_\mathrm{p}} + \mathbf{L}_{\mathrm{p}\alpha_\mathrm{p}} & -\mathbf{L}_{\mathrm{pp_d}} \\ \mathbf{0} & \mathbf{0} & \mathbf{H}_{\alpha_\mathrm{p}\mathrm{p}} + \mathbf{L}_{\alpha_\mathrm{p}\mathrm{p}} & \mathbf{H}_{\alpha_\mathrm{p}\alpha_\mathrm{p}} + \mathbf{L}_{\alpha_\mathrm{p}\alpha_\mathrm{p}} & -\mathbf{L}_{\alpha_\mathrm{p}\mathrm{p_d}} \\ \mathbf{0} & \mathbf{0} & -\mathbf{L}_{\mathrm{p_d p}} & -\mathbf{L}_{\mathrm{p_d}\alpha_\mathrm{p}} & \mathbf{H}_{\mathrm{p_d p_d}} + \mathbf{L}_{\mathrm{p_d p_d}} \end{bmatrix} \begin{bmatrix} \mathbf{d}(t_{n+1}) \\ \boldsymbol{\alpha}_\mathrm{u}(t_{n+1}) \\ \mathbf{p}(t_{n+1}) \\ \boldsymbol{\alpha}_\mathrm{p}(t_{n+1}) \\ \mathbf{p}_\mathrm{d}(t_{n+1}) \end{bmatrix}
$$
$$
+ \frac{1}{\Delta t} \begin{bmatrix} \mathbf{0} & \mathbf{0} & \mathbf{0} & \mathbf{0} & \mathbf{0} \\ \mathbf{0} & \mathbf{0} & \mathbf{0} & \mathbf{0} & \mathbf{0} \\ \mathbf{Q}_{\mathrm{pu}} & \mathbf{Q}_{\mathrm{p}\alpha_\mathrm{u}} & \mathbf{S}_{\mathrm{pp}} & \mathbf{S}_{\mathrm{p}\alpha_\mathrm{p}} & \mathbf{0} \\ \mathbf{Q}_{\alpha_\mathrm{p}\mathrm{u}} & \mathbf{Q}_{\alpha_\mathrm{p}\alpha_\mathrm{u}} & \mathbf{S}_{\alpha_\mathrm{p}\mathrm{p}} & \mathbf{S}_{\alpha_\mathrm{p}\alpha_\mathrm{p}} & \mathbf{0} \\ \mathbf{Q}_{\mathrm{p_d u}} & \mathbf{Q}_{\mathrm{p_d}\alpha_\mathrm{u}} & \mathbf{0} & \mathbf{0} & \mathbf{S}_{\mathrm{p_d p_d}} \end{bmatrix} \begin{bmatrix} \mathbf{d}(t_{n+1}) - \mathbf{d}(t_n) \\ \boldsymbol{\alpha}_\mathrm{u}(t_{n+1}) - \boldsymbol{\alpha}_\mathrm{u}(t_n) \\ \mathbf{p}(t_{n+1}) - \mathbf{p}(t_n) \\ \boldsymbol{\alpha}_\mathrm{p}(t_{n+1}) - \boldsymbol{\alpha}_\mathrm{p}(t_n) \\ \mathbf{p}_\mathrm{d}(t_{n+1}) - \mathbf{p}_\mathrm{d}(t_n) \end{bmatrix}
$$

D.1
Definition of the sub-matrices

The internal force/flow vectors $\mathbf{f}^\mathrm{i}_\bullet$ are given by

$$\mathbf{f}^\mathrm{i}_\mathrm{u} = \int_\Omega \mathbf{B}_\mathrm{u}{}^\top \boldsymbol{\Sigma}(\boldsymbol{\varepsilon})\, d\Omega, \tag{D-1}$$

$$\mathbf{f}^\mathrm{i}_{\alpha_\mathrm{u}} = \int_\Omega \mathbf{G}^\top \boldsymbol{\Sigma}(\boldsymbol{\varepsilon})\, d\Omega + \int_{\Gamma_\mathrm{d}} \mathbf{N}_{\mathrm{du}}{}^\top \mathbf{t}'_\mathrm{d}\, d\Gamma, \tag{D-2}$$

$$\mathbf{f}^\mathrm{i}_\mathrm{p} = \mathbf{0}, \tag{D-3}$$

$$\mathbf{f}^\mathrm{i}_{\alpha_\mathrm{p}} = \mathbf{0}, \tag{D-4}$$

$$\mathbf{f}^\mathrm{i}_{\mathrm{p_d}} = \mathbf{0}. \tag{D-5}$$

The external load/flow vectors $\mathbf{f}^\mathrm{e}_\bullet$ account for gravity and prescribed

Neumann data, and read

$$\mathbf{f}^{\mathrm{e}}_{\mathrm{u}} = \int_{\Gamma^{u}_{\mathrm{N}}} \mathbf{N}_{\mathrm{u}}{}^{\top}\, \mathbf{t}_0 \, d\Gamma + \int_{\Omega} \mathbf{N}_{\mathrm{u}}{}^{\top}\, \mathbf{b} \, d\Omega, \tag{D-6}$$

$$\mathbf{f}^{\mathrm{e}}_{\alpha_{\mathrm{u}}} = \mathbf{0}, \tag{D-7}$$

$$\mathbf{f}^{\mathrm{e}}_{\mathrm{p}} = \int_{\Omega} \mathbf{B}_{\mathrm{p}}{}^{\top}\, \frac{\mathbf{k}}{\mu_{\mathrm{l}}}\, \rho_{\mathrm{l}}\, \mathbf{g} \, d\Omega \; - \; \int_{\Gamma^{\mathrm{p}}_{\mathrm{N}}} \mathbf{N}_{\mathrm{p}}{}^{\top}\, q_0 \, d\Gamma, \tag{D-8}$$

$$\mathbf{f}^{\mathrm{e}}_{\alpha_{\mathrm{p}}} = \int_{\Omega} \widetilde{\mathbf{B}}_{\mathrm{p}}^{\top}\, \frac{\mathbf{k}}{\mu_{\mathrm{l}}}\, \rho_{\mathrm{l}}\, \mathbf{g} \, d\Omega \; - \; \int_{\Gamma^{\mathrm{p}}_{\mathrm{N}}} \widetilde{\mathbf{N}}_{\mathrm{p}}^{\top}\, q_0 \, d\Gamma, \tag{D-9}$$

$$\mathbf{f}^{\mathrm{e}}_{\mathrm{p_d}} = \int_{\Gamma_{\mathrm{d}}} \mathbf{B}_{\mathrm{dp}}{}^{\top}\, w\, \frac{k^{\mathrm{L}}_{\mathrm{d}}}{\mu_{\mathrm{l}}}\, \rho_{\mathrm{l}}\, \mathbf{m}_{\mathrm{d}}{}^{\top} \mathbf{g} \, d\Gamma. \tag{D-10}$$

The storage matrices, $\mathbf{S}_{\bullet\bullet}$, are

$$\mathbf{S}_{\mathrm{pp}} = \int_{\Omega} \mathbf{N}_{\mathrm{p}}{}^{\top}\, \frac{1}{M}\, \mathbf{N}_{\mathrm{p}} \, d\Omega, \tag{D-11}$$

$$\mathbf{S}_{\mathrm{p}\alpha_{\mathrm{p}}} = \int_{\Omega} \mathbf{N}_{\mathrm{p}}{}^{\top}\, \frac{1}{M}\, \widetilde{\mathbf{N}}_{\mathrm{p}} \, d\Omega, \tag{D-12}$$

$$\mathbf{S}_{\alpha_{\mathrm{p}}\mathrm{p}} = \int_{\Omega} \widetilde{\mathbf{N}}_{\mathrm{p}}^{\top}\, \frac{1}{M}\, \mathbf{N}_{\mathrm{p}} \, d\Omega, \tag{D-13}$$

$$\mathbf{S}_{\alpha_{\mathrm{p}}\alpha_{\mathrm{p}}} = \int_{\Omega} \widetilde{\mathbf{N}}_{\mathrm{p}}^{\top}\, \frac{1}{M}\, \widetilde{\mathbf{N}}_{\mathrm{p}} \, d\Omega, \tag{D-14}$$

$$\mathbf{S}_{\mathrm{p_d p_d}} = \int_{\Gamma_{\mathrm{d}}} \mathbf{N}_{\mathrm{dp}}{}^{\top}\, \frac{w}{K_{\mathrm{l}}}\, \mathbf{N}_{\mathrm{dp}} \, d\Gamma. \tag{D-15}$$

The conductivity matrices $\mathbf{H}_{\bullet\bullet}$ associated with Darcy flow in the porous matrix are

$$\mathbf{H}_{\mathrm{pp}} = \int_{\Omega} \mathbf{B}_{\mathrm{p}}{}^{\top}\, \frac{\mathbf{k}}{\mu_{\mathrm{l}}}\, \mathbf{B}_{\mathrm{p}} \, d\Omega, \tag{D-16}$$

$$\mathbf{H}_{\mathrm{p}\alpha_{\mathrm{p}}} = \int_{\Omega} \mathbf{B}_{\mathrm{p}}{}^{\top}\, \frac{\mathbf{k}}{\mu_{\mathrm{l}}}\, \widetilde{\mathbf{B}}_{\mathrm{p}} \, d\Omega, \tag{D-17}$$

$$\mathbf{H}_{\alpha_{\mathrm{p}}\mathrm{p}} = \int_{\Omega} \widetilde{\mathbf{B}}_{\mathrm{p}}^{\top}\, \frac{\mathbf{k}}{\mu_{\mathrm{l}}}\, \mathbf{B}_{\mathrm{p}} \, d\Omega, \tag{D-18}$$

$$\mathbf{H}_{\alpha_{\mathrm{p}}\alpha_{\mathrm{p}}} = \int_{\Omega} \widetilde{\mathbf{B}}_{\mathrm{p}}^{\top}\, \frac{\mathbf{k}}{\mu_{\mathrm{l}}}\, \widetilde{\mathbf{B}}_{\mathrm{p}} \, d\Omega, \tag{D-19}$$

$$\mathbf{H}_{\mathrm{p_d p_d}} = \int_{\Gamma_{\mathrm{d}}} \mathbf{B}_{\mathrm{dp}}{}^{\top}\, w\, \frac{k^{\mathrm{L}}_{\mathrm{d}}}{\mu_{\mathrm{l}}}\, \mathbf{B}_{\mathrm{dp}} \, d\Gamma. \tag{D-20}$$

The hydro–mechanical coupling matrices $\mathbf{Q}_{\bullet\bullet}$ are

$$\mathbf{Q}_{\alpha_{\rm u}\rm p} = \int_\Omega \mathbf{G}^\top \alpha\, \mathbf{m}\, \mathbf{N}_{\rm p}\, d\Omega, \tag{D-21}$$

$$\mathbf{Q}_{\alpha_{\rm u}\alpha_{\rm p}} = \int_\Omega \mathbf{G}^\top \alpha\, \mathbf{m}\, \widetilde{\mathbf{N}}_{\rm p}\, d\Omega, \tag{D-22}$$

$$\mathbf{Q}_{\alpha_{\rm u}\rm p_d} = \int_{\Gamma_{\rm d}} \mathbf{N}_{\rm du}{}^\top\, \widehat{\mathbf{n}}_{\rm d}\, \mathbf{N}_{\rm dp} d\Gamma \tag{D-23}$$

$$\mathbf{Q}_{\rm pu} = \int_\Omega \mathbf{N}_{\rm p}{}^\top \alpha\, \mathbf{m}^\top\, \mathbf{B}_{\rm u}\, d\Omega, \tag{D-24}$$

$$\mathbf{Q}_{\rm p\alpha_u} = \int_\Omega \mathbf{N}_{\rm p}{}^\top \alpha\, \mathbf{m}^\top\, \widetilde{\mathbf{B}}_{\rm u}\, d\Omega, \tag{D-25}$$

$$\mathbf{Q}_{\alpha_{\rm p}\rm u} = \int_\Omega \widetilde{\mathbf{N}}_{\rm p}^\top \alpha\, \mathbf{m}^\top\, \mathbf{B}_{\rm u}\, d\Omega, \tag{D-26}$$

$$\mathbf{Q}_{\alpha_{\rm p}\alpha_{\rm u}} = \int_\Omega \widetilde{\mathbf{N}}_{\rm p}^\top \alpha\, \mathbf{m}^\top\, \widetilde{\mathbf{B}}_{\rm u}\, d\Omega, \tag{D-27}$$

$$\mathbf{Q}_{\rm p_d u} = \int_{\Gamma_{\rm d}} \mathbf{N}_{\rm dp}{}^\top w\, \mathbf{r}_{\rm s}\, \mathbf{B}_{\rm u}\; d\Gamma, \tag{D-28}$$

$$\mathbf{Q}_{\rm p_d\alpha_u} = \int_{\Gamma_{\rm d}} \mathbf{N}_{\rm dp}{}^\top\, \widehat{\mathbf{n}}_{\rm d}^\top \mathbf{N}_{\rm du}\, d\Gamma + \int_{\Gamma_{\rm d}} \mathbf{N}_{\rm dp}{}^\top w\, \mathbf{r}_{\rm s} \left\langle \widetilde{\mathbf{B}}_{\rm u} \right\rangle\; d\Gamma. \tag{D-29}$$

where $\mathbf{r}_{\rm s} = \mathbf{r}_\varepsilon(\mathbf{m}_1) + \mathbf{r}_\varepsilon(\mathbf{m}_2)$.

The flow-coupling matrices between the porous medium and the discontinuity, $\mathbf{L}_{\bullet\bullet}$, are

$$\mathbf{L}_{\rm pp} = \int_{\Gamma_{\rm d}} \mathbf{N}_{\rm p}{}^\top \left(k_{\rm d}^{\rm t+} + k_{\rm d}^{\rm t-}\right) \mathbf{N}_{\rm p}\, d\Gamma, \tag{D-30}$$

$$\mathbf{L}_{\rm p\alpha_p} = \int_{\Gamma_{\rm d}} \mathbf{N}_{\rm p}{}^\top \left(k_{\rm d}^{\rm t+}\widetilde{\mathbf{N}}_{\rm p}^{+} + k_{\rm d}^{\rm t-}\widetilde{\mathbf{N}}_{\rm p}^{-}\right) d\Gamma, \tag{D-31}$$

$$\mathbf{L}_{\rm pp_d} = \int_{\Gamma_{\rm d}} \mathbf{N}_{\rm p}{}^\top \left(k_{\rm d}^{\rm t+} + k_{\rm d}^{\rm t-}\right) \mathbf{N}_{\rm dp}\, d\Gamma, \tag{D-32}$$

$$\mathbf{L}_{\alpha_{\rm p}\rm p} = \int_{\Gamma_{\rm d}} \widetilde{\mathbf{N}}_{\rm p}^\top \left(k_{\rm d}^{\rm t+} + k_{\rm d}^{\rm t-}\right) \mathbf{N}_{\rm p}\, d\Gamma, \tag{D-33}$$

$$\mathbf{L}_{\alpha_{\rm p}\alpha_{\rm p}} = \int_{\Gamma_{\rm d}} \widetilde{\mathbf{N}}_{\rm p}^\top \left(k_{\rm d}^{\rm t+}\widetilde{\mathbf{N}}_{\rm p}^{+} + k_{\rm d}^{\rm t-}\widetilde{\mathbf{N}}_{\rm p}^{-}\right) d\Gamma, \tag{D-34}$$

$$\mathbf{L}_{\alpha_{\rm p}\rm p_d} = \int_{\Gamma_{\rm d}} \widetilde{\mathbf{N}}_{\rm p}^\top \left(k_{\rm d}^{\rm t+} + k_{\rm d}^{\rm t-}\right) \mathbf{N}_{\rm dp}\, d\Gamma, \tag{D-35}$$

$$\mathbf{L}_{\rm p_d p} = \int_{\Gamma_{\rm d}} \mathbf{N}_{\rm dp}{}^\top\, k_{\rm d}^{\rm t}\, \mathbf{N}_{\rm p}\, d\Gamma, \tag{D-36}$$

$$\mathbf{L}_{\rm p_d\alpha_p} = \int_{\Gamma_{\rm d}} \mathbf{N}_{\rm dp}{}^\top \left(k_{\rm d}^{\rm t+}\widetilde{\mathbf{N}}_{\rm p}^{+} + k_{\rm d}^{\rm t-}\widetilde{\mathbf{N}}_{\rm p}^{-}\right) d\Gamma, \tag{D-37}$$

$$\mathbf{L}_{\rm p_d p_d} = \int_{\Gamma_{\rm d}} \mathbf{N}_{\rm dp}{}^\top\, k_{\rm d}^{\rm t}\, \mathbf{N}_{\rm dp}\, d\Gamma. \tag{D-38}$$

where $k_{\mathrm{d}}^{\mathrm{t}} = k_{\mathrm{d}}^{\mathrm{t}+} + k_{\mathrm{d}}^{\mathrm{t}-}$.

D.2 Derivatives of the residual vector with respect to the DOFs

The Jacobian blocks associated with $\mathbf{r}_u$ are

$$\frac{\partial \mathbf{r}_u}{\partial \mathbf{d}} = \frac{\partial \mathbf{f}_{\mathrm{u}}^{\mathrm{i}}}{\partial \mathbf{d}} = \int_{\Omega} \mathbf{B}_{\mathrm{u}}{}^{\top} \mathbf{D}\, \mathbf{B}_{\mathrm{u}}\, d\Omega \tag{D-39}$$

$$\frac{\partial \mathbf{r}_u}{\partial \boldsymbol{\alpha}_{\mathrm{u}}} = \frac{\partial \mathbf{f}_{\mathrm{u}}^{\mathrm{i}}}{\partial \boldsymbol{\alpha}_{\mathrm{u}}} = \int_{\Omega} \mathbf{B}_{\mathrm{u}}{}^{\top} \mathbf{D}\, \widetilde{\mathbf{B}}_{\mathrm{u}}\, d\Omega, \tag{D-40}$$

$$\frac{\partial \mathbf{r}_u}{\partial \mathbf{p}} = -\mathbf{Q}_{\mathrm{pu}}{}^{\top}, \tag{D-41}$$

$$\frac{\partial \mathbf{r}_u}{\partial \boldsymbol{\alpha}_{\mathrm{p}}} = -\mathbf{Q}_{\alpha_{\mathrm{p}}\mathrm{u}}{}^{\top}, \tag{D-42}$$

$$\frac{\partial \mathbf{r}_u}{\partial \mathbf{p}_{\mathrm{d}}} = \mathbf{0}, \tag{D-43}$$

where $\mathbf{D}$ is the bulk tangent constitutive matrix.

For $\mathbf{r}_{\alpha_{\mathrm{u}}}$, the corresponding derivatives are

$$\frac{\partial \mathbf{r}_{\alpha_{\mathrm{u}}}}{\partial \mathbf{d}} = \frac{\partial \mathbf{f}_{\alpha_{\mathrm{u}}}^{\mathrm{i}}}{\partial \mathbf{d}} = \int_{\Omega} \mathbf{G}^{\top} \mathbf{D}\, \mathbf{B}_{\mathrm{u}}\, d\Omega, \tag{D-44}$$

$$\frac{\partial \mathbf{r}_{\alpha_{\mathrm{u}}}}{\partial \boldsymbol{\alpha}_{\mathrm{u}}} = \frac{\partial \mathbf{f}_{\alpha_{\mathrm{u}}}^{\mathrm{i}}}{\partial \boldsymbol{\alpha}_{\mathrm{u}}} = \int_{\Omega} \mathbf{G}^{\top} \mathbf{D}\, \widetilde{\mathbf{B}}_{\mathrm{u}}\, d\Omega + \int_{\Gamma_{\mathrm{d}}} \mathbf{N}_{\mathrm{du}}{}^{\top} \mathbf{T}_{\mathrm{d}}\, \mathbf{N}_{\mathrm{du}}\, d\Gamma, \tag{D-45}$$

$$\frac{\partial \mathbf{r}_{\alpha_{\mathrm{u}}}}{\partial \mathbf{p}} = -\mathbf{Q}_{\alpha_{\mathrm{u}}\mathrm{p}}, \tag{D-46}$$

$$\frac{\partial \mathbf{r}_{\alpha_{\mathrm{u}}}}{\partial \boldsymbol{\alpha}_{\mathrm{p}}} = -\mathbf{Q}_{\alpha_{\mathrm{u}}\alpha_{\mathrm{p}}}, \tag{D-47}$$

$$\frac{\partial \mathbf{r}_{\alpha_{\mathrm{u}}}}{\partial \mathbf{p}_{\mathrm{d}}} = -\mathbf{Q}_{\alpha_{\mathrm{u}}\mathrm{p}_{\mathrm{d}}}, \tag{D-48}$$

where $\mathbf{T}_{\mathrm{d}}$ is the tangent cohesive matrix.

For $\mathbf{r}_p$, the corresponding derivatives are

$$\frac{\partial \mathbf{r}_p}{\partial \mathbf{d}} = \frac{1}{\Delta t}\mathbf{Q}_{\mathrm{pu}}, \tag{D-49}$$

$$\frac{\partial \mathbf{r}_p}{\partial \boldsymbol{\alpha}_{\mathrm{u}}} = \frac{1}{\Delta t}\mathbf{Q}_{\mathrm{p}\alpha_{\mathrm{u}}}, \tag{D-50}$$

$$\frac{\partial \mathbf{r}_p}{\partial \mathbf{p}} = \mathbf{H}_{\mathrm{pp}} + \mathbf{L}_{\mathrm{pp}} + \frac{1}{\Delta t}\mathbf{S}_{\mathrm{pp}}, \tag{D-51}$$

$$\frac{\partial \mathbf{r}_p}{\partial \boldsymbol{\alpha}_\mathrm{p}} = \mathbf{H}_{\mathrm{p}\alpha_\mathrm{p}} + \mathbf{L}_{\mathrm{p}\alpha_\mathrm{p}} + \frac{1}{\Delta t}\mathbf{S}_{\mathrm{p}\alpha_\mathrm{p}}, \tag{D-52}$$

$$\frac{\partial \mathbf{r}_p}{\partial \mathbf{p}_\mathrm{d}} = -\mathbf{L}_{\mathrm{p}\mathrm{p}_\mathrm{d}}. \tag{D-53}$$

For $\mathbf{r}_{\alpha_\mathrm{p}}$, the corresponding derivatives are

$$\frac{\partial \mathbf{r}_{\alpha_\mathrm{p}}}{\partial \mathbf{d}} = \frac{1}{\Delta t}\mathbf{Q}_{\alpha_\mathrm{p}\mathrm{u}}, \tag{D-54}$$

$$\frac{\partial \mathbf{r}_{\alpha_\mathrm{p}}}{\partial \boldsymbol{\alpha}_\mathrm{u}} = \frac{1}{\Delta t}\mathbf{Q}_{\alpha_\mathrm{p}\alpha_\mathrm{u}}, \tag{D-55}$$

$$\frac{\partial \mathbf{r}_{\alpha_\mathrm{p}}}{\partial \mathbf{p}} = \mathbf{H}_{\alpha_\mathrm{p}\mathrm{p}} + \mathbf{L}_{\alpha_\mathrm{p}\mathrm{p}} + \frac{1}{\Delta t}\mathbf{S}_{\alpha_\mathrm{p}\mathrm{p}}, \tag{D-56}$$

$$\frac{\partial \mathbf{r}_{\alpha_\mathrm{p}}}{\partial \boldsymbol{\alpha}_\mathrm{p}} = \mathbf{H}_{\alpha_\mathrm{p}\alpha_\mathrm{p}} + \mathbf{L}_{\alpha_\mathrm{p}\alpha_\mathrm{p}} + \frac{1}{\Delta t}\mathbf{S}_{\alpha_\mathrm{p}\alpha_\mathrm{p}}, \tag{D-57}$$

$$\frac{\partial \mathbf{r}_{\alpha_\mathrm{p}}}{\partial \mathbf{p}_\mathrm{d}} = -\mathbf{L}_{\alpha_\mathrm{p}\mathrm{p}_\mathrm{d}}. \tag{D-58}$$

For $\mathbf{r}_{\mathrm{p}_\mathrm{d}}$, the corresponding derivatives are

$$\frac{\partial \mathbf{r}_{\mathrm{p}_\mathrm{d}}}{\partial \mathbf{d}} = \frac{1}{\Delta t}\mathbf{Q}_{\mathrm{p}_\mathrm{d}\mathrm{u}}, \tag{D-59}$$

$$\frac{\partial \mathbf{r}_{\mathrm{p}_\mathrm{d}}}{\partial \boldsymbol{\alpha}_\mathrm{u}} = \frac{1}{\Delta t}\mathbf{Q}_{\mathrm{p}_\mathrm{d}\alpha_\mathrm{u}}, \tag{D-60}$$

$$\frac{\partial \mathbf{r}_{\mathrm{p}_\mathrm{d}}}{\partial \mathbf{p}} = -\mathbf{L}_{\mathrm{p}_\mathrm{d}\mathrm{p}}, \tag{D-61}$$

$$\frac{\partial \mathbf{r}_{\mathrm{p}_\mathrm{d}}}{\partial \boldsymbol{\alpha}_\mathrm{p}} = -\mathbf{L}_{\mathrm{p}_\mathrm{d}\alpha_\mathrm{p}}, \tag{D-62}$$

$$\frac{\partial \mathbf{r}_{\mathrm{p}_\mathrm{d}}}{\partial \mathbf{p}_\mathrm{d}} = \mathbf{H}_{\mathrm{p}_\mathrm{d}\mathrm{p}_\mathrm{d}} + \mathbf{L}_{\mathrm{p}_\mathrm{d}\mathrm{p}_\mathrm{d}} + \frac{1}{\Delta t}\mathbf{S}_{\mathrm{p}_\mathrm{d}\mathrm{p}_\mathrm{d}}. \tag{D-63}$$